ISOSPIN-BREAKING INTERACTIONS IN THE NUCLEAR SHELL MODEL

By

Aaron Magilligan

A DISSERTATION

Submitted to
Michigan State University
in partial fulfillment of the requirements
for the degree of

Physics – Doctor of Philosophy

2021

ABSTRACT

ISOSPIN-BREAKING INTERACTIONS IN THE NUCLEAR SHELL MODEL

By

Aaron Magilligan

The ever advancing scale of experimental nuclear physics has lit a fire under nuclear theorists. With the inevitable explosion in the number of exotic isotopes available for study at the soon to be operational Facility for Rare Isotope Beams and other rare isotope labs, the need for quantitative descriptions of nuclei far from stability is clear.

The Nuclear Shell Model allows for the calculation of realistic nuclear wavefunctions using configuration-interaction theory. This theory examines only the valence nucleons in a restricted model space or "nuclear shell" and treats the filled shells in the core of the nucleus as inert. Interactions used in this theory usually take the form of one- and two-body terms which can be built up from fundamental theory using various many-body methods and are continually being improved. The *ab initio* based methods now include three-body interactions together with improved methods for handling short range correlations and model space truncations. This enables them to describe binding energies within several MeV and energy spectra within about 500 keV.

One can phenomenologically improve upon these interactions by using the energy data for nuclei in a given mass region to obtain effective two-body matrix elements for a given model space. The best method for doing this is to start with an *ab initio* based Hamiltonian and then to modify the best determined linear combinations of interaction parameters as determined by the energy data using what is called the singular value decomposition method. This can be thought of as a truncation of the allowed parameter space. The result is that both binding and excitation energies can be described to within 150-200 keV. The relatively small modifications to the *ab initio* interaction parameters reflect deficiencies in the many-body methods and their inputs.

This method has resulted in widely used Hamiltonians for several model spaces. Universal effective *sd*-shell Hamiltonians have a history dating back to the 1970s, and the newest updates are

presented in this dissertation. The USDC interaction, as it is called, and its companion interactions are the first effective *sd*-shell interactions that incorporate energies in the fitting protocol from proton-rich nuclei and explicitly includes isospin-breaking terms. Apart from the addition of a Coulomb interaction, an isotensor term is added to the strong interaction in order to reproduce the oscillation found in the *c*-coefficients of the Isobaric Multiplet Mass Equation. A modified version of Coulomb is used in the USDCm interaction, which was constrained to better reproduce mirror energy differences.

Experimental binding and excitation energies across the shell are reproduced by USDC, apart from the known island of inversion nuclei and the neutron-rich fluorine isotopes. A single-particle model of the Thomas-Ehrman shift is developed to account for coupling to the continuum not present in the shell model results for nuclei at or near the proton dripline. Using this model and the improved theoretical binding energies, new predictions for the proton and neutron driplines are presented. The possibility of ^{34}Ca being a two-neutron emitter is explored.

Isospin level mixing of isobaric analogue states with nearby states can significantly impact nuclear decays. Several cases with experimentally measured isospin mixing are explained with the new interactions. However, USDCm over-predicts the strength of the associated matrix elements. This motivates a refinement of USDC in which an isovector term is added to the strong interaction and constrained to reproduce changes of mirror energy differences in the isobaric doublets. This is shown to provide the benefits of the modified Coulomb interaction without its detriments.

An effective *fp*-shell interaction is presented tailored to the neutron rich calcium isotopes out to ^{60}Ca. This is constrained with the nuclear interaction fitting code FINCH, developed during the creation of the USDC interactions. This interaction is shown to be a good renormalized *fp*-shell interaction and several predictions for unobserved states are presented. Using this and inter-model comparisons leads us to conclude that ^{60}Ca is likely doubly-magic to a similar level as ^{68}Ni.

Following these successful implementations of effective universal configuration-interaction Hamiltonians, future research aims to develop an *sdpf* model space interaction for deeper study of the $N =20$, 28, and 42 islands of inversion.

This work is dedicated to my brother Mikey.
Without his love, encouragement, and support this would not have been possible.

ACKNOWLEDGEMENTS

Like everyone who has ever accomplished anything, I did not do this alone. I would be remiss to not first thank my parents, Joe and Wendy, who provided me with unconditional love and support while also instilling in me an intellectual curiosity that drove me into science. Along with them, my brother Michael has been a constant foundation in my life, never more than a phone call away. To the rest of my family, who when I am able to see them always make me feel like I never even left home, thank you.

I would like to express my deepest appreciation to my committee chair and research advisor, Alex Brown. His guidance and unwavering support of my academic progress was instrumental in my completion of the program, for which I will always be grateful. Conversations I have had with Heiko Hergert and Christopher Wrede were crucial in my development as a nuclear physicist. To them and the other members of the committee, Kirsten Tollefson and Carlo Piermarocchi, who have helped to steer me through the perilous waters of graduate school, I say thank you. Early on I was taught the most important rule for success in the program: keep Kim Crosslan happy. I like to think that I've stayed on her good side and it's a shame I won't see have her to lean on at work anymore. I'd also like to thank one of the most interesting people I've ever met, Scott Pratt, for his advice and encouragement throughout my time here. Of course, I would not have had the opportunity of meeting the great people here if I did not first meet Jorge Piekarewicz. As my undergraduate research advisor, he provided indispensable advice and inspiration.

Outside of my family and academics, there have been countless people who have left an impact, big or small, on my life. While I can't list everyone, I would like to thank a few special people that deserve recognition. There are some friendships so strong that they may as well be family. Keon and Zach have been my brothers for over half of my life and, even though we've been separated by geography, they always will be. Lastly, my partner Morgan has had to put up with me more than any other person. Without your love and support during the turmoil of the past years I don't know where I'd be. You brighten up my life and I hope I brighten yours.

TABLE OF CONTENTS

LIST OF TABLES

CHAPTER 1

FOUNDATIONS

The goal of this opening chapter is to lay out the foundations of nuclear physics needed to follow along with the work contained in this dissertation. Each section will cover an individual topic, so that the reader need only review those sections with which they are unfamiliar. These are not meant to be comprehensive, but rather serve as in introduction to the terminology and ideas that will be used throughout later chapters.

It is estimated that the universe is made up of roughly 68% dark energy and 27% dark matter, with the remaining 5% being made up of the "ordinary" matter with which we are all familiar. This ordinary matter is governed by the Standard Model of particle physics and consists of quarks, leptons, and the force carrying particles called bosons. The quarks come together to achieve stability in groups of two (mesons) or three (baryons) called hadrons. Baryons primarily come in two forms and are called nucleons. These nucleons can have either a positive electric charge (protons) or a neutral charge (neutrons).

These nucleons can then in turn be held together by the nuclear strong force in groups called nuclei. Due to the positive charge of the protons, these nuclei attract electrons (a type of lepton with a negative charge) to form neutrally charged atoms. These atoms in turn make up all of the "stuff" that we interact with on a day-to-day basis. Every star, every moon, every book, every person, consists of an absolutely massive number of different kinds of atoms in different configurations.

However, it is the realm of chemistry to discuss the interactions of atoms. Instead, we are interested in what lies at the center of those atoms. Inside stars the intense heat and pressure causes atoms to become ionized and lose their electrons, leaving behind only the nucleus of protons and neutrons. It is these nuclei that drive the evolution of the stars and galaxies, so to understand those objects at the largest scales we must study the internal structure of an object 10,000,000,000,000 times smaller than a baseball.

To do so, we will first define a number of terms needed to discuss nuclei in general. Then

we will introduce gradually more and more complex models of the nucleus and its properties, culminating in the Nuclear Shell Model and the development of universal effective Hamiltonians for use in Configuration-Interaction calculations.

1.1 Building the Chart of the Nuclides

All atoms in the universe consist of a core nucleus that contains almost all of the atom's mass. The nucleus is composed of protons and neutrons, which are collectively called nucleons. A nucleus in an atom is surrounded by an "electron cloud" that is 100,000 to 1,000,000 times larger than the nucleus itself. An electrically neutral atom will have an equal number of protons and electrons. We differentiate atoms from one another first by giving them element names based on the number of protons in their nucleus which we call Z.

The Periodic Table of Elements is an organizational tool to show the chemical properties of all of the elements that exist in nature. It does this by organizing the elements in order of proton number in columns corresponding to the electron cloud configurations that control the chemical properties of the element. This is an excellent tool for chemists, however in nuclear physics we must be able to differentiate a carbon atom with 7 neutrons and a carbon atom with 8 neutrons. While they may behave similarly chemically, the structure and decay properties of the nuclei at the center of the atoms can be very different.

We call these different atoms within the same element family (same Z) "isotopes." They are denoted as $^A_N Z$ where N is the number of neutrons and A is the atomic mass number defined as the total number of protons and neutrons or $N + Z$. Each pair of proton and neutron numbers corresponds to a distinct nucleus called a nuclide. You can then imagine unfolding the periodic table into a grid, with the proton number on the Y-axis and the neutron number on the X-axis. This forms the basis of the Chart of the Nuclides, and is shown in Fig. 1.1.

While there are only 118 known elements, there are over 3,000 isotopes that have been measured experimentally! Over 70 of these were discovered at Michigan State University's National Superconducting Cyclotron Lab (NSCL) [2]. Additionally, nuclear theory predicts that there are
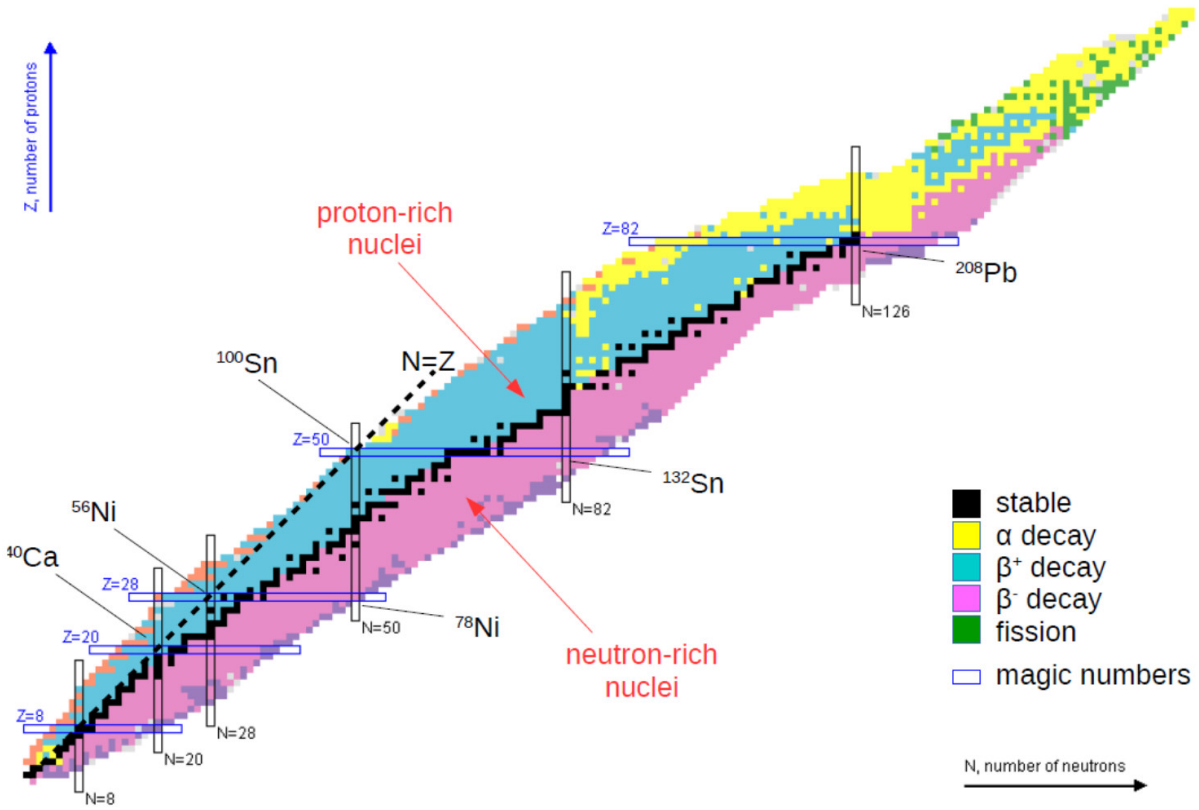
Figure 1.1: A chart of the nuclides with proton number Z on the vertical axis and neutron number N on the horizontal axis. The primary decay mode of each isotope is shown in the legend. Image taken from [1].

several thousand yet to be discovered! With the retirement of the coupled cyclotrons at the NSCL, the nuclear science community is anxiously awaiting its soon to be operational replacement. The Facility for Rare Isotope Beams (FRIB) is a United States Department of Energy funded project which uses a linear accelerator to probe the inner workings of exotic nuclei. It is expected that the new facility will extend our reach into the unprobed regions of the nuclear chart towards the neutron dripline and discover many new isotopes.

Any given element can have dozens of isotopes, and we differentiate these isotopes by referring to them by their mass number. For example, we can have ^{28}Si which is an isotope of silicon ($Z = 14$) with 14 neutrons giving is a total mass of $A = 14 + 14 = 28$. This is a stable isotope of silicon, meaning that it will not decay. An unstable isotope of silicon is ^{27}Si which has one fewer
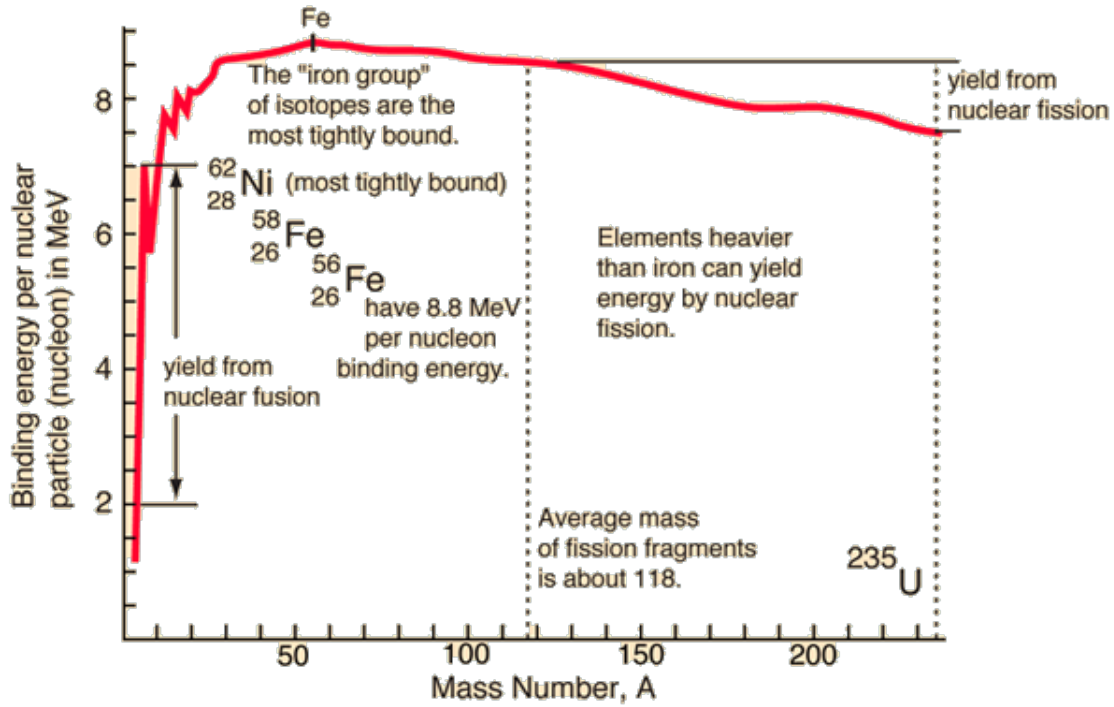
Figure 1.2: Binding energy per nucleon plotted against mass, showing the so called "iron peak". Image taken from Hyperphysics [3].

neutron. This isotope will undergo a process known as β-decay. During this process, one of its protons will convert to a neutron while emitting a positron and a neutrino resulting in the daughter nucleus ^{27}Al. The daughter nucleus has the same total mass number as the parent nucleus in a β-decay, but is now a different element. This process is discussed further in Sections 1.5 and 3.7.

The reason one nucleus may decay and one may not is due to the relative binding energy between a nucleus and its possible decay products. The binding energy of a nucleus is the difference in energy of the nucleus and that of a corresponding set of "free" nucleons (nucleons not contained in a nucleus). This can be thought of as the amount of energy you could release if you separated all of the nucleons from one another. ^{27}Si is less well bound than ^{27}Al, and so it is decays to the lower energy configuration. A mathematical definition of this binding energy difference is given by,

$$\text{BE}(N, Z) = Z M_H c^2 + N M_n c^2 - M(N, Z) c^2, \tag{1.1}$$

where the atomic mass of a nucleus is written as $M(N, Z)$. However, in the literature you are likely to see nuclear masses reported in terms of the "mass excess" of the nucleus. The mass excess, or

$\Delta(N, Z)$, is the difference between the actual mass of a nuclide and its mass number A. Therefore it is helpful to rewrite the definition of binding energy to be,

$$BE(N, Z) = Z\Delta_H c^2 + N\Delta_n c^2 - \Delta(N, Z)c^2, \tag{1.2}$$

with $\Delta_H c^2 = 7.2890$ MeV and $\Delta_n c^2 = 8.0713$ MeV. Often times we may want to discuss the total energy of a nucleus rather than its binding energy. Instead of imagining the amount of energy needed to separate the nucleons contained in a nucleus from one another, you can ask what is the energy needed to bring together free nucleons into a nucleus. We can define this energy as $E = -BE$. In this way, a stable nucleus would have a *negative* total energy but a *positive* total binding energy.

If one were to take a stable element such as ^{28}Si and continually add neutrons to it, increasing the total mass but keeping Z constant the nucleus would become unstable to β-decay. If even more neutrons were added eventually the nucleus would bump up against the neutron dripline. At this point any additional neutron added to the nucleus would immediately "drip" out of the nucleus, rather than undergo β-decay. The same is true for the addition of protons, at some point you run into the proton dripline. These driplines define the limits of stability on the Chart of Nuclides.

One can imagine examining the average binding energy per nucleon within a nucleus to reveal further insights. The binding energy per nucleon is a lot like looking at the Gross Domestic Product (GDP) per capita for a country. It would be misleading to compare the total GDP of a large country to that of a small country, but by looking at how the GDP is distributed amongst their populations you can get an idea of the relative wealth of a country. Fig. 1.2 shows the experimentally measured BE/A in MeV plotted against mass number. Starting with the simplest nucleus ^{1}H (a single proton), the binding energy is by definition zero. With an increase in mass there is a rapid increase in nuclear binding energy per nucleon up to a maximum around 8 MeV. Increasing the mass number after this point will result in a lower binding energy per nucleon. This maximum is referred to as the "iron peak" after the iron core formed through fusion in massive stars.

In the core of a newly formed star hydrogen is fused together into helium, which releases a large amount of energy in the form of radiation due to their differences in binding energy. The radiative

pressure from nuclear fusion pushing out from the core battles against the pull of gravity trying to collapse the star. Eventually, a hydro-static equilibrium is achieved and the star becomes stable. When there is no longer enough hydrogen in the core of the star to sustain the fusion reaction, the star must begin burning a new fuel source, namely helium. The helium and its products are fused into heavier and heavier elements. In a sufficiently massive star, fusion of these lighter elements will continue until a core of iron has been formed.

This is the end of the road however, as iron is essentially nuclear ash. It actually *costs* energy to fuse two iron nuclei together into a heavier nucleus, due to the lower binding energy per nucleon found in heavier nuclides. Without the pressure supplied by a sustained nuclear fusion reaction at the core, the overwhelming might of the stars own gravitational pull causes the star to collapse in on itself. What is left is an incredibly dense object, either a neutron star or black hole depending on the total mass of the star. Neutron stars are held up by nuclear degeneracy pressure (a purely quantum effect!) rather than through fusion, and the true secrets of black holes are hidden behind an event horizon beyond which nothing can escape.

One goal of nuclear physics is to further understand processes like stellar evolution that, on first glance, may seem to have very little to due with nuclear physics. Through the study of the structure of nuclei we can achieve great insight into the Cosmos, and in the next few sections we will cover more and more complex models of the nucleus.

1.2 The Liquid Drop Model

There have been many models that attempt to describe the structure of the nucleus since the discovery of the atom. From the plum pudding model first proposed by J. J. Thomson in 1904 [4] to the Bohr model of the atom in 1913 [5] that could describe electron orbitals, incremental progress was made in our understanding of the atom and its nucleus. Humbly, I would argue that the first truly scientific model of the nucleus itself is the Liquid Drop Model (LDM) proposed by George Gamow in 1930 [6] and quantified in the Semi-Empirical Mass Formula (SEMF) developed by Bethe and Weizsäcker in 1935 [7]. The LDM posits that we can understand the nucleus as a drop of
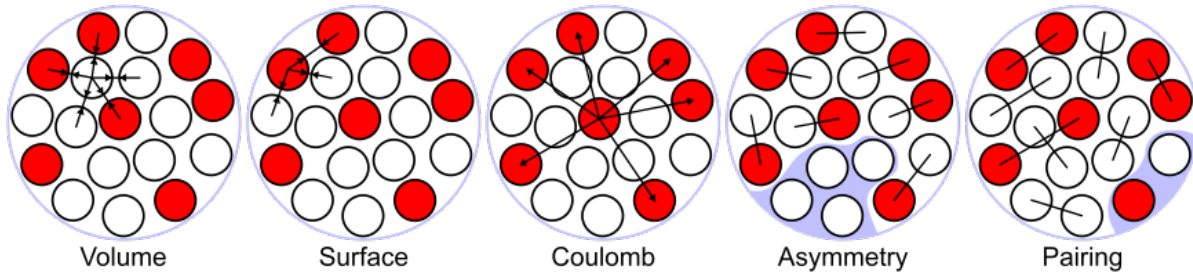
Figure 1.3: The terms of the liquid drop model visualized. Image taken from [8]

an in-compressible liquid at an extremely high pressure held together by the nuclear strong force. The strong force, as it often referred to, is a short range attractive force between nucleons. Like a liquid drop, the nucleus must perform a balancing act between different forces to maintain stability.

The SEMF estimates the binding energy of any nucleus and consists of five terms, each describing a different source of energy for the drop. The first is the *volume term* that describes the binding energy that comes from a nucleon being surrounded by other nucleons in the interior of the nucleus, each exerting an attractive force upon it. Not every nucleon is fully enveloped by other nucleons though, so the *surface term* adds a negative binding energy proportional to the surface area to correct for this.

While the nuclear strong force that binds the nucleus affects both the protons and neutrons (roughly) equally, the observant reader will recall that protons and neutrons are not identical. The proton has an electric charge, whereas the neutron does not. These positive charges repel one another and this adds an additional negative term to the total binding energy of the nuclear drop proportional to the number of proton pairs it contains.

The last two terms are contributions due to quantum effects. The first is the *asymmetry term* that seeks to balance the number of protons and neutrons within the nucleus. A greater number of neutrons than protons requires that higher energy levels be occupied for the protons, while leaving lower energy levels unoccupied for the neutrons (or vice-versa). Finally, we add a *pairing term* to account for the experimentally verified preference that protons (and neutrons) prefer to exist in pairs with zero total spin due to spin-coupling as they are spin 1/2 particles. This addition, which gives

7

energetic preference to pairs of nucleons over unpaired nucleons, results in the most tightly-bound nuclei being even-even. That is to say, the most bound nuclei will be those with an even number of protons and an even number of neutrons.

Visualizations of these terms are shown in Fig. 1.3, and putting things all together we come to the formulation of the SEMF,

$$\text{BE}_{\text{LDM}} = a_v A - a_s A^{2/3} - a_c \frac{Z(Z-1)}{A^{1/3}} - a_A \frac{(N-Z)^2}{A} + \delta(N, Z). \tag{1.3}$$

The Atomic Mass Evaluation of 2016 has 1000s of well known nuclear ground state energies, which we can use to constrain the full five-parameter model. This can be done with a simple χ^2 minimization quite quickly. Doing this and plotting the residuals from theory and experiment creates a striking pattern on the nuclear chart shown in Fig. 1.4.

The first thing to note from the figure is the fairly remarkable agreement we are able to achieve across the entire nuclear chart with just five terms. The root mean square (rms) deviation for absolute binding energy between LDM and experiment is on the order of 3 MeV (the figure shows the results per nucleon). The residuals per nucleon are on the order of only a few percent. This shows that the liquid drop model is an incredibly powerful model, but we also notice a grid like pattern where the theory is under predicting the binding energy (blue) while also over predicting (red) in between these blue bands.

As is often the case in science, it is both helpful and informative to look at these deviations in a slightly different manner. Fig. 1.5 shows a one-dimensional projection of the residuals from the nuclear chart in Fig. 1.4 plotted against both neutron number N and proton number Z. At low mass, there is no real discernible pattern to be seen through the noise. However, at higher proton/neutron number there are clear peaks in the residual binding energies between theory and experiment.

In nuclear physics we call these the "magic" numbers, as nuclei with these number of protons or neutrons display stronger binding than expected from the naive LDM. To understand the source of these peaks, and why some numbers are magic while others are not, we have to leave the world of the semi-classical and jump head first into the world of quantum mechanics!
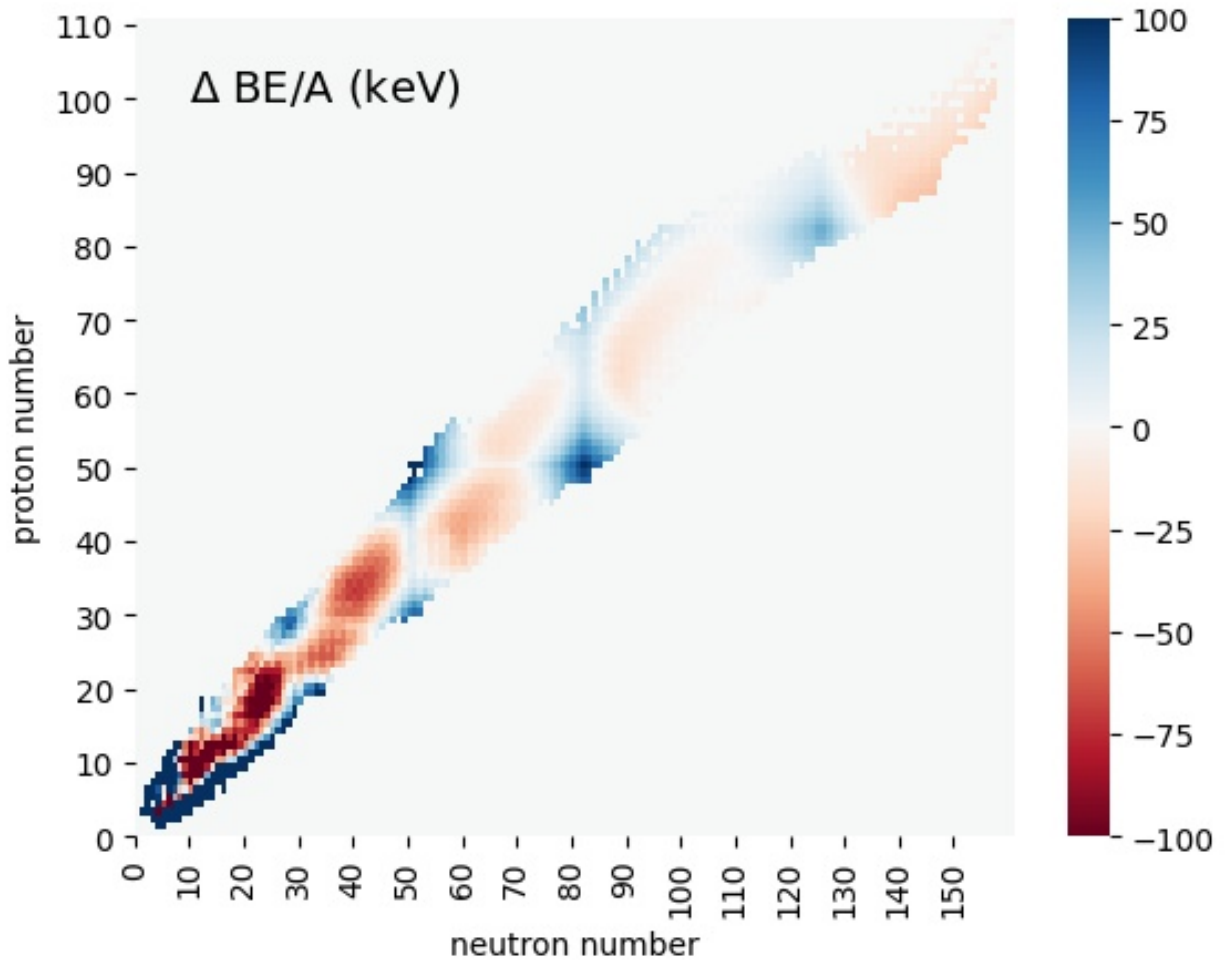
Figure 1.4: The difference in BE/A between experiment and the Liquid Drop Model. A positive number indicates that experiment is more bound than theory.

1.3 The Nuclear Shell Model

"Nature isn't classical, dammit, and if you want to make a simulation of nature, you'd better make it quantum mechanical."

Richard Feynman

Transitioning to a quantum model of reality requires that we stop thinking about the nucleons as particles, and begin thinking of them as waves with an associated wave function. Let us start at the beginning then, and write down a simple Schrödinger Equation for a nucleon to try and understand
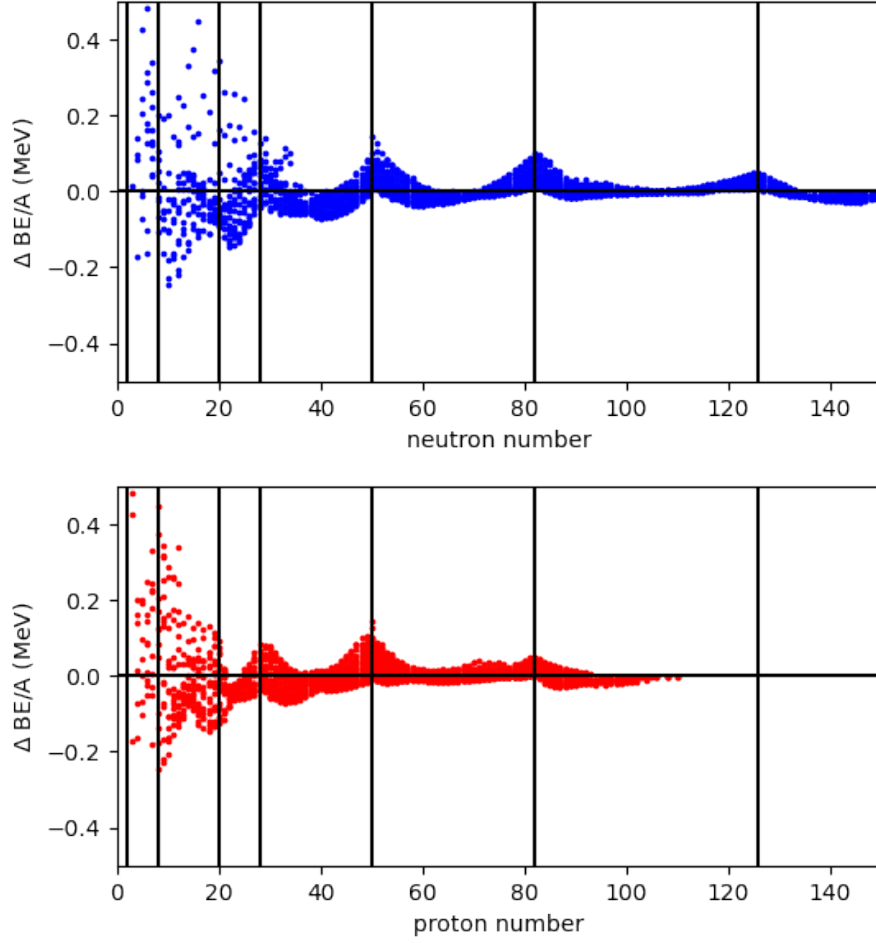
Figure 1.5: The difference in nuclear binding energy per nucleon between experiment and the Liquid Drop Model prediction plotted against neutron number (top) and proton number (bottom). The magic numbers are indicated by the black vertical lines.

the behavior of a nucleon in a nuclear potential generated collectively by all of the nucleons,

$$-\frac{\hbar^2}{2m}\nabla^2\Psi + V_{nuc}\Psi = E\Psi. \tag{1.4}$$

As the strong nuclear force is short ranged and rotationally symmetric with no preferred direction, we choose a 3-dimensional radially symmetric Woods-Saxon potential to model it. This gives us a starting potential of the form,

$$V_{WS}(r) = \frac{V_0}{1 + e^{r-R}/a}, \tag{1.5}$$

where $R \approx 1.2A^{1/3}$ fm and $a \approx 0.60$ fm. There are many standard techniques to solve the Schrödinger Equation, and we could apply those and stop here to get a relatively good quantum

mechanical model of a nucleon in a nucleus. But when we do so we find that we are unable to reproduce the magic numbers we discovered at the end of the last section.

The key addition to this simple model that won Maria Goeppert Mayer and Hans Jensen a share of the Nobel Prize for Physics in 1963 [10] was realizing that the spin of the nucleon would couple to the angular momentum of the quantum orbits. This spin-orbit coupling is defined as

$$V_{so}(r) = V_{so} \frac{1}{r} \frac{df_{so}(r)}{dr}, \tag{1.6}$$

with

$$f_{so}(r) = \left(1 + [e^{r-R_{so}}/a_{so}] \right)^{-1}. \tag{1.7}$$

With this added term, the spin S is no longer a "good" quantum number, that is to say not every eigenvector of the system maintains the same eigenvalue as time evolves. The orbital and angular momentum couple together to a definite total angular momentum J, which is a good quantum number. The eigenstates of this system are then defined by J and the projection M of the total angular momentum. Each orbit associated with a total angular momentum J can contain $2J + 1$ nucleons. The calculated energy levels from the Woods-Saxon potential with the spin-orbit coupling addition are shown in Fig. 1.6. Each orbital is labeled by its principal quantum number n, a letter corresponding to its intrinsic angular momentum l, and finally the total angular momentum J. Without the spin-orbit term, the magic numbers discovered in the previous section were not recovered, but the energy gaps are clear in the figure showing 2, 8, 20, 28, and so on.

We now have a realistic nuclear potential for individual nucleons that recreates the "shell gaps" at the expected magic numbers that were discovered experimentally. As more and more neutrons and protons are added to the system, they will naturally fill the orbitals starting at the lowest energies up to what is called the "Fermi Energy." If a hole were to be left in a lower lying orbital then it would be energetically favorable for the system to decay to this lower energy state and it would quickly do so.

We can imagine nucleons sitting "on top of" the very doubly magic ^{16}O nucleus. We call these excess nucleons "valence" nucleons. The next step is to restrict the number of orbitals that we will
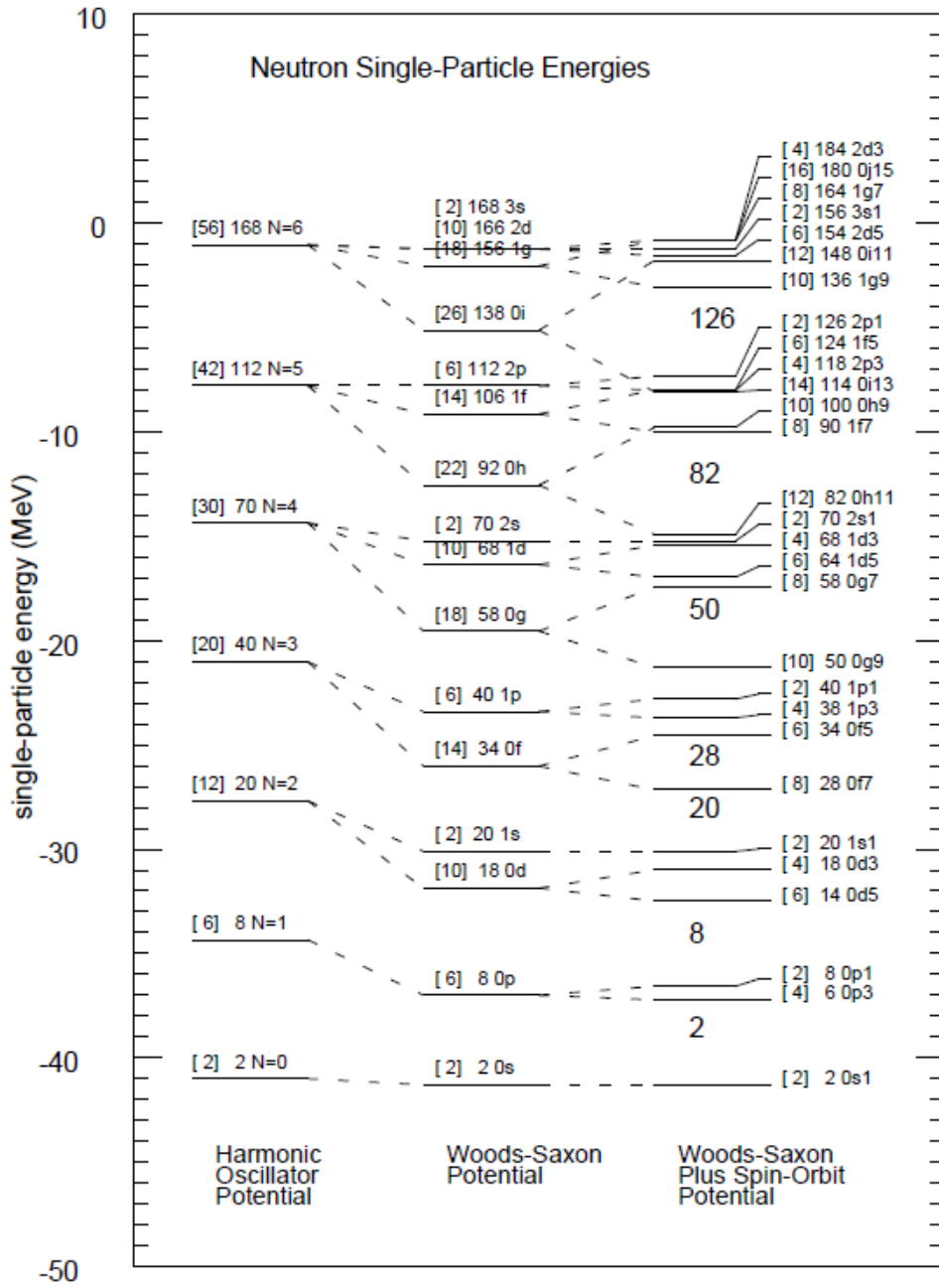
Figure 1.6: Quantum energy levels associated with the Harmonic Oscillator potential (left), the Woods-Saxon Potential (center) and the Woods-Saxon potential with a spin-orbit Coupling term (right). On the right we see the familiar nuclear magic numbers in the resulting shell gaps. Image taken from [9].
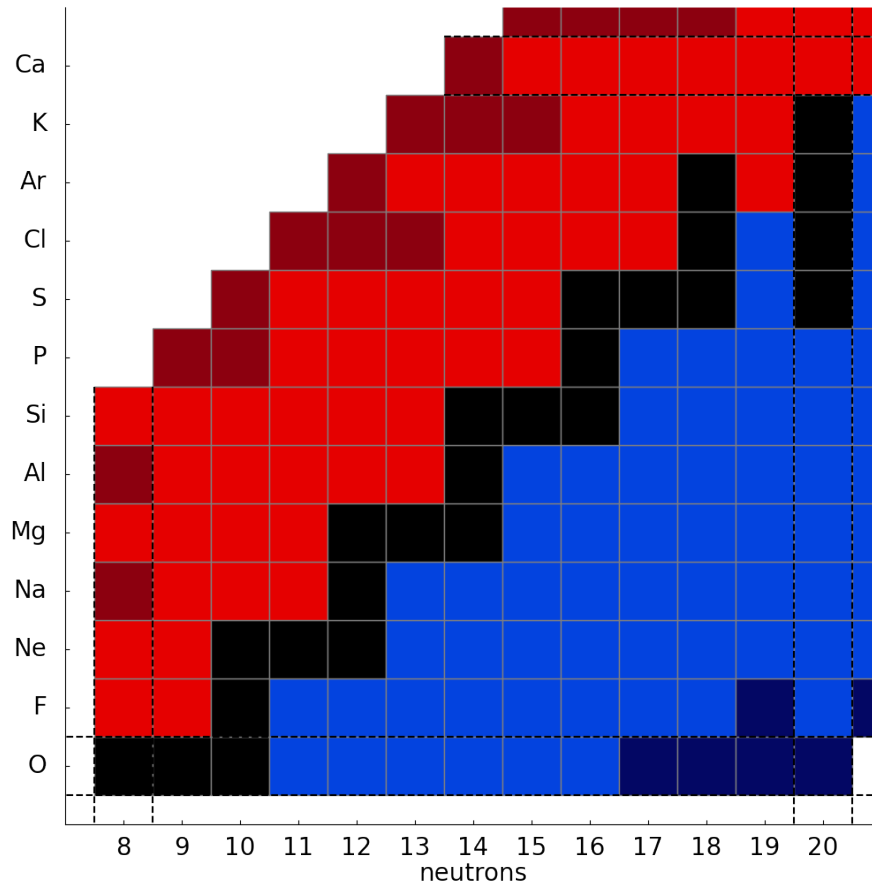
Figure 1.7: A portion of the Chart of the Nuclides showing those isotopes in the *sd*-shell. Stable nuclei are in black, nuclei that decay via β^- / β^+ in blue/red, and nuclei outside of the neutron/proton dripline are shown in dark blue/dark red.

be studying at any given time. As there are an infinite number of higher laying orbitals, this is necessary. Let us consider the three orbitals which make up the so-called *sd*-shell: $0d_{5/2}$, $0d_{3/2}$, and $1s_{1/2}$. These exist between the two magic numbers and should be relatively decoupled from the other orbits. We have now separated the infinite set of orbitals into three groups: the high lying orbitals which we assume are out of reach energetically and so will not impact the low lying energy spectra in a nucleus, the model space consisting of three orbits which we allow our valence nucleons to occupy, and an inert core of ^{16}O consisting of the filled $0s_{1/2}$, $0p_{3/2}$, and $0p_{1/2}$ orbitals.
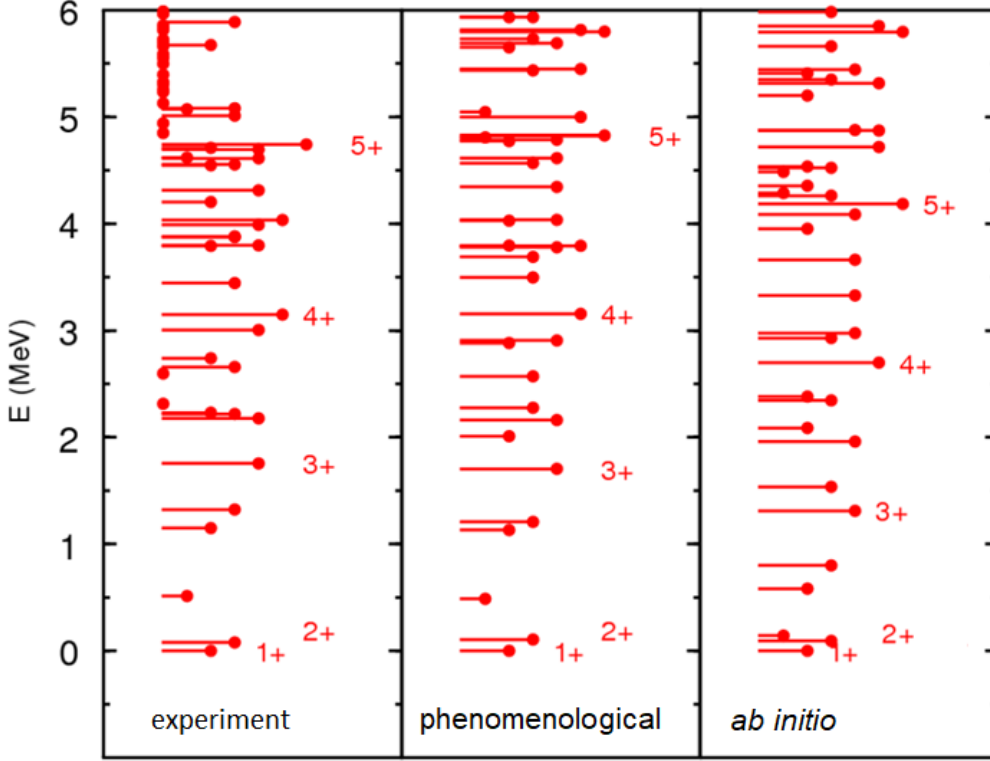
Figure 1.8: The left panel shows an example experimental spectra for a nucleus. The center panel shows the spectra calculated with an "effective" interaction, with the right panel showing the predicted spectra from an *ab initio* interaction based on *NN* scattering data.

A zoomed in portion of the nuclear chart that shows the nuclei that exist in this restricted model space is shown in Fig. 1.7, spanning from $Z = 8 - 20$ and $N = 8 - 20$. This model space separates the magic numbers 8 and 20 for protons and neutrons, and will be the focus of the middle chapters of this dissertation. A practical benefit of focusing on this model space is the relatively low computation cost compared to larger and higher energy model spaces. This allows for large sets of calculations to be completed in a reasonable time frame on a powerful desktop computer.

To complete these calculations the NuShellX codebase [11, 12] is used, which uses the shell model to calculate nuclear wavefunctions and energies. To perform the calculations, a Hamiltonian that describes the valence space interaction is needed. Hamiltonians used in configuration-interaction calculations can be written as a sum of one- and two-body operators:

$$H = \sum_a \epsilon_a \hat{n}_a + \sum_{a \leq b, c \leq d} \sum_{JT} V_{JT}(ab; cd) \hat{T}_{JT}(ab; cd), \tag{1.8}$$

14

where $\hat{n}_a$ is the number operator for the spherical orbit a with quantum numbers (n_a, l_a, j_a) and

$$\hat{T}_{JT}(ab; cd) = \sum_{MT_z} A^\dagger_{JMTT_z}(ab) A_{JMTT_z}(cd), \tag{1.9}$$

is the scalar two-body density operator for nucleon pairs in the orbits a, b, c, and d coupled to the spin quantum number JM and isospin quantum numbers TT_z.

These Hamiltonians are continually being improved. The *ab initio* based methods now include three-body interactions together with improved methods for handling short range correlations and model space truncations [13] and are now able to describe binding energies within several MeV and energy spectra within about 500 keV. A recent example for the *sd*-shell is shown in [13].

One can phenomenologically improve upon these interactions by using the experimental energy data for nuclei in a given mass region to obtain effective two-body matrix elements (TBME) for a given model space. An effective method for doing this is to start with an *ab initio* based Hamiltonian and then to modify the best determined linear combinations (LC) of TBME that are required by the energy data using the singular value decomposition (SVD) method. The result is that both binding energies and energy spectra can be described to within 150-200 keV (see Fig. 9 of [13] and Fig. 5 of [14]).

The SVD method has resulted in widely used Hamiltonians for the *sd* model space [14, 15], the *fp* model space [16–18], the mixed *sd* (protons) *fp* (neutrons) model space [19], the $sd - pf$ model space with particle-hole excitations [20, 21], and the $jj44$ model space (see the appendix in [22]). The relatively small modifications to the *ab initio* based TBME (on the order of up to 100-200 keV) reflect deficiencies in the many-body method, as well as the input NN + 3N force. This method is covered in detail in the Section 1.6.

1.4 The Isobaric Multiplet Mass Equation

Isospin, first introduced by Heisenberg in 1932 [23] allows for protons and neutrons to be treated as the same particle, a nucleon, but in different isospin projection states. Apart from the proton having an electric charge, there are many reasons to believe this is a useful tool. The masses of the two particles are very similar and their behaviour under the influence of the strong force are nearly

identical. The introduction of isospin provides two new quantum numbers, T and T_z, analogous to the spin quantum numbers, J and J_z, on which the formalism of isospin is based.

The proton and neutron are $T = 1/2$ particles with opposite isospin projection, $T_z = -1/2$ and $T_z = 1/2$ respectively. The total isospin projection of a given nucleus with N neutrons and Z protons is then $T_z = (N - Z)/2$. The convention of positive sign for neutron and negative for proton is arbitrary, but as most isotopes in nature have an excess of neutrons to protons this keeps the total isospin projection positive for most of the nuclei that we can study.

The isospin T of a particular energy level in a nucleus is less determined with possible values from,

$$T = \frac{|N - Z|}{2}, \frac{|N - Z|}{2} + 1, ..., \frac{N + Z}{2} - 1, \frac{N + Z}{2}. \tag{1.10}$$

Generally the ground state of a nucleus takes on the lowest allowed T value, with the higher values found amongst the excited states at higher energies.

We can now think of grouping together those nuclei with similar quantum numbers including isospin projection. Nuclei with the same total mass number A are known as isobars. If we add the further restriction that those isobars have the same angular momentum J, parity π, and isospin T then we have defined an *isobaric multiplet*. Member states of this multiplet are referred to as Isobaric Analogue States (IAS).

An example isobaric multiplet is the $A = 20$, $T = 2$ ground state multiplet. This consists of $2T + 1 = 5$ nuclei, namely ^{20}Mg, ^{20}Na, ^{20}Ne, ^{20}F, and ^{20}O. We take the $T = 2$ ground states of those nuclei with $|T_z| = T = 2$, and so $J^\pi = 0^+$. As the ground states of the three interior nuclei are not $T = 2$ states we have to look at their excited states for the IAS. We can then plot the absolute energies of these states to look for any pattern. The top panel of Fig. 1.9 shows unaltered energies of the five $T = 2$ IAS as well as the lower T states for the interior nuclei. The bottom panel subtracts a phenomenological correction to the IAS to remove the effects of the Coulomb interaction, leaving the IAS are now roughly in agreement.

Weinberg and Treiman first defined the relationship between the binding energies of the IAS in
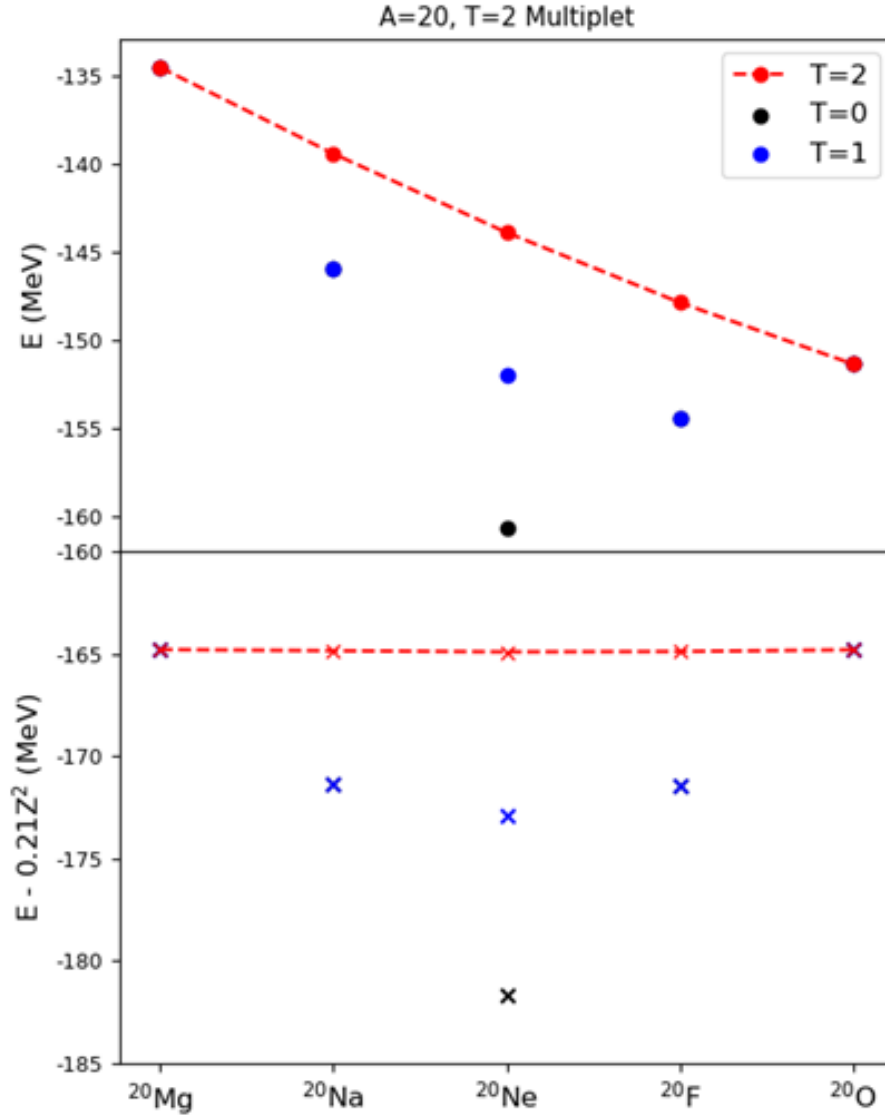
Figure 1.9: The top panel shows the unchanged T =0, 1, and 2 energies of the $A = 20, T = 2$ multiplet. The $T = 2$ states are connected to show the quadratic nature of the IMME. The bottom panel shows the same states with a phenomenological correction associated with the Coulomb interaction subtracted from their energies.

the Isobaric Multiplet Mass Equation (IMME) [24, 25],

$$\text{BE}(A,T,T_z,\alpha) = a(A,T,\alpha) + b(A,T,\alpha)T_z + c(A,T,\alpha)T_z^2, \tag{1.11}$$

with a, b, and c being coefficients dependent on A, T, and α representing all other quantum numbers except T_z.

If isospin were a good quantum number, that is if it were conserved in all cases, then the member states of this multiplet should have identical properties. However, these isobaric analogue states are known to not have identical binding energies. The obvious breakdown of isospin symmetry is clear from the existence of the Coulomb interaction which does not affect neutrons due to their lack of charge. There is also a breaking of isospin symmetry in the nuclear strong force on the order of a couple percent. First order perturbation theory shows that the binding energies of the IAS do not have terms higher than T_z^2 if the splitting is due entirely to Coulomb. The Coulomb interaction can be written as isospin tensors of rank 0, 1 and 2. Using the Wigner-Eckart theorem, one can show that the highest order allowed is quadratic in T_z [24].

For use as a sanity check later it is useful to derive the LDM predictions for the IMME coefficients. Using,

$$T_z = \frac{(N - Z)}{2} \rightarrow Z = \frac{A}{2} - T_z \tag{1.12}$$

the Coulomb term from the SEMF can be written as,

$$W_C = a_C \left(\frac{1}{4}A^2 - \frac{1}{2}A - \frac{A-1}{A^{1/3}}T_z + A^{-1/3}T_z^2 \right). \tag{1.13}$$

This expression is now quadratic in T_z and the IMME coefficients can be read directly from it. The linear coefficient,

$$b_{\text{LDM}}(A) = -a_C \frac{A-1}{A^{1/3}} \tag{1.14}$$

and the quadratic coefficient

$$c_{\text{LDM}}(A) = a_C A^{-1/3} \tag{1.15}$$

These predictions will be used later in the dissertation for comparisons to experiment and configuration-interaction calculations.
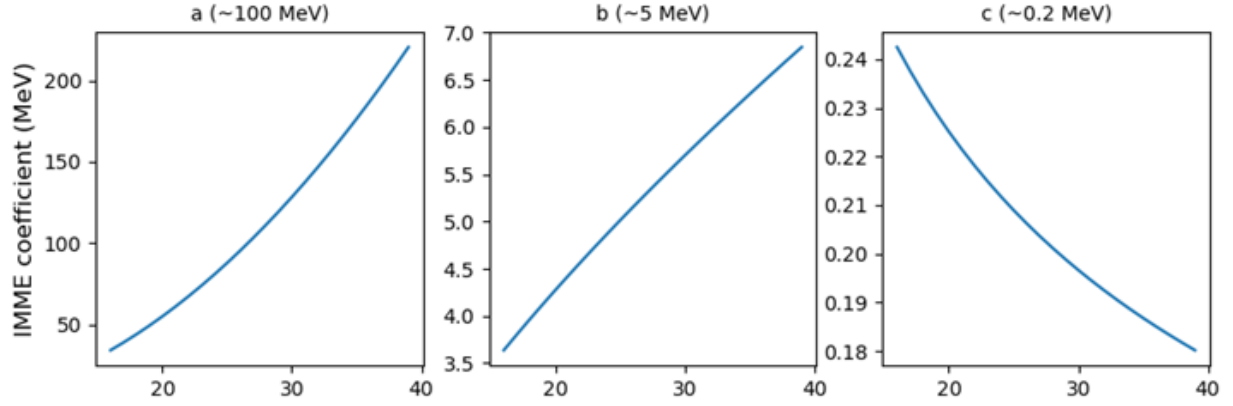
Figure 1.10: Curves showing the LDM predictions for the a-, b-, and c-coefficients of the IMME plotted against mass number.

Further breakdown of isospin symmetry can be probed by studying those isobaric multiplets with $T \geq 3/2$. When there are more members of a multiplet than there are free parameters in the IMME (3) then any deviation from the quadratic form can be exactly tested. If a nonzero cubic, $d(A,T)$, or quartic, $e(A,T)$, correction is needed to recreate the experimental energies, then that is a sign of a breakdown in isospin symmetry beyond Coulomb and involves the more subtle splitting of isospin symmetry in the nuclear strong force. We will examine some example cases of a breakdown in isospin symmetry in Chapter 3.

1.5 Understanding β-Decay

When a nucleus is unstable but within the driplines of the nuclear chart, one of the ways it can decay is through β-decay which is governed by the weak nuclear interaction. This process was discovered by Ernest Rutherford in 1899 while studying radioactive isotopes in a magnetic field. When a nucleus undergoes β-decay a proton (neutron) decays into a neutron (proton) while emitting an positron (electron) and a neutrino. Of course the protons and neutrons themselves are not fundamental particles, they are made up of quarks and gluons. A proton consists of two "up" u quarks that have charge an electric charge of $\frac{2}{3}$e each (where e is the charge of an electron) and a "down" quark d which has a negative electric charge of $-\frac{1}{3}$e. Likewise a neutron consists of two d

quarks and one u quark. The Standard Model describes the process of β^- decay most simply as

$$d \rightarrow u + e^- + \bar{\nu}_e. \tag{1.16}$$

This process changes the total isospin projection of the nucleus but does not change its mass number. The rate of this decay is dependent on the gap Q in energy between the initial nucleus and its daughter nucleus

β-decay measurements can be useful sources of information for studying the weak interaction as well as the structure of the nucleus which is largely governed by the strong and Coulomb interactions. There are many types of β-decay, and it is therefore useful to categorize them by the angular momentum transferred from the nucleus to the escaping electron and neutrino. Those decays with no angular momentum transfer, $\Delta l = 0$, are known as "allowed" β-decay for historical reasons in contract to so-called "forbidden" decays with $\Delta l = 0$.

Allowed β-decays come in two flavors. The first is the Fermi decay, which is characterized by its isospin conservation. The operator for the Fermi decay is

$$\hat{O}(F_\pm) = \sum_k t_{k\pm}, \tag{1.17}$$

where $t_{k\pm}$ are the nucleon isospin raising and lowering operators. These operators are only able to connect isobaric-analog states (IAS) making the Fermi decay a measure of isospin conservation in nuclei.

The second is the Gamow-Teller decay which does not conserve isospin. The operator for this decay is

$$\hat{O}(GT_\pm) = \sum_k \sigma_k t_{k\pm}, \tag{1.18}$$

which appears similar to that of the Fermi decay, but contains the nucleon spin operator. Since the total spin S is not a good quantum number, this operator can connect to many final states and in general does so. This makes it an excellent test of shell-model configuration mixing in the nucleus.

1.6 The Singular Value Decomposition (SVD) Fitting Method

While the results of several fitted interactions are presented in this document, they all share a similar "backbone" of statistical methods. Deviations from this outline will be noted in the results section for each interaction. This section follows much of the formalism laid out in Refs. [26, 27] for tracking uncertainties, and is a detailed description of the method used to develop USDA and USDB [15].

In a simplified notation we can write the configuration-interaction Hamiltonian in a parametrized form,

$$H(\vec{p}) = \sum_{i=1}^{N_P} p_i O_i, \tag{1.19}$$

where O_i are the operators or linear combinations of operators corresponding to parameters $p_i = 1, ..., N_p$. These Hamiltonians will have eigenvectors ϕ_α, and eigenvalues λ_α which we express as

$$\lambda_\alpha = \sum_{i=1}^{N_p} p_i < \phi_\alpha|O_i|\phi_\alpha > = \sum_{i=1}^{N_p} p_i \beta_i^\alpha. \tag{1.20}$$

The starting Hamiltonians used in these fits may be combinations of many such interactions. For the purposes of the statistical analysis, we can define a starting interaction as

$$H(\vec{p}) = H^0 + H^1(\vec{p}), \tag{1.21}$$

dividing it into a static Hamiltonian that we do not wish to fit H^0, and $H^1(\vec{p})$ that contains the full interaction's dependence on the chosen model parameters, $\vec{p}$. Likewise, the calculated energies are given by:

$$E_i(\vec{p}) = < \phi_i|H^0|\phi_i > + < \phi_i|H^1(\vec{p})|\phi_i >$$
$$= E_i^0 + \epsilon_i(\vec{p}). \tag{1.22}$$

Experimental energies are not generally reported this way, and so to obtain the expected experimental energy contribution due to $H^1(\vec{p})$, we define $\epsilon_i^{exp} = E_i^{exp} - E_i^0$.

Now we formulate the problem as a χ^2 minimization of N_p parameters p_j on a data set of size N_d.

$$\chi^2 = \sum_i^{N_d} w_i(\epsilon_i(\vec{p}) - \epsilon_i^{exp}), \tag{1.23}$$

where the weights are set to $w_i = (\sigma_i)^{-2}$. The adopted errors σ_i for the data set are a combination of the recorded experimental errors and a theoretical error $\sigma^{th} = 100$ keV chosen to normalize the minimized χ^2 to the degrees of freedom, $N_d - N_p$.

$$\sigma_i^2 = (\sigma_i^{exp})^2 + (\sigma_i^{th})^2 \tag{1.24}$$

We now denote the weighted energies as

$$z_i = \sqrt{w_i}\epsilon_i^{exp} = \sigma_i^{-1}\epsilon_i^{exp} \tag{1.25}$$

and the Jacobian matrix which contains the weighted regression coefficients

$$J_{ji} = \sqrt{w_j}\left(\frac{\partial \epsilon_j}{\partial p_i}\right) = \sqrt{w_j}\beta_i^j. \tag{1.26}$$

Starting with parameters $\vec{p^s}$ informed from theory, we calculate the β_i^j and then minimize χ^2 by requiring $\partial_{p_j}\chi^2 = 0$. This produces a set of N_p linear equations

$$G\vec{p} = \vec{e}, \tag{1.27}$$

where

$$G_{ij} = (J^T J)_{ij} = \sum_{\alpha}^{N_d} w_\alpha \beta_i^\alpha \beta_j^\alpha, \tag{1.28}$$

and

$$e_i = (J^T \vec{z})_i = \sum_{\alpha}^{N_d} w_\alpha \epsilon_i^{exp} \beta_i^\alpha. \tag{1.29}$$

An inversion of the G matrix gives the full χ^2 solution,

$$\vec{p} = G^{-1}\vec{e}. \tag{1.30}$$

If G is not invertible you may have an insufficient data set to constrain the chosen parameter space. To take into account the implicit p_i dependence of β_i^α, this procedure is repeated until convergence to determine $\vec{p_0}$ that minimizes χ^2. If you don't wish to maintain any knowledge from your starting parameter set, and trust the data to fully constrain every parameter then you can stop here. However,

In large dimensional fits, the parameters are often highly correlated. It is advisable then to reframe the problem in terms of an orthogonal basis of the model parameters.

Taking a singular value decomposition of G gives us:

$$G = A^T DA. \tag{1.31}$$

From Eq. 1.28 it is clear that G is both real and symmetric, and so we obtain a diagonal matrix D whose elements are the singular values of G, and a "rotation" matrix A made up of column vectors that define the uncorrelated linear combinations of parameters that form an orthogonal basis in parameter space.

We now introduce a new set of parameters

$$\vec{y} = A\vec{p}, \tag{1.32}$$

which represent a point in the parameter space denoted using a set of independent basis vectors y_i and not the original model parameter. When a point in parameter space is expanded in this basis, the deviations of the χ^2 from its minimum value take the form of a system of m uncoupled harmonic oscillators—with the singular-values playing the role of the m spring constants.

Inserting Eqs. 1.31 and 1.32 into 1.27, this definition and the SVD of G provides the solution

$$y_i = (D^{-1} A\vec{e})_i = d_i c_i, \tag{1.33}$$

where we have introduced the notation $d_i = 1/D_{ii}$ and defined a "rotated" data vector $\vec{c} = A\vec{e}$. It is clear that for small singular values, the resulting y_i are strongly affected by small changes in the data through c_i. As such we are motivated to truncate the effective parameter space. To get the new set of parameters, we use the "rotated" (uncorrelated) linear combination basis and replace the poorly determined values using an *ab initio* interaction with $\vec{y^s} = A\vec{p^s}$.

$$y_i = \begin{cases} d_i c_i & \text{for } i < n \\ y_i^s & \text{for } i \geq n \end{cases} \tag{1.34}$$

Where n represents the number of linear combinations allowed to vary in the minimization. We can then transform back into the original model basis to obtain $\vec{p}(n) = A^T \vec{y}(n)$, which is then used to iterate until convergence. This procedure results in a family of solutions $\vec{p}_0(n)$.

For a full χ^2 minimization, the covariance matrix S of the parameters can be obtained by

$$S = G^{-1} = (J^T J)^{-1}. \tag{1.35}$$

And then the variance Δp_i for each parameter can be taken as $\sqrt{S_{ii}}$. To obtain a dimensionless representation of the covariance matrix, we formulate the correlation matrix R defined as:

$$R_{xy} = \frac{S_{xy}}{\sqrt{S_{xx}S_{yy}}} = \frac{S_{xy}}{\Delta p_x \Delta p_y}. \tag{1.36}$$

This results in a matrix with ones along the diagonal, and off diagonal entries between -1 and 1 showing the inter-parameter correlations.

Covariance and correlation matrices can be generated for the data as well as the model variables. The data covariance matrix is dependent on the parameter covariance matrix through,

$$S_d = JSJ^T \tag{1.37}$$

This matrix can be used to generate uncertainties and determine correlations for the data in the same way as the parameter covariance matrix.

If we want to obtain the covariance matrix when only n of the uncorrelated linear combinations of parameters are allowed to vary, there are more things to consider. We wish to quantify the *statistical* uncertainty that is introduced by the fit, and separate it from the *systematic* uncertainties inherent in the model. To this end, we write the inverse of G in its deconstructed form

$$C = AD^{-1}A^T. \tag{1.38}$$

Again the diagonal entries of D^{-1} are given by $d_i = 1/D_i i$, but we make the change that

$$d_{i \geq n} = 0. \tag{1.39}$$

This then allows us to isolate the variances and covariances introduced to the model parameters from the regression, and maintain the *ab initio* model's influence on those poorly determined linear combinations. We then have a series of covariance matrices, one for each n value.

$$C(n) = Ad(n)A^T \tag{1.40}$$

Using these we can generate the statistical uncertainty introduced to the parameters and observables at each n. At $n = 0$ we expect the calculated uncertainties to be zero (this is clear in Eq. 1.40), and to grow with n.

CHAPTER 2

NEW ISOSPIN-BREAKING USD INTERACTIONS

Two new USD-type Hamiltonians, USDC and USDI, have been developed that directly incorporate Coulomb and other isospin-breaking interactions. Starting from *ab initio* interactions, linear combinations of two-body matrix elements were constrained by experimental energy levels in *sd*-shell nuclei. With this method, binding energies and excitation energies of proton-rich nuclei in the shell can be added to the data set used in the fit. USDC and USDI contain an analytic Coulomb interaction with Miller-Spencer short range correlations and an effective isotensor interaction.

Also presented are modifications to these interactions, USDCm and USDIm, that have had the Coulomb interaction constrained to better reproduce the experimental *b* coefficients of the Isobaric Mass Multiplet Equation. These Hamiltonians are used to provide new predictions for the proton-dripline and to examine isospin level mixing and other properties of *sd*-shell nuclei. Several examples of states with large Thomas-Ehrman Shifts (for more on Thomas-Ehrman Shifts) see Section 3.1) are modeled using USDC and a single-particle interaction.

The universal *sd*-shell (USD) Hamiltonian [28, 29] has provided realistic *sd*-shell ($0_{d5/2}$, $0d_{3/2}$, $1s_{1/2}$) wave functions for use in nuclear structure models, nuclear spectroscopy, and nuclear astrophysics since its development thirty-five years ago. Its successors USDA and USDB [15, 30] were developed in 2006 using an updated and expanded set of nuclear energy levels. These USD-type Hamiltonians are defined by three single-particle energies (SPE) and 63 two-body matrix elements (TBME) in isospin formalism, which are derived from a renormalized G matrix and then fit to a set of binding energies and excitation energies.

The USD-type Hamiltonians were all developed in *isospin* formalism in which the Coulomb interaction is treated as a perturbation. The interaction most widely used for isospin-breaking calculations before the development of USDC is called USDB-CD [31, 32]. While USDB-CD is quite good at predicting excited energy spectra for *sd*-shell nuclei, it does a poor job at determining absolute ground state binding energies. Further discussion of USDB-CD appears in the next section.

Lack of reliable binding energy calculations results in poor predictions for separation energies and decay properties.

We are therefore motivated to extend the derivation of USD-type Hamiltonians to include isospin-breaking interactions directly. Isospin formalism restricts the TBME so that the wavefunctions produced by the interaction have good isospin, thus the inclusion of isospin-breaking terms in the Hamiltonians requires us to move to proton-neutron (*pn*) formalism. We introduce groupings of TBME to restrict the total number of parameters and keep our results physically reasonable. For the first time, binding energies and excitation energies in proton-rich nuclei are able to be included in the fit and no *a priori* Coulomb corrections to the data are necessary. This makes us able to consider 854 states in 117 nuclei.

In this chapter, we introduce four new isospin-breaking USD-type Hamiltonians. The spiritual successor of USD and USDA/USDB, which is based on the same renormalized G matrix *sd*-shell interaction (SDBA) [33], is USDC. Additionally, we derive USDI which starts from a new *ab initio* interaction based on a set of In-Medium Similarity Renormalization Group (IMSRG) Hamiltonians [34, 35] that are nuclei-specific, but otherwise the same fitting procedure is followed.

There are many levels of many-body physics involved in the development of the IMSRG interactions in which deficiencies could arrive. The use of a harmonic oscillator basis for the intruder and continuum states may be insufficient for describing exotic nuclei near separation energy that interact strongly with the continuum states. This motivates us to employ the techniques for refining effective interactions on these new *ab initio* theories.

Also presented are USDCm and USDIm in which the Coulomb TBME are further constrained.

2.1 A brief history of Configuration-Interaction Hamiltonians for the *sd*-shell

There is a long history of using configuration-interaction calculations to study *sd*-shell nuclei. The first major development was in 1968 by Kuo and Brown. They worked to develop a theory that takes nucleon-nucleon scattering potentials and builds up two-body matrix elements (TBME) that
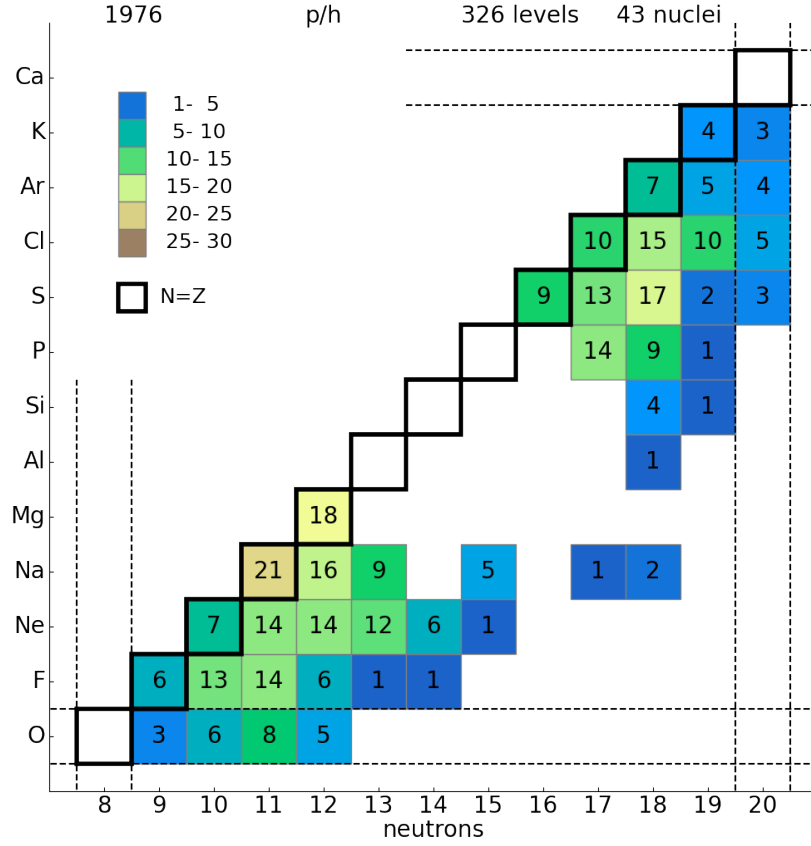
Figure 2.1: Number of energy levels in each *sd*-shell nuclei used in the data set for constraining the CWP and CWH Hamiltonians.

describe the interaction between pairs of nucleons. After accounting for short range correlations between the nuclei and the effects of the model space truncation, this model could then very well describe the behavior of two-particle (A=18) and two-hole (A=38) nuclei.

The second series of developments to describing this model space were by Chung and Wildenthal. Through the use of many-body techniques, they were able to apply the TBME to a much larger set of nuclei. It was discovered that the calculated spectra were generally worse the more particles (or holes) are included in the calculations. However, they could be improved to match more closely to experiment with only small changes to the TBME. This key insight has lead to massive improvement in interactions over the years.
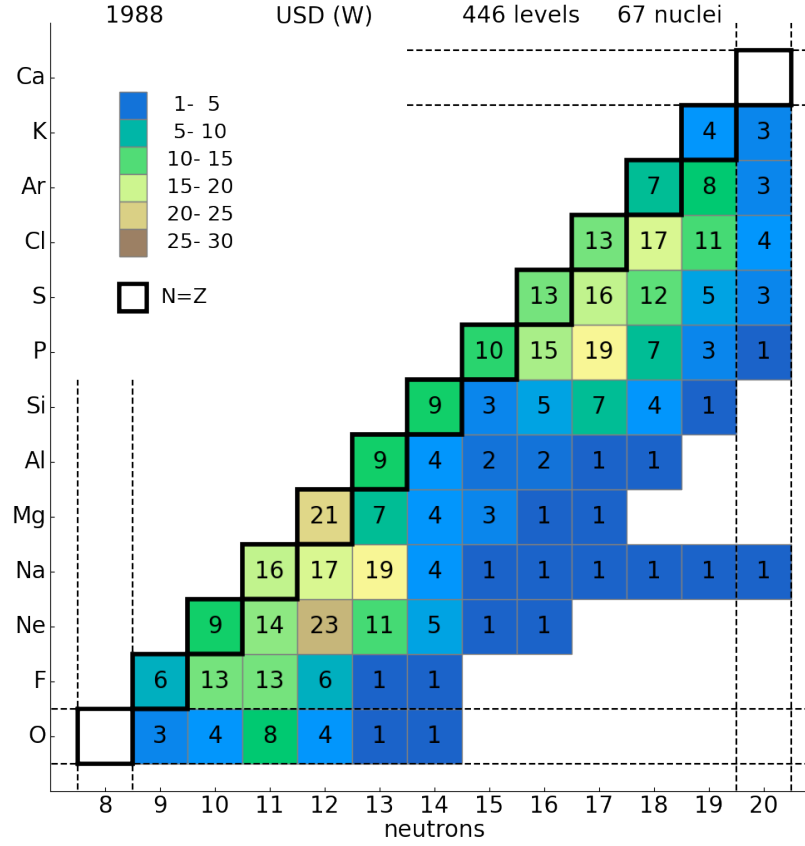
Figure 2.2: Number of energy levels in each *sd*-shell nuclei used in the data set for constraining the USD (W) Hamiltonian.

These first attempts at so called "Effective Interactions" (as opposed to the *ab initio* work of Kuo and Brown) required massive amounts of computation time as well as sufficient experimental data with which to constrain the TBME. In the end, two interactions were developed. One for the bottom of the shell called CWP and one for the top of the shell called CWH. Fig. 2.1 shows the distribution of levels used in their fits, as well as the reasonable applicability of the interactions. Calculations involving nuclei in the middle of the shell such as ^{28}Si were very costly, and so the two interactions do not connect. The statistical methods used for constraining these interactions are outlined in the final section of this Chapter.

The first truly universal *sd*-shell interaction, that is one set of TBME that could describe nuclei

29
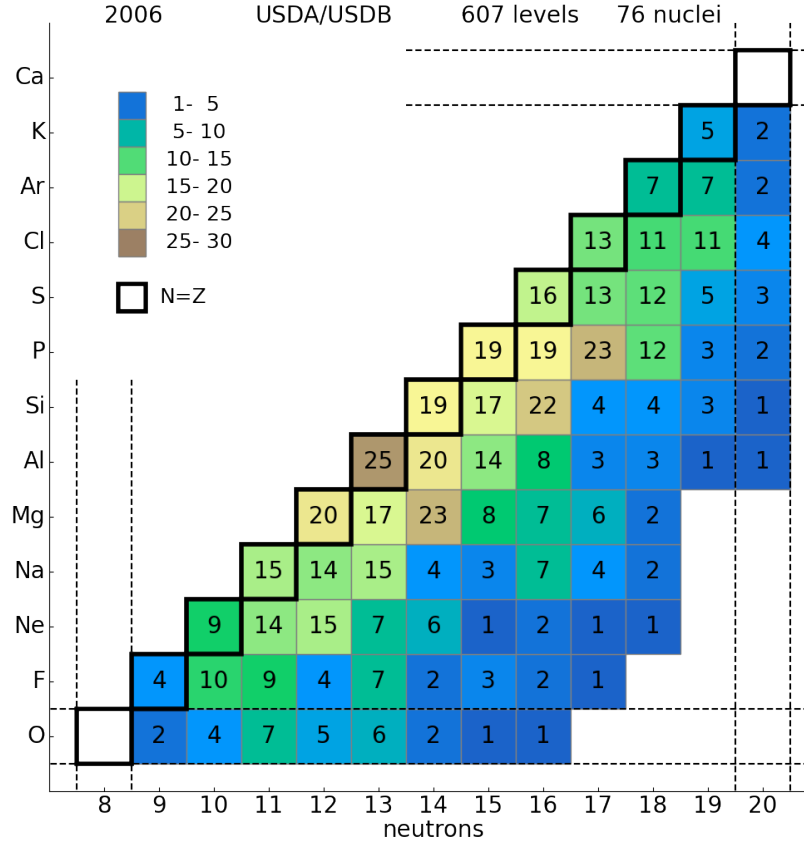
Figure 2.3: Number of energy levels in each *sd*-shell nuclei used in the data set for constraining the USDA and USDB Hamiltonians [15]

across the entire shell, was developed by Wildenthal from 1976 to 1982 as computers became more powerful. The larger set of 446 energy levels from 67 nuclei is shown in Fig. 2.2. Apart from the increased computational resources he had access to, the idea of a smooth mass scaling of the TBME was introduced. This smooth mass scaling helped to account for the difference in size between nuclei with different mass numbers while maintaining the underlying TBME. This helped to improve the predictive power of the interaction. This interaction is simply called the USD interaction, as in the Universal *sd*-shell interaction, and had an rms deviation of about 150 keV compared to the experimental excitation energies.

The next iteration of what are now called USD-type Hamiltonians came in 2006 when USDA

and USDB were developed using the same fitting procedure as USD, with 30 linear combinations of one- and two-body matrix elements varied for USDA and 56 for USDB, with the remaining linear combination fixed values determined by SDBA (the *ab initio* interaction used to develop USD). The resulting rms deviation between experimental and theoretical energies were 170 keV and 130 keV for USDA and USDB, respectively. An increased data set was used for USDA and USDB with 608 well known energy levels in 77 nuclei with $N \geq Z$ mainly added data for the middle of the *sd*-shell. The distributions of the 607 experimental energies spread across 76 nuclei used in this fit are shown in Fig. 2.3.

Something that all of these interaction have in common is that they are isospin conserving. That is, they treat the proton and neutron as different projections of a single particle called the nucleon. The pesky fact the protons are not identical to neutrons given their electric charge was dealt with perturbatively. As these were developed as isospin-conserving Hamiltonians, the energies used in the fit had to include Coulomb energy corrections [15]. These corrections were obtained from examining mirror energy differences of isobaric analog states near the $N = Z$ line. For exact values of the corrections see page 2 of Ref. [15].

As mentioned, there exist isospin non-conserving additions to USD consisting of a Coulomb interaction, an isovector term, and an isotensor term [31, 32]. These additions were fit to experimental *b*- and *c*-coefficients of the Isobaric Multiplet Mass Equation (IMME). It is important to note however that this was done *without* modifying the underlying USD interaction. The addition from [31] is often used with USDB to perform configuration-interaction calculations and is referred to as USDB-CD.

2.2   The expanded Data Set

In the last update of the "USD" Hamiltonians in 2006 [15], 607 levels in 76 nuclei were used in $N \geq Z$ nuclei in the *sd*-shell. This included the 77 ground state energies and 531 excited state energies. The distribution of these states in the shell can be seen in Fig. 2.3. The restriction to neutron-rich nuclei was made because USDA and USDB were made in isospin formalism, which

31
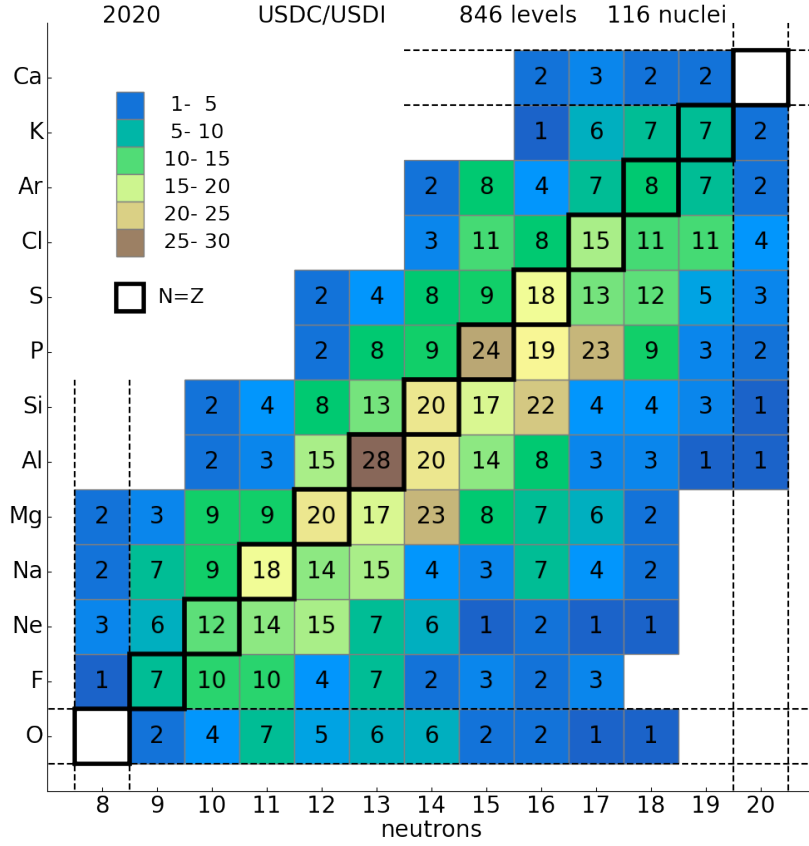
Figure 2.4: Number of energy levels in each *sd*-shell nuclei used in the data set for constraining the USDC family of Hamiltonians.

assumed that mirror nuclei were identical apart from a simple Coulomb energy correction. Also for this reason, $T = 1$ isobaric analogue states in the $N = Z$ nuclei were excluded from the data set. Those IAS excluded from previous fits but that fit all other criteria described below are included in the updated data set.

By changing our interaction to the *pn* formalism, we now allow all well known *sd*-shell states in nuclei with $8 \leq N \leq 20$ and $8 \leq Z \leq 20$, to be used in the data set to constrain our Hamiltonians. This expanded data set includes ground state energies for 116 nuclei, with at least one excited state included for 107 of those nuclei. The level distribution over *sd*-shell nuclei is shown in Fig. 2.4. Ground state binding energies used are taken from the 2016 atomic mass evaluation of Wang *et. al*

[36] and taken relative to that of ^{16}O,

$$BE(A, Z)^r = BE(A, Z) - BE(^{16}O). \tag{2.1}$$

Excited state energies are taken from the ENSDF database. The number of levels with experimental errors less than 0.2 MeV included in the data set from each nucleus are shown in Fig. 2.4. Generally, excited states were only included if the J^π for all lower states are known. This is done to ensure that only states with purely sd-shell configurations are included. So called "intruder states" that involve orbitals outside of our model space are omitted from the data set as we know that our model will not be able to replicate them. These typically occur at high excitation energies where the experimental level density is much higher than the theoretical level density.

Recently, an extensive measurement of the mirror energy differences in ^{27}Al and ^{27}Si was conducted by Gavin Lotay [37], providing 43 well known mirror pairs in the $A = 27$, $T = 1/2$ isobaric pair. This wealth of data will be used later to improve our constraints on the Coulomb interaction.

A collection of nuclei with $N = 19 - 20$ and $Z = 10 - 12$ are in the "island of inversion" [38]. The ground states of these six nuclei are bound by ≈ 2 MeV more than expected in sd-shell configuration-interaction calculations. This is understood to be due to an inversion of the standard level scheme and requires extension to the pf-shell to be properly calculated [38]. Essentially, an intruder state is so well bound that it supplants the ground state and the expected sd-shell ground state is in actuality an excited state of the nucleus. Ground states and excited states for these nuclei are therefore excluded from the fit.

Several states that have a large Thomas-Ehrman Shift (TES) are excluded from the fit. These states are in proton-rich nuclei and are near the proton separation energy. A discussion of these states and analysis of their TES is found in the first section of Chapter 3. A full list of the levels used in the fitting procedure for this work is shown in Table A1 in Appendix A.

2.3 Sensitivity levels in the fit

We will be examining energy differences at several different scales while constraining a new interaction for the *sd*-shell. Therefore it is advantageous to separate the interaction into its component pieces. In this work, we separate the Hamiltonian into three parts

$$H = H_0 + H_{INC} + H_C, \tag{2.2}$$

where H_0 is the isospin-conserving strong interaction, H_{INC} is the isospin-breaking portion of the strong interaction, and H_C is the Coulomb interaction. This allows us to separate the eigenvalues λ_k of the full Hamiltonian with eigenvectors ϕ_k into

$$
\begin{aligned}
\lambda_k &= \langle \phi_k | H | \phi_k \rangle \\
&= \langle \phi_k | H_0 | \phi_k \rangle + \langle \phi_k | H_{INC} | \phi_k \rangle + \langle \phi_k | H_C | \phi_k \rangle \\
&= \lambda_k^0 + \lambda_k^{INC} + \lambda_k^C.
\end{aligned}
\tag{2.3}
$$

The method of fitting used in this work has three levels of sensitivity. First, the H_0 was fit using all available energy levels in the shell, while H_C and H_{INC} are held constant at reasonable initial values. Second, H_C was modified in the case of USDCm and USDIm to reproduce the experimental linear (b) coefficients in the IMME. And lastly, the isotensor strength modification in H_{INC}, that is the change in strength for the $T = 1$ *pn* TBME, was set to minimize the rms deviation of the quadratic (c) coefficients of the IMME. After these steps, we once again fit H_0 while holding H_C and H_{INC} constant at the new constrained values. We explored adding an isovector component to the interactions but found that it could not be well constrained by the data set and did not significantly impact the results of the fits. This will be revisited in Chapter 4.

As in the derivation of USDA and USDB, a reformulation of the least-squares fit in terms of uncorrelated linear combinations through a SVD of the error matrix is used to constrain the SPE and TBME to experimental energies. The strength of this method is in the separation of well determined and poorly determined linear combinations, allowing us to replace those not well

constrained values using a starting *ab initio* Hamiltonian. A full explanation of the method used for USDA/USDB can be found in [15], and a generalized method can be found in Chapter 1.

Briefly, the optimization of the interaction with N_p parameters, $p_i = 1, ..., N_p$ (the SPE and TBME), that are adjusted to fit N_d experimental energies E_{exp} through the minimization of:

$$\chi^2(\mathbf{p}) = \sum_{k=1}^{N} \left(\frac{E_{exp}^k - \lambda_k(\mathbf{p})}{\sigma^k} \right)^2, \tag{2.4}$$

where σ^k are the adopted errors corresponding to the experimental energies and include both experimental and theoretical errors. To minimize the arbitrariness of the selection of the theoretical error, the adopted errors can be tuned so that the χ^2 function is normalized to the number of degrees of freedom $N_{dof} = N_d - N_p$ at the minimum $\vec{p}_0$ [27]. Here that provides a theoretical error of 140 keV.

A new addition to these isospin-breaking USD-type Hamiltonians is a statistical uncertainty for each of the fitting parameters. This was done following the prescription of [27], first defining the covariance matrix C in terms of the Jacobian J:

$$C \approx (J^T J)^{-1}, \quad J_{i\alpha} = \frac{1}{\sigma^i} \left. \frac{\partial E_{exp}^k}{\partial p_\alpha} \right|_{\vec{p}_0}. \tag{2.5}$$

Statistical uncertainties for the fitted parameters can then be calculated as $\Delta p_\alpha = \sqrt{C_{\alpha\alpha}}$. Statistical uncertainties for calculated observables can also be determined using the covariance matrix.

Recently, uncertainty quantification of shell model parameters in the *sd*-shell was carried out using principal component analysis in Ref. [39].

2.3.1 Binding and Excitation Energies

Some changes to the SVD fit method outlined in Chapter 1 are needed to transition to the *pn* formalism. It was necessary to group the strong force TBME that would be identical in an isospin-symmetric interaction. For example the following TBME in isospin formalism transforms into three equal (up to a phase) TBME in *pn*-formalism; namely a proton-proton term, a neutron-neutron

term, and a proton-neutron term.

$$V_{0,1}(k,k;k,k) \rightarrow V_{0,1}(pk,pk;pk,pk)$$

$$V_{0,1}(pk,nk;pk,nk) \tag{2.6}$$

$$V_{0,1}(nk,nk;nk,nk),$$

where the label k represents an sd-shell orbit ($s_{1/2}$, $d_{5/2}$, or $d_{3/2}$) and the prefixes p and n indicate whether it is a proton or neutron orbit, respectively. We therefore want these terms in H_0 to evolve together during the fit. This takes the 202 TBME in H_0 and puts them into 63 TBME groups. The breaking of this isospin symmetry will be brought in by H_{INC}.

Since we are not fitting the entire Hamiltonian at once, and instead are doing so in stages, we must also subtract the contributions to the energy eigenvalues due to H_{INC} and H_C from the experimental energies in the data set. This is because we wish to minimize the quantity

$$\chi^2 = \sum_{k=1}^{N} \left(\frac{E_{exp}^k - \lambda_k}{\sigma_{exp}^k} \right)^2 = \sum_{k=1}^{N} \left(\frac{\tilde{E}_{exp}^k - \lambda_k^0}{\sigma_{exp}^k} \right)^2, \tag{2.7}$$

where E_{exp}^k are the experimental energies, σ_{exp}^k are the associated errors, and $\tilde{E}_{exp}^k = E_{exp}^k - \lambda_k^{INC} - \lambda_k^C$ is the effective experimental energies used in the first stage of the fit.

2.3.2 Mirror Energy Differences

Unlike the nuclear strong froce, we can derive the Coulomb interaction for the sd-shell analytically directly from theory. Three methods of doing so were considered for the two-body Coulomb interaction. The first is an analytic Coulomb potential in the simple harmonic oscillator basis. A benefit of harmonic oscillator wave functions is the simplification of the separation into relative and center-of-mass coordinates. Using this potential requires that $\hbar\omega$ have a mass dependence $\approx 41\mathrm{A}^{-1/3}$ to adequately reproduce the experimental rms charge radii. The consequence of this is an overall mass dependence for the Coulomb TBME of $\langle 1/r \rangle \sim (\hbar\omega)^{1/2} \sim \mathrm{A}^{-1/6}$.

A more realistic basis using a Skyrme energy density functional was also used to calculate a two-body Coulomb interaction. Lastly, we can take the Coulomb component of the nuclei-specific

IMSRG Hamiltonians for nuclei with $N = Z$ in the sd-shell. The Coulomb contribution to the IMSRG TBME was determined by taking the difference of the pp and nn $T = 1$ terms. We then take an average of these IMSRG Coulomb TBME as another H_C to test in the fit.

In the first two cases, corrections may be added to the Coulomb potential to account for the short-range correlations between the protons and for the finite size of the proton. These are discussed later in the chapter.

The b-coefficient of the IMME is due primarily to the Coulomb force. Therefore, the b-coefficient rms deviation between experiment and theory calculations serves as a good test to differentiate these three choices for H_C. In the data set, there are 206 mirror energy states (38 ground state pairs, and 168 excited state pairs) with experimental errors < 0.2 MeV. It is important to exclude those pairs which have a large (TES). Due to different radial extents of the s and d orbitals, the energies of isobaric mirror states are shifted down by the Coulomb interaction [40, 41]. These excluded pairs will be discussed in Chapter 3.

Just as an SVD fit was done for H_0, the method can be applied to the 30 TBME and 3 SPE in H_C to further reduce the b-coefficient rms deviation. This requires re-framing the minimization parameter to

$$\chi_b^2 = \sum_{k=1}^{N_b} \left(\frac{b_{exp}^k - b_{fit}^k}{\sigma^k} \right)^2 , \tag{2.8}$$

where

$$b^k = \frac{E^k(T_z = T) - E^k(T_z = -T)}{2T}, \tag{2.9}$$

for a pair of states in mirror nuclei. Here the theoretical error added in quadrature with the reported experimental values is 70 keV or about half of the theoretical error associated with the energy levels.

Whether a mass dependence for the SPE should be added was investigated, but no improvement in spectra or rms deviations was achieved and so we do not include it. This is consistent with previous work in the sd-shell. A slight mass dependence was noticed in the IMSRG interactions, but they also include variable zero-body energy terms. These terms are a combination of kinetic
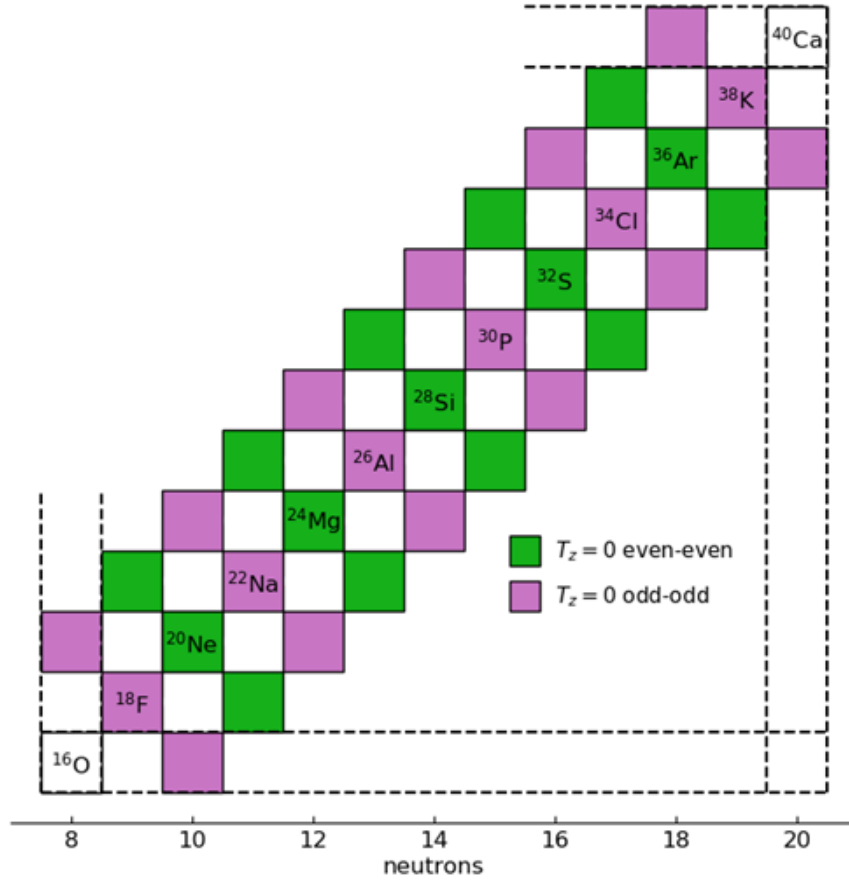
Figure 2.5: A visualization of the two types of $T = 1$ triplets in the *sd*-shell. Isobaric triplets whose $T_z = 0$ member is an even-even nucleus (green) and those whose $T_z = 0$ member is an odd-odd nucleus (violet). This difference causes the oscillation in the *c*-coefficients.

and potential energy contributions, and so trying to separate their interpretations becomes very difficult.

2.3.3 IMME *c*-coefficients

Isospin symmetry is not broken solely by the Coulomb interaction, it is also only an approximate symmetry for the strong nuclear Hamiltonian. Nucleon-nucleon scattering data has shown that the V_{nn} strength is slightly larger than V_{pp}, and further that V_{np} is greater than the average of V_{nn} and V_{pp}. This has been previously been approximated as a 1% increase in the $T = 1$ *pn* two-body matrix elements and a 1% decrease in the $T = 1$ *nn* and *pp* two-body matrix elements. For this work, the
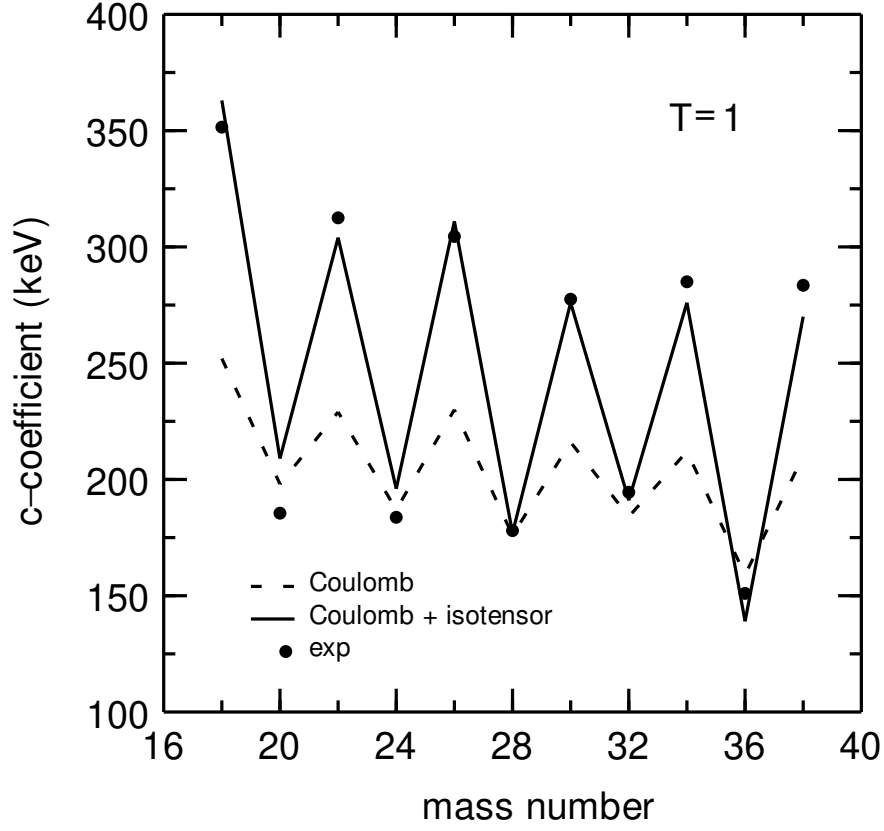
Figure 2.6: The *c*-coefficients of the lowest lying $T = 1$ *sd*-shell triplets. The crosses show predictions using USDI. The dashed line shows the contribution to the *c*-coefficients from the Coulomb interaction. The solid line shows the combined contribution from the Coulomb interaction and a 2.2% increase in the $T = 1$ *pn* TBME to capture the isotensor interaction (see text). Experiment is shown as filled circles.

same isotensor effect can be captured by simply increasing the $T = 1$ *pn* matrix elements by

$$V_{J,1}(pn) = (1 + \alpha_T) \left(\frac{V_{J,1}(pp) + V_{J,1}(nn)}{2} \right), \tag{2.10}$$

with α_T being set initially to 0.02 or 2%. This is also consistent with the results of [31]. In this work, we also take $V_{pp} = V_{nn}$ in H_0.

While the *b*-coefficient of the IMME is sensitive to the Coulomb interaction, the quadratic (c) coefficient is sensitive to the asymmetry between the *pn* interaction to the strong components of the *nn* and *pp* interactions. This is due to a cancellation of other terms in the calculation of the *c*-coefficients, most evident in the equation for $T = 1$ multiplets.

The triplets can be categorized into two groups, shown in Fig. 2.5. The first is those with an even-even $T_z = 0$ nucleus (shown in green) and those with an odd-odd $T_z = 0$ nucleus. This results in an oscillation of the c-coefficients as you move up the shell.

Fig. 2.6 shows this odd-odd to even-even oscillation of the c-coefficients for the ground-state $T = 1$ triplets in the sd-shell. Including Coulomb as a source of isospin breaking can only partially explain the size of the oscillation. However, the addition of an isotensor component creates much better agreement with experiment.

The oscillations in the c-coefficients arise from the J-dependence of the TBME. The values of the $V_{J,T=1}(5,5;5,5)$ TBME are -2.5601 MeV ($J = 0$), -0.9894 MeV ($J = 2$), and -0.1982 MeV ($J = 4$) for the strong (isospin-conserving) interaction and 0.4386 MeV ($J = 0$), 0.3852 MeV ($J = 2$), and 0.3612 MeV ($J = 4$). As J increases, there is a much steeper drop-off in the isospin-conserving TBME compared to the Coulomb TBME. And as the isotensor interaction is modeled as proportional to the isospin-conserving TBME, the same drop-off is found in the isotensor TBME.

If there were no J dependence in the TBME, there would be no oscillations in Fig. 2.6. The weak J dependence in the Coulomb TBME result in small oscillations. It is the strong J dependence in the isotensor interaction that creates the large oscillations in the c-coefficients.

2.4 The USDC and USDI interactions

The calculations for the wavefunctions and energies were carried out with the configuration-interaction code NuShellX. One iteration for the strong interaction fit took around 2 hours on a powerful multi-core desktop PC.

The criteria used to include experimental data in the fit is described in Sec. II. These allow us to consider 854 states in 116 nuclei with errors of less than 0.2 MeV. The uncertainties used show the experimental errors σ^k_{exp} added in quadrature with a theoretical error set to 140 keV,

$$(\sigma^k)^2 = (\sigma^k_{exp})^2 + (\sigma^k_{th})^2, \tag{2.11}$$

in order to normalize the χ^2 to the number of degrees of freedom.

Table 2.1: Comparison of *ab initio* and fitted isospin-conserving TBME for the *sd*-shell in isospin formalism with $T = 1$ (in MeV). Note that $\mathrm{v}(abcd; JT) = V_{JT}(ab; cd)(A = 18)$ The orbits are labeled by $1 = s_{1/2}$, $3 = d_{3/2}$, and $5 = d_{5/2}$. The $\Delta\mathrm{v}$ column shows the statistical uncertainties for USDI which are representative for all of our new Hamiltonians.

ME	SDBA	USDC	USDCm	IMSRG	USDI	USDIm	$\Delta\mathrm{v}$
v(5 5 5 5; 0)	−2.5418	−2.5601	−2.5700	−2.5284	−2.3690	−2.3796	0.0932
v(5 5 3 3; 0)	−2.9807	−3.1774	−3.2194	−4.6033	−3.5295	−3.5705	0.1666
v(5 5 1 1; 0)	−1.0885	−1.5666	−1.5843	−1.5239	−1.6163	−1.6341	0.0621
v(3 3 3 3; 0)	−1.1624	−1.8877	−1.9070	−0.5971	−1.8648	−1.8826	0.0921
v(3 3 1 1; 0)	−0.7911	−1.0370	−1.0578	−1.1893	−0.9147	−0.9328	0.0849
v(1 1 1 1; 0)	−2.0617	−1.6433	−1.6622	−1.3890	−1.6762	−1.6962	0.0794
v(5 3 5 3; 1)	−0.4249	0.6030	0.6126	0.6542	0.4130	0.4265	0.1190
v(5 3 3 1; 1)	−0.0304	−0.1531	−0.1704	0.1021	−0.2856	−0.3247	0.2107
v(3 1 3 1; 1)	0.3994	0.5638	0.6042	0.3115	0.6230	0.6655	0.0646
v(5 5 5 5; 2)	−0.9932	−0.9894	−1.0151	−0.9087	−0.9777	−1.0076	0.0409
v(5 5 5 3; 2)	−0.1394	−0.2289	−0.2254	−0.3810	−0.1917	−0.1924	0.0478
v(5 5 5 1; 2)	−0.7957	−0.9274	−0.9579	−0.9790	−0.8992	−0.9241	0.0478
v(5 5 3 3; 2)	−0.9399	−1.1421	−1.1623	−1.0623	−1.2787	−1.3037	0.1450
v(5 5 3 1; 2)	0.8477	0.9137	0.9432	1.0809	0.9979	1.0254	0.0800
v(5 3 5 3; 2)	−0.4043	−0.0041	−0.0300	0.4747	0.1943	0.1624	0.1023
v(5 3 5 1; 2)	−0.2469	−0.3128	−0.3166	0.1527	−0.3647	−0.3682	0.0603
v(5 3 3 3; 2)	−0.9871	−0.7064	−0.7041	−0.7988	−0.8317	−0.8325	0.1020
v(5 3 3 1; 2)	0.6449	0.4256	0.4292	0.8469	0.3580	0.3515	0.0910
v(5 1 5 1; 2)	−1.2335	−0.9690	−0.9939	−0.8554	−0.9738	−1.0042	0.0426
v(5 1 3 3; 2)	−0.6317	−0.3807	−0.3791	−0.6018	−0.2549	−0.2519	0.0962
v(5 1 3 1; 2)	1.4633	1.5668	1.5727	1.4230	1.6142	1.6209	0.0774
v(3 3 3 3; 2)	0.1427	−0.0615	−0.0422	−0.1102	−0.0852	−0.0626	0.0282
v(3 3 3 1; 2)	0.1787	0.3135	0.3247	0.2766	0.3313	0.3427	0.0474
v(3 1 3 1; 2)	−0.2767	−0.3338	−0.2940	−0.0167	−0.3463	−0.3048	0.0476
v(5 3 5 3; 3)	0.5050	0.6476	0.6551	0.2937	0.6708	0.6802	0.0918
v(5 3 5 1; 3)	−0.1021	−0.4971	−0.4956	−0.2474	−0.4647	−0.4656	0.0536
v(5 1 5 1; 3)	0.2781	0.6725	0.6690	0.6042	0.6536	0.6493	0.0536
v(5 5 5 5; 4)	0.0356	−0.1982	−0.2087	−0.0631	−0.1906	−0.2032	0.0206
v(5 5 5 3; 4)	−1.4942	−1.3256	−1.3133	−1.4737	−1.3335	−1.3215	0.0339
v(5 3 5 3; 4)	−1.6941	−1.3904	−1.4069	−0.7751	−1.4937	−1.5106	0.0716

Table 2.2: Same as Table 2.1 but for the $T = 0$ isospin formalism strong TBME.

ME	SDBA	USDC	USDCm	IMSRG	USDI	USDIm	Δv
v(5 5 5 5; 1)	−1.4315	−1.4302	−1.4317	−1.7115	−1.3929	−1.3981	0.1449
v(5 5 5 3; 1)	3.1790	3.3480	3.3348	4.8436	3.5507	3.5267	0.1210
v(5 5 3 3; 1)	1.7666	1.7134	1.7204	1.5594	1.1894	1.2067	0.4152
v(5 5 3 1; 1)	0.3628	0.2639	0.2854	−0.0049	0.3140	0.3424	0.1734
v(5 5 1 1; 1)	−0.8749	−0.5303	−0.5304	−1.0724	−0.3500	−0.3566	0.1734
v(5 3 5 3; 1)	−6.5104	−5.9698	−5.9608	−7.4545	−5.6815	−5.6813	0.1595
v(5 3 3 3; 1)	−0.0200	−0.2165	−0.2261	0.3890	−0.2293	−0.2489	0.1747
v(5 3 3 1; 1)	1.7250	1.6755	1.6867	2.8536	1.6872	1.7019	0.1224
v(5 3 1 1; 1)	1.8887	1.9722	1.9991	2.8861	2.1688	2.1917	0.1049
v(3 3 3 3; 1)	−1.3404	−1.6712	−1.6859	−0.0999	−1.5575	−1.5736	0.0947
v(3 3 3 1; 1)	−0.8402	−0.6838	−0.6716	−1.2388	−0.7949	−0.7795	0.0893
v(3 3 1 1; 1)	0.0405	0.1022	0.0821	−0.2347	0.2309	0.2189	0.1387
v(3 1 3 1; 1)	−3.3056	−3.8748	−3.9136	−3.7679	−4.0006	−4.0260	0.0912
v(3 1 1 1; 1)	−0.2441	−0.9583	−0.9417	−1.0430	−1.0963	−1.0773	0.1054
v(1 1 1 1; 1)	−3.3313	−3.6510	−3.6842	−3.0068	−3.5766	−3.6058	0.0944
v(5 3 5 3; 2)	−4.5004	−4.2675	−4.2872	−5.1309	−4.5096	−4.5269	0.1454
v(5 3 5 1; 2)	−1.2555	−0.7692	−0.7537	−1.6854	−0.8428	−0.8296	0.0986
v(5 3 3 1; 2)	−1.4793	−0.2953	−0.2881	−1.6810	−0.3153	−0.3067	0.1317
v(5 1 5 1; 2)	−0.4109	−0.3329	−0.3060	−0.4944	−0.3223	−0.2941	0.1331
v(5 1 3 1; 2)	−2.7050	−2.4310	−2.4331	−2.6000	−2.2262	−2.2209	0.2112
v(3 1 3 1; 2)	−1.3883	−1.9103	−1.9525	−1.6706	−1.8622	−1.9173	0.0860
v(5 5 5 5; 3)	−0.8478	−1.5969	−1.5745	−1.2752	−1.6701	−1.6343	0.0766
v(5 5 5 3; 3)	2.1769	2.2564	2.2574	2.0175	2.1962	2.1934	0.1175
v(5 5 5 1; 3)	−1.4992	−1.1785	−1.1770	−2.1032	−1.1734	−1.1821	0.0652
v(5 5 3 3; 3)	0.8466	1.3317	1.3410	0.2661	1.1406	1.1452	0.1928
v(5 3 5 3; 3)	−1.0712	−1.2549	−1.2850	−1.2610	−1.5308	−1.5592	0.1455
v(5 3 5 1; 3)	1.0367	1.2484	1.2324	1.5017	1.2434	1.2349	0.1455
v(5 3 3 3; 3)	2.1625	1.1584	1.1576	2.3693	1.2987	1.2928	0.1462
v(5 1 5 1; 3)	−3.6000	−4.1134	−4.1194	−3.9772	−4.1631	−4.1546	0.0650
v(5 1 3 3; 3)	0.1668	0.1126	0.1224	0.0608	−0.1896	−0.1566	0.2127

As was done for the previous USD-type Hamiltonians, the SPE are taken to be mass independent. The *ab initio* ISMRG interactions are nucleus dependent and can have different zero-body terms (the binding energy of the core) and some apparent mass dependence for the SPE. We performed fits allowing a variable zero-body term, and with mass dependent SPE using the IMSRG for the *ab initio* Hamiltonian. These resulted in no improvement or a decrease in fit quality. Therefore, we keep a constant zero-body term and SPE for the fits. This does not have a significant effect on the rms deviations as changes in the TBME can compensate.

The TBME have a mass scaling of the form

$$V_{JT}(ab; cd)(A) = \left(\frac{18}{A}\right)^p V_{JT}(ab; cd)(A = 18). \tag{2.12}$$

For the matrix elements in H_0 and H_{INC}, we take $p = 0.3$ as described in [15, 28]. The Coulomb TBME scale analytically with $p = 1/6$ as previously shown.

The poorly determined linear combinations of the TBME and SPE were first constrained either with the renormalized G matrix Hamiltonian SDBA, or an average of the $N = Z$ sd-shell IMSRG interactions with the Coulomb matrix elements subtracted out to extract the strong component of the TBME. There exist other *ab initio* interactions that could be used to develop an effective interaction, such as those derived from chiral effective field theory in [42], but we would not expect much better agreement with experiment. Using SDBA as the constraining interaction resulted in the USDC Hamiltonian, and replacing SDBA with IMSRG resulted in the USDI Hamiltonian. Variants of USDC and USDI will also be introduced.

In this first stage of the fit there are a total of 69 parameters: the 63 groupings of the isospin-conserving matrix elements, the 3 SPE due to the strong interaction, and the 3 SPE due to the Coulomb interaction. The Coulomb TBME were held constant up to the mass scaling, and the isotensor strength was set initially to 2%.

For the first iteration, the USDB matrix elements in *pn* formalism were used for the strong interaction. Starting at $n = 5$ linear combinations being allowed to vary and the remaining poorly determined linear combinations being replaced with the *ab initio* values, we increased n every three iterations until we reached 56 varying linear combinations as used in the derivation of USDB. This
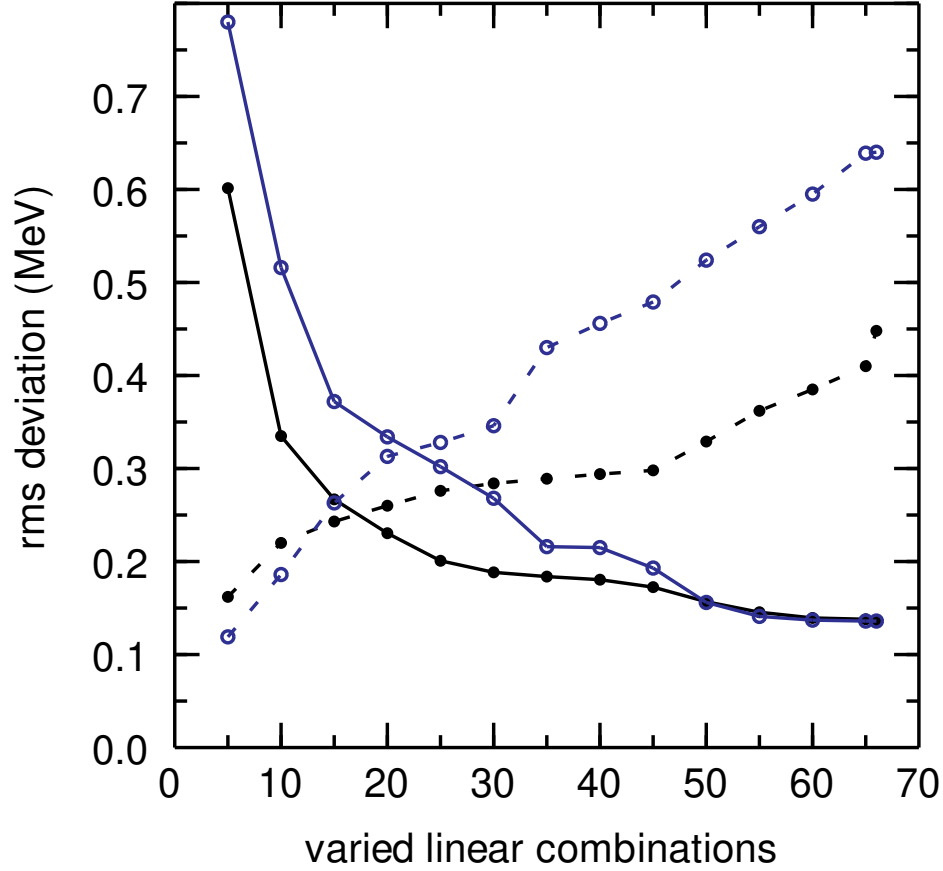
Figure 2.7: The rms deviations as a function of varied linear combinations for the strong interaction. In black filled circles are the results for USDC, with the blue open circles showing the results for USDI. The solid lines show the energy rms deviation between experimental and theoretical *sd*-shell energies. The dashed lines show the rms deviation for the interaction parameters between the resulting Hamiltonians and the *ab initio* interactions on which they are based.

Table 2.3: Comparison of fitted strong interaction SPE. The orbits are labeled by $1 = 1s_{1/2}$, $3 = 0d_{3/2}$, and $5 = 0d_{5/2}$. All numbers in MeV.

Interaction	ϵ_5	ϵ_3	ϵ_1
USDB	-3.923	2.112	-3.208
USDC	-3.952(20)	1.894(113)	-3.158(55)
USDCm	-3.896(19)	1.889(113)	-3.139(54)
USDI	-3.936(20)	1.857(112)	-3.127(55)
USDIm	-3.878(19)	1.852(112)	-3.111(54)

was done to allow for a slow evolution of the Hamiltonians through parameter space and allow the two different *ab initio* backgrounds to search for different minima in the parameter space. We then iterated until the Hamiltonian parameters converged to the level of about 10 keV. Results of this SVD fit can be seen in Fig. 2.7, showing the drop in energy rms deviation as the number of linear combinations allowed to vary is increased, along with an increase in the parameter rms deviation between the *ab initio* Hamiltonian used and the resulting fitted Hamiltonians.

The rms deviation between experimental and theoretical energies,

$$rms = \sqrt{\frac{1}{N} \sum_{k=1}^{N} (E_{exp}^k - E_{th}^k)^2},$$ (2.13)

for USDC and USDI are 139 keV and 140 keV, respectively. USDC and SDBA have a similar rms deviation between their TBME to that of USDB and SDBA, about 390 keV.

The rms deviation between the USDI and IMSRG TBME is somewhat higher, at 560 keV. As the IMSRG Hamiltonian is an average of several nuclei-specific IMSRG Hamiltonians it is not too surprising that the fit diverges more so than it did for SDBA. It's notable that even though the USDC and USDI were allowed to slowly converge from different starting values, they have an rms deviation for their TBME of 150 keV. The TBME and SPE, and their statistical uncertainties, of these Hamiltonians as well as two others to be discussed can be found in Tables 2.1, 2.2, and 2.3. We now have two new Hamiltonians based on two different *ab initio* models: USDC from SDBA, and USDI from IMSRG. However, we still have the isospin-breaking interactions to consider.

The deviations between experiment and theory for the ground state and excited state energies are shown in Fig. 2.8 for USDB-CD and Fig. 2.9 for USDC. Included in the figure are eight points that are not used in the fit. These are the six island of inversion ground states and the ground states of ^{27,28}F. The figure shows the results for USDC as at this scale there is no significant differences between USDI and USDC. For each element, the states in neutron deficient isotopes are to the left in the figure and those states in neutron-rich isotopes are to the right.

The ground states of the six nuclei in the island of inversion (^{29,30}Ne, ^{30,31}Na, and ^{31,32}Mg) that were not included in the fit, are under-bound compared to experiment by 1-2 MeV as shown in the
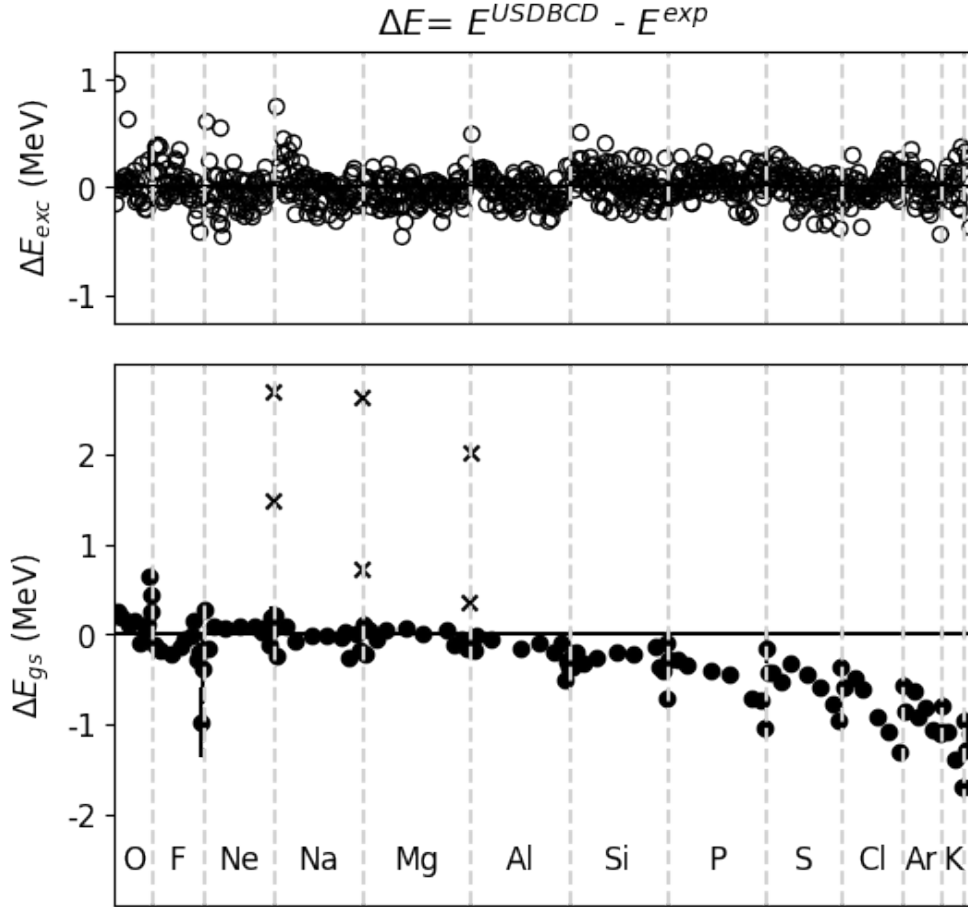
Figure 2.8: Deviations between experimental and theoretical energies for USDB-CD. The ground state binding energy deviations are plotted on the top, with the excited state energy deviations plotted on the bottom. The crosses show the deviations for the "island of inversion" nuclei. The fluorine isotopes with large deviations for their ground state binding energies are discussed in the text.

figures. Deviations this large demonstrate the need to expand into the pf model space in order to account for their binding energies [38].

For the new Hamiltonians the neutron-rich Fluorine isotopes ($A = 25, 26$) used in the fit show a clear pattern of the theory being over-bound when compared to experiment. The ground states of ^{27,28}F are significantly over-bound as well, but due to their larger experimental errors of 0.39 MeV they have no impact in the χ^2 minimization. Can we reproduce the energies of these fluorine isotopes without damaging agreement elsewhere? The fit was rerun with artificially suppressed errors for these fluorine isotopes to test this. The result was that these isotopes could not be
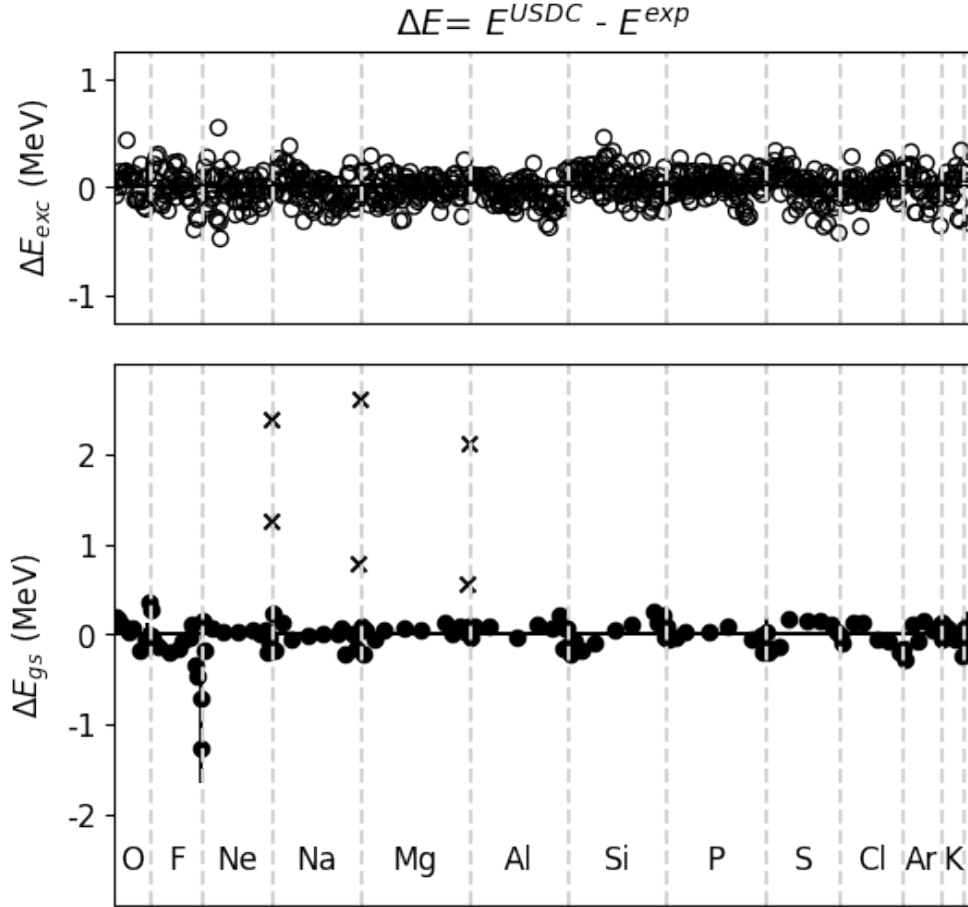
Figure 2.9: Same as Fig. 2.8 but for USDC.

forced to these values without significantly harming the fit. We suggest then that the reported binding energies of these isotopes is incorrect. The need for further more precise experimental measurements of the neutron-rich Fluorine isotopes is clear.

2.5 The USDCm and USDIm interactions

The largest source of isospin symmetry breaking in the nucleus is from the electromagnetic interaction between the protons. We investigated the effects of three distinct sets of Coulomb TBME. The IMSRG Coulomb interaction resulted in a b-coefficient rms deviation of 72 keV for our set of mirror states. It was found that for the analytic potential, both the Skyrme energy density functional basis and the simple harmonic oscillator basis resulted in only minor variations of the TBME and produced rms deviations of around 67 keV. Based on these results and to aid in reproducibility, the

Table 2.4: Comparison of fitted Coulomb interaction SPE. The orbits are labeled by $1 = 1s_{1/2}$, $3 = 0d_{3/2}$, and $5 = 0d_{5/2}$. These are for proton orbits only.

Interaction	ϵ_5	ϵ_3	ϵ_1
CD	3.575	3.526	3.484
w/ SRC	3.628(14)	3.451(18)	3.324(43)
Fitted	3.512(46)	3.464(270)	3.314(84)

simple harmonic oscillator basis was chosen as the source for the two-body Coulomb interaction.

Two corrections to the Coulomb potential were then analyzed to try and improve the b-coefficient rms deviation. The first is to include the short range correlations (SRC) of Miller and Spencer [43] through the form factor

$$F_{SRC}(r) = 1 - e^{-\alpha r^2}(1 - \beta r^2), \tag{2.14}$$

with $\alpha = 1.1$ fm^{-2} and $\beta = 0.68$ fm^{-2}. The finite size of the proton (FSP) can be accounted for using the form factor from R. B. Wiringa [44],

$$F_{FSP}(r) = 1 - e^{-x}(1 - (1 + \frac{11}{16}x + \frac{3}{16}x^2 + \frac{1}{48}x^3)), \tag{2.15}$$

with $x = br$ where $b = 4.27$ fm^{-1}. Interestingly, both of these modifications to the underlying analytic potential produce remarkably similar TBME when applied separately. When applied together, the TBME decrease noticeably.

With these three options (SRC, FSP, and SRC+FSP) we can once again check the b rms deviations. Each produces a moderate improvement of a few keV to the rms deviation. Given this and for simplicity, we chose to include only the Miller-Spencer short range correlations to the potential. This Coulomb potential with SRC in the simple harmonic oscillator basis was used to produce the Coulomb TBME used in USDC and USDI, and will be referred to as Coulomb w/ SRC.

With a Coulomb interaction chosen and two new effective interactions generated from our two *ab initio* interactions, we now examine whether further modifying the interaction through a secondary SVD fit can improve our results. As before, states with large TES that are near proton separation energy are excluded from this fit and discussed and are instead discussed in Chapter

Table 2.5: Comparison of Coulomb TBME. All orbits are for protons, with $1 = 1s_{1/2}$, $3 = 0d_{3/2}$, and $5 = 0d_{5/2}$.

Matrix element	CD	w/ SRC	Fitted
v(5 5 5 5; 0)	0.4386	0.467	0.4830
v(3 3 3 3; 0)	0.4243	0.4525	0.4872
v(1 1 1 1; 0)	0.4068	0.4335	0.4469
v(5 3 5 3; 1)	0.3958	0.4234	0.4196
v(3 1 3 1; 1)	0.3645	0.3901	0.3315
v(5 5 5 5; 2)	0.3852	0.4117	0.4732
v(3 3 3 3; 2)	0.3615	0.3866	0.3432
v(5 3 5 3; 2)	0.3807	0.4071	0.4271
v(5 1 5 1; 2)	0.3885	0.4153	0.4747
v(3 1 3 1; 2)	0.3805	0.4069	0.3322
v(5 3 5 3; 3)	0.3512	0.3758	0.4043
v(5 1 5 1; 3)	0.3645	0.3901	0.3902
v(5 5 5 5; 4)	0.3612	0.3863	0.3969
v(5 3 5 3; 4)	0.3913	0.4178	0.4601
v(5 5 3 3; 0)	0.035	0.0355	0.0908
v(5 5 1 1; 0)	0.0346	0.0363	0.1019
v(3 3 1 1; 0)	0.0283	0.0296	0.1177
v(5 3 3 1; 1)	0	0	0.0005
v(5 5 5 3; 2)	−0.0112	−0.0123	−0.0209
v(5 5 5 1; 2)	0.0238	0.0251	0.1032
v(5 5 3 3; 2)	0.0042	0.0041	0.0154
v(5 5 3 1; 2)	−0.0194	−0.0205	−0.0482
v(5 3 5 1; 2)	0.0168	0.0177	−0.0115
v(5 3 3 3; 2)	0.0145	0.0152	0.0162
v(5 3 3 1; 2)	−0.0137	−0.0145	−0.0005
v(5 1 3 3; 2)	0.0182	0.0192	0.0252
v(5 1 3 1; 2)	−0.0196	−0.0205	−0.0123
v(3 3 3 1; 2)	−0.0148	−0.0156	−0.0564
v(5 3 5 1; 3)	0	0	0.0008
v(5 5 5 3; 4)	0.0201	0.021	−0.0326
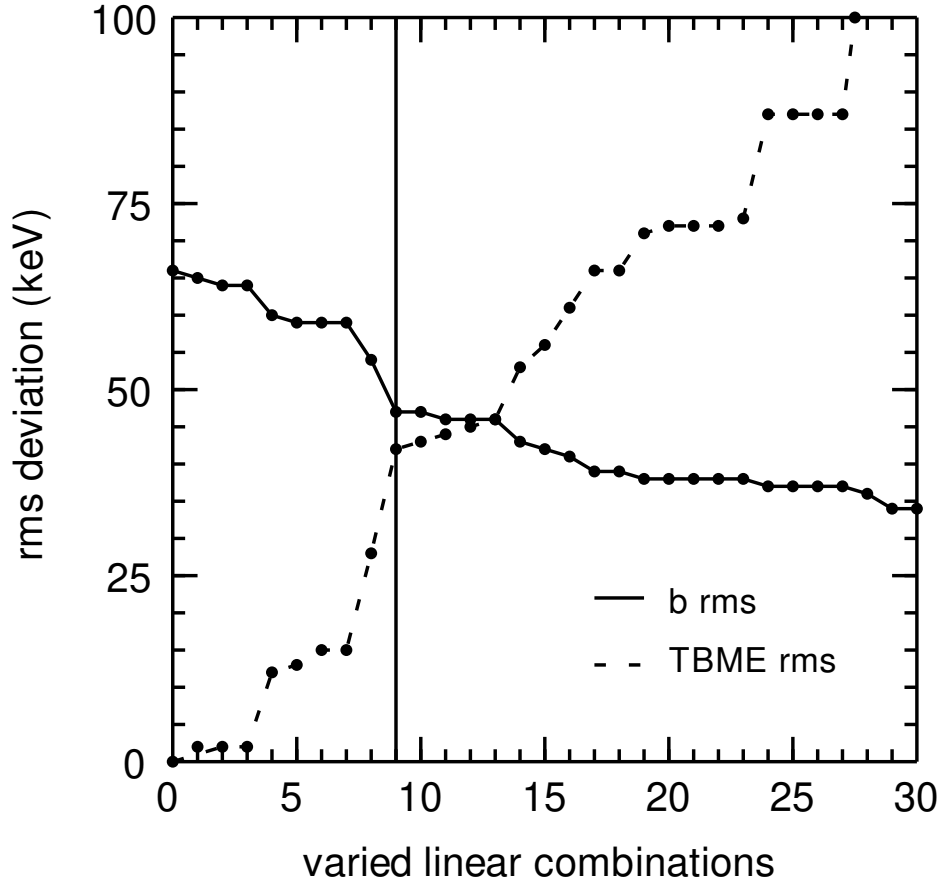
Figure 2.10: Results of the SVD fit for the Coulomb interaction. The solid line shows the rms deviation between experiment and theory of the IMME *b*-coefficients. The dashed line shows the interaction rms deviation. The vertical black line at 9 varied linear combinations shows our chosen "modified" Coulomb interaction.

3. A "residual" TES that is present throughout the shell could be accounted for with a modified Coulomb interaction. Such a modification could also be needed due to changes in radii for nuclei in excited sates. Since the Coulomb energy goes as $1/R$, a 1% increase in the radius would reduce the binding energy by about 110 keV. Any model space truncations would also be captured.

The results of the secondary SVD fit can be seen in Fig. 2.10 showing the rms deviation of the *b*-coefficients and Coulomb Hamiltonian parameters as a function of the number of varied linear combinations. A "modified" Coulomb interaction was chosen by allowing 9 linear combinations to vary in the fit. This was motivated by a drop in the rms deviation and the first significant change
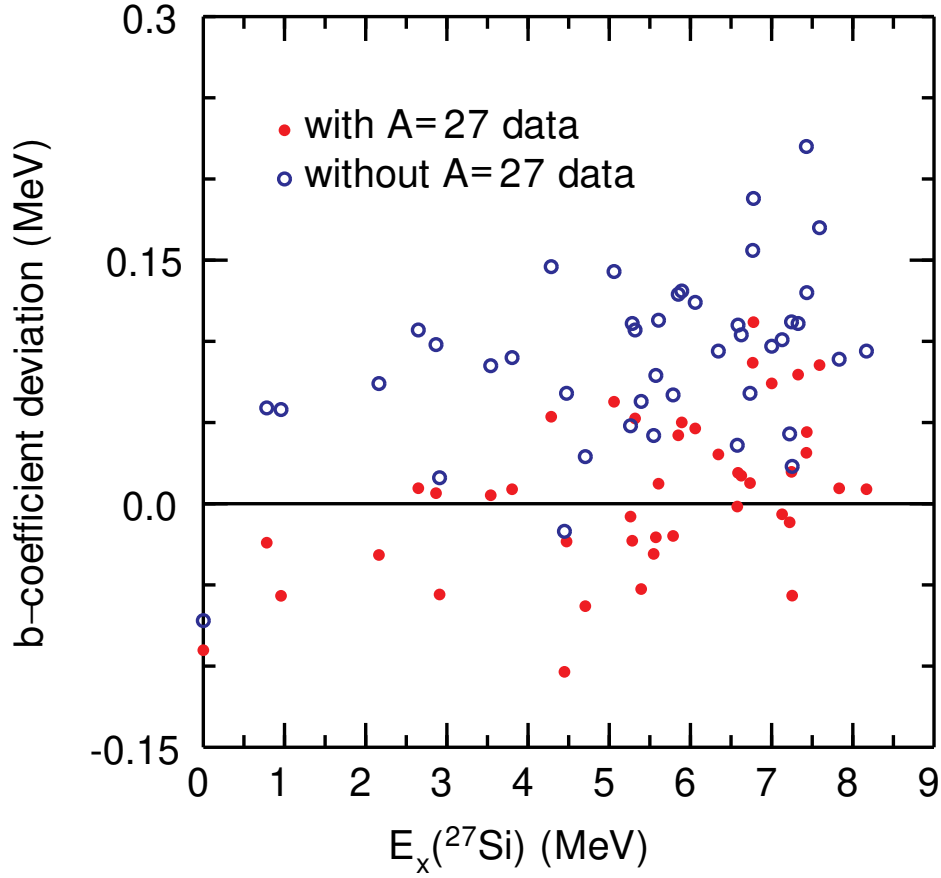
Figure 2.11: The $\Delta b = b_{exp} - b_{th}$ deviations for the $A = 27$, $T = 1/2$ isobaric pair plotted against the experimental excitation energy of ^{27}Si.

in the TBME and SPE occurring at this point.

The additional data for the $A = 27$, $T = 1/2$ isobaric pair provided by Gavin Lotay [37] allows us to compare our modified Coulomb interaction to experiment. It was found that the deviation from experimental b-coefficients increased as a function of excitation energy for this mirror pair, with an overall rms deviation of 104 keV. After refitting the Coulomb interaction with these additional data points, this problem was reduced with a new rms deviation for the $A = 27$ data of 48 keV. This improvement can be seen in Fig. 2.11.

The TBME of this new fitted Coulomb are compared to the Coulomb w/ SRC TBME in Table 2.5 and Fig. 2.12. Similarly, the SPE are compared in Table 2.4. The fitted Coulomb TBME and SPE are used in USDCm and USDIm, and referred to as the modified Coulomb interaction. These
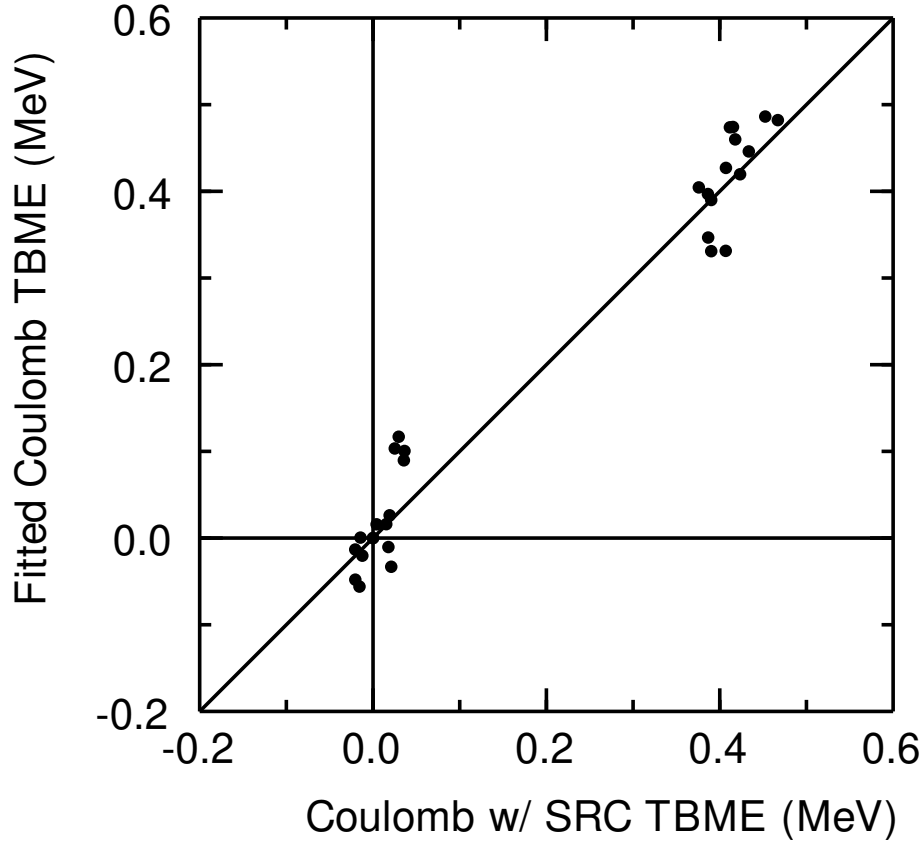
Figure 2.12: Comparison of the Coulomb w/ SRC TBME and the Fitted Coulomb TBME. The Fitted Coulomb was taken as the Coulomb interaction resulting from 9 varied linear combinations in Fig. 2.10. Values for the TBME are shown in Table 2.5.

additional Hamiltonians produce similar plots to Fig. 2.9 at that scale.

With the modified Coulomb in place, the isospin conserving strong TBME in H_0 were refit for USDCm and USDIm. All that is left to constrain now is H_{INC}, with some surprising results.

For each of our four new Hamiltonians, we adjusted the isotensor strength increase α_T from 0-4% to find the value that produced the lowest c-coefficient rms deviation for 26 isobaric multiplets in the data set. The set of multiplets were composed of 11 triplets ($T = 1$), 10 quartets ($T = 3/2$), and 5 quintets ($T = 2$). All multiplets used involved the ground states of the $|T_Z| = T$ nuclei.

This search determined that the ideal α_T is 2.2% for USDC and USDI which use Coulomb w/ SRC, which agrees well with our initial setting of 2% based on nucleon-nucleon scattering experiments and is consistent with previous theory. For USDCm and USDIm which use the fitted
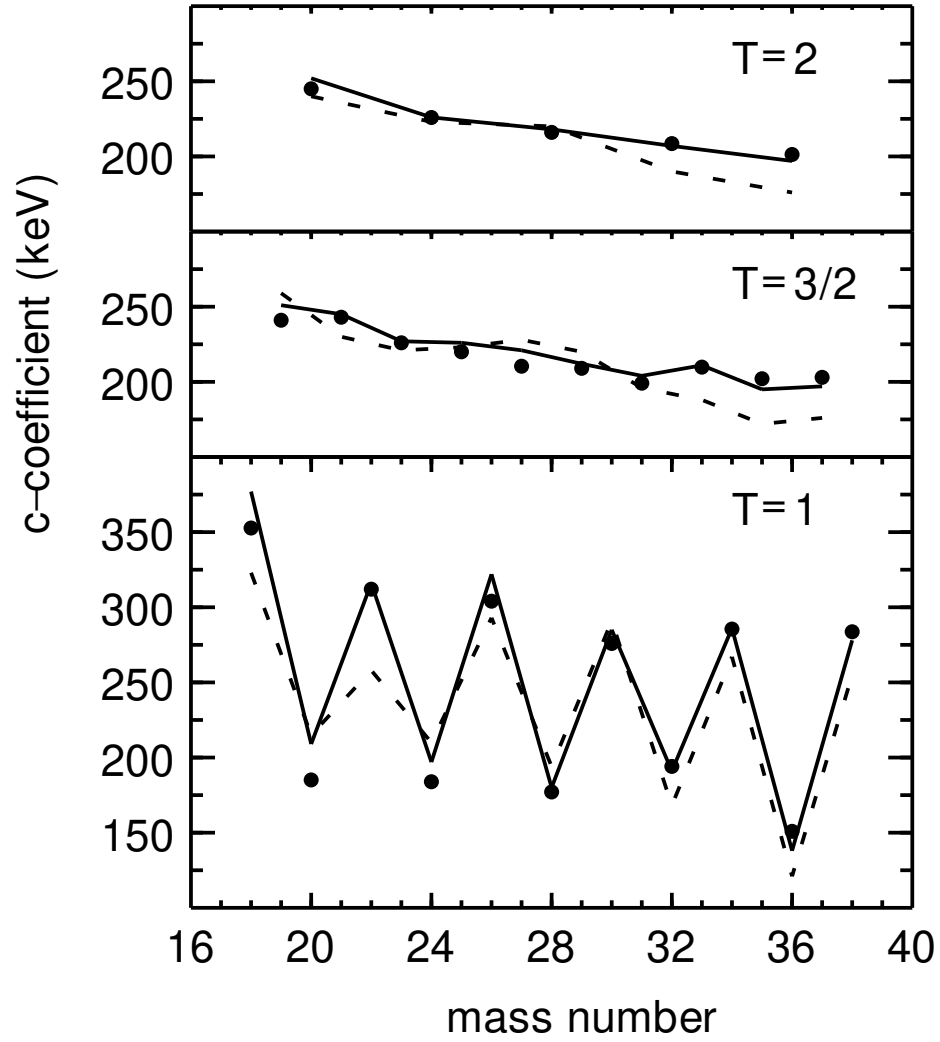
Figure 2.13: The *c*-coefficients for the lowest laying triplets, quartets, and quintets in the *sd*-shell. The solid black line shows the values for USDI, the dashed line for USDIm, and experiment is shown as filled circles.
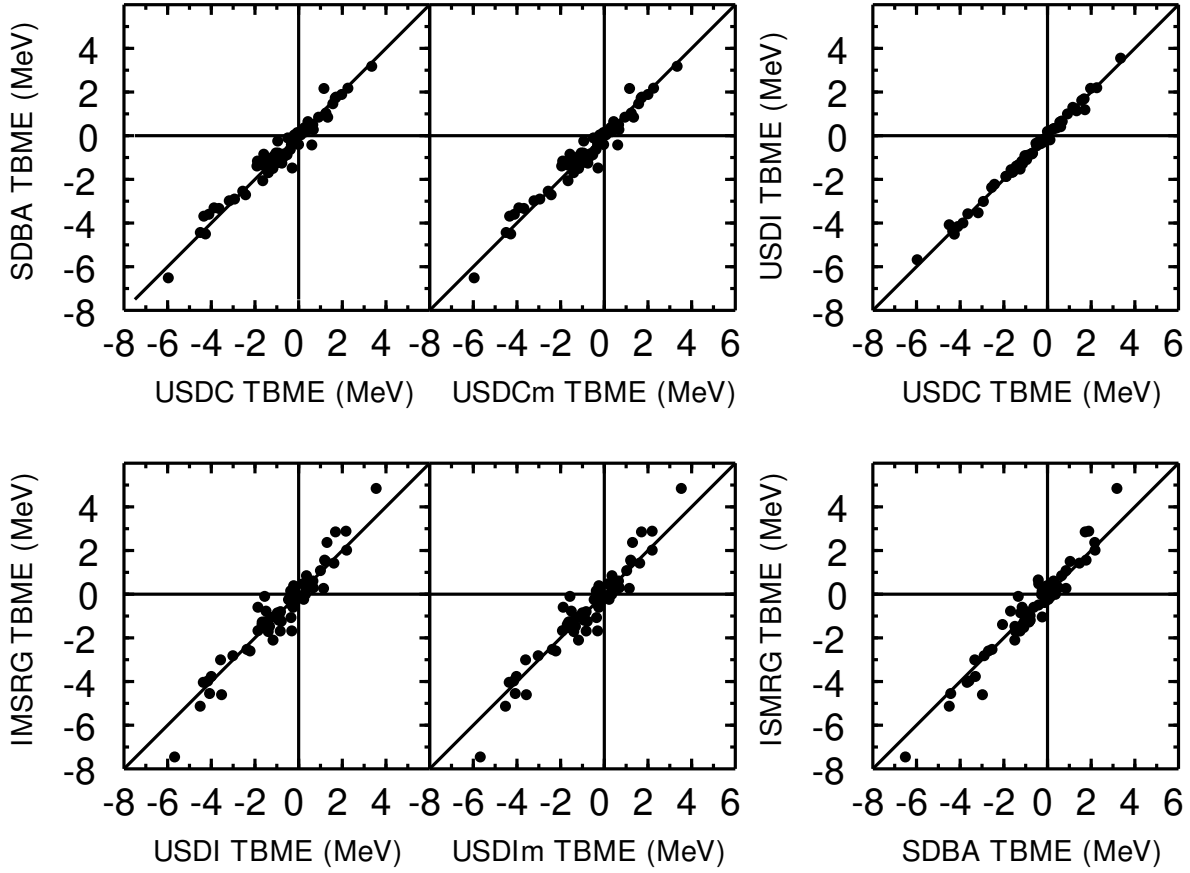
Figure 2.14: Comparisons of the fitted and *ab initio* TBME. Only the isospin-conserving TBME in isospin formalism are shown. These are representative of the 63 strong TBME groups.

Coulomb we find that the minimizing α_T is 0.8%. This lower isotensor strength increase indicates that the fitting of the Coulomb parameters is attempting to capture some of the effects of the isotensor component of the interaction.

Fig. 2.13 shows the theoretical and experimental c-coefficients used to constrain α_T. It is clear from the figure that USDI better reproduces the c-coefficients with an rms deviation of 8 keV compared to the rms deviation for USDIm of 21 keV. Similar results are seen with USDC compared to USDCm.

With the Coulomb and isotensor components of the new Hamiltonians fit or chosen, we once again fit the isospin-conserving strong interaction. Only one or two iterations were needed for each interaction to converge, and their final values are shown in Tabs. 2.1, 2.2, and 2.3. Visual

comparisons to the *ab initio* Hamiltonians are shown in Fig. 2.14.

To recap, the four new interactions we've introduced are:

- **USDC**: a constrained G-Matrix interaction, an analytic Coulomb term, and a 2.2% increase in the $T = 1$ *pn* matrix elements.

- **USDCm**: a constrained G-Matrix interaction, a constrained Coulomb term, and a 0.8% increase in the $T = 1$ *pn* matrix elements.

- **USDI**: a constrained IMSRG interaction, an analytic Coulomb term, and a 2.2% increase in the $T = 1$ *pn* matrix elements.

- **USDIm**: a constrained IMSRG interaction, a constrained Coulomb term, and a 0.8% increase in the $T = 1$ *pn* matrix elements.

2.6   Comparing the new Hamiltonians

The average, or monopole, interaction energy between two orbits a and b is defined as:

$$\bar{V}_{ab,T} = \frac{\sum_J (2J + 1) V_{JT}(ab; ab)}{\sum_J (2J + 1)}. \tag{2.16}$$

These monopole interaction energies combine with the SPE to create effective SPE with Z and N dependence. The monopole interactions for our new Hamiltonians are compared in Fig. 2.15 (a similar figure appearing in [15] is known to show incorrect values). They are split into three groups, the $T = 0$ and $T = 1$ isospin-conserving monopoles, and the Coulomb only $T = 1$ monopoles that involve only *pp* TBME. The isospin-conserving monopole interactions for USDC, USDCm, USDI, and USDIm are all very similar with the largest deviation being around 100 keV.

The terms with the largest variance among the new Hamiltonians, $d_{5/2} - d_{3/2}, T = 0$ and $s_{1/2} - s_{1/2}, T = 0$, are also the terms that differ from USDB the most. The IMSRG and SDBA monopole strengths differ by up to 600 keV in some cases, but have a similar pattern.
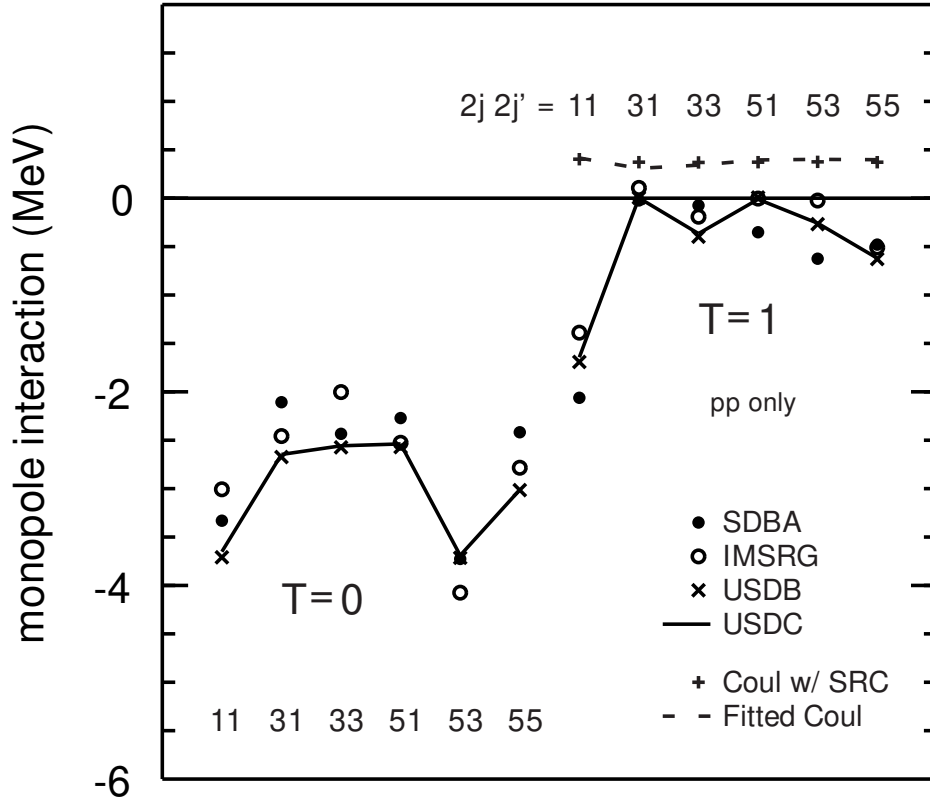
Figure 2.15: The *sd*-shell monopole interactions. The solid lines show USDC, which is representative of all four new interactions at this scale. The filled circles are for SDBA, the open circles for IMSRG, and the crosses for USDB. The Coulomb monopole interactions for *pp* matrix elements only are also shown, with Coulomb with SRC as pluses and the fitted Coulomb shown as a dashed line.

The six $T = 1$ monopole terms for our fitted Coulomb are shown to be in good agreement with the Coulomb w/ SRC, with most being within 5%. The $pd_{3/2} - ps_{1/2}$ term has the largest shift, with a decrease of 64 keV or 17% of the unfitted value.

Looking at the differences between energy level predictions using our new Hamiltonians can serve to help understand the theoretical uncertainties in those predictions. In Fig. 2.16 the residuals between USDC and USDI are shown for both the ground states and excited states, having rms deviations of 24 keV and 70 keV for each group, respectively. The rms deviation for all of the data is 30 keV, but is is clear that the spread is larger in the middle of the shell for the excited states. This tells us that the choice of *ab initio* interaction from which we build our Hamiltonians has a
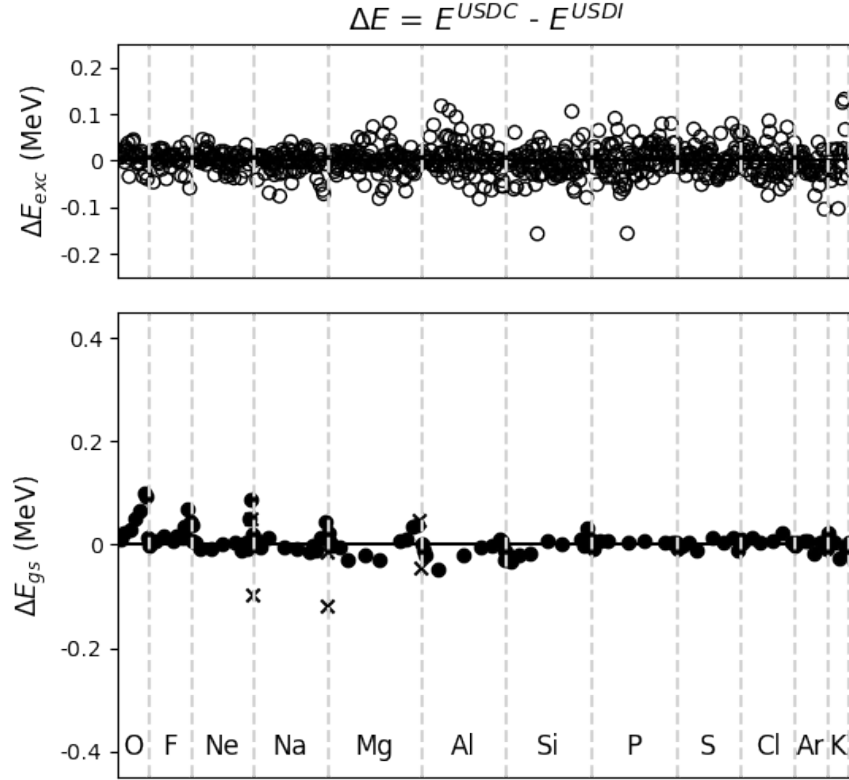
Figure 2.16: Ground state binding energy and excitation energy differences between USDC and USDI. Excited states are shown in the top panel, with ground states in the bottom. The crosses indicate the ground states for the island of inversion nuclei.

larger effect on the excited state energies than it does on the ground state binding energies.

We can also examine the effect of modifying the Coulomb interaction and isotensor strength by looking at the residuals between USDC and USDCm in Fig. 2.17. There is a larger change in calculated ground state binding energies between these two Hamiltonians, with an rms deviation of 70 keV. The excited state energy residuals are smaller than those between USDC and USDI with an rms of 24 keV. The rms deviation for all of the data is 30 keV.

In the next Chapter, we will cover several applications of these new interactions in the sd-shell.

57
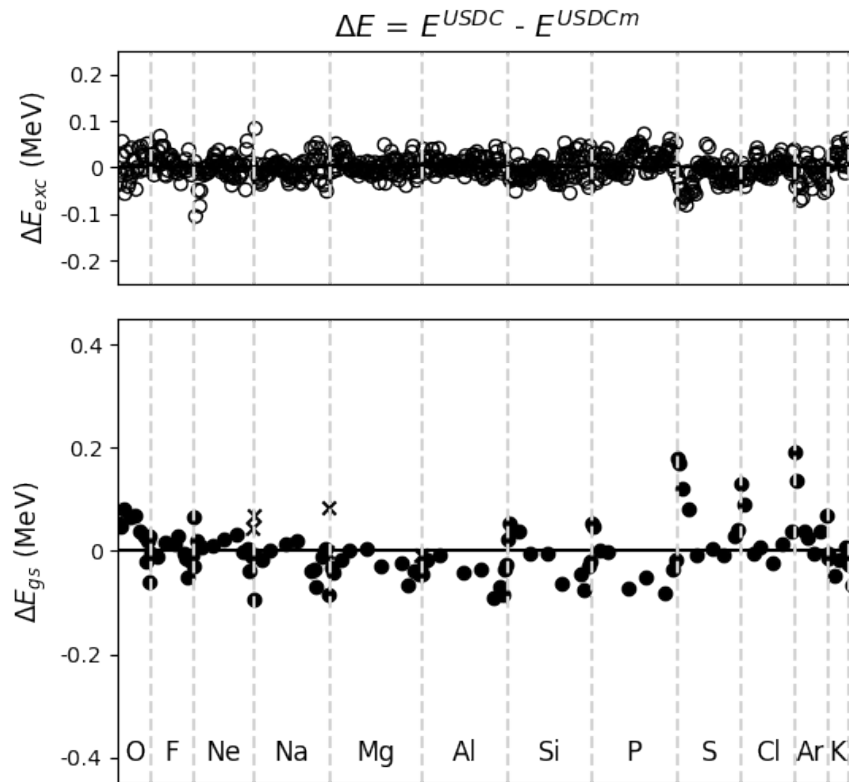
Figure 2.17: Ground state binding energy and excitation energy differences between USDC and USDCm. Excited states are shown in the top panel, with ground states in the bottom. The crosses indicate the ground states for the island of inversion nuclei.

CHAPTER 3

APPLICATIONS IN THE SD-SHELL

It is all well and good to develop these effective interactions that can reproduce experimental binding and excitation energies for a large number of isotopes. However, the reader may object that of course they agree with experiment! They were made to do so after all.

This is not an unfair critique, and so in this chapter we will explore applications of these new interactions for things beyond just calculating individual energies for an isotope. The benefit of having a full shell model interaction when compared to say the LDM is the ability to generate realistic quantum mechanical wavefunctions. These wavefunctions can then be used to calculate any property of the state you desire.

We are now able to extract spectroscopic factors for tackling the Thomas-Ehrman Shift (TES), calculate separation energies for determining the drip lines, and determine the strength of isospin level mixing and its effect on decay schemes. Portions of this chapter were published in [14] while others are connected to collaborations with experimental groups both within NSCL/FRIB and at other research institutions.

3.1 Modeling the Thomas-Ehrman Shift (TES)

When we renormalize an interaction to a model space, we are attempting to decouple the relevant orbits from orbits outside of the model space. This is a very effective and powerful technique, but there are some effects that the Nuclear Shell Model is unable to capture in this process. The TES is such an effect.

The TES is described as a drop in energy of a state with a valence proton in the $s_{1/2}$ orbit at or near its separation energy. This is due to an increased radial extent of the proton's wavefunction due to the lack of a centrifugal barrier for $l = 0$ [40, 41]. An end result is that some excited states in proton-rich nuclei that would otherwise be unbound remain bound to proton-emission. To an extent, there is a weaker TES between the $0d_{3/2}$ and $0d_{5/2}$ orbit as well.
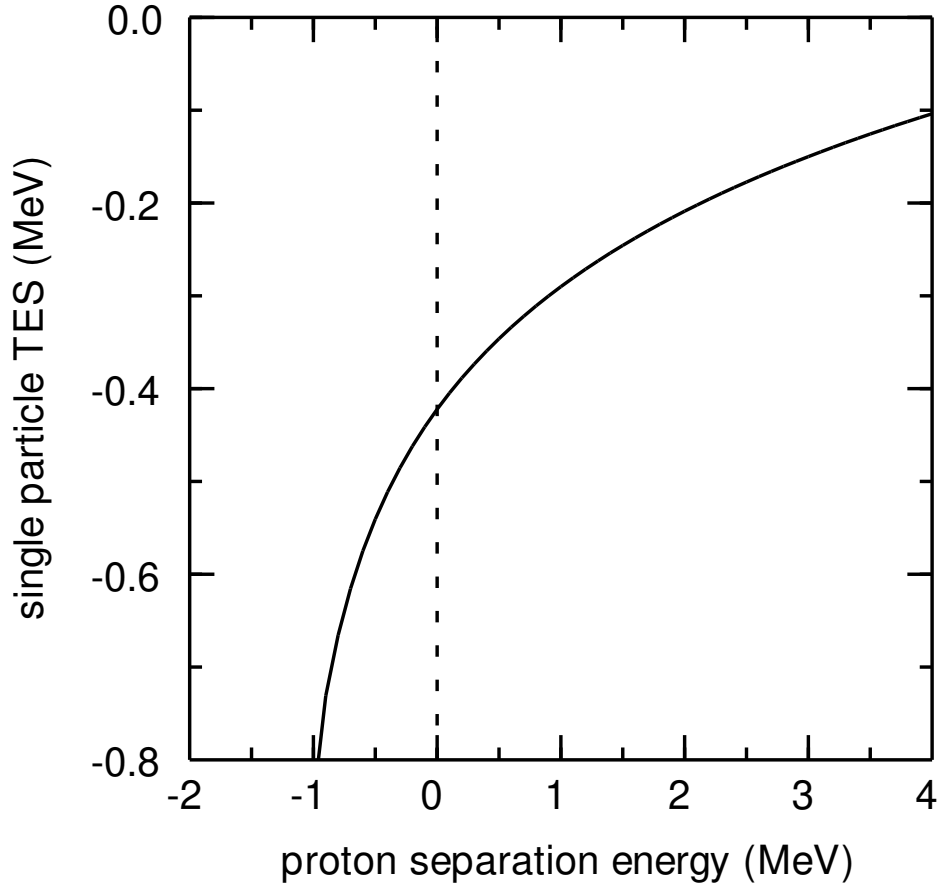
Figure 3.1: The expected single-particle TES as function of proton separation energy, fit to calculations using a Skyrme interaction.

Initial work on modeling this effect as a correction to the shell model calculations can be found in [45]. This section will cover the development of a single-particle model of the TES.

A definition of the TES is given by looking at the difference in proton and neutron single particle energies for the $0s_{1/2}$ and $0d_{5/2}$ orbits,

$$TES_{sp} = [\epsilon(\pi d_{5/2}) - \epsilon(\pi s_{1/2})] - [\epsilon(\nu d_{5/2}) - \epsilon(\nu s_{1/2})]. \tag{3.1}$$

Using this we can extract a single-particle TES strength if we can calculate the energies of these four orbits. What we mean by single-particle is that this value would apply to a pure single particle state.

Using the Skyrme interaction from [46] with an ^{16}O core, we adjust the depth of the valence

$s_{1/2}$ proton orbit while holding the other orbits constant in order to model the single particle TES. This enables us to calculate the expected TES for any given proton separation energy for the orbit. Doing this at many different separation energies shows that a logarithmic curve fit can be used to predict the TES as a function of proton separation energy. This was then done for a ^{28}Si core and it was found that the single-particle TES curve generated was very similar to the curve of the ^{16}O core. This allows us to use a single curve to model the single-particle TES, of the form:

$$\text{TES}_{sp} = -0.4582 + 0.2154 \times \ln\left(S_p + 1.1818\right), \tag{3.2}$$

where TES_{sp} is the single-particle TES in MeV, and S_p is the valence proton separation energy in MeV. This function is plotted in 3.1.

In reality, the valence proton is not in a pure $s_{1/2}$ state, and so only some fraction of the state experiences a TES. This fraction corresponds to the spectroscopic factors of the state to the proton $s_{1/2}$ orbit. We can write the total TES for a nucleus $^A Z$, using the appropriate spectroscopic factors to states in the $^{A-1}Z - 1$ nucleus, as

$$\text{TE}_{total} = \sum_{E_x < 4\,\text{MeV}} \text{TE}_{\text{sp}}(S'_p) \times \text{C}^2\text{S}(E_x), \tag{3.3}$$

where E_x is the excitation energy of the $^{A-1}Z - 1$ nucleus, and $S'_p = S_p(^A Z) + E_x(^{A-1}Z-1) - E_x(^A Z)$ is the separation energy specific to the state we are examining.

3.2   Estimating TES in *sd*-shell nuclei

The data used in the creation of the modified Coulomb interaction had six mirror state pairs removed from the fit. These were removed due to large TE-shifts in the proton-rich member of the pair. In this section we will examine these and select other cases with large TES in the *sd*-shell.

Table 3.1 shows the analysis of the cases excluded from the *b*-coefficient SVD fit. The TES of ground states of these nuclei were calculated and found to be negligible, and so the shift for the excited levels are all that are shown. The TE_{sp} for these cases were taken from the curve in Fig. 3.1. The 3$^+$ state in ^{20}Na reported in the table at 2645 keV was originally reported as a 1$^+$ in [47], guided

by the spin sequence of the mirror nucleus ^{20}F. Indeed, the NNDC database still lists this state as (1^+). It was later argued to be a 3^+ in [48–52] by process of elimination of possible mirror states.

For each case in the table, the calculated TE_{total} is in better agreement with the experimentally measured shift than is the shift calculated using USDC alone. The shift that is built-in to USDC ranges from 30% to 75% of the calculated TE_{total}, with the average being about 50%. This can be seen in Fig. 3.2, where the TE_{total} calculation is labeled as Skyrme. Also shown in this figure are the TES built into USDCm, which are similar in magnitude to those in USDC.

This analysis can also be applied to ground states with large $s_{1/2}$ spectroscopic factors, however we can not simply add the calculated shift to the mirror energy to compare with experiment.

With USDC, ^{26}P is calculated to have $S_p = -146$ keV. Estimates for the unmeasured S_p for ^{26}P include 140(200) keV [36], 0(90) keV [53], 85(30) keV [54], and $-119(16)$ keV [55]. Using this range of values and the method outlined above, we calculate an expected TES_{total} of $-255(14)$ keV. If we assume that USDC again has 30-75% of the shift built into it, we can revise the separation energy to include the additional shift from this analysis. The predicted USDC+TES one-proton separation energy is then $-12(65)$ keV, the central value of -12 keV corresponding to a proton emission half-life of 7.6×10^{20} years.

We model the one-proton decay as a proton in a single-particle $s_{1/2}$ orbit with a ^{25}Si core, and then calculate the width of the unbound state at various values of S_p. With this method, we calculate a half-life of 0.046 ms for our most unbound separation energy prediction within uncertainty, $S_p = -77$ keV. A typical beta-decay half-life of 100 ms corresponds to $S_p = 57.5$ keV in this approximation. The beta-decay half-life of ^{26}P has been measured as 43.7(6) ms [53]. We conclude that lifetime is likely dominated by the beta-decay,

Table 3.1: Calculated TES for selected nuclei using USDC and the single-particle TES model. Spectroscopic factors are to the $s_{1/2}$ orbit and calculated with USDC. The C^2S, S'$_p$, and J^π_f (spin-parity of the state in the $^{A-1}Z-1$ nucleus) for the dominant term of the sum in Eq. 19 are shown. $E^{exp}_{mirr+TE}$ is the experimental energy for the neutron-rich state in the mirror pair plus the calculated TE_{total}.

	J^π	C^2S	J^π_f	S'$_p$ (keV)	TE_{sp} (keV)	Mir	E^{exp}_{mirr} (keV)	$E^{exp}_{mirr+TE}$ (keV)	E^{exp} (keV)	TE_{th} (keV)	TE_{total} (keV)	TE_{exp} (keV)
^{17}F	1/2$^+$	1.000	0$^+$	105	-404	^{17}O	870	466	495	-304	-404	-375
^{19}Na	1/2$^+$	0.789	0$^+$	-1068	-926	^{19}O	1472	741	745(12)	-225	-731	-727(12)
^{20}Na	3$^+$	0.406	5/2$^+$	-580	-568	^{20}F	2966	2736	2645(2)	-156	-230	-321(6)
	1$^+$	0.413	1/2$^+$	-811	-672		3448	3168	3001(6)	-122	-281	-447(2)
	0$^+$	0.559	1/2$^+$	-896	-728		3526	3098	3086(2)	-247	-407	-440(2)
^{23}Al	1/2$^+$	0.704	0$^+$	-409	-514	^{23}Ne	1017	655	550(20)	-146	-362	-467(20)
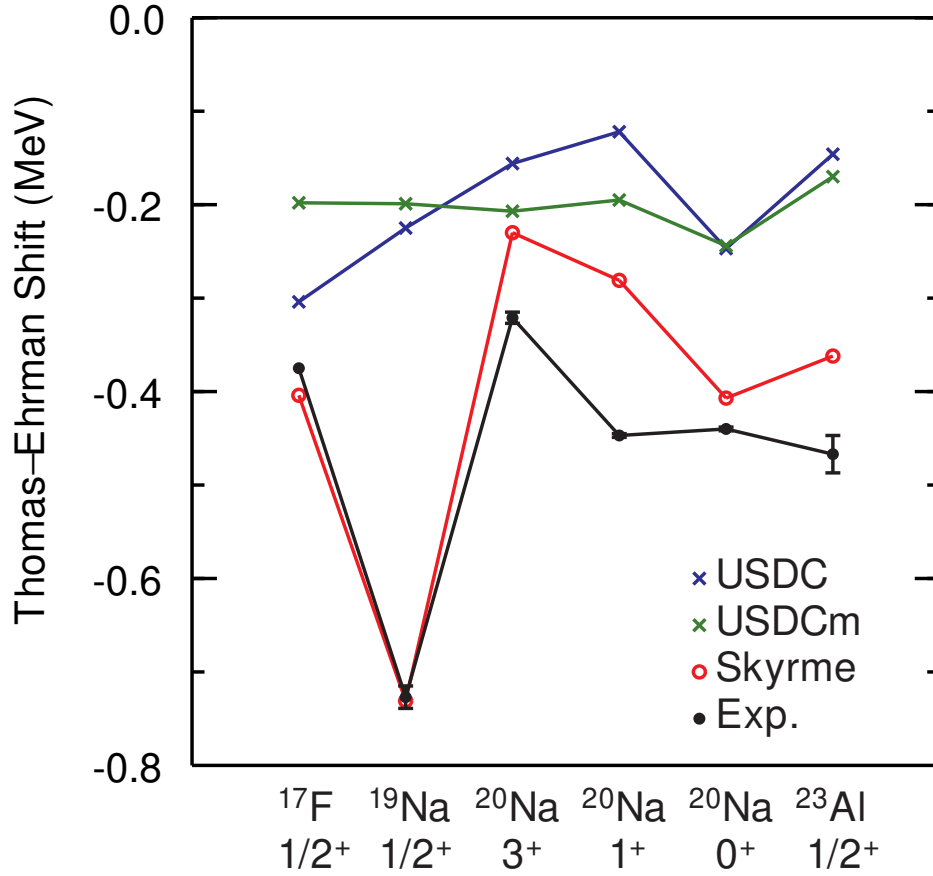
Figure 3.2: Comparison of TES found in Table 3.1.

3.3 Improved predictions for Driplines and Separation Energies

One motivation for the development of isospin-breaking USD-type Hamiltonians comes from the relatively poor predictions for ground state binding energies with USDB-CD. Its residuals when compared to experiment for the *sd*-shell nuclei included in our updated data set for constraining USDC/USDI are shown in Fig. 3.3. Theory is under-bound at the bottom of the shell and becomes over-bound as you move up the shell (that is as you increase the mass number), causing calculated separation energies to be systematically larger than experiment at the top of the shell. Also present are the large deviations for the neutron-rich fluorine isotopes and island of inversion nuclei discussed in the previous chapter for the new Hamiltonians.

The binding energy residuals for USDC are shown in Fig. 3.4. The results for USDCm, USDI,
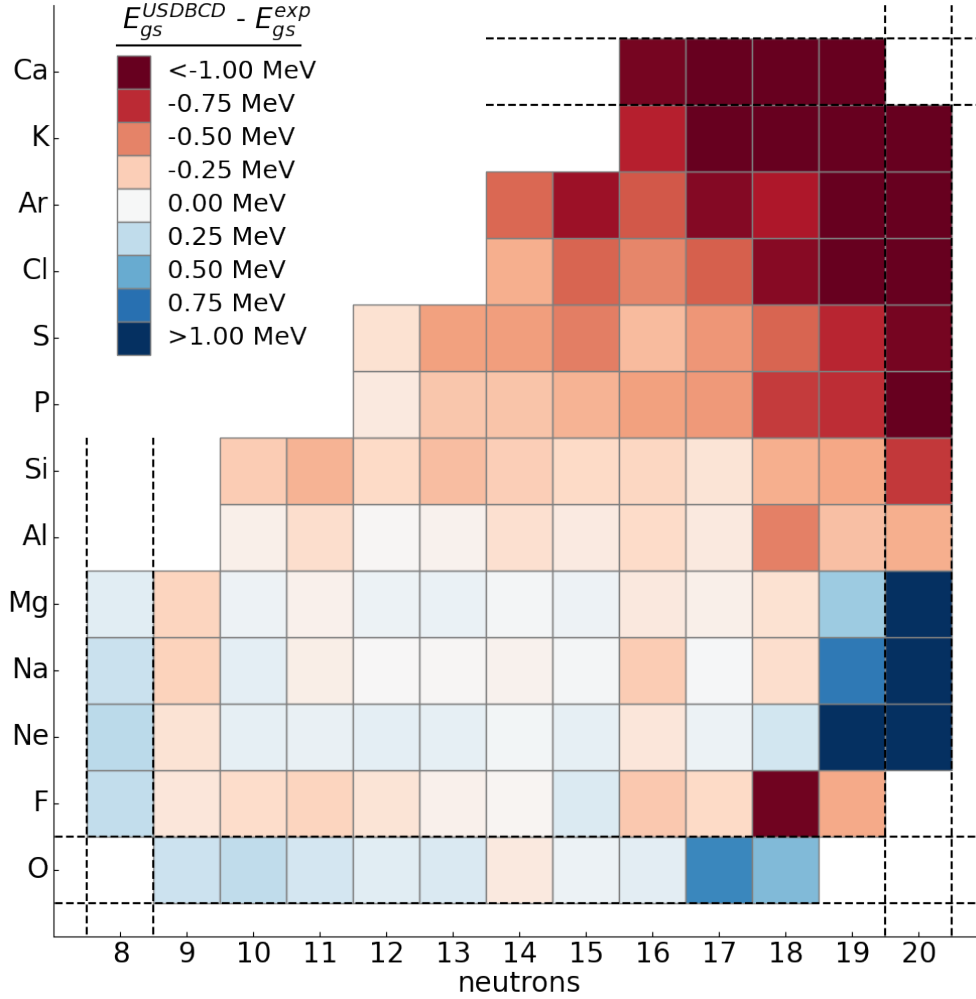
Figure 3.3: Differences between the experimental and USDB-CD ground state binding energies. Positive values indicate that experiment is more bound than theory.

and USDIm are similar at this scale. The problem of over-binding towards the top of the shell is solved, allowing for better predictions of separation energies. As expected though we still see the disagreement for the island of inversion and fluorine isotopes. Fig. 3.5 shows the USDC two-proton and two-neutron separation energies for sd-shell nuclei with $Z \geq 10$ and $N \geq 10$, respectively. The patterns for two-proton separation energies along isotopic chains and for two-neutron separation energies along isotonic chains are similar in shape, with a shift up in energy due to the Coulomb interaction.

The proton-dripline can be defined as the point in an isotonic chain at which adding an additional proton to the nucleus results in a negative one- or two-proton separation energy. At this point the
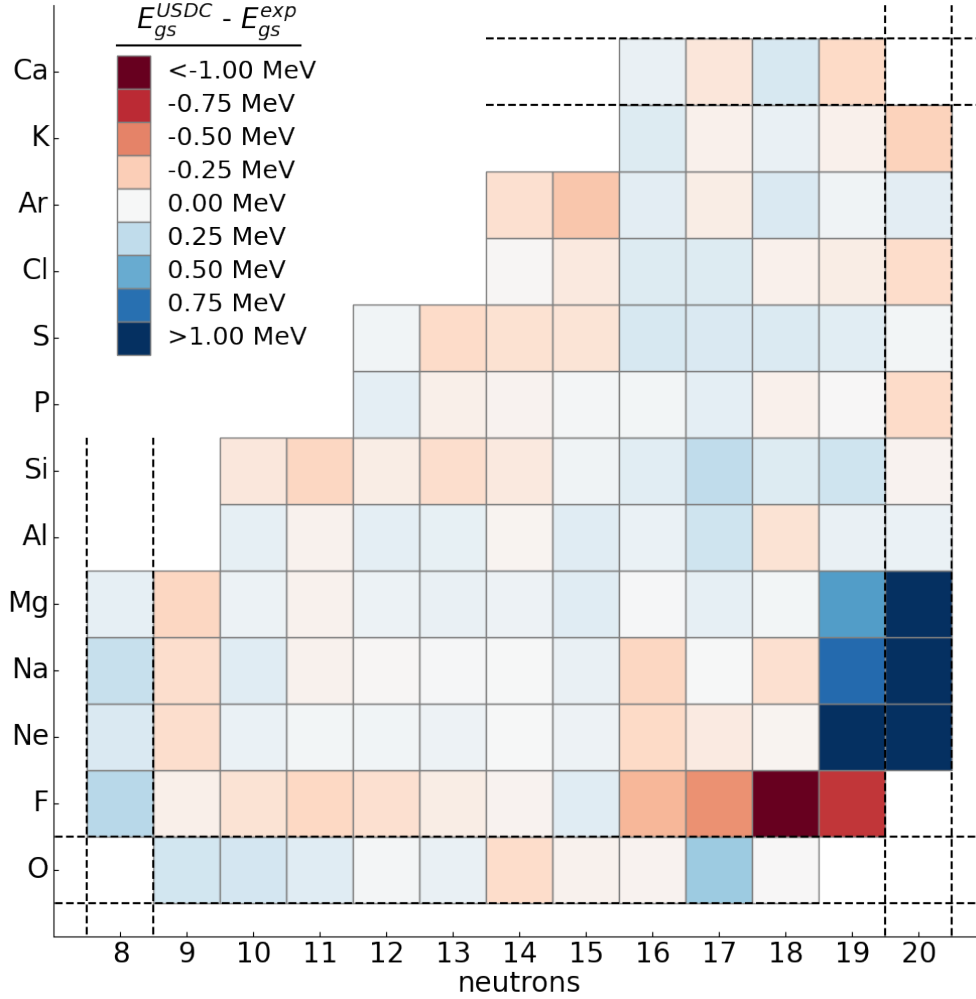
Figure 3.4: Differences between the experimental and USDC ground state binding energies. Positive values indicate that experiment is more bound than theory. There are no significant differences at this scale for calculations using USDI, USDCm, or USDIm. The dark green/blue Fluorine isotopes are discussed in the text.

nucleus would undergo decay via proton emission rather than β-decay. With this definition, our prediction of the ^{26}P one-proton separation energy of $-12(65)$ keV puts the nucleus outside of the dripline (ignoring uncertainty). However, up until a negative S$_p$ of about 100 keV the nucleus is still able to undergo beta-decay. The point at which proton emission dominates over β-decay is another definition of the proton-dripline.

USDC predicts the one- and two-proton separation energies for ^{26}S to be -217 keV and -1820 keV, respectively. For ^{30}Ar, it predicts one- and two-proton separation energies of -199 keV
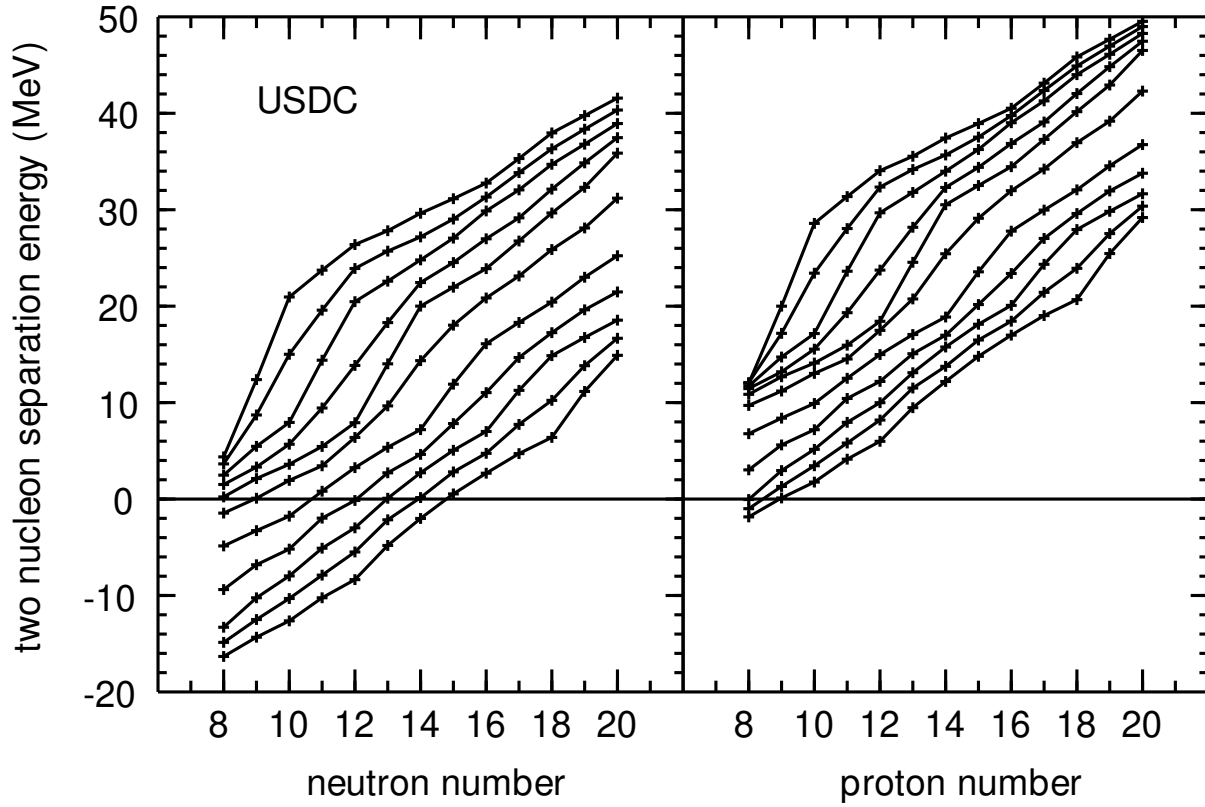
Figure 3.5: Isotonic chains of S_{2p} (left) and isotopic chains of S_{2n} (right) calculated with USDI. There are no discernible differences at this scale for calculations using USDC, USDCm, or USDIm.

and -2976 keV. These nuclei are then good candidates to consider as two-proton emitters, as a large enough TES could cause them to be bound to one-proton emission while leaving the two-proton channel open. However, the daughter nuclei from one-proton decay (^{29}Cl and ^{25}P) also have ground states with large $s_{1/2}$ spectroscopic factors. This has the effect of keeping the ^{26}S and ^{30}Ar unbound to single proton emission by a few hundred keV.

Single proton and neutron separation energies were also calculated, allowing us to define the entire proton and neutron driplines. Consistent with experiment, the oxygen isotopes with $A > 24$ are unbound. ^{26,28}O are single neutron bound, but have negative two-neutron separation energies. Fig. 3.6 shows the predictions for the proton dripline and proton separation energies using USDI. For the purposes of this figure, the proton-dripline is defined as the point at which proton-emission dominates the decay scheme. The dripline location is the same for the other new interactions
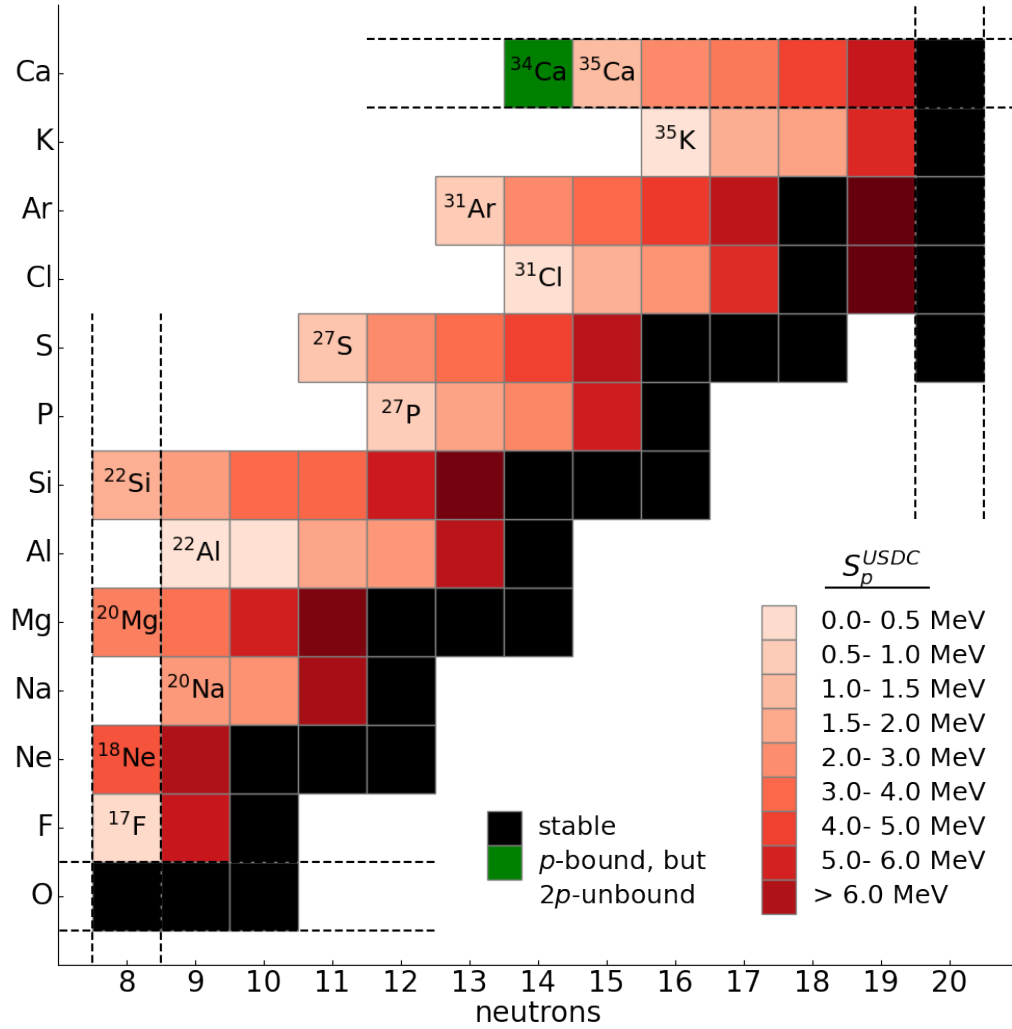
Figure 3.6: Predicted proton dripline and separation energies for proton-rich nuclei in the *sd*-shell.

68
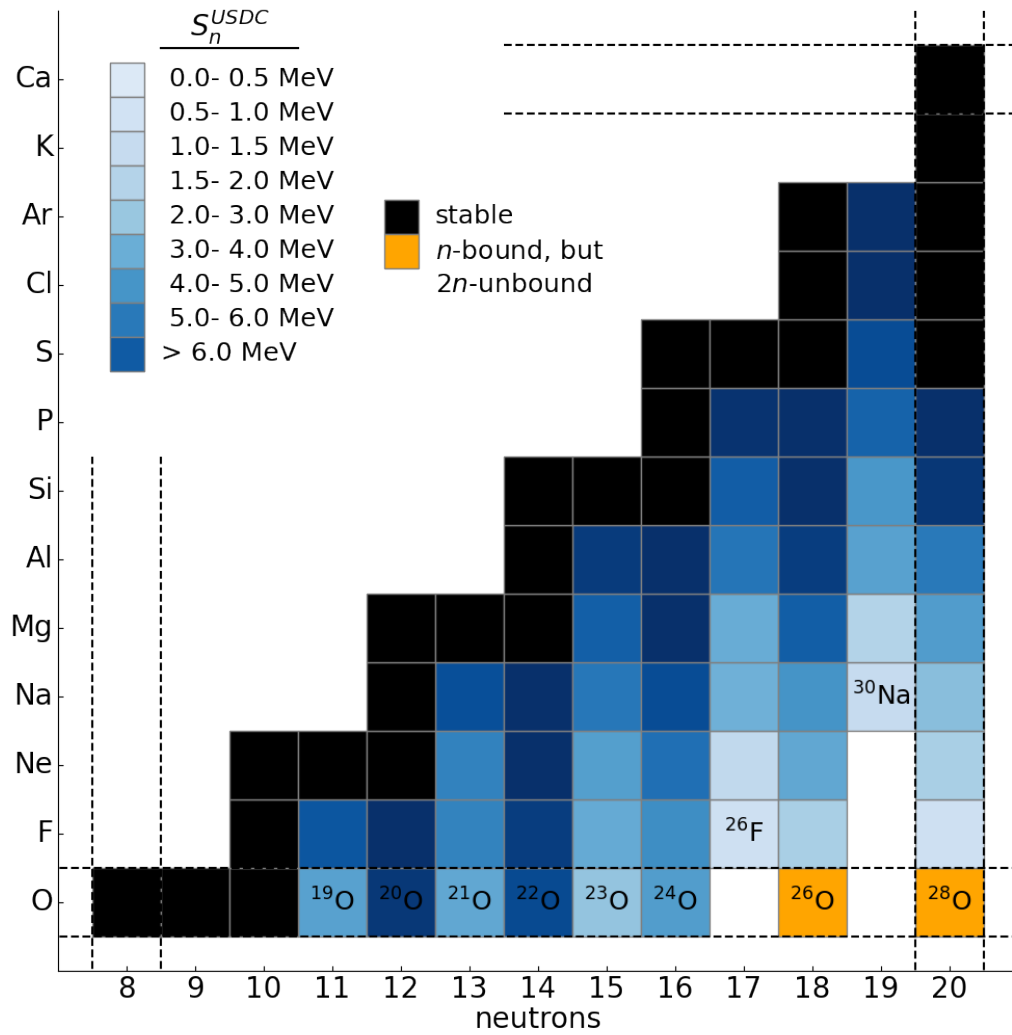
Figure 3.7: Predicted neutron dripline and separation energies for neutron-rich nuclei in the *sd*-shell.

with small changes to the separation energies between them. Fig. 3.7 shows the neutron dripline calculated with USDI, which contains larger disagreement with experiment due to the island of inversion.

One interesting possibility raised by the new interactions comes in examining the stability of ^{26}O to various decays. While USDB-CD predicts the isotope to be unbound to two-neutron decay by a few hundred keV, there is disagreement between USDC and USDI on the possibility of two-neutron decay, with USDC predicting a slightly more negative separation energy than reported by the NNDC, and USDI predicting the nucleus to be bound to two-neutron emission. The two-neutron separation energies for ^{26}O are shown in Fig. 3.8. The interactions agree on the status of ^{28}O as two-neutron bound but neutron unbound.

There is only one isotope in the *sd*-shell that is predicted to be bound to proton emission but unbound to two-proton emission, ^{34}Ca. It has a two-proton separation energy of -2.011 MeV for USDC, -1.991 MeV for USDCm, -2.027 MeV for USDI, and -1.976 MeV for USDIm. These are significantly more negative than the extrapolated mass evaluation value of $-1.46(31)$ MeV [56]. This is shown in Fig. 3.9. These predictions were included in an FRIB PAC1 proposal to study the neutron-deficient calcium isotopes.

All four new Hamiltonians predict that ^{26}P is proton unbound by about 150 keV. However, as discussed in the TES section earlier in the chapter, a large TES brings the proton separation energy to $-12(65)$ keV, allowing the nucleus to predominately undergo β-decay rather than emit a proton. For further discussion on ^{26}P and its neighboring isotopes see [45].

Recently, the two-proton separation energy for ^{31}Ar was measured as $6(34)$ keV [57]. Fig. 3.10 shows the theory predictions for USDB-CD and the new interactions compared to this experimental value. The decrease in the separation energy for the new Hamiltonians against USDB-CD is expected, and they are in better agreement with experiment. We see that the USDCm and USDIm predictions even fall within the reported experimental uncertainty. Further measurement is needed to determine the decay properties of ^{31}Ar.

A notably large deviation between experiment and theory is found for the proton separation
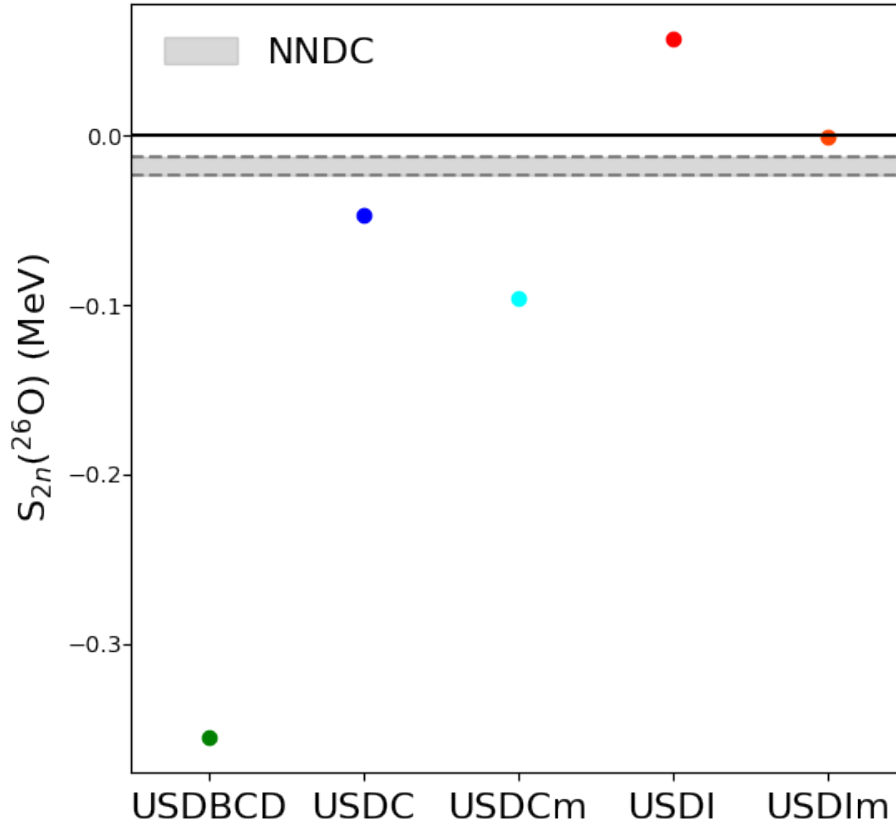
Figure 3.8: Experimental and predicted two-neutron separation energies for ^{26}O. The gray band shows experiment and its uncertainty.

energy of ^{29}Cl. Experiment places the ground state at 1.8(2) MeV above the proton threshold and assigns it as a $1/2^+$ state [58], with an excited $3/2^+$ state at 0.5 MeV. Our configuration-interaction calculations all agree on a ground state at 2.7 MeV above the proton threshold, but with a $3/2^+$ assignment. The first excited state is then the $1/2^+$ at 0.08 MeV. As discussed in the TES section of this chapter, the $1/2^+$ state has a large proton $s_{1/2}$ spectroscopic factor. A TES of -0.389 MeV is calculated for the $1/2^+$ which causes the inversion of the level scheme as seen in experiment.
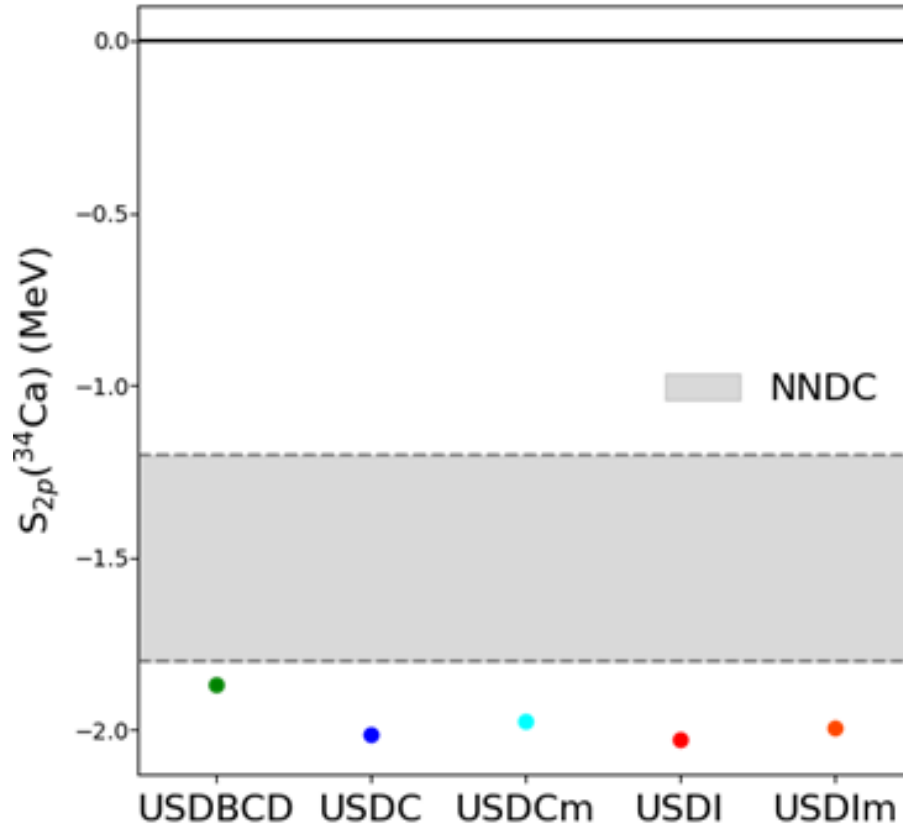
Figure 3.9: Experimental and predicted two-proton separation energies for ^{34}Ca. The gray band shows experiment and its uncertainty.

3.4 Examining the large IAS mixing in ^{31,32}S

It is tempting to view the different states in a nucleus as being states with a *particular* configuration and set properties. But of course we know that the rules of quantum mechanics don't allow this. There is a mixing up of the basis states to create eigenstates of the Hamiltonian with definite energy eigenvalues. But these eigenstates can be a superposition of many different pure states with different isospin.

During a beta-decay, level-mixing of the IAS in the daughter nucleus with similar J^π states can cause the level to shift in energy and greatly affect the rate of the decay and the decay strength to
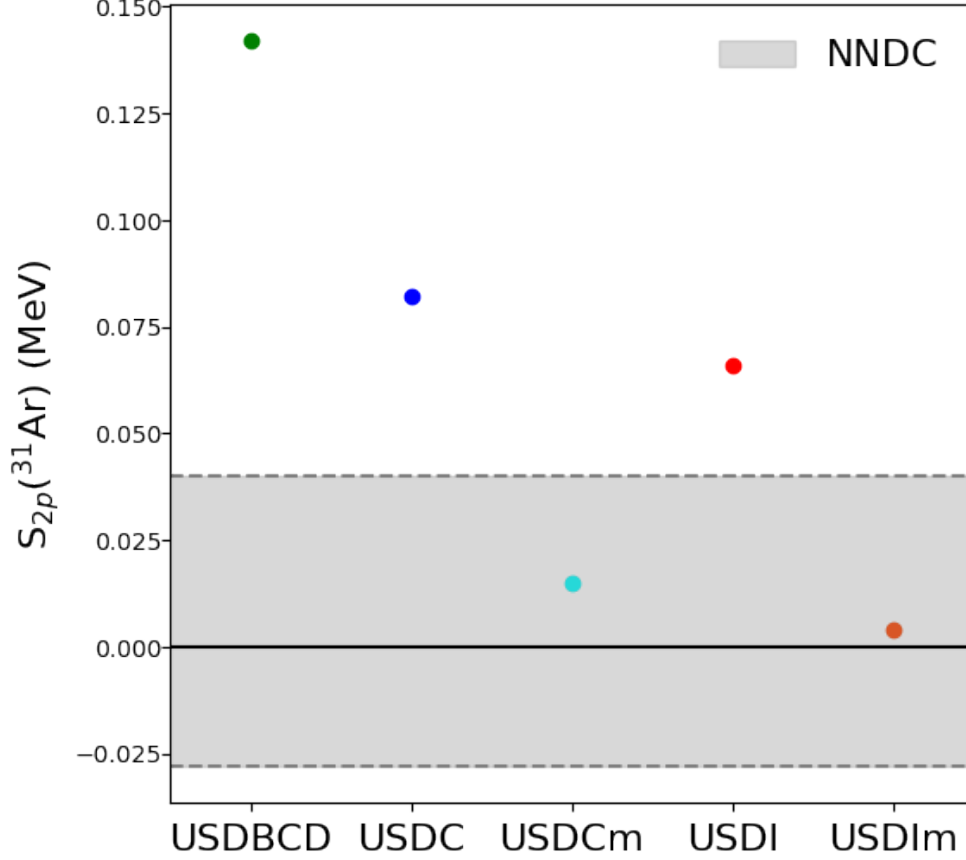
Figure 3.10: Experimental and predicted two-proton separation energies for ^{31}Ar. The gray band shows experiment and its uncertainty.

final states in the daughter. Using a two-level mixing framework, as in Ref. [59], we define the strength of this mixing between the IAS and a single level n as,

$$< v >= \frac{< \text{IAS}|T^2|n >}{< \text{IAS}|T^2|\text{IAS} > - < n|T^2|n >}\Delta E, \tag{3.4}$$

where ΔE is the difference in energy between the two states. The resulting shift in energy from the expected energy of the IAS is then,

$$\Delta E_{\text{IAS}} = \frac{< v >^2}{\Delta E}. \tag{3.5}$$

It is clear that if there is a large off diagonal element if the T^2 matrix between the IAS and a nearby non-IAS level, the shift in energy can be significant. With our new isospin-breaking effective interactions, we can examine this isospin level mixing and extract the mixing matrix elements in order to compare to experiment.

Table 3.2: Isospin-mixing matrix elements between the 6th and 8th $\frac{3}{2}^+$ sd-shell levels in ^{31}S, and the 2nd and 3rd 1^+ sd-shell levels in ^{32}S.

Interaction	$v(^{31}\mathrm{S})$	$v(^{32}\mathrm{S})$
USDB-CD	28	16
USDC	36	23
USDCm	51	42
USDI	38	22
USDIm	56	40
Experiment	41(1)	26(3)

Two examples of known large isospin mixing can be found in ^{31}S [59] and ^{32}S [60, 61]. The $3/2^+$ levels at 6279 keV (IAS) and 6390 keV in ^{31}S have a deduced empirical isospin mixing matrix element, v, of 41(1) keV. Study of the super-allowed β transition for ^{32}Cl provided an experimental branching ratio to the 7190 keV state in ^{31}S [61]. Treating this as a two-level mixing problem with the IAS at 7001 keV the branching ratio was used to deduce $M^2 = 0.0625(42)$. Using our new interactions, we calculate a theoretical B(GT) value of 0.0147(17) (this includes the quenching factor of 0.6). Given that

$$M^2 = \mathrm{B}(F) + \left(\frac{g_A}{g_V}\right)^2 \mathrm{B}(GT), \tag{3.6}$$

where $(g_A/g_V)^2 = 1.588$, we arrive at a Fermi decay strength of B(F) = 0.039(5). For more on these decays see Section 3.5. This then translates to an isospin mixing matrix element for the two states of $v = 26(3)$ keV .

Our results for the four new interactions and USDB-CD are compared to these two experimental mixing matrix elements in Table 3.2. In both cases, we see better agreement with experiment for the new USD-type Hamiltonians compared to USDB-CD. Amongst the new interactions, USDC and USDI and in better agreement with both $v(^{31}\mathrm{S})$ and $v(^{31}\mathrm{S})$ compared to USDCm and USDIm. There is an overestimation of the mixing strength in the interactions containing the modified Coulomb interaction. In Chapter 4 we will revisit these.

Table 3.3: Examining the decay strengths to low laying levels in ^{19}Ne from the ground state of ^{20}Mg via a β delayed proton emission using USDB-CD. The two branching ratio columns use experimental data from [63] for BR^1 and [64] for BR^2 to normalize to the theoretical value for $5/2^+$. Calculated C^2S for this decay are small, and so are reported in the table in units of 10^{-6}.

J_f^π	E_x (MeV)	C^2S	Q (MeV)	BR^1 (exp) (%)	BR^2 (exp) (%)	$\Gamma_{p,sp}$ (MeV)	Γ_p (eV)	Γ_p [*] (eV)
1/2+	0	36	4.3	0.97(9)	1.8	5 (guess)	180	320
5/2+	0.238	149	4.06	0.3(2)	0.59	0.7	104	104
1/2-	0.275	?	4.06	0.31(7)	0.32	1 (guess)		56
5/2-	1.508	0		0.4(2)	0.07			12
3/2+	1.536	35	2.76	0.47(7)	0.51	0.17	6	90
3/2-	1.616	?						
Σ				2.45	3.3			580

3.5 β-delayed proton emission and the superallowed β-decay of ^{20}Mg

As discussed in Chapter 1, there are two main types of β-decay, Fermi and Gamow-Teller. The Fermi decay operates as simply the isospin ladder operator which can connect states between isotopes that differ only in T_z. The special case of connecting IAS is known as superallowed Fermi β-decay. Gamow-Teller decay allows for a change of angular momentum l during the decay.

Superallowed $0^+ \rightarrow 0^+$ β decays can serve as precise tests of the Standard Model's description of the electro-weak force. Recently, Glassman *et al* [62] performed an experiment in which ^{20}Mg was implanted in a plastic scintillator inside an array of high-purity germanium detectors. When the sample underwent β decay, the resulting γ ray spectrum was captured in high-resolution and analyzed. From this, they were able to report a highly precise value of the β-delayed γ branching ratio through the IAS in ^{20}Na and the associated Q_{EC}. Initial shell-model calculations were carried out with USDB-CD, the isospin-breaking extension to the USDB interaction, as this project coincided with the development of USDC.

The experimentalists were able to measure the intensities $I_{\beta\gamma}$ and $I_{\beta p}$ for the two decay paths. We have two problems when trying to compare these measurements to our calculations. First, several unnatural parity states are involved in the decay process for which *sd*-shell interactions are

Table 3.4: Results for γ- and p-decay widths using three USD-type interactions, with comparisons made to the experimental decay width ratio and branching ratio. Calculated C^2S values for this decay are small, and so are reported in the table in units of 10^{-6}. The reported spectroscopic factors are to the $5/2^+$ level in ^{19}Ne.

Interaction	E_x^{IAS} (MeV)	Γ_γ (eV)	Γ_p (eV)	Γ_γ/Γ_p	C^2S	β BR
USDB-CD	6.840	7.52	580	0.0129	149	0.0306
USDC	6.722	6.76	1026	0.0066	263	0.0330
USDI	6.729	6.92	1058	0.0065	271	0.0317
Exp.	6.498	-	-	0.0063(9)	-	0.0254(17)

unable to provide results. These are intruder states that involve nuclear orbits outside of the sd-shell model space. To counter this, we normalize to the experimental results in [64] using the theoretical value for the $5/2^+$ state at 238 keV. Second, our calculations produce decay widths rather than intensities. However, the ratio $I_{\beta\gamma}/I_{\beta p}$ is equal to the ratio Γ_γ/Γ_p where Γ_γ and Γ_p are the partial widths for γ and proton emission from the IAS in ^{20}Na, respectively. So we instead calculate the associated widths for those decays to determine the same ratio.

With reasonable values for the single particle decay widths, we can calculate the full decay width by multiplying the widths by their associated spectroscopic factors. These decay widths are then scaled to the experimental branching ratios to produce Γ_p^*, and these individual decay widths can then be summed to get the decay's full Γ_p of 580 eV with USDB-CD. Lastly we take the ratio of this width to the calculated Γ_γ of 7.5 eV, to get a $\beta - \gamma$ branching ratio of 0.032%. This is a factor of 2 difference with the experimentally measured ratio of 0.016%.

Shell-model calculations were also carried out with two new USD-type interactions, USDC and USDI. The new interactions predict the excitation energy of the IAS to be 6.722 MeV (USDC) and 6.729 MeV (USDI), placing them about 0.1 MeV closer to experiment than USDB-CD. The C^2S for the first excited state in ^{19}Ne is higher in these interactions than it is in USDB-CD, which results in a Γ_p of 1026 eV (USDC) and 1058 eV (USDI) when the same scaling to experimental branching ratios is used. Along with a small decrease in Γ_γ, the Γ_γ/Γ_p ratios are .0066 (USDC) and .0065 (USDI) which are in remarkable agreement with the experimentally determined ratio of 0.0063(9).

These results are summarized in Table 3.4, and show the marked improvement over USDB-CD

in describing this decay.

3.6 Explaining the Cubic IMME for the A=32, T=2 Isospin Quintet

The $A = 32, T = 2$ isobaric multiplet consists of states in five nuclei. This multiplet has been long known to have a breakdown of the IMME's quadratic nature [65]. The source of this breakdown has been elusive, and recent work has attempted to explain the energies of this multiplet.

Isospin admixtures with non-analog $J^{\pi} = 0^+$ states cause a shift in the energy of the IAS in ^{32}Cl, ^{32}S, and ^{32}P. Shell model calculations reveal that this mixing is due primarily to a single $T = 1$ state that sits a few hundred keV below the IAS in the three interior nuclei of the multiplet. It primarily effects the energy of the IAS in ^{32}Cl, but also influences the other two states. We study the mixing using the new USDC and USDI interactions [14], as well as the USDB-CD interaction. The energy differences between this important $T = 1$ state and the IAS are displayed in Table. 3.5, along with the calculated isospin mixing matrix element v between these states, for the three nuclei in Fig. 3.11.

The previous section in this chapter discusses two other cases of large isospin-mixing affecting Fermi decays, found in ^{31}S [59] and ^{32}S [60, 61]. We will use a similar method to examine possible mixing in this multiplet.

A comparison of v for this important $T = 1$ state is shown in Fig. 3.11 for ^{32}Cl, ^{32}S, and ^{32}P. The largest mixing is found in the $T_z = -1$ member of the multiplet ^{32}Cl, with a drop off in mixing as you move up in isospin projection. The USDC and USDI interactions again predict larger v than that predicted by USDB-CD. The experimental value from this work for the mixing in chlorine is 39.0 ± 2.4 keV, which is consistent with the USDC and USDI values.

The energy shift in the IAS depends on both the isospin mixing matrix element and the energy difference between the two states. The USD-type interactions have an energy rms deviation on the order of 150 keV, which can be relevant for the present discussion. So we examine the effect of shifting the energy difference between the $T = 1$ and $T = 2$ states to the experimental values. This is accomplished by adding an isospin-dependent term to the Hamiltonian resulting in a shift of all
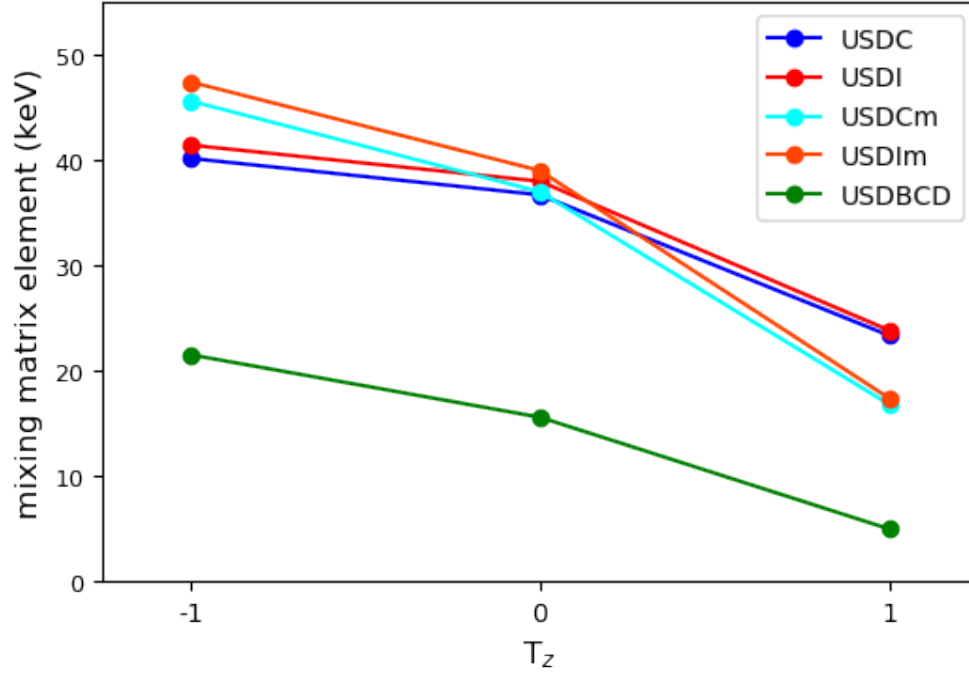
Figure 3.11: Isospin mixing matrix elements between the important T=1 state and the IAS in ^{32}Cl, ^{32}S, and ^{32}P.

Table 3.5: Energy differences between the $J^\pi = 0^+, T = 2$ IAS and the nearby $J^\pi = 0^+, T = 1$ state in ^{32}Cl, ^{32}S, and ^{32}P, along with the isospin mixing matrix element in ^{32}Cl. All values in keV.

Interaction	ΔE			v
	^{32}Cl	^{32}S	^{32}P	^{32}Cl
USDC	-226	-186	-237	40
USDI	-308	-266	-326	41
USDCm	-324	-239	-293	46
USDIm	-405	-321	-383	47
USDB-CD	-440	-378	-427	22
Exp.	-596	–	-452	39.0(2.4)
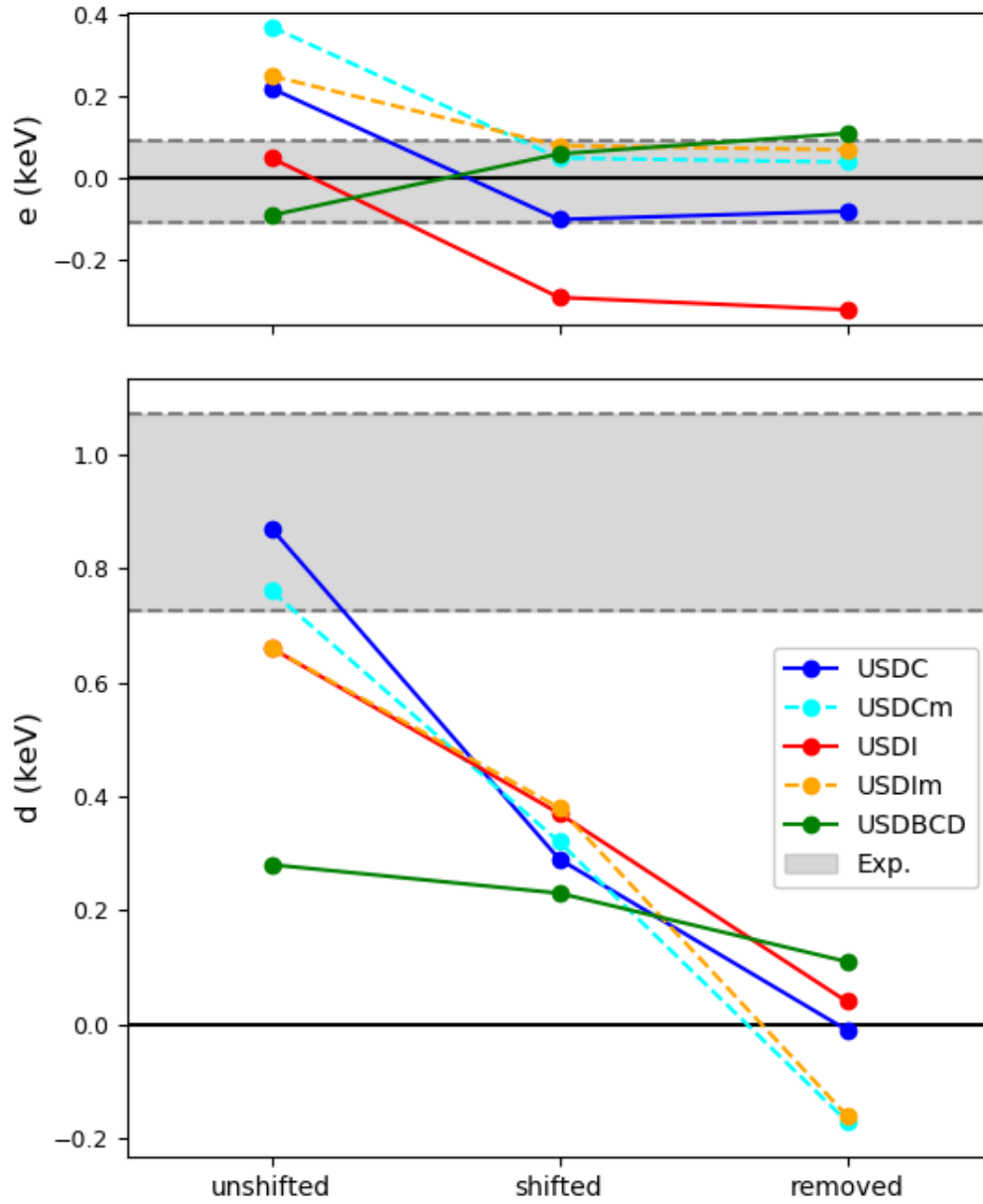
Figure 3.12: Cubic and quartic corrections (d and e) for the $A = 32$, $J^\pi = 0^+$, $T = 2$ isobaric multiplet. See text for descriptions of the shift procedure.

$T = 2$ states relative to the $T = 1$ and $T = 0$ states without changing the isospin-mixing matrix elements.

This results in mild changes to the e-coefficient due to changes in the mixing of the $T = 2$ state in ^{32}S, but a fairly universal decrease in the d-coefficient, in the case of the new interactions by around 50%. Fig. 3.12 shows the change in d- and e-coefficients for the five interactions, first for the unshifted shell model calculations, and then again when the $T = 2$ states have been shifted.

We can examine the contribution to the d- and e- coefficients caused by mixing of non isobaric analog states in the three interior nuclei of the multiplet. First we can look at the exact solution for the d- and e- coefficients in a $T = 2$ multiplet with energies E_{T_Z},

$$d = \frac{1}{12} (E_2 - 2E_1 + 0E_0 + 2E_{-1} - E_{-2})$$
$$e = \frac{1}{24} (E_2 - 4E_1 + 6E_0 - 4E_{-1} + E_{-2}).$$
(3.7)

Then, treating the isospin mixing as a two-level problem between the IAS and nearby non-analog states, we can calculate the shift in the IAS due to that mixing in each nucleus as

$$s = -\frac{v^2}{\Delta E}.$$
(3.8)

This allows us to rewrite the d- and e- coefficients as a sum of single state contributions d_i and e_i from the $T = 0$ and $T = 1$ levels. These take the form,

$$d_i = -\frac{1}{6} s_P + \frac{1}{6} s_{Cl}$$
$$e_i = -\frac{1}{6} s_P + \frac{1}{4} s_S - \frac{1}{6} s_{Cl}.$$
(3.9)

It is then clear that mixing in ^{32}S can not impact the d-coefficient.

We can then remove the contribution to the IMME corrections coming from mixing with the important $T = 1$ state, and this is shown as the "removed" set of data in the figure. When the mixing for the $T = 1$ state is turned off, we see very small d- and e-coefficients that are near zero. What is left is the cumulative effect of the other non-analog $J^{\pi} = 0^+$ states, and in the case of the large negative e-coefficient in USDI the mixing is found in a nearby $T = 0$, 0^+ state in ^{32}S. This $T = 0$ mixing in ^{32}S can not be used to explain the large experimental d-coefficient, and there are no other states with large enough mixing to explain it.

It is therefore our conclusion that isospin-mixing alone can not explain this experimental multiplet, as the known sources of mixing can not be shown to explain the experimentally measured multiplet masses. This leads us to suggest that one of the experimental masses is incorrect, and is the source of this discrepancy.

Results from this section are included in Ref. [66] and in a manuscript prepared by Smarajit Triambak set to be submitted for publication.

3.7 Quenching of the Gamow-Teller Decay Strength Function

In the introductory chapter, the two types of β-decay (Fermi and Gamow-Teller) were discussed. And earlier in this chapter oblique references to a *quenching* of the Gamow-Teller decay strength were made. This quenching is widely used and is necessary to accurately reproduce experimental results. But what does it mean to quench the Gamow-Teller decay in calculations?

A sum rule for each of the two types of decays can be derived in the "free" nucleon model. The Fermi sum rule is

$$\sum_f \left[B_{i,f}(F_-) - B_{i,f}(F_+) \right] = \pm(N_i - Z_i), \tag{3.10}$$

where the sign in positive for neutron-rich nuclei and negative for proton-rich nuclei. The Gamow-Teller sum rule is

$$\sum_f \left[B_{i,f}(GT_-) - B_{i,f}(GT_+) \right] = 3(N_i - Z_i). \tag{3.11}$$

In theoretical models of complex nuclei the sum rule for the Fermi decay generally matches up well to experiment, but that is not the case for the Gamow-Teller sum rule. There are many potential reasons for this disagreement. The first is that the true nuclear wave functions are more complicated than the theoretical ones we compute in the valence configuration-interaction approach. The shell-model can only account for the valence nucleons behavior and does not account for degrees of freedom from missing nuclear correlations and contributions from meson-exchange currents. There have been many theoretical explorations for the cause of this discrepancy.

The method of accounting for this in shell model calculations is to implement an "effective" operator for the Gamow-Teller matrix elements. This can be thought of as a "quenching" of the
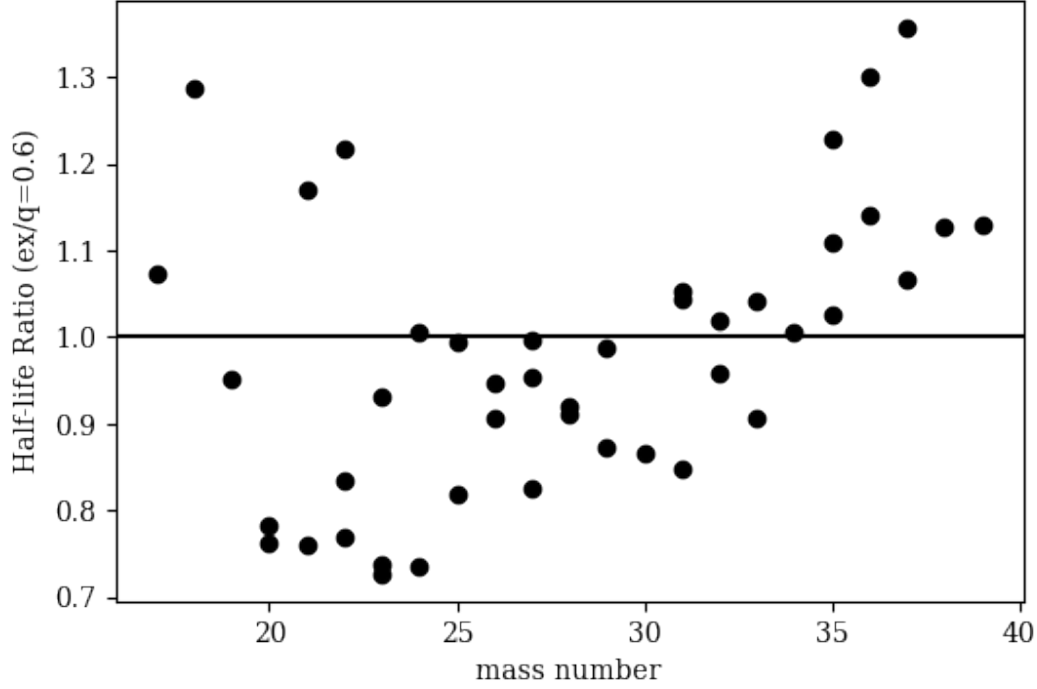
Figure 3.13: The ratios of the experimentally measured β^--decay half-lives to those calculated with USDC using $q = 0.6$..

transition strength. The quenching factor has generally been set to $q = 0.6$ [67–71] in the *sd*-shell. But can this be refined to provide an even greater agreement with experiment?

An advantage of the development of the USDC interaction is that previous interactions were not reliable throughout the shell for accurate Q values for nuclear decays, and β-decays of particular interest here. The improvement of predictions for the ground state binding energy of *sd*-shell nuclei allows for a purely theoretical description of the beta-decay process that does not rely on experimental Q values.

With this, we calculate the expected half lives for all well-known β^- decays in the *sd*-shell using USDC and plot the ratio to the experimental half lives against mass number in the top panel of Fig. 3.13. Apart from a few notable outliers which we will discuss, there is a consistent underestimation of the decay half-lives for nuclei at the top of the shell and a consistent overestimation of those β-decays that are primarily GT at the bottom of the shell.

In this section, we attempt to transition away from a single parameter fit of the GT quenching
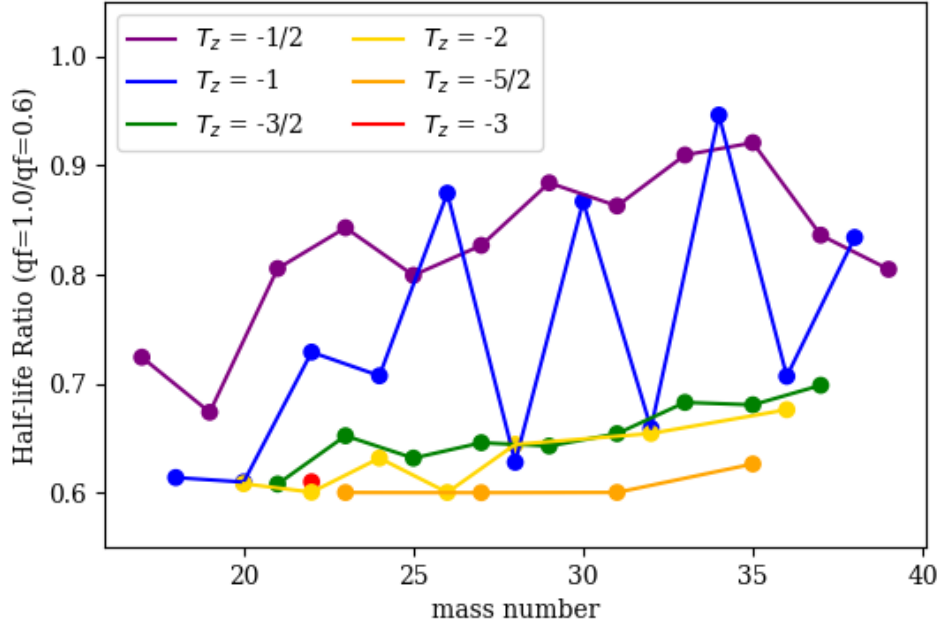
Figure 3.14: Scatter plot of the ratios of the β^--decay half-lives calculated using USDC with no quenching ($q = 1.0$) to those calculated with the typical quenching factor ($q = 0.6$).

for the *sd*-shell. That is, we seek a linear relationship dependent on the mass of a nucleus for the quenching factor $q(A)$. If we connect those points with similar T_z in Fig. 3.13 we can see the need for this change. We see that those nuclei that are further from zero total isospin projection (that is the same number of protons and neutrons), the stronger this linear relationship with mass is.

To investigate the cause of this, we can examine the effect of removing this quenching factor on the predicted USDC half-lives by setting $q = 1.0$ which leaves the GT operator unchanged. The ratios of these calculations compared to the standard calculations with $q = 0.6$ are plotted against mass number in Fig. 3.14 with the isospin groups still shown.

In this figure, if a decay was purely a Fermi decay with no Gamow-Teller transitions then we would expect this ratio to be exactly equal to one as we do not quench the Fermi operator. On the other hand, if there were no Fermi decay then we would expect this ratio to be 0.6 as any decay would be entirely Gamow-Teller in nature so the entire decay is quenched. In the case of β-decay in nuclei with $T_z = 1/2, 1$ we see ratios that approach 1.0 but it is not consistent for all cases.

We want to avoid including those decays in which a large fraction of the decay is Fermi while still

83
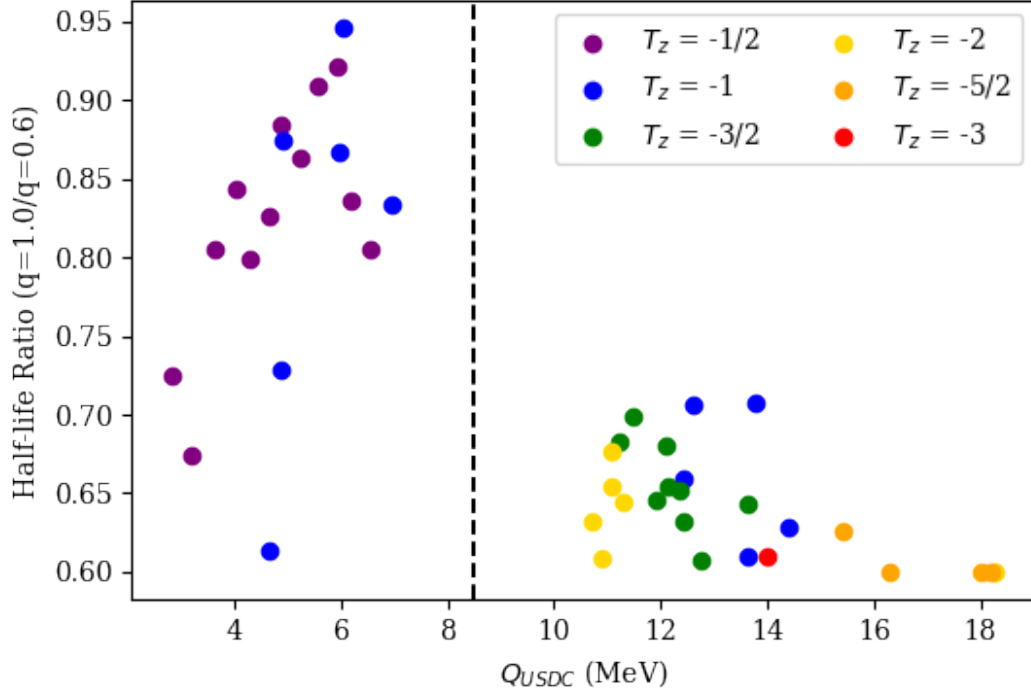
Figure 3.15: The same ratios plotted in Fig. 3.14 plotted against their theoretical Q value instead of mass number. The vertical line separates the two groupings of the data.

retaining as much good data as possible. It is therefore necessary that we implement a consistent standard to include or exclude a decay in the fitting of the quenching factor. To this end, it is helpful to plot the same half-life ratios found in Fig. 3.14 against the USDC Q value rather than against mass number, as shown in Fig. 3.15. We see an immediate separation into two groups: (1) those β-decays in nuclei with a low Q value (<8 MeV) that have a large spread across the range of possible ratios, and those β-decays in nuclei with large Q values and low half life ratios. For nuclei with small Q values, the possible levels in the daughter nucleus open to the decay will be energetically limited. If the IAS is one of those few available levels to decay to, then the Fermi decay can dominate and interfere in the fitting of the quenching factor. It is therefore necessary to use the second group, with large Q values, to determine the mass scaling quenching factor.

A standard least squares fit to this data with a linear model results in the following relationship,

$$q(A) = 0.95 - 0.025(A - 16),\tag{3.12}$$

which has been written in terms of $A - 16$ to quickly show the strength at either end of the shell.
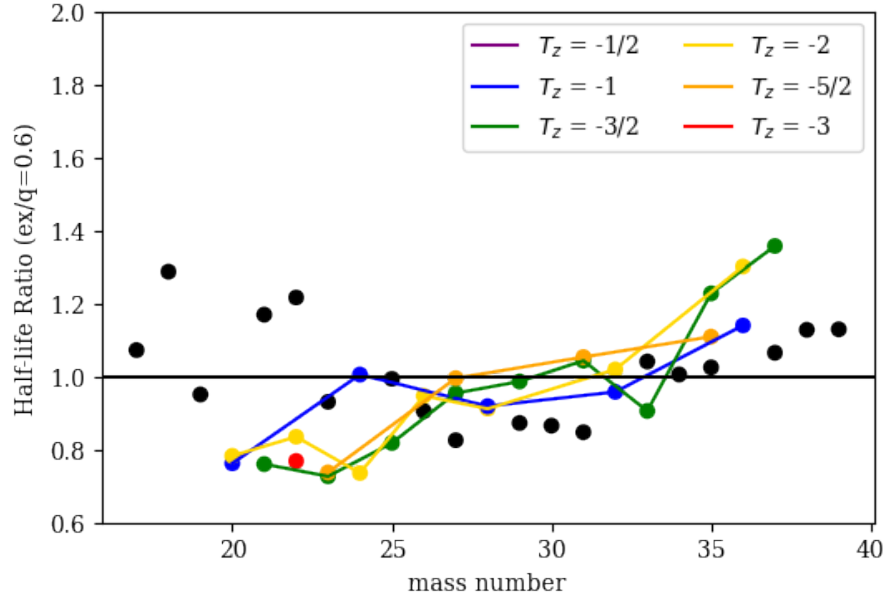
(a) Constant quenching factor.
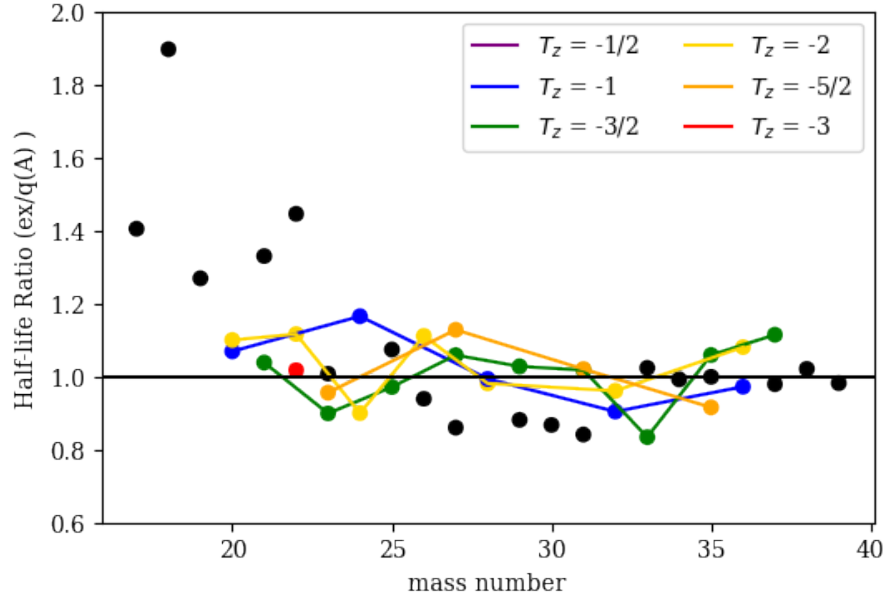
(b) Mass dependent quenching factor.

Figure 3.16: (a) Same data as in Fig. 3.13 using the typical quenching, with lines connecting similar T_z nuclei that were included in the fit. (b) Same as above but using the new mass dependent quenching developed in this section. The black circles show the results for the excluded decays with low Q values.

This now runs from a quenching of 0.95 for $A = 16$ to 0.35 for $A = 40$.

When we recalculate the β-decay half lives using this new mass dependent quenching factor $q(A)$ we see an improvement in agreement with experiment across the shell for those nuclei with a sufficiently high Q value (and therefore small half life). This is shown in Fig. 3.16, with the top panel again showing the results from Fig. 3.13. This new mass dependent relationship allows for more realistic calculations of β-decay properties for *sd*-shell nuclei in future work.

To further improve this mass dependence of the quenching factor, one could look at *partial* half-lives. That is to say, we could remove the portion of the half-life coming from the Fermi decay and examine the contribution from the GT decay separately. This could then allow us to incorporate those decays excluded from the fit in this work to achieve a better result overall.

CHAPTER 4

FURTHER REFINEMENT OF THE USDC INTERACTION

During the development of the USDC/USDI interactions, we explored the possibility of adding in an isovector term to account for the expected small deviation between the *nn* and *pp* interaction strengths in the nuclear strong force. This term was included in the charge-dependent extension to USD, USD-CD [31, 32] which is often used in conjunction with USDB as USDB-CD. However, due to a lack of sufficiently constraining data for this term, it was excluded. In this chapter, we will revisit this decision and search for a way to precisely determine the isovector strength of the strong force in a renormalized *sd*-shell interaction.

The work contained in this chapter serves as the foundation of a larger scale project that is ongoing with the goal of improving the USDC interaction and studying isospin breaking in the *sd*-shell.

4.1   Sources of Isospin Breaking in the Nuclear Hamiltonian

We begin with the assumption that the nuclear strong force is symmetric with respect to isospin. Setting aside the electric charge of the proton, the concept of isospin was introduced to describe the similarity in behavior under the strong force for the proton and neutron. This description has resulted in many useful tools and models to understand the behavior of nuclei. However, under the Standard Model we can determine the limits of isospin symmetry in nuclear physics.

In nuclear structure physics, the nucleons are often treated as fundamental particles. This is because, for the energies we are considering, it is essentially true. In actuality, the nucleon is made up of three quarks being held together by gluons to achieve a neutral color charge. A detailed description of this process is outside of the scope of this dissertation, but the interested reader can find more in any Quantum Chromodynamics textbook. The difference between a proton and neutron comes in the types of quarks that compose them, as described in Section 1.5.

The strong force for protons and neutrons is therefore able to be described as a sum of three

terms,

$$H_{\text{strong}} = H_0 + H_{IV} + H_{IT} \tag{4.1}$$

in which the strong force has been decomposed into a scalar, vector, and tensor term. The isospin-conserving interaction H_0 accounts for the majority of the strength of the interaction and is independent of the isospin projection of the interacting nucleons. The remaining terms are the isovector and isotensor components of the interaction which result in the breaking of isospin symmetry in different ways.

The isotensor interaction can be understood as a breaking of the charge-independence (CIB) of the strong force. This breaking manifests in our interactions as a small percentage increase in the strength of the *pn* $T = 1$ TBME relative to the corresponding *nn* and *pp* TBME. From the standard model, we also expect charge-symmetry breaking (CSB) of the nuclear strong force [72]. This manifests as a subtle splitting of the *pp* and *nn* strong TBME, the strength of which has been difficult to determine precisely through experiment. While the source of CIB is rather complex, the source of CSB in the strong force can be explained by the difference in masses between the proton and neutron. The neutron is slightly more massive than the proton, which results in differences in their kinetic energies. These differences then influence the overall effect of the nuclear strong force on the nucleons.

The strength of these corrections compared to H_0 is on the order of a couple percent, and so do not effect overall binding energies or excitation energies significantly (except in cases of increased isospin level mixing as explored in Chapter 3). The effects of these terms are best found when looking at the energy differences found in isobaric multiplets. Recreating the experimental coefficients of the IMME with an interaction is a strong indicator of a reasonable modeling of isospin breaking effects. Effective interactions are generally able to reproduce these well when constrained appropriately, while *ab initio* methods are generally lacking in this area.

In a recently accepted, but not yet published, article in Physical Review C, Martin *et al.* [73] presented the first steps in bench marking isospin-breaking in *ab initio* nuclear theory for superallowed Fermi β-decay. Isobaric multiplets from $A = 10$ to $A = 74$ were examined. They
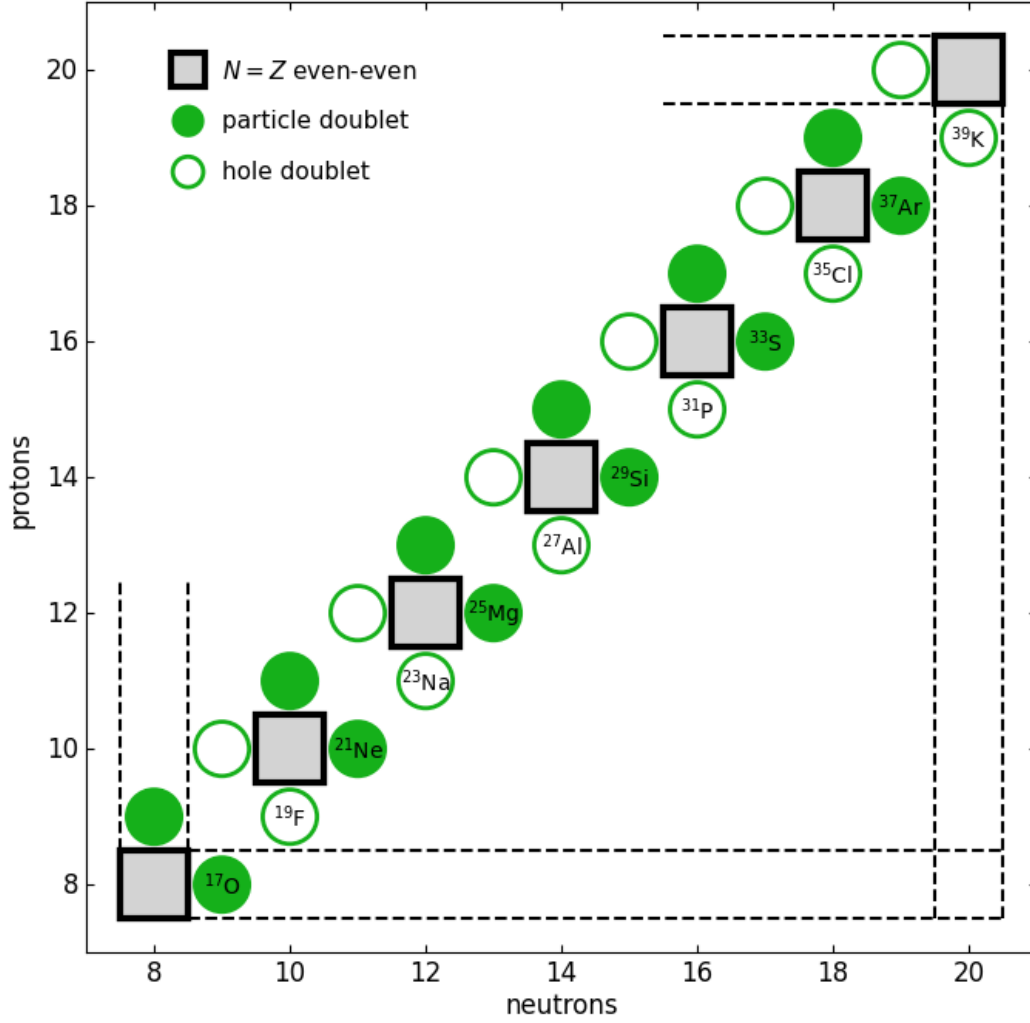
Figure 4.1: Visualizing the $T = 1/2$ doublets as proton/neutron hole and particle states around even-even $T_z = 0$ nuclei.

are able to achieve an agreement in the overall scale of the b- and c-coefficients on the order of 250 keV, but fail to reproduce the oscillatory pattern for the c-coefficients found in experiment and replicated by USDC/USDI.

4.2 Isolating the effects of Charge-Symmetry Breaking

Isospin non-conservation in the nucleus comes from multiple sources, two of which were considered in Chapter 2 covering the USDC/USDI interactions. Those were the Coulomb force felt by the protons, and an isotensor interaction that broke the charge-independence of the strong force for

proton/neutron pairs. The isotensor interaction was modeled as a percent increase in the $T = 1$ pn TBME over their nn and pp counterparts. These were able to be constrained as they are primarily responsible for specific energy differences between isobaric multiplets, namely the linear and quadratic coefficients of the IMME. The dependence of the c-coefficients is shown in the top panel of Fig. 4.2, and discussed in depth in Chapter 2.

As noted in [14] and earlier in this work the determination of an isovector interaction was excluded due to the lack of constraining information. Previous works in the sd-shell have included an isovector interaction constrained alongside an isotensor interaction using the b- and c-coefficients of the IMME as constraints. However, we saw no improvement in rms deviations of these quantities with an isovector interaction so instead we explored the modification of the Coulomb interaction to achieve better agreement with experiment.

Lacking an isovector term, the fits resulted in an isotensor strength of 2.2% for the USDC and USDI interactions, but a reduced isotensor strength of 0.8% for the USDCm and USDIm interactions containing the modified Coulomb. This reduction in isotensor strength can be interpreted as the SVD fit of the Coulomb TBME attempting to compensate for non-Coulomb isospin-breaking effects in the nucleus. This is less than ideal due to the different mass dependencies in the Coulomb TBME and in the strong TBME. This resulted in sub-optimal performance of the modified Coulomb in Chapter 3.

To isolate the effects of the isovector component of the nuclear strong force in a measurable way, we will dive deeper into the mirror energy differences of the $T = 1/2$ multiplets (doublets). Fig. 4.1 shows the relevant doublets in the sd-shell separated into two groups. A doublet can be viewed as either a "particle" or "hole" pair, based on whether the member nuclei can be modeled as a single particle or single hole around an even-even $T_z = 0$ core nucleus. For example, the $A = 17$, $T = 1/2$ doublet consists of the ground states of ^{17}O and ^{17}F which can be modeled simply as a core ^{16}O nucleus with a valence neutron/proton. It is clear then that the $A = 19$ doublet can be modeled as a neutron/proton hole in ^{20}Ne.

An important note, for this section we will be examining the isobaric doublets that have J^π
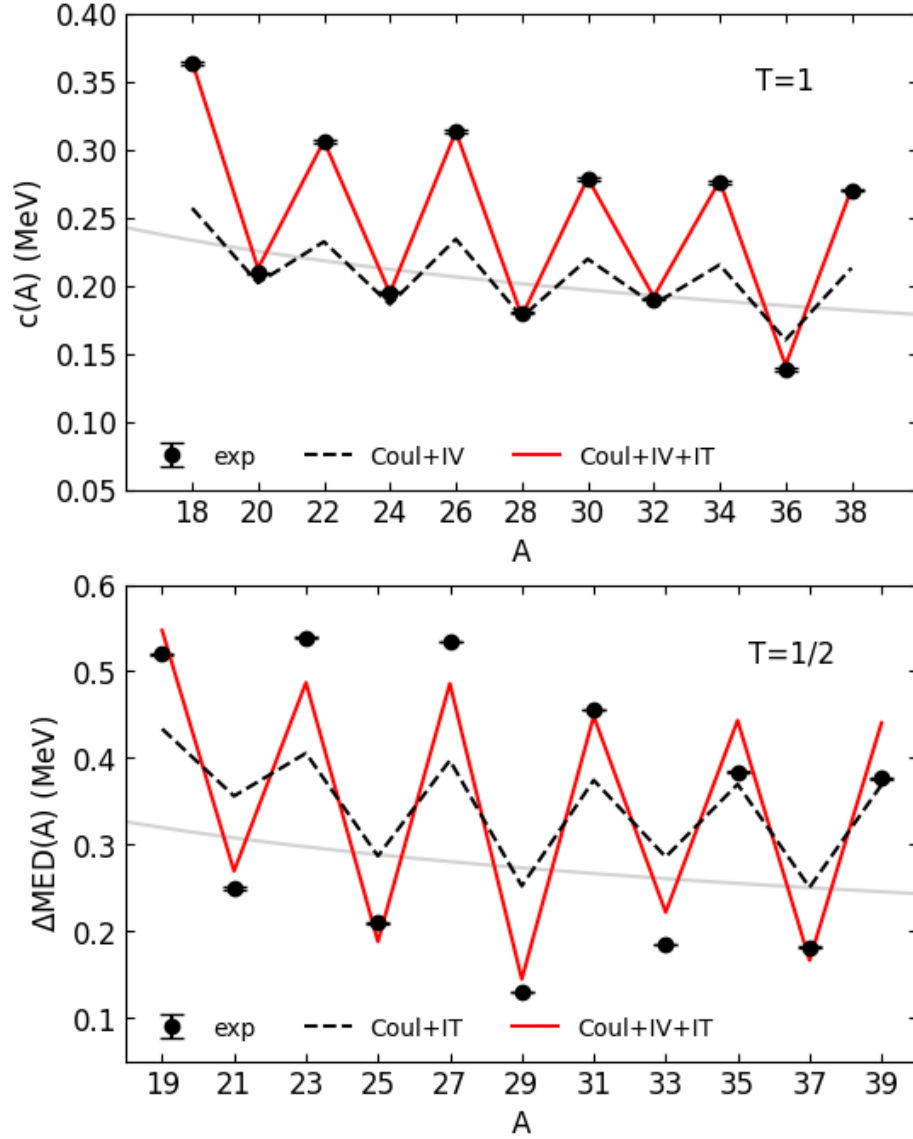
Figure 4.2: The *c*-coefficients of the lowest lying $T = 1$ triplets and the ΔMED for the $T = 1/2$ doublets. We see visually that the isotensor interaction is primarily responsible for reproducing the *c*-coefficients, and independently the isovector strength is responsible for the oscillations in the double energy difference of the mirror pairs. The LDM predictions are shown in grey as a sanity check.

assignments determined by the quantum numbers of the highest energy orbit the valence nucleons would be occupying in a standard Fermi filling order. In practice this means looking at excited states rather than the true ground state for some pairs.

The mirror energy difference in these doublets are due primarily to the Coulomb interaction, which has a much larger effect than either the isotensor or isovector terms. Motivated by [72] we then define a new quantity by taking the difference between two calculated mirror energy differences (MED) for $A = 17$ and $A = 19$,

$$\Delta \text{MED}(A = 19) = \text{MED}(A = 19, T = 1/2) - \text{MED}(A = 17, T = 1/2). \quad (4.2)$$

This is defined for every odd A pair up to $A = 39$. For $T = 1/2$ pairs, the mirror energy difference is equal to the b-coefficient of the IMME. The experimental ΔMED are shown in the bottom panel of Fig. 4.2 where we see a similar oscillation about the LDM predicted value in gray. The contributions to ΔMED from the various components of our isospin-breaking shell model interaction are also included in the figure. The dotted black line represents an INC interaction consisting only of Coulomb and isotensor with no isovector term. This tells us that the ΔMED is independent of the isotensor interaction.

We see then that the isovector interaction of the nuclear strong force is the source of the oscillatory pattern of this double energy difference. Just as we know the oscillations of the c-coefficients are caused by the isotensor interaction, which can be seen in the top panel Fig. 4.2. We used that observation to constrain the strength of the charge-independence breaking, and now we can use the experimental ΔMED to extract the strength of the charge-symmetry breaking .

4.3 Results for the new Refined USDC interaction

With our constraining data set given in the previous section, we are able to use 11 ΔMED in the sd-shell in the determination of the isovector strength. Table 4.1 lists these 11 cases and includes the results for the USDB-CD, USDC, and USDCm interaction compared to the experimental values. We can see the USDB-CD, which also includes an isovector strength, has the lowest rms deviation among the previously discussed interactions at 49 keV. The USDC interaction is unable to provide

Table 4.1: Comparison of calculated and experimental ΔMED for *sd*-shell $T = 1/2$ doublets, labeled by the mass and spin of the higher mass pair. All positive parity. All values in MeV

A	J	USDB-CD	USDC	USDCm	New	Exp.	error
19	5/2	0.491	0.392	0.519	0.5049	0.520	0.001
21	5/2	0.270	0.387	0.321	0.2998	0.249	0.002
23	5/2	0.454	0.388	0.441	0.4655	0.539	0.001
25	5/2	0.196	0.286	0.267	0.1974	0.210	0.001
27	5/2	0.459	0.364	0.463	0.45	0.535	0.000
29	1/2	0.194	0.195	0.123	0.1005	0.129	0.000
31	1/2	0.436	0.369	0.515	0.4324	0.456	0.000
33	3/2	0.249	0.336	0.174	0.2539	0.185	0.000
35	3/2	0.421	0.381	0.438	0.4427	0.384	0.001
37	3/2	0.166	0.238	0.106	0.1627	0.181	0.001
39	3/2	0.411	0.372	0.421	0.4361	0.377	0.001
	rms:	0.049	0.109	0.058	0.051		

such good agreement, and in fact does not follow the oscillation pattern found in experiment very well as shown in Fig. 4.3. However, the modified Coulomb interaction in USDCm does an excellent job of improving agreement with experiment by construction when compared to USDC, dropping the rms deviation to 58 keV. Our aim then, is to lower the USDC interaction's ΔMED rms deviation through the addition of an isovector term while keeping the overall agreement with experiment in other areas (energy levels, MED, *c*-coefficients) as shown in Chapters 2 and 3.

To provide a facsimile of the modified Coulomb fitting procedure, we further include the full energy level data set as well as any MED contained in the data set as inputs for the constraining of the isovector strength. We then include the following terms in the fitting procedure: an overall strength for the Coulomb TBME, the three Coulomb SPE, and the isovector strength. The isovector strength is modeled as a percentage increase (decrease) of the *nn* (*pp*) $T = 1$ TBME. We split the effect of the isovector term between the *nn* and *pp* TBME to avoid any influence on the isotensor strength, which is dependent on the average of the *nn* and *pp* TBME.

Doing so results in the following changes from the Coulomb in the USDC interaction. First, the Coulomb TBME are increased very modestly by 0.26%. Second the Coulomb SPE are left essentially unaltered at 3.451 MeV, 3.628 MeV, and 3.324 MeV for the $0d_{3/2}$, $0d_{5/2}$, and $1s_{1/2}$ orbits. These can be compared to the other interactions by looking at Table 2.4.
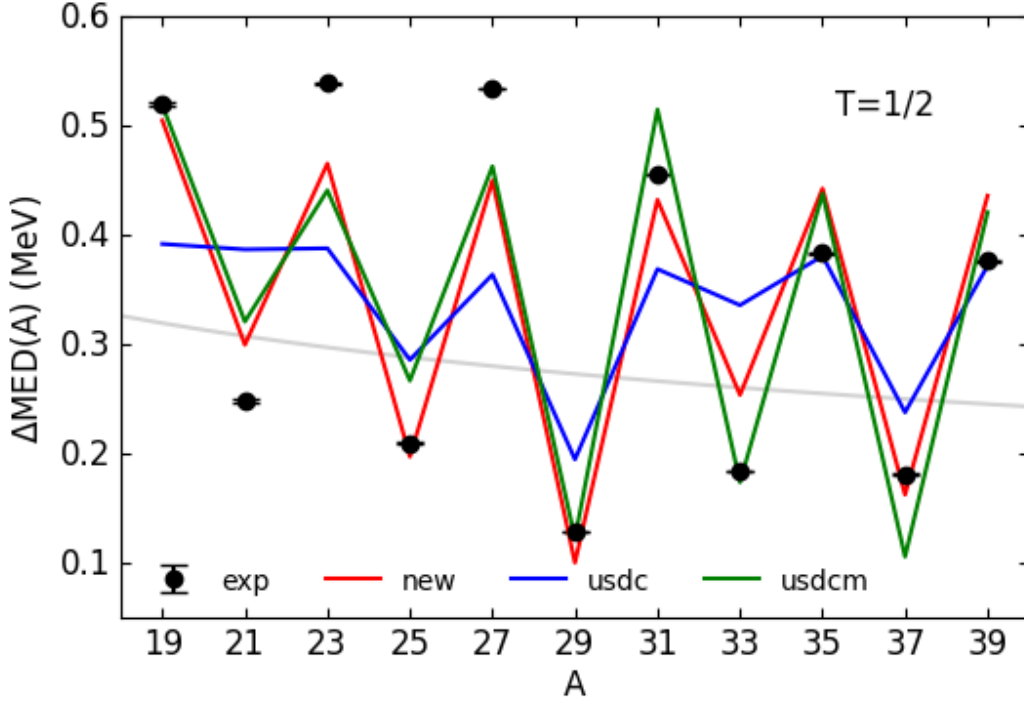
Figure 4.3: A comparison of predictions for the ΔMED using the new interaction and USDC/USDCm, with experiment shown in black circles. The liquid drop model predictions are shown in grey.

Lastly we now have a fitted isovector interaction strength of 1.4%. This new version of the USDC interaction has a similar energy rms deviation of around 150 keV, and a similar MED rms deviation of around 75 keV. The newly gained benefit is an rms deviation for the ΔMED of 51 keV which is an improvement over even USDCm. The rms for the new interaction is also on par with the USDB-CD interaction.

This new interaction would ideally follow the fitting procedure laid out in Chapter 2, in which with the INC interactions determined a refitting of the isospin-conserving TBME in the strong interaction is completed. This is an area of ongoing research.

4.4 Improvement in the calculated ^{27}Si spectra

One of the motivations in Chapter 2 for exploring a secondary SVD fit for the Coulomb TBME was a desire to better describe the exhaustively measured mirror pairs in ^{27}Si and ^{27}Al. The new data provided by Gavin Lotay [37] consists of 45 mirror states with well known energies and spin
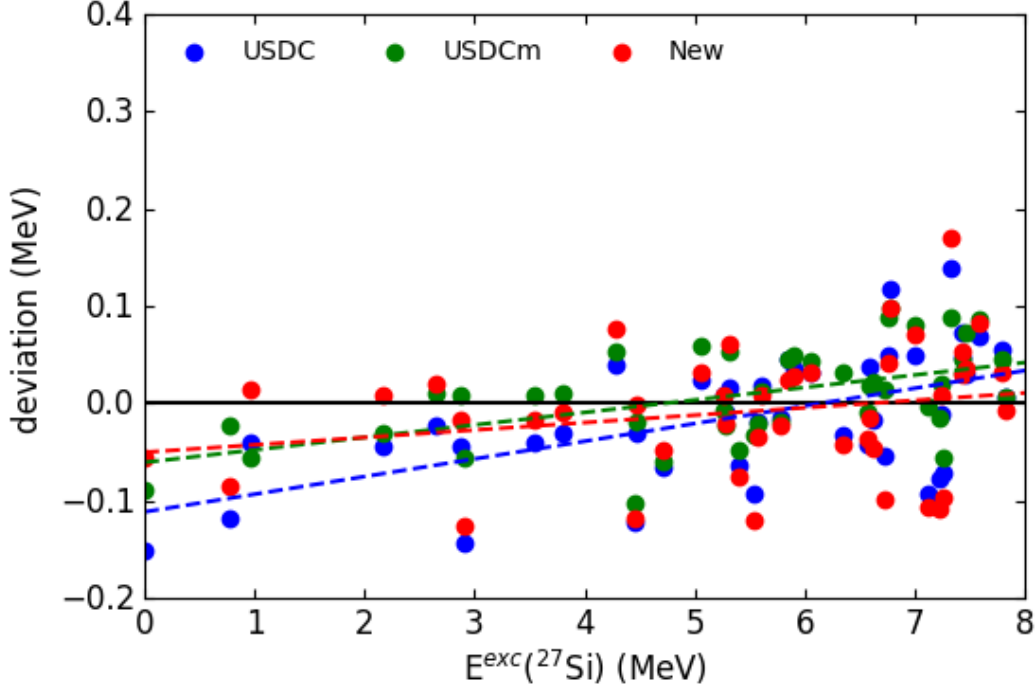
Figure 4.4: Deviations from experiment in the calculated MED for mirror pairs in ^{27}Si and ^{27}Al for the new interaction compared to USDC and USDCm.

assignments. When these mirror energy differences are calculated with our new interaction and compared to the experimental results, we see several pairs at high energy with poor agreement.

However, the new interaction results in a mixing of the level order at high excitation energies (above 5 MeV) that would need to be resolved more carefully, so these deviations are due to a mixing up of the mirror pairs rather than any real deficiency in the theory. So when comparing to the previous USDC and USDCm interactions we will discuss the rms deviation for the low lying levels.

For those mirror pairs with $E_x < 5$ MeV, the USDC and USDCm interactions have rms deviations of 82 keV and 51 keV, respectively. The new interaction with an added isovector interaction term manages to reduce this rms deviation to 61 keV, a marked improvement over USDC, but it is still unable to fully replicate the agreement found in USDCm. This issue may be resolved with a refitting of the isospin-conserving strong interaction with the newly determined INC interactions strengths.

4.5 New IAS mixing calculations in ^{31,32}S

In Chapter 3, we examined two cases of known large isospin level-mixing in two sulfur isotopes discovered by studying the β-decay of chlorine isotopes. Level-mixing of the IAS in the daughter nuclei with similar J^{π} will cause the level to shift in energy, and so the study of isospin level mixing is important to understand β-decay.

The USDC interactions all showed improved agreement with the extracted experimental mixing matrix elements when compared to USDB-CD. However, with USDCm and USDIm which contained the old modified Coulomb interaction, we saw an overestimation of the mixing strength. Can our new interaction improve upon these results or at the least maintain reasonable agreement with experiment?

As before, we assume two level mixing and small isospin mixing with the states $|1\rangle$ and $|2\rangle$ where $|1\rangle$ is the IAS and $|2\rangle$ is the state it is mixing with so that,

$$|1\rangle = |T_1\rangle + \alpha\,|T_2\rangle \tag{4.3}$$

where $\alpha = \langle V_{INC}\rangle\,/\,(E_1 - E_2)$ is small. We can then solve for the isospin mixing matrix element as

$$\langle V_{INC}\rangle = \langle 2|\,T^2\,|1\rangle\,(E_1 - E_2)/\langle 2|\,T^2\,|2\rangle \tag{4.4}$$

This simple equation can be used when primarily one level is the cause of the large isospin mixing.

The new interaction results in 33.5 keV and 28.5 keV for the strong mixing found in ^{31}S and ^{32}S, respectively. The results for the previous USD-type interactions are shown in Table 3.2 and are compared to the experimental results of 41(1) keV and 26(3) keV for the two mixing cases. The issue in the modified Coulomb interactions of overestimating the isospin mixing strength in these sulfur isotopes seems to have been resolved. We can see that our new interaction is able to have agreement with experiment on par with USDC and USDI for these mixing matrix elements, along with the improved agreement in describing mirror energy differences shown earlier.

This new interaction has not yet been named and is still in the process of being improved, but the preliminary results presented in this work are a positive sign that this strategy to improve the USDC interaction is effective.

CHAPTER 5

MODELING THE NEUTRON-RICH CALCIUM ISOTOPES

Next generation experiments performed at newly built rare-isotope facilities will provide a greatly expanded view of the nuclear landscape. While qualitative predictions are available, quantitative predictions for those soon-to-be-discovered nuclei are needed to guide and motivate these experiments. In this chapter we present a process to quantitatively describe the calcium isotopes out to ^{60}Ca, probably the last doubly-magic nucleus to be discovered by the new radioactive-beam facilities.

We show that a data-driven method for improving the Hamiltonian provides an excellent description of the known binding energies and spectra for the calcium isotopes within the fp model space. A new universal fp interaction for calcium (UFP-CA) is presented. Configuration-Interaction calculations with UFP-CA together with comparisons to results from energy-density functional (EDF) models leads us to conclude that ^{60}Ca is doubly-magic at a level that is similar to that observed in ^{68}Ni.

The work contained in this Chapter serves as a jumping off point for a larger project. The goal is to generate interactions for the $sd - pf$ model space below the calcium isotopes as well as the fp and fpg model space above calcium.

5.1 The Calcium Data Set

The data set used for this work contains the absolute binding energies for $^{46-57}$Ca, with the available experimental values from the 2016 Atomic Mass Evaluation [56] used for $A < 55$. Recently the first mass measurements of $^{55-57}$Ca were published [74], and these are adopted here for the fit. Additionally, 23 well-known fp excited states are included in the fit as they contain important information for constraining the matrix elements involving the high lying $0f_{5/2}$ and $1p_{1/2}$ orbits.

Along with the 12 ground state binding energies, our data set consists of 35 energy levels for these fp-shell calcium isotopes. Energies for $A < 46$ were excluded to avoid the influence of low

lying intruder states on the $0f_{7/2}$ parameters in the interaction. The excited states included in the fit are shown as green points at their experimental excitation energies in Fig. 5.1 along with a broad look at the energy spectra calculated with UFP-CA for the calcium isotopes with $A > 45$. Each line corresponds to a predicted energy level with the length and color representing the spin and parity of the level. We will show that we can confidently predict that the levels shown in Fig. 5.1 exist and their energies are correct within around 200 keV.

5.2 Modifying the SVD Procedure for Small Data Sets

The fit begins by formulating the problem as a χ^2 minimization of N_p parameters p_j on a data set of size N_d.

$$\chi^2 = \sum_i^{N_d} w_i(E(\vec{p}) - E_i^{exp}), \tag{5.1}$$

where the weights are set to $w_i = (\sigma_i)^{-2}$ with the adopted errors σ_i for the data set being a combination of the recorded experimental errors and a theoretical error. To normalize the minimized χ^2 to the degrees of freedom ($N_d - N_p$), we set $\sigma^{th} = 75$ keV. The adopted errors are taken as the theoretical and experimental errors added in quadrature. The χ^2 is minimized when $\vec{p} = \vec{p}_0$, which can be found using standard methods. However, the chosen parameters are highly correlated and the states included in this fit will be more dependent on some LC of p_i than others. This motivates us to truncate the parameter space using a SVD as and explained in depth in Ref. [15] and Section 1.6, and produces a family of solutions $\vec{p}_0(n)$, where n is the number of LC allowed to vary in the fit.

The parameter variance-covariance matrix S can be determined for each $\vec{p}_0(n)$ by inverting the SVD of the data matrix G, with the $i > n$ diagonal terms of the D matrix set to zero in order to capture only the statistical uncertainties from the regression. With $S(n)$, parameter uncertainties can be taken as $\Delta p_i(n) = \sqrt{S(n)_{ii}}$. This defines a "reasonable domain of model parameters" [27] around the minimum that provides interactions of similar quality to $\vec{p}_0$.
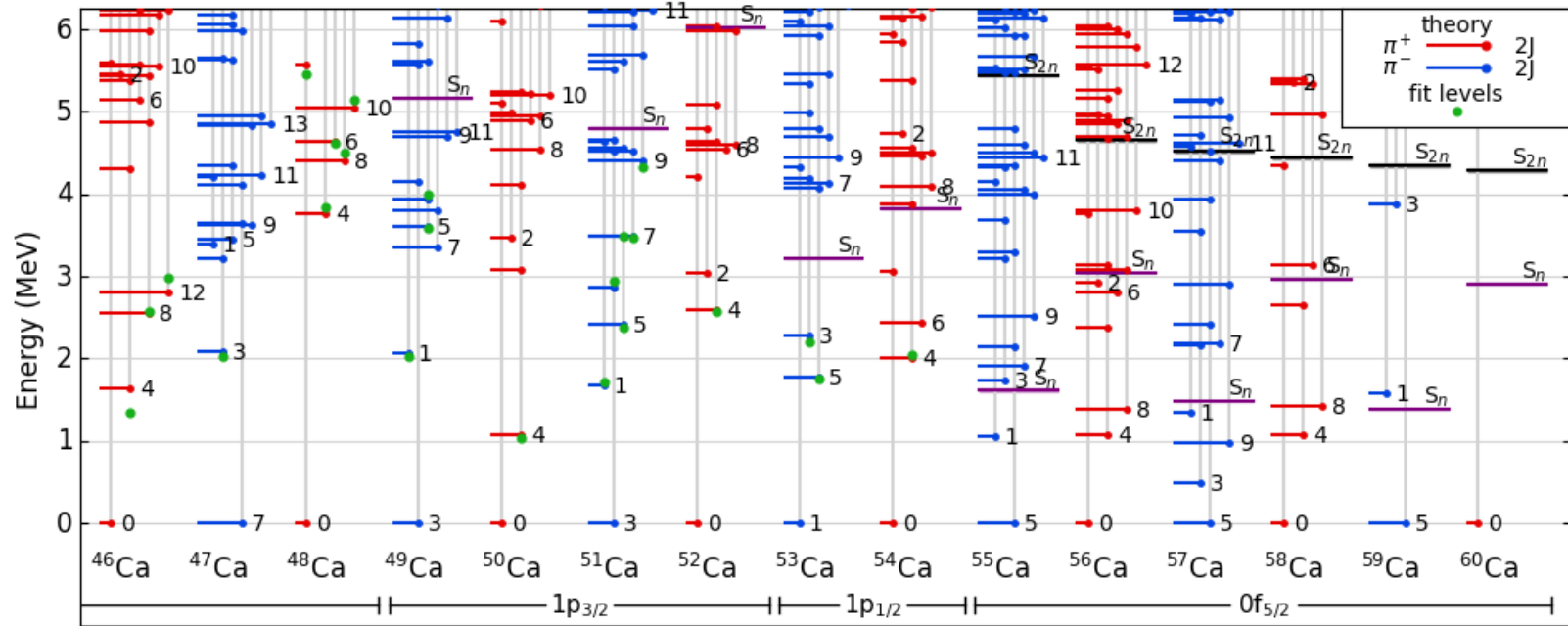
Figure 5.1: Calculated level schemes for $^{46-60}$Ca calculated using the newly constrained UFP-CA. The experimental levels (green) included in the fit show good agreement with the theory predictions. Positive parity states are shown in red, and negative parity states are shown in blue. The one- and two-neutron separation energies are shown as the purple and black lines, respectively.

Naturally then, the model calculated observables O will then have an acceptable range of values in this parameter domain. The observables variance-covariance matrix is defined as

$$S_d(n) = JS(n)J^T, \tag{5.2}$$

with the Jacobian $J_{ji} = \partial_{p_i} E_j$.

Using this we can generate the statistical uncertainty introduced to the calculated observables at each n. At $n = 0$ the calculated ΔO^{stat} will be zero, and tend to grow with n. The full uncertainty is a combination of the statistical uncertainty with the model uncertainty of around 100-200 keV for these effective interactions. The SVD truncation of the parameter space allows us to incorporate physics from the *ab initio* interaction where our data is least able to determine the parameters. Therefore, we can minimize the statistical uncertainty and parameter rms deviation while only moderately increasing the resulting energy rms deviation of the interaction.

5.3 Results of the UFP-CA Interaction

A reasonable starting interaction is needed for this procedure in order to effectively navigate the parameter space and maintain a physically grounded interaction. The calcium *fp*-shell data set allows us to think of our nuclei as a core of ^{40}Ca in its ground state, interacting with valence neutrons in the *fp* orbits. We construct a Hamiltonian for this system using a zero-body term (H_0), a one-body term (H_1), and a two-body term (H_2). Higher order terms are effectively folded into $H_{1,2}$ by the fitting procedure.

$$H = H_0 + H_1 + H_2. \tag{5.3}$$

H_0 is a fixed zero-body energy term set equal to the experimental energy of ^{40}Ca (-342.052 MeV). H_1 is accounted for through single-particle energies, ϵ_α, for each neutron *fp* orbit α. We set these initially to the values found in the GPFX1A interaction and then allow them to vary.

H_2 describes the interactions among the valence neutrons, and contains the TBME, $v_{JT}(\alpha, \beta; \gamma, \delta)$, to be constrained. The TBME have a mass scaling of the form,

$$v_{JT}(ab; cd)(A) = \left(\frac{42}{A}\right)^p v_{JT}(ab; cd)(A = 42). \tag{5.4}$$
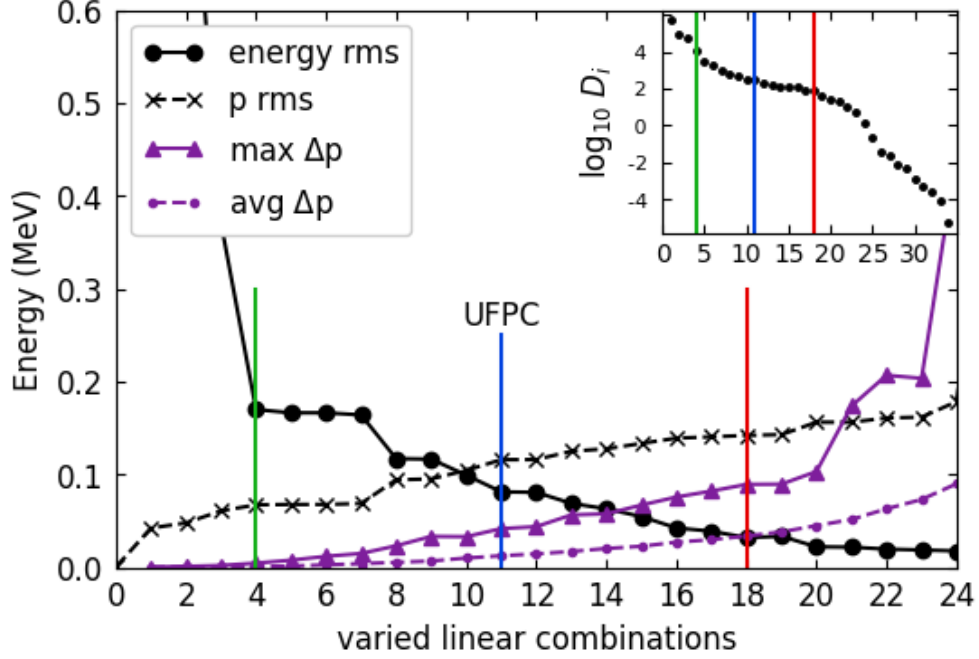
Figure 5.2: The rms deviations plotted against varied LC. The black circles show the energy rms deviation between theory and experiment. The black crosses show the parameter rms deviation from the starting interaction. The average and maximum Δp are denoted by the purple triangles and points. The singular values are plotted on a log scale in an inset figure. The red, blue, and green vertical lines are described in the text.

The two-body nuclear strong interaction terms contained in H_2 scale with $p = 0.3$ consistent with Refs. [14, 15, 28]. Higher order effects are then folded into $H_{1,2}$ by the fitting procedure. For this work, the TBME are set initially to values taken from a VS-IMSRG calculation [75]. Beginning with the EM1.8/2.0 NN+3N interaction [76] in an oscillator basis of frequency $\hbar\omega = 16$ MeV and $2n + \ell \le e_{max} = 14$, we normal order with respect to the Hartree-Fock ground state of ^{48}Ca and decouple the neutron fp valence space.

The limited size of our data set prevents us from fitting every TBME as the SVD of the full parameter data matrix fails. We limit our parameters to only the diagonal TBME and the ϵ_α for each fp orbit, the terms most impacted by three-body interactions and coupling to the continuum [77]. This gives us a total of 30 parameters p_i with which to perform the modified χ^2 minimization as done in Ref. [14]. This family of solutions can be compared by examining their energy rms deviations from the data set and the parameter rms deviations from the initial parameters. These
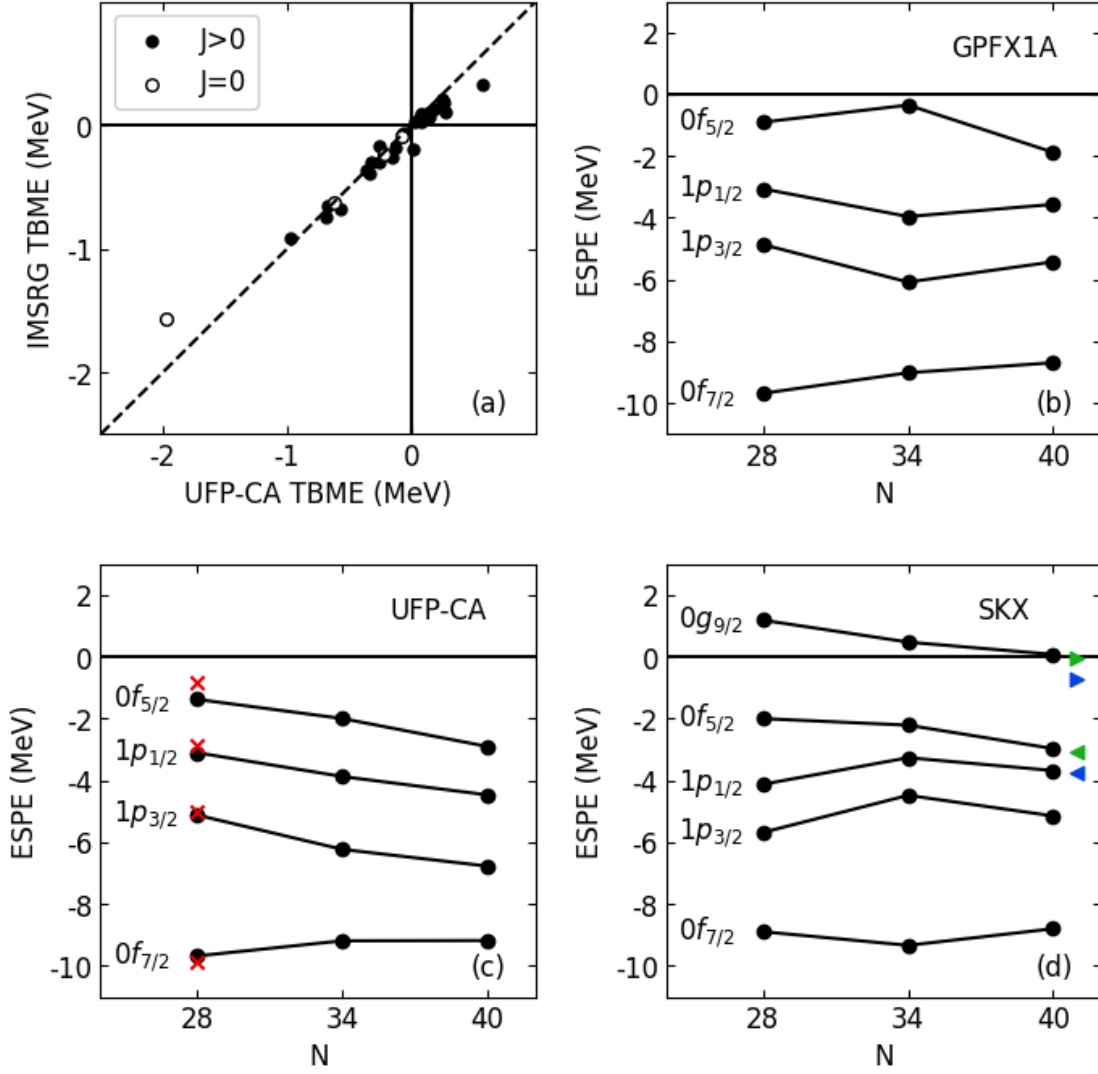
Figure 5.3: A comparison of the TBME between UFP-CA and the initial IMSRG interaction is shown in (a). The ESPE discussed in the text are shown for GPFX1A (b), UFP-CA (c), and a representative Skyrme interaction (d). The red crosses show the IMSRG values at N=28. The $0f_{5/2}$ (◁) and $0g_{9/2}$ (▷) are shown for the SKM* (green) and UNEDF0 (blue) EDF functionals.

results are shown in Fig. 5.2.

At $n = 4$ (green) there is a sharp drop in the energy rms deviation to around 180 keV which indicates that the four ϵ_α are the most important parameters to achieve good agreement with experiment. The energy rms deviation continues to decline to around 30 keV, however the maximum statistical uncertainty among the interaction parameters increases rapidly after $n = 20$, suggesting that the data is unable to constrain the interaction sufficiently after this point. To avoid this, we stop at $n = 18$ (red). The parameter rms deviation grows smoothly from around 60 keV at $n = 4$ to around 150 keV at $n = 18$. Results for the whole range of solutions from $n = 4$ to $n = 18$ are similar and beyond $n = 11$ (blue) the improvements are very small.

As it is representative of our results we choose the $n = 11$ solution as UFP-CA, a universal fp shell interaction for the calcium isotopes. Fig. 5.3 contains a scatter plot comparing the TBME in UFP-CA against the initial IMSRG interaction, and the diagonal TBME are shown in Table 5.1. The $(0f_{7/2})^2$ $J = 0$ term is shifted the most by the fit, which is the result of the ground state of ^{46}Ca mixing with two-proton excited states from the sd-shell [78]. The off diagonal TBME that are not changed by the fit are shown in Table 5.2.

The UFP-CA energy spectra for $^{46-60}$Ca are shown in Fig. 5.1 along with the one- and two-neutron separation energies. While the σ^{stat} for the absolute ground state binding energies can be large (up to 0.5 MeV), σ^{stat} for the one and two-neutron separation energies are small when correlations are taken into account. In addition to these states, unnatural-parity intruder states involving the $1s - 0d$ orbits start at an excitation energy of 4 MeV near $A = 48$, and, as we will show in a weak-coupling model, intruder states involving the $2s - 1d - 0g$ orbits will come as low as 1.4 MeV near $A = 60$.

There are several experimentally observed states with no definite spin assignment in this region that were not included in the fit. In ^{49}Ca, the NNDC reports the level at 3.354 MeV as $(9/2^+)$ but has recently been corrected to $7/2^-$ [79]. We predict a $7/2^-$ state at approximately this energy along with a second nearby $7/2^-$ state. Apart from this, there are 9 levels with unknown spin in $^{49-55}$Ca that fall within 150 keV of our predictions. There are no known levels up to 5 MeV that are contrary

Table 5.1: Comparison of $v(a, b; J)$ between the starting IMSRG interaction and the fitted interaction UFP-CA. Here, $v(a, b; J) = v(ab, ab; J)$ are the diagonal TBME allowed to vary. All values are in units of MeV.

ME	IMSRG	UFP-CA	Δv
$v(7, 7; 0)$	-1.5605	-1.9757	0.4152
$v(7, 7; 2)$	-0.7426	-0.6860	-0.0566
$v(7, 7; 4)$	-0.1782	-0.1314	-0.0468
$v(7, 7; 6)$	0.0899	0.0737	0.0162
$v(7, 5; 1)$	0.2081	0.2445	-0.0364
$v(7, 5; 2)$	0.1099	0.1483	-0.0384
$v(7, 5; 3)$	0.0250	0.0837	-0.0587
$v(7, 5; 4)$	0.1850	0.2552	-0.0702
$v(7, 5; 5)$	0.1528	0.2409	-0.0881
$v(7, 5; 6)$	-0.6799	-0.5713	-0.1086
$v(7, 3; 2)$	-0.6317	-0.6173	-0.0144
$v(7, 3; 3)$	0.0654	0.1454	-0.0800
$v(7, 3; 4)$	-0.1704	-0.2633	0.0929
$v(7, 3; 5)$	0.3339	0.5740	-0.2401
$v(7, 1; 3)$	0.1099	0.2748	-0.1649
$v(7, 1; 4)$	-0.1941	0.0077	-0.2018
$v(5, 5; 0)$	-0.6549	-0.6802	0.0253
$v(5, 5; 2)$	-0.3665	-0.365	-0.0015
$v(5, 5; 4)$	-0.0746	-0.0733	-0.0013
$v(5, 3; 1)$	-0.0660	-0.0697	0.0037
$v(5, 3; 2)$	0.0853	0.0783	0.0070
$v(5, 3; 3)$	-0.0842	-0.0764	-0.0078
$v(5, 3; 4)$	-0.2935	-0.2570	-0.0365
$v(5, 1; 2)$	-0.3052	-0.3182	0.0130
$v(5, 1; 3)$	0.0324	0.0314	0.0010
$v(3, 3; 0)$	-0.9154	-0.9741	0.0587
$v(3, 3; 2)$	-0.2538	-0.1551	-0.0987
$v(3, 1; 1)$	0.1358	0.1782	-0.0424
$v(3, 1; 2)$	-0.3935	-0.3397	-0.0538
$v(1, 1; 0)$	-0.2372	-0.2243	-0.0129

to our predictions, except for the unnatural parity states and three states in ^{51}Ca only observed in one three-nucleon transfer reaction [80].

The calculated S_{2n} for UFP-CA are compared to experiment in the top panel of Fig. 5.4. We see excellent agreement with experiment across the shell. We see the expected minor deviation for ^{46}Ca as well as for ^{40}Ca for the aforementioned reasons. The bottom panel of Fig. 5.4 highlights

Table 5.2: IMSRG values for the off-diagonal matrix elements, $v(a, b; cd; J)$. These remain unchanged during the fit and are included in UFP-CA. Reported in two columns to fit on a single page. All values are in units of MeV.

ME	IMSRG	ME	IMSRG
v(7 7; 5 5: 0 1)	−3.0868	v(5 3; 3 3: 2 1)	0.1321
v(7 7; 3 3: 0 1)	−0.9991	v(5 3; 3 1: 2 1)	0.2673
v(7 7; 1 1: 0 1)	−0.8050	v(5 1; 3 3: 2 1)	−0.1709
v(5 5; 3 3: 0 1)	−0.9847	v(5 1; 3 1: 2 1)	−0.3533
v(5 5; 1 1: 0 1)	−0.5217	v(3 3; 3 1: 2 1)	−0.4883
v(3 3; 1 1: 0 1)	−1.1357	v(7 5; 7 3: 3 1)	−0.1674
v(7 5; 5 3: 1 1)	0.0314	v(7 5; 7 1: 3 1)	0.1202
v(7 5; 3 1: 1 1)	−0.0643	v(7 5; 5 3: 3 1)	−0.1267
v(5 3; 3 1: 1 1)	−0.0102	v(7 5; 5 1: 3 1)	0.0941
v(7 7; 7 5: 2 1)	0.1068	v(7 3; 7 1: 3 1)	−0.0893
v(7 7; 7 3: 2 1)	−0.6079	v(7 3; 5 3: 3 1)	−0.0031
v(7 7; 5 5: 2 1)	−0.5954	v(7 3; 5 1: 3 1)	−0.0584
v(7 7; 5 3: 2 1)	0.4105	v(7 1; 5 3: 3 1)	0.1007
v(7 7; 5 1: 2 1)	−0.6550	v(7 1; 5 1: 3 1)	−0.0320
v(7 7; 3 3: 2 1)	−0.3280	v(5 3; 5 1: 3 1)	0.0535
v(7 7; 3 1: 2 1)	−0.3165	v(7 7; 7 5: 4 1)	−0.4281
v(7 5; 7 3: 2 1)	0.3068	v(7 7; 7 3: 4 1)	−0.3661
v(7 5; 5 5: 2 1)	−0.5007	v(7 7; 7 1: 4 1)	−0.3392
v(7 5; 5 3: 2 1)	0.3198	v(7 7; 5 5: 4 1)	−0.4583
v(7 5; 5 1: 2 1)	−0.3613	v(7 7; 5 3: 4 1)	0.4789
v(7 5; 3 3: 2 1)	−0.0048	v(7 5; 7 3: 4 1)	−0.0494
v(7 5; 3 1: 2 1)	−0.1150	v(7 5; 7 1: 4 1)	0.1202
v(7 3; 5 5: 2 1)	−0.3762	v(7 5; 5 5: 4 1)	−0.4002
v(7 3; 5 3: 2 1)	0.4002	v(7 5; 5 3: 4 1)	0.5818
v(7 3; 5 1: 2 1)	−0.9654	v(7 3; 7 1: 4 1)	−0.4273
v(7 3; 3 3: 2 1)	−0.4297	v(7 3; 5 5: 4 1)	−0.1542
v(7 3; 3 1: 2 1)	−0.4953	v(7 3; 5 3: 4 1)	0.6300
v(5 5; 5 3: 2 1)	0.0167	v(7 1; 5 5: 4 1)	−0.2313
v(5 5; 5 1: 2 1)	−0.1721	v(7 1; 5 3: 4 1)	0.5625
v(5 5; 3 3: 2 1)	−0.1723	v(5 5; 5 3: 4 1)	0.1453
v(5 5; 3 1: 2 1)	−0.3228	v(7 5; 7 3: 5 1)	−0.1078
v(5 3; 5 1: 2 1)	0.2458	v(7 7; 7 5: 6 1)	−0.9000
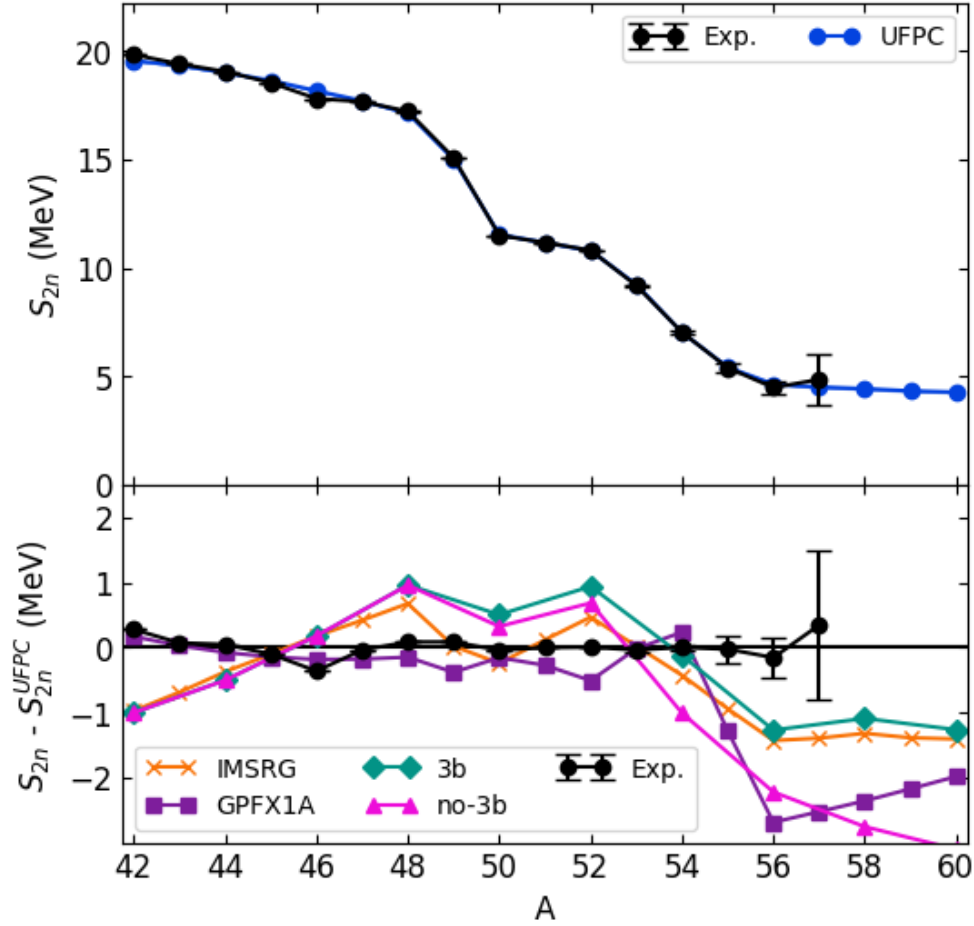
Figure 5.4: Experimental and calculated S_{2n} for the calcium isotopes. The bottom panel highlights the deviations from the UFP-CA predictions for experiment and several interactions: see the text for details. These theories all predict significantly lower two-neutron separation energies at the top of the $f_{5/2}$ shell.

the deviations from the UFP-CA predictions for experiment and several interactions: the GPFX1A interaction [16–18], results from Ref. [81] both with and without three-body correlations, and from using nucleus-specific IMSRG interactions [75]. These theories all predict significantly lower two-neutron separation energies at the top of the $f_{5/2}$ shell.

Our results show that the calcium isotopes are stable to neutron decay out to ^{60}Ca as observed experimentally [82]. This suggests many experiments that can be done to observe the predicted levels in these exotic calcium isotopes. Coulomb excitation could reveal the low lying 2^+ and 4^+ levels in ^{56,58}Ca. The structure of these levels are related to the $0f_{5/2}$ orbit and will be the most

sensitive indicator for the need to include the $0g_{9/2}$ orbit in the model space. Indeed the properties of all $A > 56$ calcium isotopes are dependent on the gap in energies between these orbits. Neutron decay experiments are key for further investigation of this $0f_{5/2}$ region.

5.4   On the Closed-Shell Status of ^{60}Ca

The consistency of the fit for all known data indicates that a renormalized Hamiltonian in the fp model space can be obtained and applied all the way to ^{60}Ca. The renormalization of the fp Hamiltonian implicitly contains the effects from sdg admixtures. This means that the shell gap between fp and sdg orbitals at $Z = 28$ and $N = 40$ is large enough to prevent the $2p - 2h$ configurations from becoming ground states as they do in the islands of inversion [83]. The known regions of islands of inversion involve deformations driven by the proton-neutron interaction. Thus, ^{54}Cr and ^{56}Fe are known to be inside the $N = 40$ island of inversion. Is there an island of inversion for ^{60}Ca? A signature would be if $^{58-60}$Ca are more bound than we predict. Low-lying excited states not described by our predictions will also give direct information on the location of the $0g_{9/2}$, $1d_{5/2}$ and $2s_{1/2}$ orbitals.

An important goal of this work is to help determine whether ^{60}Ca can indeed be treated as a closed shell nucleus. This designation is dependent on the magnitude of the energy gap between the $0f_{5/2}$ orbit and the $0g_{9/2}$ orbit. As our model space does not include this orbit, we must extrapolate through comparisons to energy-density functional (EDF) calculations. To allow inter-model comparisons, we introduce the "effective" single particle energies (ESPE) that evolve with the nuclear mass. These are a combination of the TBME and ϵ_α for the one-particle and one-hole configurations around a closed shell at $N = 28$, 34, and 40. The four ESPE calculated with GPFX1A and UFP-CA are plotted in Fig. 5.3 (b) and (c).

The shell gap can be inferred from EDF calculations based on a closed-shell configuration for ^{60}Ca. The EDF can be tested against the ESPE we obtain from the binding energy differences of ^{60}Ca and ^{59}Ca with one hole in fp. As an example, the results with the Skx functional are shown in Fig. 5.3 (d). The Skx results are reasonable agreement with UFP-CA at a level that is similar to

those obtained for other doubly-magic nuclei [84]. In the Mass Explorer [85], binding energies of ^{61,60,59}Ca are given for the SKM* [86] and UNEDF0 [87] models. The results implied for the $0d_{5/2}$ and $0g_{9/2}$ ESPE are shown on the right-hand side of Fig. 5.3 (d). The gap of about 3 MeV between $0f_{5/2}$ and $0g_{9/2}$ is similar to that observed in ^{68}Ni. Therefore, we expect the properties around ^{60}Ca to be comparable to those around ^{68}Ni.

For ^{68}Ni one can use the weak-coupling model to give energies of particle-hole states in terms of one and two neutron separation energies. For ^{68}Ni the results (compared to experiment) are 1.22 (1.01) MeV for the $(1p-2h)$ $9/2^+$ excited state in ^{67}Ni, 3.21 (2.89) MeV for the $(1p-1h)$ 5^- excited state in ^{68}Ni. and 1.71 (1.77) MeV for the $(2p-2h)$ 0^+ excited state in ^{68}Ni.

We can apply this to the ^{60}Ca region with three sources of uncertainty: (1) an overall model error that we take from the ^{68}Ni results, (2) the uncertainties on the $S_{1n,2n}$ derived in this chapter, and (3) the e_9 supplied from the Skyrme interaction. The results are 1.37 - e_9 MeV for the $(1p-2h)$ $9/2^+$ state in ^{59}Ca, 2.90 - e_9 MeV for the $(1p-1h)$ $2^- - 7^-$ multiplet in ^{60}Ca, and $4.27 - 2e_9 - V_0$ for $(2p-2h)$ 0^+ excited state in ^{60}Ca. With $e_9 = 0$ and V_0 = -2.72 (taken from the results for ^{68}Ni) this gives 1.55 MeV for the energy of the $2p-2h$ 0^+ state in ^{60}Ca. This is below the S_{2n} value of 4.27 MeV. Thus, like in ^{68}Ni, the first excited state in ^{60}Ca is predicted to be a bound 0^+ that would be observed via its two electron $E0$ transition.

For ^{61}Ca, $S_{1n} = e_9$ where e_9 is the single-particle energy of the $0g_{9/2}$ orbital. With Skx, e_9 is near zero energy, and ^{61}Ca may or may not be bound. For ^{62}Ca $S_{2n} = 2e_9 + V_0$ where V_0 is the effective TBME for $0g^2_{9/2}, J = 0$ which is on the order of 2 MeV. Thus ^{62}Ca is likely to be inside the neutron drip line. These conclusions are in line with the Bayesian Model Averaging results of Neufcourt et al. [88] which predict a bound ^{60}Ca with S_{2n} = 5(1) MeV and report an existence probability of 46% for ^{61}Ca. They further conclude that even-even calcium isotopes out to $A = 70$ are likely to exist.

However, Lenzi et al. [89] have extrapolated the neutron effective single-particle energies from Z=28 down to Z=20 based on their LNPS Hamiltonian. Their $0f_{5/2} - 0g_{9/2}$ ESPE gap for ^{60}Ca is close to zero (see Fig. 1 in Ref. [89]) in contrast to the EDF gaps of about 3 MeV. As shown in

[90], the ESPE of the $0g_{9/2}$ has a strong influence on the structure of $^{56-60}$Ca that can be tested by experiment. Other previous theoretical work on the neutron-rich calcium isotopes using *ab initio* methods include [91–95].

5.5 Examining Sc and Ti isotopes using UFP-CA and Looking Forward

We now have a $T = 1$ interaction for the *fp*-shell model space, so let us try to extend our results into a full *fp*-shell model space. We can take the $T = 0$ interaction from GX1A and add on an *ab initio* Coulomb interaction to create a full *pn* formalism interaction.

The Coulomb interaction is chosen to be the analytical solution in a Harmonic Oscillator basis with short range correlations, as in USDC and USDI, but for the *fp*-shell rather than the *sd*-shell. Using this, we calculate the two-neutron separation energies for the scandium and titanium isotopes. This is motivated by the recent first direct mass measurements of the neutron-rich scandium and titanium isotopes around the neutron number 40 at the RIKEN RI Beam Factory [96]. Other recent experiments that have measured the scandium isotopes include [97, 98]. There is some disagreement in the mass excess of ^{57}Sc which causes changes in the S_2n in that region by around 1 MeV.

Given the appropriate choice of single particle energies for the protons, we would expect reasonable agreement with experiment for the scandium isotopes, with some breakdown in agreement for the titanium isotope due to pairing effects not captured in our interaction.

Fig. 5.5 shows these results, and they come out about as expected. The agreement with the results from [96] for the scandium ($Z = 21$) separation energies is within the experimental error out to $N = 39$, the heaviest measured isotope. The large gap between the calcium and scandium curves at $N = 35, 36$ is due to a spreading of the band of states that comes from coupling the $\pi 0 f_{7/2}$ (proton) with a $\nu 0 p_{1/2}$ (neutron). The centroid of this band of states may very well follow the same pattern as in calcium, but the ground state is lower than expected. We see a flattening of the separation energies at the top of the shell.

In titanium ($Z = 22$) the disagreements with experiment begin at $N = 35$ when the $0p_{1/2}$ orbit
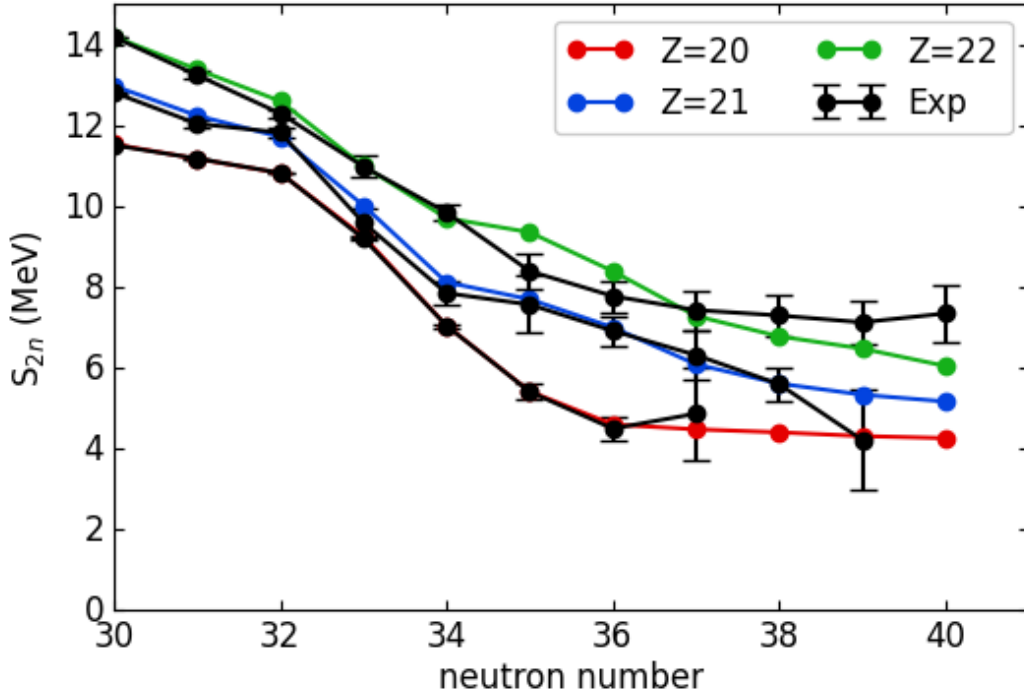
Figure 5.5: Experimental and calculated S_{2n} for the fp-shell Ca, Sc, and Ti isotopes.

becomes involved in the ground state configurations. This could be due to a measurement error. At the top of the shell, experiment is more heavily bound than our predictions. This is a typical signature of an "island of inversion" at $N = 40$ which we expect to occur in this region.

With sufficient computation power, this new full interaction for the fp-shell can also be refined in the same manner as USDC in Chapter 2. This large scale project is an exciting opportunity for future work in this area.

To further refine a shell model view of this isotopic chain, more experimental data involving the $0f_{5/2}$ and the $0g_{9/2}$ orbits is needed. This data will help to determine the validity of the closed shell approach for ^{60}Ca that we employed, and will lead the way into developing a phenomenological interaction in the $fpj4$ (fp for the protons and $jj44$ for the neutrons) model space that can produce dripline predictions out to ^{70}Ca.

This change relies on the assumption that the filled neutron $0f_{7/2}$ creates a good closed shell. This then allows us to include the $0g_{9/2}$ orbit whose energy difference to the $0f_{5/2}$ orbit in neutrons will greatly effect the structure of nuclei around ^{60}Ca. Using the FINCH (Fitting Isospin Non-

Conserving Hamiltonian) python code whose user manual is included in Appendix B, preliminary work has begun on this project.

CHAPTER 6

SUMMARIES

6.1 Chapter 1

This opening chapter serves as a foundation of knowledge from which the rest of this document builds. Starting with constructing the Nuclear Chart and giving a basic description of the nucleus, gradually more and more complex models are introduced and discussed. The Liquid Drop Model treats the nucleus as a liquid drop and uses five simple clear terms to describe the binding energies of nuclei across the entire nuclear chart. Predictions from this model are useful as a "sanity" check when looking at new results in later chapters.

A broad overview of the fundamentals of the Nuclear Shell Model is given. A realistic model of the nuclear potential is developed and used to recover the nuclear "magic" numbers observed in experiment. From here the *sd* model space is defined and discussed in preparation for Chapters 2-4 of this Thesis. As we will be discussing isobaric multiplets throughout the document, a primer on the Isobaric Multiplet Mass Equation is given. The final section of this chapter serves as a detailed description of the statistical methods, namely the Singular Value Decomposition method and its associated uncertainty quantification, used in the development of effective interactions.

6.2 Chapter 2

Here we cover the history of universal interactions in the *sd*-shell, and the development of isospin-breaking universal *sd*-shell Hamiltonians in proton-neutron formalism is detailed for the first time. The available experimental data now includes levels from proton-rich nuclei, greatly increasing the data set for constraining these interactions. The fitting procedure is broken down into three stages based on different levels of sensitivity for constraining the nuclear strong interaction with an isotensor term, and the Coulomb interaction. The isotensor strength can be determined precisely by fitting it to the c-coefficients of the IMME, and is modeled as a percent increase in the strength

of the *pn T* = 1 two-body matrix elements.

Four new "USD" type interactions are presented. These were developed by taking linear combinations of *ab initio* interaction parameters that define the natural basis of the parameter space and constraining them with the increased data set. The first of which is USDC based on the same renormalized G matrix *sd*-shell interaction (SDBA) [33]. Additionally, we derive USDI which is based on a set of In-Medium Similarity Renormalization Group (IMSRG) Hamiltonians [34, 35] that are nucleus-specific. USDC and USDI use a reasonable Coulomb interaction with no fitting of the Coulomb TBME, and result in an isotensor strength increase of 2.2% over the *nn* and *pp T* = 1 matrix elements.

USDCm and USDIm are modifications to these interactions that have had their Coulomb interaction constrained by a SVD fit to better reproduce the *b*-coefficients of the IMME. An apparent trade-off for this further fitting is a decrease in accuracy for calculating the *c*-coefficients of the IMME, as well as a decreased isotensor strenght of 0.8%. We therefore suggest the use of USDC and USDI for precise predictions of isospin mixing in low-lying states, and USDCm and USDIm for mirror energy differences. The update to the USDC interaction in Chapter 4 serves as functional replacement of the modified Coulomb interactions.

6.3   Chapter 3

The opening of this chapter introduces the concept of a Thomas-Ehrman Shift (TES) experienced by poorly bound valence protons. This effect is not fully incorporated into configuration-interaction theory, so a single-particle model based on a Skyrme interaction to determine the strength of this effect is developed and used in tandem with the new interactions. We see much improved agreement with several *sd*-shell states that have experimentally known large TES.

All four new interactions improve predictions for separation energies throughout the shell, eliminating the systematic over-estimation present in calculations using USDB-CD. This increases the utility of these new interactions, as for the first time reasonable decay Q values can be taken directly from theory and used in calculations. However, the calculated binding energies for the

neutron-rich Fluorine ($N = 16 - 19$) isotopes are significantly higher than the experimental values found in the 2016 Atomic Mass Evaluation. We suggest more precise experiments to lower the uncertainties on these measurements, and to correct or reaffirm the current experimental energies.

The development of these new "USD" Hamiltonians opens up new avenues to examine isospin mixing and other isospin symmetry breaking effects in the sd-shell. In this Chapter we also examine several cases of large isospin mixing in sulfur isotopes and in isobaric multiplets. Work in these areas has resulted in several publications in collaboration with experimental groups.

6.4 Chapter 4

During the development of the USDC interaction, the addition of an isovector term that would subtly split the nuclear strong force interaction strength in nn and pp pairs was explored. However, due to a lack of sufficiently constraining data this addition was not included in the final product. Instead, a secondary SVD of the Coulomb TBME was done to create modified interactions that better explained mirror energy differences in the shell.

Recently, a refinement to the USDC interaction was begun that would use "double" differences of mirror energies to attempt to extract the experimental strength of this isovector splitting. As was noticed in the c-coefficients, there is an oscillation of these double differences that is dependent primarily upon the charge-symmetry breaking of the nuclear strong force. Using this, we are able to extract a strength of 1.4% for the isovector term modeled as an increase in the nn interaction and a decrease in the pp interaction strengths. This results in an improved USDC interaction that replicates the advantages of the modified Coulomb interaction without its detriments.

6.5 Chapter 5

Following the many successful implementations of effective universal configuration-interaction Hamiltonians, we endeavored to produce a universal fp shell interaction tailored for the calcium isotopes which we call UFP-CA. Starting from a state-of-the-art IMSRG interaction, linear combinations of Hamiltonian parameters that define the natural basis of the parameter space are constrained

by the latest experimental data for the neutron-rich calcium isotopes. We show that this data-driven method for improving the Hamiltonian provides an excellent description of the known binding energies and spectra for the calcium isotopes within the *fp* model space.

We have presented UFP-CA, a new interaction tailored to the *fp* shell calcium isotopes, based on the best available experimental data. Using this we have provided extrapolated predictions out the ^{60}Ca and compared those results to experiment and other theoretical works. Our extrapolation along with comparisons to EDF calculations lead us to believe that ^{60}Ca is doubly-magic at a level similar to ^{68}Ni. Several predictions are presented for unobserved low lying excited states in $^{55-59}$Ca that will be accessible to future experiments.

APPENDICES

USDC LEVELS

Table A1: A table showing the experimental energy levels used to constrain the USDC interactions along with the USDC predictions. All energies in MeV.

Nucleus	T_z	J^π	J_i^π	Exp.	Error	USDC	ΔE
^{17}O	$\frac{1}{2}$	$\frac{5}{2}^+$	1	-131.762	0.000	-131.555	0.207
^{17}O	$\frac{1}{2}$	$\frac{1}{2}^+$	1	0.870	0.001	0.810	-0.060
^{17}O	$\frac{1}{2}$	$\frac{3}{2}^+$	1	5.083	0.500	5.790	0.707
^{18}O	1	0^+	1	-139.808	0.000	-139.613	0.195
^{18}O	1	2^+	1	1.982	0.001	2.048	0.066
^{18}O	1	4^+	1	3.555	0.001	3.563	0.008
^{18}O	1	3^+	1	5.378	0.001	5.541	0.163
^{19}O	$\frac{3}{2}$	$\frac{5}{2}^+$	1	-143.763	0.003	-143.626	0.137
^{19}O	$\frac{3}{2}$	$\frac{3}{2}^+$	1	0.096	0.001	0.165	0.069
^{19}O	$\frac{3}{2}$	$\frac{1}{2}^+$	1	1.472	0.001	1.585	0.113
^{19}O	$\frac{3}{2}$	$\frac{9}{2}^+$	1	2.372	0.001	2.394	0.022
^{19}O	$\frac{3}{2}$	$\frac{7}{2}^+$	1	2.779	0.001	2.927	0.148
^{19}O	$\frac{3}{2}$	$\frac{5}{2}^+$	2	3.154	0.001	3.340	0.186
^{19}O	$\frac{3}{2}$	$\frac{3}{2}^+$	3	5.455	0.001	5.858	0.403
^{20}O	2	0^+	1	-151.371	0.001	-151.329	0.042
^{20}O	2	2^+	1	1.674	0.001	1.796	0.122
^{20}O	2	4^+	1	3.570	0.007	3.657	0.087
^{20}O	2	2^+	2	4.072	0.004	4.206	0.134
^{20}O	2	0^+	2	5.387	0.001	5.494	0.107
^{21}O	$\frac{5}{2}$	$\frac{5}{2}^+$	1	-155.177	0.012	-155.070	0.107
^{21}O	$\frac{5}{2}$	$\frac{1}{2}^+$	1	1.220	0.001	1.358	0.138
^{21}O	$\frac{5}{2}$	$\frac{3}{2}^+$	1	2.133	0.001	2.029	-0.104
^{21}O	$\frac{5}{2}$	$\frac{5}{2}^+$	2	3.026	0.001	3.092	0.066
^{21}O	$\frac{5}{2}$	$\frac{7}{2}^+$	1	3.073	0.001	2.939	-0.134
^{21}O	$\frac{5}{2}$	$\frac{9}{2}^+$	1	4.927	0.001	4.819	-0.108
^{22}O	3	0^+	1	-162.027	0.057	-162.178	-0.151

Nucleus	T_z	J^π	J_i^π	Exp.	Error	USDC	ΔE
^{22}O	3	2^+	1	3.199	0.001	3.146	-0.053
^{22}O	3	3^+	1	4.584	0.001	4.807	0.223
^{22}O	3	0^+	2	4.909	0.001	4.796	-0.113
^{22}O	3	2^+	2	6.509	0.001	6.351	-0.158
^{22}O	3	4^+	1	6.936	0.001	6.752	-0.184
^{23}O	$\frac{7}{2}$	$\frac{1}{2}^+$	1	-164.760	0.122	-164.760	0.000
^{23}O	$\frac{7}{2}$	$\frac{5}{2}^+$	1	2.800	0.100	2.571	-0.229
^{24}O	4	0^+	1	-168.952	0.165	-168.964	-0.012
^{24}O	4	2^+	1	4.790	0.110	4.867	0.077
^{25}O	$\frac{9}{2}$	$\frac{3}{2}^+$	1	-168.195	0.000	-167.844	0.351
^{26}O	5	0^+	1	-168.934	0.000	-169.042	-0.108
^{17}F	$-\frac{1}{2}$	$\frac{5}{2}^+$	1	-128.220	0.000	-127.927	0.293
^{18}F	0	1^+	1	-137.369	0.001	-137.422	-0.053
^{18}F	0	3^+	1	0.937	0.001	0.950	0.013
^{18}F	0	0^+	1	1.042	0.001	1.270	0.228
^{18}F	0	5^+	1	1.121	0.001	1.197	0.076
^{18}F	0	2^+	1	3.062	0.001	3.359	0.297
^{18}F	0	1^+	2	3.724	0.001	3.673	-0.051
^{18}F	0	4^+	1	4.652	0.001	4.974	0.322
^{19}F	$\frac{1}{2}$	$\frac{1}{2}^+$	1	-147.801	0.000	-147.930	-0.129
^{19}F	$\frac{1}{2}$	$\frac{5}{2}^+$	1	0.197	0.001	0.049	-0.148
^{19}F	$\frac{1}{2}$	$\frac{3}{2}^+$	1	1.554	0.001	1.748	0.194
^{19}F	$\frac{1}{2}$	$\frac{9}{2}^+$	1	2.779	0.001	2.603	-0.176
^{19}F	$\frac{1}{2}$	$\frac{13}{2}^+$	1	4.647	0.001	4.590	-0.057
^{19}F	$\frac{1}{2}$	$\frac{5}{2}^+$	2	5.106	0.001	4.972	-0.134
^{19}F	$\frac{1}{2}$	$\frac{1}{2}^+$	2	6.255	0.001	6.291	0.036
^{19}F	$\frac{1}{2}$	$\frac{11}{2}^+$	1	6.500	0.001	6.684	0.184
^{19}F	$\frac{1}{2}$	$\frac{11}{2}^+$	2	7.937	0.001	7.939	0.002
^{19}F	$\frac{1}{2}$	$\frac{13}{2}^+$	2	10.411	0.001	10.219	-0.192
^{20}F	1	2^+	1	-154.403	0.000	-154.587	-0.184
^{20}F	1	3^+	1	0.656	0.001	0.619	-0.037

Nucleus	T_z	J^π	J_i^π	Exp.	Error	USDC	ΔE
^{20}F	1	4^+	1	0.822	0.001	0.823	0.001
^{20}F	1	1^+	1	1.057	0.001	1.135	0.078
^{20}F	1	5^+	1	1.823	0.001	1.782	-0.041
^{20}F	1	2^+	2	2.044	0.001	2.273	0.229
^{20}F	1	3^+	2	2.194	0.001	2.402	0.208
^{20}F	1	3^+	3	2.966	0.001	2.886	-0.080
^{20}F	1	1^+	2	3.488	0.001	3.485	-0.003
^{20}F	1	0^+	2	6.512	0.005	6.753	0.241
^{21}F	$\frac{3}{2}$	$\frac{5}{2}^+$	1	-162.504	0.002	-162.660	-0.156
^{21}F	$\frac{3}{2}$	$\frac{1}{2}^+$	1	0.280	0.001	0.323	0.043
^{21}F	$\frac{3}{2}$	$\frac{3}{2}^+$	1	1.730	0.001	1.821	0.091
^{21}F	$\frac{3}{2}$	$\frac{9}{2}^+$	1	1.755	0.001	1.784	0.029
^{22}F	2	4^+	1	-167.734	0.012	-167.797	-0.063
^{22}F	2	3^+	1	0.072	0.001	0.186	0.114
^{22}F	2	2^+	1	0.710	0.001	0.785	0.075
^{22}F	2	5^+	1	1.414	0.001	1.385	-0.029
^{22}F	2	1^+	1	1.625	0.001	1.519	-0.106
^{22}F	2	2^+	2	2.006	0.001	2.008	0.002
^{22}F	2	1^+	2	2.572	0.001	2.433	-0.139
^{23}F	$\frac{5}{2}$	$\frac{5}{2}^+$	1	-175.314	0.033	-175.354	-0.040
^{23}F	$\frac{5}{2}$	$\frac{7}{2}^+$	1	2.920	0.001	2.773	-0.147
^{24}F	3	3^+	1	-179.126	0.098	-179.005	0.121
^{24}F	3	2^+	1	0.521	0.001	0.577	0.056
^{24}F	3	1^+	1	1.831	0.001	1.405	-0.426
^{25}F	$\frac{7}{2}$	$\frac{5}{2}^+$	1	-183.408	0.096	-183.755	-0.347
^{25}F	$\frac{7}{2}$	$\frac{9}{2}^+$	1	3.916	0.001	3.672	-0.244
^{26}F	4	1^+	1	-184.164	0.111	-184.614	-0.450
^{26}F	4	4^+	1	0.643	0.001	0.354	-0.289
^{26}F	4	2^+	1	0.657	0.007	0.615	-0.042
^{27}F	$\frac{9}{2}$	$\frac{5}{2}^+$	1	-185.434	0.390	-186.722	-1.288
^{28}F	5	3^+	1	-185.214	0.393	-185.968	-0.754

Table A1: (cont'd)

Nucleus	T_z	J^π	J_i^π	Exp.	Error	USDC	ΔE
^{29}F	$\frac{11}{2}$	$\frac{5}{2}^+$	1	-186.877	0.525	-187.032	-0.155
^{18}Ne	-1	0^+	1	-132.143	0.000	-131.982	0.161
^{18}Ne	-1	2^+	1	1.887	0.001	1.991	0.104
^{18}Ne	-1	4^+	1	3.376	0.001	3.575	0.199
^{19}Ne	$-\frac{1}{2}$	$\frac{1}{2}^+$	1	-143.780	0.000	-143.945	-0.165
^{19}Ne	$-\frac{1}{2}$	$\frac{5}{2}^+$	1	0.238	0.001	0.082	-0.156
^{19}Ne	$-\frac{1}{2}$	$\frac{3}{2}^+$	1	1.536	0.001	1.823	0.287
^{19}Ne	$-\frac{1}{2}$	$\frac{9}{2}^+$	1	2.795	0.001	2.598	-0.197
^{19}Ne	$-\frac{1}{2}$	$\frac{13}{2}^+$	1	4.635	0.001	4.609	-0.026
^{19}Ne	$-\frac{1}{2}$	$\frac{5}{2}^+$	2	5.092	0.006	4.981	-0.111
^{20}Ne	0	0^+	1	-160.645	0.000	-160.576	0.069
^{20}Ne	0	2^+	1	1.634	0.001	1.731	0.097
^{20}Ne	0	4^+	1	4.248	0.001	4.154	-0.094
^{20}Ne	0	0^+	2	6.724	0.001	6.748	0.024
^{20}Ne	0	2^+	2	7.422	0.001	7.537	0.115
^{20}Ne	0	2^+	3	10.273	0.001	10.014	-0.259
^{20}Ne	0	6^+	1	8.777	0.001	8.496	-0.281
^{20}Ne	0	3^+	1	9.873	0.001	10.414	0.541
^{20}Ne	0	3^+	2	10.884	0.001	10.588	-0.296
^{20}Ne	0	8^+	1	11.951	0.001	11.521	-0.430
^{20}Ne	0	6^+	2	12.585	0.001	12.777	0.192
^{20}Ne	0	8^+	2	15.874	0.001	15.970	0.096
^{21}Ne	$\frac{1}{2}$	$\frac{3}{2}^+$	1	-167.406	0.000	-167.377	0.029
^{21}Ne	$\frac{1}{2}$	$\frac{5}{2}^+$	1	0.351	0.001	0.283	-0.068
^{21}Ne	$\frac{1}{2}$	$\frac{7}{2}^+$	1	1.746	0.001	1.776	0.030
^{21}Ne	$\frac{1}{2}$	$\frac{1}{2}^+$	1	2.796	0.001	2.913	0.117
^{21}Ne	$\frac{1}{2}$	$\frac{9}{2}^+$	1	2.866	0.001	2.836	-0.030
^{21}Ne	$\frac{1}{2}$	$\frac{5}{2}^+$	2	3.734	0.001	3.739	0.005
^{21}Ne	$\frac{1}{2}$	$\frac{11}{2}^+$	1	4.432	0.001	4.394	-0.038
^{21}Ne	$\frac{1}{2}$	$\frac{5}{2}^+$	3	4.524	0.001	4.646	0.122
^{21}Ne	$\frac{1}{2}$	$\frac{3}{2}^+$	2	4.684	0.001	4.945	0.261

Table A1: (cont'd)

Nucleus	T_z	J^π	J_i^π	Exp.	Error	USDC	ΔE
^{21}Ne	$\frac{1}{2}$	$\frac{7}{2}^+$	2	5.430	0.001	5.405	-0.025
^{21}Ne	$\frac{1}{2}$	$\frac{3}{2}^+$	3	5.549	0.001	5.563	0.014
^{21}Ne	$\frac{1}{2}$	$\frac{9}{2}^+$	2	6.265	0.001	6.138	-0.127
^{21}Ne	$\frac{1}{2}$	$\frac{13}{2}^+$	1	6.447	0.001	6.212	-0.235
^{21}Ne	$\frac{1}{2}$	$\frac{1}{2}^+$	3	7.212	0.001	7.106	-0.106
^{22}Ne	1	0^+	1	-177.770	0.000	-177.733	0.037
^{22}Ne	1	2^+	1	1.275	0.001	1.357	0.082
^{22}Ne	1	4^+	1	3.357	0.001	3.353	-0.004
^{22}Ne	1	2^+	2	4.457	0.001	4.298	-0.159
^{22}Ne	1	1^+	1	5.329	0.001	5.384	0.055
^{22}Ne	1	2^+	3	5.365	0.001	5.116	-0.249
^{22}Ne	1	4^+	2	5.523	0.001	5.408	-0.115
^{22}Ne	1	3^+	1	5.641	0.001	5.492	-0.149
^{22}Ne	1	2^+	4	6.119	0.001	6.189	0.070
^{22}Ne	1	0^+	2	6.237	0.001	6.216	-0.021
^{22}Ne	1	6^+	1	6.311	0.001	6.267	-0.044
^{22}Ne	1	4^+	3	6.345	0.001	6.320	-0.025
^{22}Ne	1	2^+	5	6.817	0.001	6.602	-0.215
^{22}Ne	1	1^+	2	6.854	0.001	6.546	-0.308
^{22}Ne	1	0^+	3	7.341	0.001	7.460	0.119
^{23}Ne	$\frac{3}{2}$	$\frac{5}{2}^+$	1	-182.971	0.000	-182.918	0.053
^{23}Ne	$\frac{3}{2}$	$\frac{1}{2}^+$	1	1.017	0.001	1.035	0.018
^{23}Ne	$\frac{3}{2}$	$\frac{7}{2}^+$	1	1.701	0.001	1.788	0.087
^{23}Ne	$\frac{3}{2}$	$\frac{3}{2}^+$	1	1.822	0.001	1.845	0.023
^{23}Ne	$\frac{3}{2}$	$\frac{5}{2}^+$	2	2.315	0.001	2.284	-0.031
^{23}Ne	$\frac{3}{2}$	$\frac{9}{2}^+$	1	2.517	0.001	2.449	-0.068
^{23}Ne	$\frac{3}{2}$	$\frac{3}{2}^+$	2	3.432	0.001	3.241	-0.191
^{24}Ne	2	0^+	1	-191.840	0.001	-191.860	-0.020
^{24}Ne	2	2^+	1	1.981	0.001	2.094	0.113
^{24}Ne	2	2^+	2	3.871	0.001	3.688	-0.183
^{24}Ne	2	4^+	1	3.962	0.001	3.933	-0.029

Nucleus	T_z	J^π	J_i^π	Exp.	Error	USDC	ΔE
^{24}Ne	2	0^+	2	4.765	0.001	4.893	0.128
^{24}Ne	2	3^+	1	4.886	0.001	4.787	-0.099
^{25}Ne	$\frac{5}{2}$	$\frac{1}{2}^+$	1	-195.995	0.029	-195.961	0.034
^{26}Ne	3	0^+	1	-201.550	0.018	-201.787	-0.237
^{26}Ne	3	2^+	1	2.018	0.001	2.011	-0.007
^{27}Ne	$\frac{7}{2}$	$\frac{3}{2}^+$	1	-203.051	0.091	-203.135	-0.084
^{28}Ne	4	0^+	1	-206.874	0.126	-206.869	0.005
^{19}Na	$-\frac{3}{2}$	$\frac{5}{2}^+$	1	-131.820	0.011	-131.570	0.250
^{19}Na	$-\frac{3}{2}$	$\frac{3}{2}^+$	1	0.120	0.010	0.136	0.016
^{20}Na	-1	2^+	1	-145.970	0.001	-146.124	-0.154
^{20}Na	-1	3^+	1	0.596	0.008	0.559	-0.037
^{20}Na	-1	4^+	1	0.802	0.007	0.779	-0.023
^{20}Na	-1	1^+	1	0.984	0.001	1.127	0.143
^{20}Na	-1	3^+	2	2.057	0.012	2.329	0.272
^{20}Na	-1	3^+	3	2.645	0.006	2.730	0.085
^{20}Na	-1	0^+	2	6.534	0.013	6.727	0.193
^{21}Na	$-\frac{1}{2}$	$\frac{3}{2}^+$	1	-163.076	0.000	-162.952	0.124
^{21}Na	$-\frac{1}{2}$	$\frac{5}{2}^+$	1	0.332	0.000	0.265	-0.067
^{21}Na	$-\frac{1}{2}$	$\frac{7}{2}^+$	1	1.716	0.000	1.758	0.042
^{21}Na	$-\frac{1}{2}$	$\frac{1}{2}^+$	1	2.424	0.000	2.666	0.242
^{21}Na	$-\frac{1}{2}$	$\frac{9}{2}^+$	1	2.829	0.000	2.774	-0.055
^{21}Na	$-\frac{1}{2}$	$\frac{5}{2}^+$	2	3.544	0.000	3.617	0.073
^{21}Na	$-\frac{1}{2}$	$\frac{5}{2}^+$	3	4.294	0.000	4.516	0.222
^{21}Na	$-\frac{1}{2}$	$\frac{11}{2}^+$	1	4.419	0.002	4.348	-0.071
^{21}Na	$-\frac{1}{2}$	$\frac{3}{2}^+$	2	4.468	0.000	4.847	0.379
^{22}Na	0	3^+	1	-174.145	0.000	-174.168	-0.023
^{22}Na	0	1^+	1	0.583	0.001	0.315	-0.268
^{22}Na	0	0^+	1	0.657	0.001	0.741	0.084
^{22}Na	0	4^+	1	0.891	0.001	0.930	0.039
^{22}Na	0	5^+	1	1.528	0.001	1.501	-0.027
^{22}Na	0	1^+	2	1.937	0.001	2.101	0.164

Nucleus	T_z	J^π	J_i^π	Exp.	Error	USDC	ΔE
^{22}Na	0	2^+	1	1.952	0.001	2.128	0.176
^{22}Na	0	3^+	2	1.984	0.001	1.856	-0.128
^{22}Na	0	3^+	3	2.969	0.001	2.950	-0.019
^{22}Na	0	2^+	2	3.060	0.001	3.229	0.169
^{22}Na	0	6^+	1	3.707	0.001	3.773	0.066
^{22}Na	0	1^+	3	3.944	0.001	4.095	0.151
^{22}Na	0	4^+	2	4.071	0.001	4.153	0.082
^{22}Na	0	2^+	3	4.360	0.001	3.977	-0.383
^{22}Na	0	7^+	1	4.524	0.001	4.478	-0.046
^{22}Na	0	5^+	2	4.710	0.001	4.564	-0.146
^{22}Na	0	3^+	4	4.771	0.001	4.630	-0.141
^{22}Na	0	4^+	3	5.101	0.001	5.084	-0.017
^{23}Na	$\frac{1}{2}$	$\frac{3}{2}^+$	1	-186.564	0.000	-186.573	-0.009
^{23}Na	$\frac{1}{2}$	$\frac{5}{2}^+$	1	0.439	0.001	0.407	-0.032
^{23}Na	$\frac{1}{2}$	$\frac{7}{2}^+$	1	2.076	0.001	2.175	0.099
^{23}Na	$\frac{1}{2}$	$\frac{1}{2}^+$	1	2.390	0.001	2.191	-0.199
^{23}Na	$\frac{1}{2}$	$\frac{9}{2}^+$	1	2.703	0.001	2.771	0.068
^{23}Na	$\frac{1}{2}$	$\frac{3}{2}^+$	2	2.982	0.001	2.778	-0.204
^{23}Na	$\frac{1}{2}$	$\frac{5}{2}^+$	2	3.914	0.001	3.747	-0.167
^{23}Na	$\frac{1}{2}$	$\frac{1}{2}^+$	2	4.429	0.001	4.395	-0.034
^{23}Na	$\frac{1}{2}$	$\frac{7}{2}^+$	2	4.774	0.001	4.731	-0.043
^{23}Na	$\frac{1}{2}$	$\frac{5}{2}^+$	3	5.378	0.001	5.320	-0.058
^{23}Na	$\frac{1}{2}$	$\frac{11}{2}^+$	1	5.534	0.001	5.564	0.030
^{23}Na	$\frac{1}{2}$	$\frac{5}{2}^+$	4	5.741	0.001	5.753	0.012
^{23}Na	$\frac{1}{2}$	$\frac{3}{2}^+$	3	5.766	0.001	5.834	0.068
^{23}Na	$\frac{1}{2}$	$\frac{1}{2}^+$	3	6.307	0.001	6.307	0.000
^{24}Na	1	4^+	1	-193.524	0.000	-193.515	0.009
^{24}Na	1	1^+	1	0.472	0.001	0.549	0.077
^{24}Na	1	2^+	1	0.563	0.001	0.645	0.082
^{24}Na	1	2^+	2	1.341	0.001	1.051	-0.290
^{24}Na	1	3^+	1	1.344	0.001	1.372	0.028

Nucleus	T_z	J^π	J_i^π	Exp.	Error	USDC	ΔE
^{24}Na	1	1^+	2	1.346	0.001	1.300	-0.046
^{24}Na	1	5^+	1	1.512	0.001	1.552	0.040
^{24}Na	1	2^+	3	1.846	0.001	1.790	-0.056
^{24}Na	1	3^+	2	1.885	0.001	1.778	-0.107
^{24}Na	1	3^+	3	2.513	0.001	2.288	-0.225
^{24}Na	1	3^+	4	2.904	0.001	2.653	-0.251
^{24}Na	1	1^+	3	3.413	0.001	3.331	-0.082
^{24}Na	1	1^+	4	3.589	0.001	3.619	0.030
^{24}Na	1	3^+	5	3.628	0.001	3.469	-0.159
^{24}Na	1	0^+	1	3.682	0.001	3.515	-0.167
^{25}Na	$\frac{3}{2}$	$\frac{5}{2}^+$	1	-202.535	0.001	-202.542	-0.007
^{25}Na	$\frac{3}{2}$	$\frac{3}{2}^+$	1	0.089	0.001	0.115	0.026
^{25}Na	$\frac{3}{2}$	$\frac{1}{2}^+$	1	1.069	0.001	0.958	-0.111
^{25}Na	$\frac{3}{2}$	$\frac{3}{2}^+$	2	2.202	0.001	1.980	-0.222
^{26}Na	2	3^+	1	-208.109	0.004	-208.046	0.063
^{26}Na	2	1^+	1	0.082	0.001	0.014	-0.068
^{26}Na	2	2^+	1	0.233	0.001	0.084	-0.149
^{27}Na	$\frac{5}{2}$	$\frac{5}{2}^+$	1	-214.838	0.004	-215.078	-0.240
^{27}Na	$\frac{5}{2}$	$\frac{3}{2}^+$	1	0.062	0.001	0.007	-0.055
^{27}Na	$\frac{5}{2}$	$\frac{1}{2}^+$	1	1.728	0.001	1.574	-0.154
^{27}Na	$\frac{5}{2}$	$\frac{7}{2}^+$	1	2.191	0.001	2.302	0.111
^{27}Na	$\frac{5}{2}$	$\frac{9}{2}^+$	1	2.224	0.001	2.198	-0.026
^{27}Na	$\frac{5}{2}$	$\frac{5}{2}^+$	2	2.799	0.001	2.939	0.140
^{27}Na	$\frac{5}{2}$	$\frac{3}{2}^+$	2	3.019	0.001	3.193	0.174
^{28}Na	3	1^+	1	-218.379	0.010	-218.384	-0.005
^{28}Na	3	2^+	1	0.055	0.001	-0.091	-0.146
^{28}Na	3	1^+	2	2.118	0.001	1.932	-0.186
^{28}Na	3	1^+	3	2.714	0.001	2.439	-0.275
^{29}Na	$\frac{7}{2}$	$\frac{3}{2}^+$	1	-222.782	0.007	-222.931	-0.149
^{29}Na	$\frac{7}{2}$	$\frac{5}{2}^+$	1	0.072	0.001	-0.074	-0.146
^{20}Mg	-2	0^+	1	-134.560	0.002	-134.454	0.106

Table A1: (cont'd)

Nucleus	T_z	J^π	J_i^π	Exp.	Error	USDC	ΔE
^{20}Mg	-2	2^+	1	1.598	0.010	1.756	0.158
^{21}Mg	$-\frac{3}{2}$	$\frac{5}{2}^+$	1	-149.206	0.001	-149.416	-0.210
^{21}Mg	$-\frac{3}{2}$	$\frac{1}{2}^+$	1	0.201	0.004	0.346	0.145
^{21}Mg	$-\frac{3}{2}$	$\frac{3}{2}^+$	1	1.651	0.004	1.802	0.151
^{22}Mg	-1	0^+	1	-168.581	0.000	-168.520	0.061
^{22}Mg	-1	2^+	1	1.247	0.000	1.355	0.108
^{22}Mg	-1	4^+	1	3.308	0.000	3.338	0.030
^{22}Mg	-1	2^+	2	4.402	0.000	4.220	-0.182
^{22}Mg	-1	2^+	3	5.035	0.001	4.986	-0.049
^{22}Mg	-1	1^+	1	5.089	0.001	5.351	0.262
^{22}Mg	-1	3^+	1	5.452	0.000	5.353	-0.099
^{22}Mg	-1	6^+	1	6.254	0.001	6.178	-0.076
^{22}Mg	-1	4^+	3	6.313	0.005	6.183	-0.130
^{23}Mg	$-\frac{1}{2}$	$\frac{3}{2}^+$	1	-181.726	0.000	-181.768	-0.042
^{23}Mg	$-\frac{1}{2}$	$\frac{5}{2}^+$	1	0.451	0.000	0.395	-0.056
^{23}Mg	$-\frac{1}{2}$	$\frac{7}{2}^+$	1	2.052	0.000	2.157	0.105
^{23}Mg	$-\frac{1}{2}$	$\frac{1}{2}^+$	1	2.359	0.001	2.163	-0.196
^{23}Mg	$-\frac{1}{2}$	$\frac{9}{2}^+$	1	2.715	0.001	2.731	0.016
^{23}Mg	$-\frac{1}{2}$	$\frac{3}{2}^+$	2	2.908	0.002	2.771	-0.137
^{23}Mg	$-\frac{1}{2}$	$\frac{5}{2}^+$	2	3.864	0.005	3.737	-0.127
^{23}Mg	$-\frac{1}{2}$	$\frac{1}{2}^+$	2	4.353	0.006	4.404	0.051
^{23}Mg	$-\frac{1}{2}$	$\frac{13}{2}^+$	1	6.191	0.006	6.170	-0.021
^{24}Mg	0	0^+	1	-198.257	0.000	-198.221	0.036
^{24}Mg	0	2^+	1	1.369	0.001	1.496	0.127
^{24}Mg	0	4^+	1	4.123	0.001	4.372	0.249
^{24}Mg	0	2^+	2	4.238	0.001	4.082	-0.156
^{24}Mg	0	3^+	1	5.236	0.001	5.042	-0.194
^{24}Mg	0	4^+	2	6.010	0.001	5.892	-0.118
^{24}Mg	0	2^+	3	7.348	0.001	7.512	0.164
^{24}Mg	0	1^+	1	7.747	0.001	7.780	0.033
^{24}Mg	0	5^+	1	7.812	0.001	7.809	-0.003

Table A1: (cont'd)

Nucleus	T_z	J^π	J_i^π	Exp.	Error	USDC	ΔE
^{24}Mg	0	6^+	1	8.113	0.001	8.267	0.154
^{24}Mg	0	4^+	3	8.437	0.001	8.356	-0.081
^{24}Mg	0	4^+	4	9.298	0.001	9.451	0.153
^{24}Mg	0	6^+	2	9.528	0.001	9.560	0.032
^{24}Mg	0	1^+	2	9.827	0.001	9.764	-0.063
^{24}Mg	0	5^+	2	10.575	0.001	10.494	-0.081
^{24}Mg	0	8^+	1	11.860	0.001	11.787	-0.073
^{24}Mg	0	6^+	3	12.000	0.001	11.681	-0.319
^{24}Mg	0	8^+	2	13.210	0.001	13.217	0.007
^{24}Mg	0	8^+	3	14.152	0.001	14.071	-0.081
^{24}Mg	0	10^+	1	19.200	0.100	18.846	-0.354
^{25}Mg	$\frac{1}{2}$	$\frac{5}{2}^+$	1	-205.588	0.000	-205.519	0.069
^{25}Mg	$\frac{1}{2}$	$\frac{1}{2}^+$	1	0.585	0.001	0.616	0.031
^{25}Mg	$\frac{1}{2}$	$\frac{3}{2}^+$	1	0.975	0.001	1.069	0.094
^{25}Mg	$\frac{1}{2}$	$\frac{7}{2}^+$	1	1.611	0.001	1.707	0.096
^{25}Mg	$\frac{1}{2}$	$\frac{5}{2}^+$	2	1.964	0.001	2.019	0.055
^{25}Mg	$\frac{1}{2}$	$\frac{1}{2}^+$	2	2.564	0.001	2.641	0.077
^{25}Mg	$\frac{1}{2}$	$\frac{7}{2}^+$	2	2.737	0.001	2.875	0.138
^{25}Mg	$\frac{1}{2}$	$\frac{3}{2}^+$	2	2.801	0.001	2.856	0.055
^{25}Mg	$\frac{1}{2}$	$\frac{9}{2}^+$	1	3.405	0.001	3.439	0.034
^{25}Mg	$\frac{1}{2}$	$\frac{5}{2}^+$	3	3.907	0.001	3.992	0.085
^{25}Mg	$\frac{1}{2}$	$\frac{9}{2}^+$	2	4.059	0.001	3.871	-0.188
^{25}Mg	$\frac{1}{2}$	$\frac{3}{2}^+$	3	4.359	0.001	4.334	-0.025
^{25}Mg	$\frac{1}{2}$	$\frac{9}{2}^+$	3	4.711	0.001	4.730	0.019
^{25}Mg	$\frac{1}{2}$	$\frac{7}{2}^+$	3	5.012	0.001	4.932	-0.080
^{25}Mg	$\frac{1}{2}$	$\frac{11}{2}^+$	1	5.251	0.001	5.106	-0.145
^{25}Mg	$\frac{1}{2}$	$\frac{13}{2}^+$	1	5.460	0.001	5.402	-0.058
^{25}Mg	$\frac{1}{2}$	$\frac{1}{2}^+$	3	5.475	0.001	5.288	-0.187
^{26}Mg	1	0^+	1	-216.681	0.000	-216.655	0.026
^{26}Mg	1	2^+	1	1.808	0.001	1.871	0.063
^{26}Mg	1	2^+	2	2.938	0.001	2.998	0.060

Table A1: (cont'd)

Nucleus	T_z	J^π	J_i^π	Exp.	Error	USDC	ΔE
^{26}Mg	1	0^+	2	3.588	0.001	3.562	-0.026
^{26}Mg	1	3^+	1	3.941	0.001	3.944	0.003
^{26}Mg	1	4^+	1	4.318	0.001	4.342	0.024
^{26}Mg	1	2^+	3	4.332	0.001	4.389	0.057
^{26}Mg	1	3^+	2	4.350	0.001	4.285	-0.065
^{26}Mg	1	2^+	4	4.835	0.001	4.825	-0.010
^{26}Mg	1	4^+	2	4.901	0.001	4.902	0.001
^{26}Mg	1	0^+	3	4.972	0.001	4.985	0.013
^{26}Mg	1	2^+	5	5.291	0.001	5.479	0.188
^{26}Mg	1	4^+	3	5.476	0.001	5.513	0.037
^{26}Mg	1	1^+	1	5.691	0.001	5.699	0.008
^{26}Mg	1	4^+	4	5.715	0.001	5.849	0.134
^{26}Mg	1	3^+	3	6.125	0.001	6.194	0.069
^{26}Mg	1	0^+	4	6.256	0.001	6.162	-0.094
^{26}Mg	1	4^+	5	6.622	0.001	6.672	0.050
^{26}Mg	1	5^+	1	6.978	0.001	7.054	0.076
^{26}Mg	1	2^+	7	7.099	0.001	6.870	-0.229
^{26}Mg	1	5^+	2	7.395	0.001	7.340	-0.055
^{26}Mg	1	6^+	1	8.201	0.001	8.085	-0.116
^{26}Mg	1	6^+	2	8.472	0.001	8.407	-0.065
^{27}Mg	$\frac{3}{2}$	$\frac{1}{2}^+$	1	-223.124	0.000	-222.992	0.132
^{27}Mg	$\frac{3}{2}$	$\frac{3}{2}^+$	1	0.985	0.001	0.988	0.003
^{27}Mg	$\frac{3}{2}$	$\frac{5}{2}^+$	1	1.698	0.001	1.645	-0.053
^{27}Mg	$\frac{3}{2}$	$\frac{5}{2}^+$	2	1.940	0.001	1.884	-0.056
^{27}Mg	$\frac{3}{2}$	$\frac{7}{2}^+$	1	3.109	0.001	3.027	-0.082
^{27}Mg	$\frac{3}{2}$	$\frac{1}{2}^+$	2	3.476	0.001	3.443	-0.033
^{27}Mg	$\frac{3}{2}$	$\frac{9}{2}^+$	1	3.884	0.001	3.930	0.046
^{27}Mg	$\frac{3}{2}$	$\frac{1}{2}^+$	3	5.028	0.001	4.946	-0.082
^{28}Mg	2	0^+	1	-231.628	0.002	-231.612	0.016
^{28}Mg	2	2^+	1	1.473	0.001	1.509	0.036
^{28}Mg	2	0^+	2	3.863	0.001	3.988	0.125

Nucleus	T_z	J^π	J_i^π	Exp.	Error	USDC	ΔE
^{28}Mg	2	4^+	1	4.020	0.001	4.131	0.111
^{28}Mg	2	2^+	2	4.557	0.001	4.515	-0.042
^{28}Mg	2	1^+	1	4.560	0.001	4.677	0.117
^{28}Mg	2	2^+	3	4.878	0.001	4.752	-0.126
^{29}Mg	$\frac{5}{2}$	$\frac{3}{2}^+$	1	-235.283	0.011	-235.173	0.110
^{29}Mg	$\frac{5}{2}$	$\frac{1}{2}^+$	1	0.054	0.001	0.014	-0.040
^{29}Mg	$\frac{5}{2}$	$\frac{5}{2}^+$	1	1.638	0.001	1.511	-0.127
^{29}Mg	$\frac{5}{2}$	$\frac{3}{2}^+$	2	2.500	0.001	2.222	-0.278
^{29}Mg	$\frac{5}{2}$	$\frac{1}{2}^+$	2	2.615	0.001	2.599	-0.016
^{29}Mg	$\frac{5}{2}$	$\frac{3}{2}^+$	3	3.224	0.001	3.486	0.262
^{30}Mg	3	0^+	1	-241.635	0.003	-241.591	0.044
^{30}Mg	3	2^+	1	1.482	0.001	1.554	0.072
^{23}Al	$-\frac{3}{2}$	$\frac{5}{2}^+$	1	-168.722	0.000	-168.637	0.085
^{23}Al	$-\frac{3}{2}$	$\frac{3}{2}^+$	1	1.773	0.035	1.712	-0.061
^{24}Al	-1	4^+	1	-183.590	0.000	-183.634	-0.044
^{24}Al	-1	1^+	1	0.426	0.000	0.549	0.123
^{24}Al	-1	2^+	1	0.511	0.004	0.587	0.076
^{25}Al	$-\frac{1}{2}$	$\frac{5}{2}^+$	1	-200.528	0.000	-200.439	0.089
^{25}Al	$-\frac{1}{2}$	$\frac{1}{2}^+$	1	0.452	0.001	0.502	0.050
^{25}Al	$-\frac{1}{2}$	$\frac{3}{2}^+$	1	0.945	0.001	1.014	0.069
^{25}Al	$-\frac{1}{2}$	$\frac{7}{2}^+$	1	1.613	0.001	1.722	0.109
^{25}Al	$-\frac{1}{2}$	$\frac{5}{2}^+$	2	1.790	0.001	1.889	0.099
^{25}Al	$-\frac{1}{2}$	$\frac{1}{2}^+$	2	2.485	0.001	2.562	0.077
^{25}Al	$-\frac{1}{2}$	$\frac{3}{2}^+$	2	2.673	0.001	2.763	0.090
^{25}Al	$-\frac{1}{2}$	$\frac{7}{2}^+$	2	2.720	0.001	2.825	0.105
^{25}Al	$-\frac{1}{2}$	$\frac{9}{2}^+$	1	3.424	0.001	3.446	0.022
^{25}Al	$-\frac{1}{2}$	$\frac{5}{2}^+$	3	3.859	0.001	3.958	0.099
^{25}Al	$-\frac{1}{2}$	$\frac{9}{2}^+$	2	4.026	0.002	3.900	-0.126
^{25}Al	$-\frac{1}{2}$	$\frac{3}{2}^+$	3	4.192	0.004	4.257	0.065
^{25}Al	$-\frac{1}{2}$	$\frac{9}{2}^+$	3	4.516	0.005	4.586	0.070
^{25}Al	$-\frac{1}{2}$	$\frac{5}{2}^+$	4	4.582	0.002	4.667	0.085

Table A1: (cont'd)

Nucleus	T_z	J^π	J_i^π	Exp.	Error	USDC	ΔE
^{25}Al	$-\frac{1}{2}$	$\frac{7}{2}^+$	3	4.906	0.004	4.860	-0.046
^{26}Al	0	5^+	1	-211.894	0.000	-211.846	0.048
^{26}Al	0	0^+	1	0.228	0.000	0.140	-0.088
^{26}Al	0	3^+	1	0.416	0.001	0.523	0.107
^{26}Al	0	1^+	1	1.058	0.001	1.140	0.082
^{26}Al	0	2^+	1	1.759	0.001	1.609	-0.150
^{26}Al	0	1^+	2	1.850	0.001	1.752	-0.098
^{26}Al	0	4^+	1	2.068	0.001	2.109	0.041
^{26}Al	0	2^+	2	2.069	0.001	2.050	-0.019
^{26}Al	0	1^+	3	2.072	0.001	2.046	-0.026
^{26}Al	0	3^+	2	2.365	0.001	2.232	-0.133
^{26}Al	0	3^+	3	2.545	0.001	2.431	-0.114
^{26}Al	0	2^+	3	2.660	0.001	2.510	-0.150
^{26}Al	0	1^+	4	2.739	0.001	2.789	0.050
^{26}Al	0	2^+	4	2.913	0.001	2.915	0.002
^{26}Al	0	3^+	4	3.073	0.001	3.093	0.020
^{26}Al	0	2^+	5	3.160	0.001	3.174	0.014
^{26}Al	0	5^+	2	3.403	0.001	3.410	0.007
^{26}Al	0	6^+	1	3.507	0.001	3.423	-0.084
^{26}Al	0	3^+	5	3.596	0.001	3.509	-0.087
^{26}Al	0	4^+	2	3.674	0.001	3.543	-0.131
^{26}Al	0	3^+	6	3.680	0.001	3.614	-0.066
^{26}Al	0	1^+	5	3.723	0.001	3.595	-0.128
^{26}Al	0	2^+	6	3.750	0.001	3.820	0.070
^{26}Al	0	0^+	2	3.754	0.001	3.722	-0.032
^{26}Al	0	4^+	3	4.205	0.001	4.024	-0.181
^{26}Al	0	4^+	4	4.773	0.001	4.613	-0.160
^{26}Al	0	5^+	3	4.940	0.001	4.765	-0.175
^{26}Al	0	1^+	6	5.010	0.001	4.948	-0.062
^{27}Al	$\frac{1}{2}$	$\frac{5}{2}^+$	1	-224.952	0.000	-224.986	-0.034
^{27}Al	$\frac{1}{2}$	$\frac{1}{2}^+$	1	0.844	0.001	0.876	0.032

Nucleus	T_z	J^π	J_i^π	Exp.	Error	USDC	ΔE
^{27}Al	$\frac{1}{2}$	$\frac{3}{2}^+$	1	1.014	0.001	1.075	0.061
^{27}Al	$\frac{1}{2}$	$\frac{7}{2}^+$	1	2.211	0.001	2.290	0.079
^{27}Al	$\frac{1}{2}$	$\frac{5}{2}^+$	2	2.735	0.001	2.681	-0.054
^{27}Al	$\frac{1}{2}$	$\frac{3}{2}^+$	2	2.982	0.001	2.829	-0.153
^{27}Al	$\frac{1}{2}$	$\frac{9}{2}^+$	1	3.004	0.001	3.007	0.003
^{27}Al	$\frac{1}{2}$	$\frac{1}{2}^+$	2	3.680	0.001	3.750	0.070
^{27}Al	$\frac{1}{2}$	$\frac{3}{2}^+$	3	3.957	0.001	3.922	-0.035
^{27}Al	$\frac{1}{2}$	$\frac{5}{2}^+$	3	4.410	0.001	4.388	-0.022
^{27}Al	$\frac{1}{2}$	$\frac{11}{2}^+$	1	4.510	0.001	4.535	0.025
^{27}Al	$\frac{1}{2}$	$\frac{7}{2}^+$	2	4.580	0.001	4.688	0.108
^{27}Al	$\frac{1}{2}$	$\frac{5}{2}^+$	4	4.811	0.001	4.751	-0.060
^{27}Al	$\frac{1}{2}$	$\frac{5}{2}^+$	5	5.248	0.001	5.287	0.039
^{27}Al	$\frac{1}{2}$	$\frac{9}{2}^+$	2	5.419	0.001	5.324	-0.095
^{27}Al	$\frac{1}{2}$	$\frac{11}{2}^+$	2	5.499	0.001	5.458	-0.041
^{27}Al	$\frac{1}{2}$	$\frac{9}{2}^+$	3	5.667	0.001	5.907	0.240
^{27}Al	$\frac{1}{2}$	$\frac{1}{2}^+$	3	5.752	0.001	5.821	0.069
^{27}Al	$\frac{1}{2}$	$\frac{1}{2}^+$	4	7.071	0.001	6.897	-0.174
^{27}Al	$\frac{1}{2}$	$\frac{11}{2}^+$	3	7.400	0.001	7.187	-0.213
^{28}Al	1	3^+	1	-232.677	0.000	-232.553	0.124
^{28}Al	1	2^+	1	0.030	0.001	0.000	-0.030
^{28}Al	1	0^+	1	0.972	0.001	0.986	0.014
^{28}Al	1	3^+	2	1.013	0.001	1.044	0.031
^{28}Al	1	1^+	1	1.372	0.001	1.169	-0.203
^{28}Al	1	1^+	2	1.620	0.001	1.441	-0.179
^{28}Al	1	2^+	2	1.622	0.001	1.478	-0.144
^{28}Al	1	2^+	3	2.138	0.001	1.999	-0.139
^{28}Al	1	1^+	3	2.201	0.001	2.098	-0.103
^{28}Al	1	4^+	1	2.486	0.001	2.176	-0.310
^{28}Al	1	5^+	1	2.582	0.001	2.485	-0.097
^{28}Al	1	4^+	2	2.656	0.001	2.499	-0.157
^{28}Al	1	0^+	2	3.012	0.001	2.643	-0.369

Nucleus	T_z	J^π	J_i^π	Exp.	Error	USDC	ΔE
^{28}Al	1	0^+	3	3.760	0.001	3.531	-0.229
^{29}Al	$\frac{3}{2}$	$\frac{5}{2}^+$	1	-242.105	0.000	-242.040	0.065
^{29}Al	$\frac{3}{2}$	$\frac{1}{2}^+$	1	1.398	0.001	1.161	-0.237
^{29}Al	$\frac{3}{2}$	$\frac{7}{2}^+$	1	1.754	0.001	1.846	0.092
^{29}Al	$\frac{3}{2}$	$\frac{3}{2}^+$	1	2.222	0.001	1.978	-0.244
^{29}Al	$\frac{3}{2}$	$\frac{3}{2}^+$	2	2.866	0.001	2.656	-0.210
^{29}Al	$\frac{3}{2}$	$\frac{5}{2}^+$	2	3.062	0.001	2.912	-0.150
^{29}Al	$\frac{3}{2}$	$\frac{5}{2}^+$	3	3.184	0.001	3.043	-0.141
^{29}Al	$\frac{3}{2}$	$\frac{1}{2}^+$	2	3.433	0.001	3.346	-0.087
^{30}Al	2	3^+	1	-247.834	0.003	-247.622	0.212
^{30}Al	2	2^+	1	0.243	0.001	0.072	-0.171
^{30}Al	2	1^+	1	0.687	0.001	0.437	-0.250
^{31}Al	$\frac{5}{2}$	$\frac{5}{2}^+$	1	-254.991	0.002	-255.138	-0.147
^{31}Al	$\frac{5}{2}$	$\frac{1}{2}^+$	1	0.946	0.001	0.883	-0.063
^{31}Al	$\frac{5}{2}$	$\frac{3}{2}^+$	1	1.612	0.001	1.707	0.095
^{32}Al	3	1^+	1	-259.211	0.007	-259.155	0.056
^{33}Al	$\frac{7}{2}$	$\frac{5}{2}^+$	1	-264.680	0.007	-264.651	0.029
^{24}Si	-2	0^+	1	-172.014	0.019	-172.154	-0.140
^{24}Si	-2	2^+	1	1.879	0.011	2.061	0.182
^{25}Si	$-\frac{3}{2}$	$\frac{5}{2}^+$	1	-187.003	0.010	-187.239	-0.236
^{25}Si	$-\frac{3}{2}$	$\frac{3}{2}^+$	1	0.040	0.005	0.116	0.076
^{25}Si	$-\frac{3}{2}$	$\frac{1}{2}^+$	1	0.815	0.015	0.975	0.160
^{25}Si	$-\frac{3}{2}$	$\frac{3}{2}^+$	2	1.963	0.015	1.936	-0.027
^{26}Si	-1	0^+	1	-206.042	0.000	-206.144	-0.102
^{26}Si	-1	2^+	1	1.797	0.000	1.880	0.083
^{26}Si	-1	2^+	2	2.787	0.000	2.950	0.163
^{26}Si	-1	0^+	2	3.336	0.000	3.450	0.114
^{26}Si	-1	3^+	1	3.758	0.000	3.863	0.105
^{26}Si	-1	4^+	1	4.446	0.001	4.386	-0.060
^{26}Si	-1	2^+	3	4.139	0.000	4.287	0.148
^{26}Si	-1	3^+	2	4.188	0.000	4.249	0.061

Nucleus	T_z	J^π	J_i^π	Exp.	Error	USDC	ΔE
^{27}Si	$-\frac{1}{2}$	$\frac{5}{2}^+$	1	-219.357	0.000	-219.543	-0.186
^{27}Si	$-\frac{1}{2}$	$\frac{1}{2}^+$	1	0.781	0.000	0.847	0.066
^{27}Si	$-\frac{1}{2}$	$\frac{3}{2}^+$	1	0.957	0.000	1.129	0.172
^{27}Si	$-\frac{1}{2}$	$\frac{7}{2}^+$	1	2.164	0.000	2.347	0.183
^{27}Si	$-\frac{1}{2}$	$\frac{5}{2}^+$	2	2.648	0.000	2.721	0.073
^{27}Si	$-\frac{1}{2}$	$\frac{3}{2}^+$	2	2.866	0.000	2.821	-0.045
^{27}Si	$-\frac{1}{2}$	$\frac{9}{2}^+$	1	2.910	0.000	2.919	0.009
^{27}Si	$-\frac{1}{2}$	$\frac{1}{2}^+$	2	3.540	0.001	3.721	0.181
^{27}Si	$-\frac{1}{2}$	$\frac{3}{2}^+$	3	3.804	0.001	3.892	0.088
^{27}Si	$-\frac{1}{2}$	$\frac{5}{2}^+$	3	4.289	0.001	4.451	0.162
^{27}Si	$-\frac{1}{2}$	$\frac{11}{2}^+$	1	4.447	0.001	4.497	0.050
^{27}Si	$-\frac{1}{2}$	$\frac{7}{2}^+$	2	4.475	0.001	4.700	0.225
^{27}Si	$-\frac{1}{2}$	$\frac{5}{2}^+$	4	4.704	0.001	4.728	0.024
^{28}Si	0	0^+	1	-236.537	0.000	-236.644	-0.107
^{28}Si	0	2^+	1	1.779	0.001	1.933	0.154
^{28}Si	0	4^+	1	4.618	0.001	4.618	0.000
^{28}Si	0	0^+	2	4.979	0.001	4.965	-0.014
^{28}Si	0	3^+	1	6.276	0.001	6.324	0.048
^{28}Si	0	4^+	2	6.888	0.001	7.029	0.141
^{28}Si	0	3^+	2	7.799	0.001	7.993	0.194
^{28}Si	0	1^+	1	8.328	0.001	8.176	-0.152
^{28}Si	0	6^+	1	8.543	0.001	8.462	-0.081
^{28}Si	0	3^+	3	8.589	0.001	8.906	0.317
^{28}Si	0	5^+	1	8.945	0.001	9.261	0.316
^{28}Si	0	4^+	3	9.164	0.001	9.404	0.240
^{28}Si	0	1^+	2	9.496	0.001	9.690	0.194
^{28}Si	0	3^+	4	9.316	0.001	9.452	0.136
^{28}Si	0	3^+	5	10.209	0.001	10.475	0.266
^{28}Si	0	5^+	2	10.418	0.001	10.231	-0.187
^{28}Si	0	6^+	2	11.100	0.001	11.014	-0.086
^{28}Si	0	6^+	3	11.331	0.001	11.511	0.180

Nucleus	T_z	J^π	J_i^π	Exp.	Error	USDC	ΔE
^{28}Si	0	6^+	4	11.510	0.001	11.847	0.337
^{28}Si	0	5^+	4	11.778	0.001	11.963	0.185
^{29}Si	$\frac{1}{2}$	$\frac{1}{2}^+$	1	-245.010	0.000	-244.949	0.061
^{29}Si	$\frac{1}{2}$	$\frac{3}{2}^+$	1	1.273	0.001	1.268	-0.005
^{29}Si	$\frac{1}{2}$	$\frac{5}{2}^+$	1	2.028	0.001	2.050	0.022
^{29}Si	$\frac{1}{2}$	$\frac{3}{2}^+$	2	2.426	0.001	2.514	0.088
^{29}Si	$\frac{1}{2}$	$\frac{5}{2}^+$	2	3.067	0.001	3.282	0.215
^{29}Si	$\frac{1}{2}$	$\frac{7}{2}^+$	1	4.080	0.001	4.186	0.106
^{29}Si	$\frac{1}{2}$	$\frac{9}{2}^+$	1	4.741	0.001	4.653	-0.088
^{29}Si	$\frac{1}{2}$	$\frac{1}{2}^+$	2	4.840	0.001	4.741	-0.099
^{29}Si	$\frac{1}{2}$	$\frac{5}{2}^+$	3	4.895	0.001	4.824	-0.071
^{29}Si	$\frac{1}{2}$	$\frac{7}{2}^+$	2	5.285	0.001	5.134	-0.151
^{29}Si	$\frac{1}{2}$	$\frac{9}{2}^+$	2	5.652	0.001	5.600	-0.052
^{29}Si	$\frac{1}{2}$	$\frac{7}{2}^+$	3	5.812	0.001	5.830	0.018
^{29}Si	$\frac{1}{2}$	$\frac{3}{2}^+$	3	5.949	0.001	6.050	0.101
^{29}Si	$\frac{1}{2}$	$\frac{9}{2}^+$	3	6.616	0.001	6.755	0.139
^{29}Si	$\frac{1}{2}$	$\frac{11}{2}^+$	1	7.139	0.001	7.077	-0.062
^{29}Si	$\frac{1}{2}$	$\frac{11}{2}^+$	2	8.173	0.001	7.904	-0.269
^{29}Si	$\frac{1}{2}$	$\frac{13}{2}^+$	1	8.641	0.001	8.578	-0.063
^{30}Si	1	0^+	1	-255.620	0.000	-255.504	0.116
^{30}Si	1	2^+	1	2.235	0.001	2.240	0.005
^{30}Si	1	2^+	2	3.499	0.001	3.446	-0.053
^{30}Si	1	1^+	1	3.770	0.001	4.038	0.268
^{30}Si	1	0^+	2	3.788	0.001	3.915	0.127
^{30}Si	1	2^+	3	4.810	0.001	4.862	0.052
^{30}Si	1	3^+	1	4.831	0.001	4.796	-0.035
^{30}Si	1	3^+	2	5.232	0.001	5.080	-0.152
^{30}Si	1	4^+	1	5.280	0.001	5.317	0.037
^{30}Si	1	0^+	3	5.372	0.001	5.408	0.036
^{30}Si	1	2^+	4	5.614	0.001	5.878	0.264
^{30}Si	1	4^+	2	5.950	0.001	5.830	-0.120

Table A1: (cont'd)

Nucleus	T_z	J^π	J_i^π	Exp.	Error	USDC	ΔE
^{30}Si	1	2^+	5	6.537	0.001	6.576	0.039
^{30}Si	1	0^+	4	6.641	0.001	6.672	0.031
^{30}Si	1	3^+	3	6.865	0.001	6.799	-0.066
^{30}Si	1	2^+	6	6.913	0.001	6.823	-0.090
^{30}Si	1	5^+	1	7.001	0.001	7.030	0.029
^{30}Si	1	3^+	4	7.079	0.001	7.147	0.068
^{30}Si	1	4^+	3	7.223	0.001	6.967	-0.256
^{30}Si	1	0^+	5	7.443	0.001	7.604	0.161
^{30}Si	1	1^+	2	7.623	0.001	7.433	-0.190
^{30}Si	1	6^+	1	9.371	0.001	9.185	-0.186
^{31}Si	$\frac{3}{2}$	$\frac{3}{2}^+$	1	-262.207	0.000	-261.941	0.266
^{31}Si	$\frac{3}{2}$	$\frac{1}{2}^+$	1	0.752	0.001	0.720	-0.032
^{31}Si	$\frac{3}{2}$	$\frac{5}{2}^+$	1	1.695	0.001	1.559	-0.136
^{31}Si	$\frac{3}{2}$	$\frac{3}{2}^+$	2	2.317	0.001	2.340	0.023
^{32}Si	2	0^+	1	-271.407	0.000	-271.276	0.131
^{32}Si	2	2^+	1	1.941	0.001	2.034	0.093
^{32}Si	2	2^+	2	4.232	0.001	4.228	-0.004
^{32}Si	2	0^+	2	4.983	0.001	4.926	-0.057
^{33}Si	$\frac{5}{2}$	$\frac{3}{2}^+$	1	-275.915	0.001	-275.682	0.233
^{33}Si	$\frac{5}{2}$	$\frac{1}{2}^+$	1	1.010	0.016	0.779	-0.231
^{33}Si	$\frac{5}{2}$	$\frac{5}{2}^+$	1	4.290	0.016	4.489	0.199
^{34}Si	3	0^+	1	-283.429	0.014	-283.451	-0.022
^{27}P	$-\frac{3}{2}$	$\frac{1}{2}^+$	1	-206.913	0.026	-206.811	0.102
^{27}P	$-\frac{3}{2}$	$\frac{3}{2}^+$	1	1.120	0.001	1.062	-0.058
^{28}P	-1	3^+	1	-221.409	0.001	-221.472	-0.063
^{28}P	-1	2^+	1	0.106	0.001	0.031	-0.075
^{28}P	-1	3^+	2	1.134	0.001	1.130	-0.004
^{28}P	-1	1^+	1	1.313	0.002	1.242	-0.071
^{28}P	-1	2^+	2	1.516	0.002	1.589	0.073
^{28}P	-1	1^+	2	1.567	0.003	1.544	-0.023
^{28}P	-1	2^+	3	2.104	0.001	2.064	-0.040

Table A1: (cont'd)

Nucleus	T_z	J^π	J^π_i	Exp.	Error	USDC	ΔE
^{28}P	-1	1^+	3	2.143	0.005	2.217	0.074
^{29}P	$-\frac{1}{2}$	$\frac{1}{2}^+$	1	-239.286	0.000	-239.311	-0.025
^{29}P	$-\frac{1}{2}$	$\frac{3}{2}^+$	1	1.384	0.000	1.347	-0.037
^{29}P	$-\frac{1}{2}$	$\frac{5}{2}^+$	1	1.954	0.000	2.064	0.110
^{29}P	$-\frac{1}{2}$	$\frac{3}{2}^+$	2	2.423	0.000	2.590	0.167
^{29}P	$-\frac{1}{2}$	$\frac{5}{2}^+$	2	3.106	0.000	3.356	0.250
^{29}P	$-\frac{1}{2}$	$\frac{7}{2}^+$	1	4.081	0.001	4.226	0.145
^{29}P	$-\frac{1}{2}$	$\frac{9}{2}^+$	1	4.642	0.001	4.642	0.000
^{29}P	$-\frac{1}{2}$	$\frac{1}{2}^+$	2	4.759	0.003	4.743	-0.016
^{29}P	$-\frac{1}{2}$	$\frac{5}{2}^+$	3	4.954	0.000	4.922	-0.032
^{30}P	0	1^+	1	-250.605	0.000	-250.571	0.034
^{30}P	0	0^+	1	0.677	0.001	0.630	-0.047
^{30}P	0	1^+	2	0.709	0.001	0.661	-0.048
^{30}P	0	2^+	1	1.454	0.001	1.557	0.103
^{30}P	0	3^+	1	1.974	0.001	1.973	-0.001
^{30}P	0	3^+	2	2.539	0.001	2.433	-0.106
^{30}P	0	2^+	2	2.723	0.001	2.620	-0.103
^{30}P	0	3^+	3	2.840	0.001	2.956	0.116
^{30}P	0	2^+	3	2.937	0.001	2.933	-0.004
^{30}P	0	1^+	3	3.019	0.001	3.217	0.198
^{30}P	0	1^+	4	3.731	0.001	3.750	0.019
^{30}P	0	2^+	4	3.834	0.001	3.823	-0.011
^{30}P	0	3^+	4	3.928	0.001	4.077	0.149
^{30}P	0	2^+	5	4.183	0.001	4.166	-0.017
^{30}P	0	4^+	1	4.298	0.001	4.316	0.018
^{30}P	0	5^+	1	4.343	0.001	4.308	-0.035
^{30}P	0	2^+	6	4.424	0.001	4.351	-0.073
^{30}P	0	0^+	2	4.468	0.001	4.620	0.152
^{30}P	0	1^+	5	4.502	0.001	4.729	0.227
^{30}P	0	3^+	5	4.735	0.001	4.674	-0.061
^{30}P	0	1^+	6	4.945	0.001	4.787	-0.158

Table A1: (cont'd)

Nucleus	T_z	J^π	J_i^π	Exp.	Error	USDC	ΔE
^{30}P	0	3^+	6	5.206	0.001	5.296	0.090
^{30}P	0	2^+	7	5.576	0.001	5.612	0.036
^{30}P	0	1^+	7	5.701	0.001	5.670	-0.031
^{31}P	$\frac{1}{2}$	$\frac{1}{2}^+$	1	-262.916	0.000	-262.876	0.040
^{31}P	$\frac{1}{2}$	$\frac{3}{2}^+$	1	1.266	0.001	1.193	-0.073
^{31}P	$\frac{1}{2}$	$\frac{5}{2}^+$	1	2.234	0.001	2.268	0.034
^{31}P	$\frac{1}{2}$	$\frac{1}{2}^+$	2	3.134	0.001	3.277	0.143
^{31}P	$\frac{1}{2}$	$\frac{5}{2}^+$	2	3.295	0.001	3.258	-0.037
^{31}P	$\frac{1}{2}$	$\frac{7}{2}^+$	1	3.415	0.001	3.463	0.048
^{31}P	$\frac{1}{2}$	$\frac{3}{2}^+$	2	3.506	0.001	3.663	0.157
^{31}P	$\frac{1}{2}$	$\frac{5}{2}^+$	3	4.190	0.001	4.213	0.023
^{31}P	$\frac{1}{2}$	$\frac{3}{2}^+$	3	4.261	0.001	4.363	0.102
^{31}P	$\frac{1}{2}$	$\frac{3}{2}^+$	4	4.594	0.001	4.691	0.097
^{31}P	$\frac{1}{2}$	$\frac{7}{2}^+$	2	4.634	0.001	4.700	0.066
^{31}P	$\frac{1}{2}$	$\frac{5}{2}^+$	4	4.783	0.001	4.807	0.024
^{31}P	$\frac{1}{2}$	$\frac{5}{2}^+$	5	5.115	0.001	5.197	0.082
^{31}P	$\frac{1}{2}$	$\frac{9}{2}^+$	1	5.343	0.001	5.417	0.074
^{31}P	$\frac{1}{2}$	$\frac{9}{2}^+$	2	5.892	0.001	5.881	-0.011
^{31}P	$\frac{1}{2}$	$\frac{9}{2}^+$	3	6.080	0.001	6.037	-0.043
^{31}P	$\frac{1}{2}$	$\frac{1}{2}^+$	5	6.337	0.001	6.374	0.037
^{31}P	$\frac{1}{2}$	$\frac{11}{2}^+$	1	6.453	0.001	6.601	0.148
^{31}P	$\frac{1}{2}$	$\frac{11}{2}^+$	2	7.441	0.001	7.664	0.223
^{32}P	1	1^+	1	-270.852	0.000	-270.746	0.106
^{32}P	1	2^+	1	0.078	0.001	0.126	0.048
^{32}P	1	0^+	1	0.513	0.001	0.483	-0.030
^{32}P	1	1^+	2	1.150	0.001	1.109	-0.041
^{32}P	1	2^+	2	1.323	0.001	1.234	-0.089
^{32}P	1	3^+	1	1.754	0.001	1.704	-0.050
^{32}P	1	3^+	2	2.178	0.001	2.196	0.018
^{32}P	1	2^+	3	2.219	0.001	2.292	0.073
^{32}P	1	1^+	3	2.230	0.001	2.051	-0.179

Table A1: (cont'd)

Nucleus	T_z	J^π	J^π_i	Exp.	Error	USDC	ΔE
^{32}P	1	2^+	4	2.658	0.001	2.590	-0.068
^{32}P	1	1^+	4	2.740	0.001	2.848	0.108
^{32}P	1	3^+	3	3.005	0.001	2.952	-0.053
^{32}P	1	4^+	1	3.149	0.001	3.143	-0.006
^{32}P	1	2^+	5	3.445	0.001	3.494	0.049
^{32}P	1	1^+	5	3.796	0.001	3.808	0.012
^{32}P	1	3^+	4	3.989	0.001	3.811	-0.178
^{32}P	1	4^+	2	4.035	0.001	3.811	-0.224
^{32}P	1	1^+	6	4.203	0.001	4.078	-0.125
^{32}P	1	3^+	5	4.312	0.001	4.074	-0.238
^{32}P	1	1^+	7	4.548	0.001	4.752	0.204
^{32}P	1	2^+	7	4.554	0.001	4.644	0.090
^{32}P	1	3^+	6	4.611	0.001	4.367	-0.244
^{32}P	1	5^+	1	4.743	0.001	4.849	0.106
^{33}P	$\frac{3}{2}$	$\frac{1}{2}^+$	1	-280.956	0.001	-281.007	-0.051
^{33}P	$\frac{3}{2}$	$\frac{3}{2}^+$	1	1.432	0.001	1.467	0.035
^{33}P	$\frac{3}{2}$	$\frac{5}{2}^+$	1	1.848	0.001	1.962	0.114
^{33}P	$\frac{3}{2}$	$\frac{3}{2}^+$	2	2.539	0.001	2.581	0.042
^{33}P	$\frac{3}{2}$	$\frac{3}{2}^+$	3	3.275	0.001	3.400	0.125
^{33}P	$\frac{3}{2}$	$\frac{5}{2}^+$	2	3.490	0.001	3.577	0.087
^{33}P	$\frac{3}{2}$	$\frac{7}{2}^+$	1	3.628	0.001	3.820	0.192
^{33}P	$\frac{3}{2}$	$\frac{5}{2}^+$	3	4.048	0.001	4.037	-0.011
^{33}P	$\frac{3}{2}$	$\frac{3}{2}^+$	4	4.856	0.001	5.130	0.274
^{34}P	2	1^+	1	-287.238	0.001	-287.246	-0.008
^{34}P	2	2^+	1	0.429	0.001	0.464	0.035
^{34}P	2	1^+	2	1.608	0.001	1.539	-0.069
^{35}P	$\frac{5}{2}$	$\frac{1}{2}^+$	1	-295.619	0.002	-295.808	-0.189
^{35}P	$\frac{5}{2}$	$\frac{3}{2}^+$	1	2.386	0.001	2.587	0.201
^{28}S	-2	0^+	1	-209.406	0.160	-209.374	0.032
^{28}S	-2	2^+	1	1.507	0.007	1.544	0.037
^{29}S	$-\frac{3}{2}$	$\frac{5}{2}^+$	1	-224.707	0.050	-224.907	-0.200

Nucleus	T_z	J^π	J_i^π	Exp.	Error	USDC	ΔE
^{29}S	$-\frac{3}{2}$	$\frac{1}{2}^+$	1	1.222	0.020	1.265	0.043
^{29}S	$-\frac{3}{2}$	$\frac{7}{2}^+$	1	1.727	0.037	1.896	0.169
^{29}S	$-\frac{3}{2}$	$\frac{5}{2}^+$	2	2.887	0.040	2.975	0.088
^{30}S	-1	0^+	1	-243.681	0.000	-243.832	-0.151
^{30}S	-1	2^+	1	2.211	0.001	2.288	0.077
^{30}S	-1	2^+	2	3.402	0.001	3.533	0.131
^{30}S	-1	0^+	2	3.668	0.001	3.932	0.264
^{30}S	-1	1^+	1	3.676	0.003	4.038	0.362
^{30}S	-1	3^+	1	4.704	0.005	4.858	0.154
^{30}S	-1	3^+	2	5.136	0.002	5.216	0.080
^{30}S	-1	4^+	1	5.168	0.006	5.322	0.154
^{31}S	$-\frac{1}{2}$	$\frac{1}{2}^+$	1	-256.736	0.000	-256.870	-0.134
^{31}S	$-\frac{1}{2}$	$\frac{3}{2}^+$	1	1.249	0.000	1.201	-0.048
^{31}S	$-\frac{1}{2}$	$\frac{5}{2}^+$	1	2.234	0.000	2.373	0.139
^{31}S	$-\frac{1}{2}$	$\frac{1}{2}^+$	2	3.077	0.000	3.289	0.212
^{31}S	$-\frac{1}{2}$	$\frac{5}{2}^+$	2	3.285	0.000	3.354	0.069
^{31}S	$-\frac{1}{2}$	$\frac{7}{2}^+$	1	3.351	0.000	3.467	0.116
^{31}S	$-\frac{1}{2}$	$\frac{3}{2}^+$	2	3.436	0.000	3.709	0.273
^{31}S	$-\frac{1}{2}$	$\frac{9}{2}^+$	1	5.301	0.000	5.446	0.145
^{31}S	$-\frac{1}{2}$	$\frac{11}{2}^+$	1	6.394	0.000	6.691	0.297
^{32}S	0	0^+	1	-271.780	0.000	-271.625	0.155
^{32}S	0	2^+	1	2.230	0.001	2.201	-0.029
^{32}S	0	0^+	2	3.778	0.001	3.493	-0.285
^{32}S	0	2^+	2	4.282	0.001	4.395	0.113
^{32}S	0	4^+	1	4.459	0.001	4.662	0.203
^{32}S	0	1^+	1	4.695	0.001	4.815	0.120
^{32}S	0	3^+	1	5.413	0.001	5.397	-0.016
^{32}S	0	2^+	3	5.549	0.001	5.430	-0.119
^{32}S	0	4^+	2	6.411	0.001	6.207	-0.204
^{32}S	0	2^+	4	6.666	0.001	6.707	0.041
^{32}S	0	4^+	3	6.852	0.001	6.873	0.021

Nucleus	T_z	J^π	J_i^π	Exp.	Error	USDC	ΔE
^{32}S	0	1^+	2	7.001	0.001	6.859	-0.142
^{32}S	0	1^+	3	7.189	0.001	7.227	0.038
^{32}S	0	3^+	2	7.350	0.001	7.403	0.053
^{32}S	0	2^+	5	7.115	0.001	7.017	-0.098
^{32}S	0	2^+	6	7.484	0.001	7.488	0.004
^{32}S	0	5^+	1	7.566	0.001	7.586	0.020
^{32}S	0	4^+	4	7.882	0.001	7.995	0.113
^{33}S	$\frac{1}{2}$	$\frac{3}{2}^+$	1	-280.422	0.000	-280.257	0.165
^{33}S	$\frac{1}{2}$	$\frac{1}{2}^+$	1	0.841	0.001	0.873	0.032
^{33}S	$\frac{1}{2}$	$\frac{5}{2}^+$	1	1.966	0.001	1.957	-0.009
^{33}S	$\frac{1}{2}$	$\frac{3}{2}^+$	2	2.312	0.001	2.322	0.010
^{33}S	$\frac{1}{2}$	$\frac{5}{2}^+$	2	2.867	0.001	2.950	0.083
^{33}S	$\frac{1}{2}$	$\frac{7}{2}^+$	1	2.968	0.001	2.952	-0.016
^{33}S	$\frac{1}{2}$	$\frac{5}{2}^+$	3	3.831	0.001	3.830	-0.001
^{33}S	$\frac{1}{2}$	$\frac{3}{2}^+$	3	3.934	0.001	3.591	-0.343
^{33}S	$\frac{1}{2}$	$\frac{9}{2}^+$	1	4.047	0.001	4.179	0.132
^{33}S	$\frac{1}{2}$	$\frac{1}{2}^+$	2	4.055	0.001	3.899	-0.156
^{33}S	$\frac{1}{2}$	$\frac{7}{2}^+$	2	4.094	0.001	4.180	0.086
^{33}S	$\frac{1}{2}$	$\frac{1}{2}^+$	3	4.375	0.001	4.266	-0.109
^{33}S	$\frac{1}{2}$	$\frac{5}{2}^+$	4	4.746	0.001	4.572	-0.174
^{34}S	1	0^+	1	-291.839	0.000	-291.692	0.147
^{34}S	1	2^+	1	2.127	0.001	2.157	0.030
^{34}S	1	2^+	2	3.304	0.001	3.092	-0.212
^{34}S	1	0^+	2	3.916	0.001	3.712	-0.204
^{34}S	1	1^+	1	4.074	0.001	3.713	-0.361
^{34}S	1	2^+	3	4.114	0.001	4.107	-0.007
^{34}S	1	4^+	1	4.689	0.001	4.826	0.137
^{34}S	1	3^+	1	4.876	0.001	4.681	-0.195
^{34}S	1	2^+	4	4.889	0.001	4.568	-0.321
^{34}S	1	0^+	3	5.228	0.001	5.194	-0.034
^{34}S	1	1^+	2	5.380	0.001	5.571	0.191

Nucleus	T_z	J^π	J_i^π	Exp.	Error	USDC	ΔE
^{34}S	1	2^+	5	5.998	0.001	5.955	-0.043
^{35}S	$\frac{3}{2}$	$\frac{3}{2}^+$	1	-298.825	0.000	-298.701	0.124
^{35}S	$\frac{3}{2}$	$\frac{1}{2}^+$	1	1.572	0.001	1.685	0.113
^{35}S	$\frac{3}{2}$	$\frac{5}{2}^+$	1	2.717	0.001	2.683	-0.034
^{35}S	$\frac{3}{2}$	$\frac{3}{2}^+$	2	2.939	0.001	2.739	-0.200
^{35}S	$\frac{3}{2}$	$\frac{5}{2}^+$	2	3.421	0.001	3.339	-0.082
^{36}S	2	0^+	1	-308.714	0.000	-308.706	0.008
^{36}S	2	2^+	1	3.291	0.001	3.365	0.074
^{36}S	2	1^+	1	4.523	0.001	4.160	-0.363
^{31}Cl	$-\frac{3}{2}$	$\frac{3}{2}^+$	1	-243.945	0.003	-243.948	-0.003
^{31}Cl	$-\frac{3}{2}$	$\frac{5}{2}^+$	1	1.746	0.005	1.638	-0.108
^{31}Cl	$-\frac{3}{2}$	$\frac{3}{2}^+$	2	2.436	0.005	2.469	0.033
^{32}Cl	-1	1^+	1	-258.317	0.001	-258.406	-0.089
^{32}Cl	-1	2^+	1	0.090	0.000	0.134	0.044
^{32}Cl	-1	0^+	1	0.461	0.000	0.492	0.031
^{32}Cl	-1	1^+	2	1.169	0.000	1.185	0.016
^{32}Cl	-1	2^+	2	1.331	0.001	1.264	-0.067
^{32}Cl	-1	3^+	1	1.737	0.001	1.731	-0.006
^{32}Cl	-1	3^+	2	2.131	0.000	2.253	0.122
^{32}Cl	-1	1^+	3	2.210	0.001	2.083	-0.127
^{32}Cl	-1	2^+	3	2.284	0.001	2.392	0.108
^{32}Cl	-1	1^+	4	2.611	0.005	2.863	0.252
^{32}Cl	-1	2^+	4	2.675	0.005	2.616	-0.059
^{33}Cl	$-\frac{1}{2}$	$\frac{3}{2}^+$	1	-274.057	0.000	-273.911	0.146
^{33}Cl	$-\frac{1}{2}$	$\frac{1}{2}^+$	1	0.811	0.000	0.880	0.069
^{33}Cl	$-\frac{1}{2}$	$\frac{5}{2}^+$	1	1.986	0.000	1.964	-0.022
^{33}Cl	$-\frac{1}{2}$	$\frac{3}{2}^+$	2	2.352	0.000	2.340	-0.012
^{33}Cl	$-\frac{1}{2}$	$\frac{5}{2}^+$	2	2.839	0.000	2.948	0.109
^{33}Cl	$-\frac{1}{2}$	$\frac{7}{2}^+$	1	2.975	0.000	2.912	-0.063
^{33}Cl	$-\frac{1}{2}$	$\frac{5}{2}^+$	3	3.816	0.000	3.811	-0.005
^{33}Cl	$-\frac{1}{2}$	$\frac{3}{2}^+$	3	3.971	0.000	3.569	-0.402

Nucleus	T_z	J^π	J_i^π	Exp.	Error	USDC	ΔE
^{34}Cl	0	0^+	1	-285.565	0.000	-285.426	0.139
^{34}Cl	0	3^+	1	0.146	0.000	0.012	-0.134
^{34}Cl	0	1^+	1	0.461	0.001	0.366	-0.095
^{34}Cl	0	1^+	2	0.666	0.001	0.619	-0.047
^{34}Cl	0	2^+	1	1.230	0.001	1.058	-0.172
^{34}Cl	0	2^+	2	1.887	0.001	1.769	-0.118
^{34}Cl	0	2^+	3	2.158	0.000	2.185	0.027
^{34}Cl	0	3^+	2	2.181	0.001	2.166	-0.015
^{34}Cl	0	4^+	1	2.377	0.001	2.312	-0.065
^{34}Cl	0	1^+	3	2.580	0.001	2.433	-0.147
^{34}Cl	0	3^+	3	2.611	0.001	2.452	-0.159
^{34}Cl	0	1^+	4	3.129	0.001	3.172	0.043
^{34}Cl	0	3^+	4	3.334	0.001	3.408	0.074
^{34}Cl	0	5^+	1	3.646	0.001	3.741	0.095
^{34}Cl	0	4^+	2	3.964	0.001	3.998	0.034
^{35}Cl	$\frac{1}{2}$	$\frac{3}{2}^+$	1	-298.210	0.000	-298.259	-0.049
^{35}Cl	$\frac{1}{2}$	$\frac{1}{2}^+$	1	1.219	0.001	1.225	0.006
^{35}Cl	$\frac{1}{2}$	$\frac{5}{2}^+$	1	1.763	0.001	1.723	-0.040
^{35}Cl	$\frac{1}{2}$	$\frac{7}{2}^+$	1	2.645	0.001	2.734	0.089
^{35}Cl	$\frac{1}{2}$	$\frac{3}{2}^+$	2	2.694	0.001	2.666	-0.028
^{35}Cl	$\frac{1}{2}$	$\frac{5}{2}^+$	2	3.003	0.001	3.057	0.054
^{35}Cl	$\frac{1}{2}$	$\frac{3}{2}^+$	3	3.918	0.001	3.941	0.023
^{35}Cl	$\frac{1}{2}$	$\frac{9}{2}^+$	1	3.943	0.001	4.171	0.228
^{35}Cl	$\frac{1}{2}$	$\frac{1}{2}^+$	2	3.967	0.014	3.984	0.017
^{35}Cl	$\frac{1}{2}$	$\frac{3}{2}^+$	4	4.624	0.001	4.667	0.043
^{35}Cl	$\frac{1}{2}$	$\frac{1}{2}^+$	3	4.720	0.001	5.036	0.316
^{36}Cl	1	2^+	1	-306.790	0.000	-306.846	-0.056
^{36}Cl	1	3^+	1	0.788	0.001	0.828	0.040
^{36}Cl	1	1^+	1	1.165	0.001	1.184	0.019
^{36}Cl	1	1^+	2	1.601	0.001	1.681	0.080
^{36}Cl	1	2^+	2	1.959	0.001	1.979	0.020

Nucleus	T_z	J^π	J^π_i	Exp.	Error	USDC	ΔE
^{36}Cl	1	2^+	3	2.492	0.001	2.469	-0.023
^{36}Cl	1	3^+	2	2.864	0.001	3.095	0.231
^{36}Cl	1	1^+	3	2.676	0.001	2.585	-0.091
^{36}Cl	1	0^+	1	3.120	0.001	3.209	0.089
^{36}Cl	1	1^+	4	3.469	0.001	3.408	-0.061
^{36}Cl	1	4^+	1	3.830	0.001	3.668	-0.162
^{37}Cl	$\frac{3}{2}$	$\frac{3}{2}^+$	1	-317.100	0.000	-317.284	-0.184
^{37}Cl	$\frac{3}{2}$	$\frac{1}{2}^+$	1	1.726	0.001	1.887	0.161
^{37}Cl	$\frac{3}{2}$	$\frac{5}{2}^+$	1	3.087	0.001	3.182	0.095
^{37}Cl	$\frac{3}{2}$	$\frac{3}{2}^+$	2	4.016	0.001	4.061	0.045
^{32}Ar	-2	0^+	1	-246.400	0.002	-246.559	-0.159
^{32}Ar	-2	2^+	1	1.867	0.008	2.066	0.199
^{33}Ar	$-\frac{3}{2}$	$\frac{1}{2}^+$	1	-261.656	0.000	-261.931	-0.275
^{33}Ar	$-\frac{3}{2}$	$\frac{3}{2}^+$	1	1.359	0.002	1.420	0.061
^{33}Ar	$-\frac{3}{2}$	$\frac{5}{2}^+$	1	1.798	0.002	1.997	0.199
^{33}Ar	$-\frac{3}{2}$	$\frac{3}{2}^+$	2	2.439	0.003	2.536	0.097
^{33}Ar	$-\frac{3}{2}$	$\frac{3}{2}^+$	3	3.154	0.009	3.343	0.189
^{33}Ar	$-\frac{3}{2}$	$\frac{5}{2}^+$	2	3.361	0.005	3.565	0.204
^{33}Ar	$-\frac{3}{2}$	$\frac{7}{2}^+$	1	3.456	0.006	3.788	0.332
^{33}Ar	$-\frac{3}{2}$	$\frac{5}{2}^+$	3	3.819	0.003	4.040	0.221
^{34}Ar	-1	0^+	1	-278.721	0.000	-278.615	0.106
^{34}Ar	-1	2^+	1	2.091	0.000	2.124	0.033
^{34}Ar	-1	2^+	2	3.288	0.001	3.043	-0.245
^{34}Ar	-1	0^+	2	3.873	0.003	3.615	-0.258
^{35}Ar	$-\frac{1}{2}$	$\frac{3}{2}^+$	1	-291.461	0.001	-291.533	-0.072
^{35}Ar	$-\frac{1}{2}$	$\frac{1}{2}^+$	1	1.184	0.001	1.131	-0.053
^{35}Ar	$-\frac{1}{2}$	$\frac{5}{2}^+$	1	1.751	0.000	1.704	-0.047
^{35}Ar	$-\frac{1}{2}$	$\frac{7}{2}^+$	1	2.603	0.000	2.699	0.096
^{35}Ar	$-\frac{1}{2}$	$\frac{3}{2}^+$	2	2.638	0.000	2.577	-0.061
^{35}Ar	$-\frac{1}{2}$	$\frac{5}{2}^+$	2	2.983	0.000	3.029	0.046
^{35}Ar	$-\frac{1}{2}$	$\frac{1}{2}^+$	2	3.884	0.010	3.927	0.043

Nucleus	T_z	J^π	J_i^π	Exp.	Error	USDC	ΔE
^{36}Ar	0	0^+	1	-306.717	0.000	-306.581	0.136
^{36}Ar	0	2^+	1	1.970	0.014	1.828	-0.142
^{36}Ar	0	0^+	2	4.329	0.001	4.480	0.151
^{36}Ar	0	2^+	2	4.440	0.001	4.177	-0.263
^{36}Ar	0	4^+	1	4.414	0.001	4.481	0.067
^{36}Ar	0	4^+	2	6.356	0.001	6.230	-0.126
^{36}Ar	0	2^+	3	6.611	0.001	6.443	-0.168
^{36}Ar	0	3^+	1	7.140	0.001	7.051	-0.089
^{37}Ar	$\frac{1}{2}$	$\frac{3}{2}^+$	1	-315.504	0.000	-315.459	0.045
^{37}Ar	$\frac{1}{2}$	$\frac{1}{2}^+$	1	1.410	0.001	1.412	0.002
^{37}Ar	$\frac{1}{2}$	$\frac{7}{2}^+$	1	2.217	0.001	2.111	-0.106
^{37}Ar	$\frac{1}{2}$	$\frac{5}{2}^+$	1	2.796	0.001	2.751	-0.045
^{37}Ar	$\frac{1}{2}$	$\frac{5}{2}^+$	2	3.171	0.001	3.166	-0.005
^{37}Ar	$\frac{1}{2}$	$\frac{3}{2}^+$	2	3.602	0.001	3.542	-0.060
^{37}Ar	$\frac{1}{2}$	$\frac{7}{2}^+$	2	4.624	0.001	4.506	-0.118
^{38}Ar	1	0^+	1	-327.343	0.000	-327.246	0.097
^{38}Ar	1	2^+	1	2.168	0.001	1.823	-0.345
^{35}K	$-\frac{3}{2}$	$\frac{3}{2}^+$	1	-278.804	0.001	-278.651	0.153
^{36}K	-1	2^+	1	-293.120	0.000	-293.148	-0.028
^{36}K	-1	3^+	1	0.810	0.000	0.829	0.019
^{36}K	-1	1^+	1	1.112	0.000	1.136	0.024
^{36}K	-1	1^+	2	1.619	0.001	1.629	0.010
^{36}K	-1	2^+	2	1.918	0.001	1.897	-0.021
^{36}K	-1	2^+	3	2.282	0.001	2.428	0.146
^{37}K	$-\frac{1}{2}$	$\frac{3}{2}^+$	1	-308.574	0.000	-308.494	0.080
^{37}K	$-\frac{1}{2}$	$\frac{1}{2}^+$	1	1.371	0.000	1.410	0.039
^{37}K	$-\frac{1}{2}$	$\frac{7}{2}^+$	1	2.285	0.000	2.158	-0.127
^{37}K	$-\frac{1}{2}$	$\frac{5}{2}^+$	1	2.750	0.000	2.788	0.038
^{37}K	$-\frac{1}{2}$	$\frac{5}{2}^+$	2	3.240	0.000	3.191	-0.049
^{37}K	$-\frac{1}{2}$	$\frac{3}{2}^+$	2	3.623	0.002	3.612	-0.011
^{37}K	$-\frac{1}{2}$	$\frac{7}{2}^+$	2	4.413	0.000	4.477	0.064

Nucleus	T_z	J^π	J_i^π	Exp.	Error	USDC	ΔE
^{38}K	0	3^+	1	-320.646	0.000	-320.717	-0.071
^{38}K	0	0^+	1	0.130	0.001	0.349	0.219
^{38}K	0	1^+	1	0.459	0.001	0.560	0.101
^{38}K	0	1^+	2	1.698	0.001	1.528	-0.170
^{38}K	0	2^+	1	2.401	0.001	2.284	-0.117
^{38}K	0	2^+	2	3.431	0.001	3.245	-0.186
^{38}K	0	1^+	3	3.857	0.001	4.272	0.415
^{39}K	$\frac{1}{2}$	$\frac{3}{2}^+$	1	-333.724	0.000	-333.958	-0.234
^{39}K	$\frac{1}{2}$	$\frac{1}{2}^+$	1	2.522	0.001	2.639	0.117
^{39}K	$\frac{1}{2}$	$\frac{5}{2}^+$	1	6.479	0.500	7.673	1.194
^{36}Ca	-2	0^+	1	-281.372	0.040	-281.308	0.064
^{36}Ca	-2	2^+	1	3.045	0.002	3.259	0.214
^{37}Ca	$-\frac{3}{2}$	$\frac{3}{2}^+$	1	-296.128	0.001	-296.247	-0.119
^{37}Ca	$-\frac{3}{2}$	$\frac{1}{2}^+$	1	1.606	0.001	1.735	0.129
^{37}Ca	$-\frac{3}{2}$	$\frac{5}{2}^+$	1	2.939	0.002	3.081	0.142
^{38}Ca	-1	0^+	1	-313.122	0.000	-312.956	0.166
^{38}Ca	-1	2^+	1	2.213	0.000	1.886	-0.327
^{39}Ca	$-\frac{1}{2}$	$\frac{3}{2}^+$	1	-326.417	0.001	-326.623	-0.206
^{39}Ca	$-\frac{1}{2}$	$\frac{1}{2}^+$	1	2.465	0.001	2.531	0.066

Over the course of the past four years, I have developed from the ground up a Python application to constrain configuration-interaction Hamiltonians for use with NuShellX and similar programs. This code requires an installation of NuShellX@MSU and Python 3 to run properly. The code is called Fitting Isospin Non-Conserving Hamiltonians, or FINCH.

FINCH takes in an initial interaction to ensure the first iteration's nuclear wavefunctions are realistic, and an *ab initio* interaction with which those poorly determined parameter linear combinations will be replaced. FINCH also needs a data set for a given model space. The Singular-Value Decomposition Fitting method is implemented. It comes preconfigured to slowly evolve the interaction and generate a series of solutions for each number of allowed varied linear combinations.

B.1 How it Works

The initial interaction is broken into several groups of parameters by whichever method the user chooses.

FINCH then calculates the wavefunctions and spectra for each nucleus included in the data set, along with the contribution from each group of parameters and collects this data.

The experimental data and group contributions are then used to generate an error matrix and error vector. The error matrix can then be decomposed into a diagonal matrix containing the **singular values** of the error matrix, along with a rotation matrix that defines the natural basis of the parameter space.

At this stage, we can replace the poorly determined linear combinations with those from the *ab initio* interaction. A choice must be made here as to how many linear combinations to replace. A new interaction can then be determined, and this process is iterated until convergence.

By default, the program will start with a small number of varied linear combinations (VLC) and increase until a full chi-squared fit is completed, and then begin "back propagating" by decreasing

the number of varied linear combinations until we simply recreate the *ab initio* interaction. This slow evolution prevents us from wandering too far in the parameter space.

If you run into any error you don't see an immediate cause for, try rerunning in a fresh folder. This fixes 9/10 problems with NuShellX manipulations done by the code.

B.2   FINCH Answer File

The code is designed to need very little alteration for a new fit with a new model space, a new set of parameter groups, or for the introduction of new data. To this end, the necessary declarations one would want to change in the code are gathered in a single file format *input.fans*. This file is copied over into *fit-inputs.py* and imported as a module in FINCH. The variables in the fans file are

- MODEL_SPACE: the name of the model space

- ZERO_BODY_TERM: the energy contribution from the core in the shell model

- A_MIN, A_MAX: the range of mass values in the model space

- PROTON_ORBITS, NEUTRON_ORBITS: the number of the orbits in order for the .mod file, using the NushellX k labeling

- DATA_FILE_NAME: Name of input file containing level data (*.levels)

- AI and INITIAL interactions: Can be the same or can choose more realistic initial interaction for the first iteration. Defined in parts by,

    - _SPE: name of input file containing single-particle energies and orbit references (*.spe)

    - _STRONG: name of input file containing the TBME for the strong interaction (*.tbme)

    - _COUL: name of input file containing the TBME for the Coulomb interaction (if left as " then Coulomb is not included)

    - _ISOV: input value for isovector strength (0.01 is 1%) (if left as " then Coulomb is not included)

- _ISOT: input value for isotensor strength (0.01 is 1%) (if left as " then Coulomb is not included)

- DATA_FILE: the file containing the levels/nuclei in the fit. Columns show: element symbol, A, Tz, T, 2J, P, jnum, Energy, and error followed by any relevant comments.

- NEW_RUN: True or False, allows you to rerun a fit in the same folder (by default the last folder ran)

- SKIP_RUNS: how many iterations in the fit you wish to skip over as the calculations had been done before

- PAUSE_BETWEEN: T or F, allows you to have the program pause between iterations to allow debugging/testing.

- fit_to_energies: T or F, include energies in .levels file in the fit

- fit_to_MED: T or F, include mirror energy differences for pairs in .levels file in the fit

- fit_to_TED: T or F, include c coefficients for triplets found in .levels file in the fit

- fit_to_delMED: T or F, (meant for *sd*-shell only) include energies in .levels file in the fit

- STBME_CHOICE: A setting for choosing the grouping method use on the strong interaction TBME

  - 1 - all TBME in one group with one overall strength parameter

  - 2 - all TBME in two groups based on isospin value (T=0,1)

  - 3 - all TBME in three groups evolving separately: pp, nn, and pn

  - 4 - TBME in isospin formalism groups so that pp,nn, and pn evolve together

  - 5 - TBME in isospin formalism groups, but only the diagonal are fit

  - 6 - All TBME in their own groups, each allowed to fit on their own

147

- 7 - Specific to the calcium fit in the fp shell UFP-CA

- 8 - Fit diagonal matrix elements except those involving excluded orbits

- 9 - Takes group numbers from '*custom.dat*' file (see sample input section)

- EXCLUDE_ORBIT_LIST: a list of integers corresponding to the absolute orbit reference for excluding TBME involving these orbits to fit. Used in conjunction with STBME_CHOICE=8

- DO_NOT_FIT: a list of integers corresponding to the group numbers for the parameters you wish to hold constant in the fit. See "fit_labels.dat"

- max_groups: by default the program will increase VLC until a full fit is reached. However, if the data set is lacking or you wish to save time, you can set a maximum number of VLC the program will iterate up to before "back propagating"

- CALCULATE_ALL: T or F, calculate the overlaps for excluded groups. Set to False for faster iterations, but lose information you may want later.

- VLC_CHOICES: Default is an empty list for a full fit. Or include integers in list to converge only at those VLC.

- FORWARD_ITER_MAX: The maximum number of iterations to spend on any VLC in the forward phase before moving on. The fit may be oscillating between two minima and never actually converge otherwise.

- FORWARD_ITER_MAX: The maximum number of iterations to spend on any VLC in the backward phase before moving on. The fit may be oscillating between two minima and never actually converge otherwise.

- MAX_GROUPS_CHOICE: The maximum number of VLC the fit will try to fit. If it is known that a full SVD will wail, set a reduced number here. A default of 0 sets this to the total number of groups in the fit.

- STORE_EVERY_VLC: T or F, store a copy of each possible VLC choice at each iteration. In cases with a large number of groups, this may cause significant delay between iterations.

B.3   Sample Inputs

Any new fit requires a handful of inputs. A list of levels to be included in the fit, the single-particle energies, and the two-body matrix elements, and an FINCH answer file to define the Hamiltonian.

B.3.1   Level Data (*.levels)

The level data includes the ground states and excited states in ascending mass order. It is important that the excited states of a nucleus be listed directly after the ground state.

The columns represent: The chemical symbol, the mass number A, $2T_z$, $2T$, $2J$, P, the J numbered ordering of the level, the experimental energy (important to note that the code assumes a negative ground state energy), and the associated error of the experimental energy. Comments can be added at the end of each line.

The experimental error is also used to include/exclude data from the fitting procedure. In some cases, a user might want to track a level during the fit but there is no well known value for that level, or you know the level will be wrong due to a breakdown of the model space. For this case use an error that is greater than 4 MeV. The output energy rms will include only those levels with less than a 0.3 MeV error, but this can be changed in the code around line 1000.

The below is a sample input for a *fpj4* model space fit to the Calcium isotopes.

```
Ca 48     8  8      0   0   1    -416.0009     4.0001
Ca 49     9  9      3   1   1    -421.1474     0.0002
Ca 49     9  9      1   1   1       2.0232     0.0003
Ca 49     9  9      5   1   1       3.9910     0.0002
Ca 50    10 10      0   0   1    -427.5082     0.0016
Ca 50    10 10      4   0   1       1.0267     0.0001
```

149

Ca	51	11	11	3	1	1	−432.3226	0.0005
Ca	51	11	11	1	1	1	1.7180	0.0010
Ca	51	11	11	5	1	1	2.3781	0.0002
Ca	51	11	11	3	1	2	2.9341	0.0010
Ca	51	11	11	7	1	1	3.4621	0.0002
Ca	51	11	11	5	1	2	3.4775	0.0023
Ca	51	11	11	9	1	1	4.3201	0.0004
Ca	52	12	12	0	0	1	−438.3278	0.0007
Ca	52	12	12	4	0	1	2.5630	0.0010
Ca	53	13	13	1	1	1	−441.5218	0.0424
Ca	53	13	13	5	1	1	1.7530	0.0150
Ca	53	13	13	3	1	1	2.2000	0.1000
Ca	54	14	14	0	0	1	−445.3650	0.0486
Ca	54	14	14	4	0	1	2.0430	0.0190
Ca	55	15	15	5	1	1	−446.9255	0.1600
Ca	56	16	16	0	0	1	−449.8568	0.2500
Ca	56	16	16	4	0	1	1.4560	0.0120
Ca	57	17	17	5	1	1	−451.7881	0.9900
Ca	58	18	18	0	0	1	−454.4447	0.0000
Ca	58	18	18	4	0	1	1.1150	0.0340
Ca	59	19	19	5	1	1	−455.8211	0.0000
Ca	59	19	19	9	0	1	1.3700	0.2501
Ca	60	20	20	0	0	1	−458.7272	0.0001
Ca	60	20	20	0	0	2	1.5500	0.2501

B.3.2   Single-Particle Energies *.spe

For a fit in the *fp*-shell with no Coulomb interaction, we set up the following file. fp.spe has columns indicating the SPE type (Coulomb 'c', or strong 's', not important unless adding mass dependence), the orbit label, and the SPE value.

```
s        5     -1.5615

s        6     -5.1465

s        7     -3.1233

s        8      2.6100
```

The lack of values for orbits $k = 1 - 4$ tells FINCH that it is only fitting neutron orbits.

B.3.3   Two-Body Matrix Elements *.tbme

This format is used for both the Coulomb and strong interaction TBME.

A two-body matrix element input is shown below with columns: k_1, k_2, k_3, k_4, J, T, and v with the k-orbits being labeled as in NuShellX .int files.

```
5   5   5   5    0   1   -1.1858

5   5   5   5    2   1   -0.0139

5   5   5   5    4   1    0.3571

5   5   6   5    2   1   -0.2710

5   5   6   5    4   1   -0.6748

5   5   8   8    4   1    0.0652
```

This is also the format of the '*custom.dat*' file for use with STBME_CHOICE=9 for specifying the strong TBME groups. The difference is instead of values in the seventh column, there is a group name. A group name of '0' will result in the TBME not being fit, and then all other unique group names form their own parameter group. For example, we can define three groups for the above TBME as,

151

```
5   5   5   5   0   1   1

5   5   5   5   2   1   2

5   5   5   5   4   1   3

5   5   6   5   2   1   0

5   5   6   5   4   1   0

5   5   8   8   4   1   0
```

which places each of the first three matrix elements in their own group and keeps the rest unconstrained.

A copy of '*custom.dat*' with all zeros is generated and placed in the 'groups/' folder each time FINCH is run. To use this, simply place it in the main working directory.

B.4   Sample Outputs

B.4.1   Extracted overlap files *.xfit

A csv file containing the calculated energy of a level and then it's overlaps corresponding to the fitting groups in order, example for "Ca59-5-1-1.xfit" (Nucleus-2J-P-jnum.xfit).

```
-445.6423,-7.3953,-20.1276,-6.139,1.0112,-0.7308,-0.0398,1.8355,...
```

B.4.2   Output Energies

A list of levels showing the input experimental energy and error, along with the interactions prediction for the level. NOTE: the output-energy.dat file in an iteration folder corresponds to the hamil.int files created in the previous iteration.

```
Ca48-0-0-1               -416.0009    4.0001 -416.0009    0.0000

Ca49-3-1-1               -421.1474    0.0002 -421.1474    0.0000

Ca49-1-1-1                  2.0232    0.0003    2.0232    0.0000

Ca49-5-1-1                  3.9910    0.0002    3.5850   -0.4060
```

Ca50-0-0-1	-427.5082	0.0016	-427.9231	-0.4149
Ca50-4-0-1	1.0267	0.0001	1.7820	0.7553
Ca51-3-1-1	-432.3226	0.0005	-431.4804	0.8422
Ca51-1-1-1	1.7180	0.0010	0.6319	-1.0861
Ca51-5-1-1	2.3781	0.0002	1.7708	-0.6073
Ca51-3-1-2	2.9341	0.0010	2.4860	-0.4481
Ca51-7-1-1	3.4621	0.0002	3.8833	0.4212
Ca51-5-1-2	3.4775	0.0023	2.1706	-1.3069
Ca51-9-1-1	4.3201	0.0004	3.5787	-0.7414
Ca52-0-0-1	-438.3278	0.0007	-436.7397	1.5881
Ca52-4-0-1	2.5630	0.0010	1.8999	-0.6631
Ca53-1-1-1	-441.5218	0.0424	-439.3412	2.1806
Ca53-5-1-1	1.7530	0.0150	1.2991	-0.4539
Ca53-3-1-1	2.2000	0.1000	1.5365	-0.6635
Ca54-0-0-1	-445.3650	0.0486	-442.6918	2.6732
Ca54-4-0-1	2.0430	0.0190	1.9621	-0.0809
Ca55-5-1-1	-446.9255	0.1600	-443.4941	3.4314
Ca56-0-0-1	-449.8568	0.2500	-445.7714	4.0854
Ca56-4-0-1	1.4560	0.0120	1.3203	-0.1357
Ca57-5-1-1	-451.7881	0.9900	-445.5049	6.2832
Ca58-0-0-1	-454.4447	0.0000	-446.9030	7.5417
Ca58-4-0-1	1.1150	0.0340	1.5160	0.4010
Ca59-5-1-1	-455.8211	0.0000	-445.6423	10.1788
Ca59-9-0-1	1.3700	0.2501	1.3755	0.0055
Ca60-0-0-1	-458.7272	0.0001	-446.2499	12.4773
Ca60-0-0-2	1.5500	0.2501	2.9802	1.4302

```
rms deviation:       3.6262
28
```

The final row corresponds to the number of well known levels included in the rms deviation calculation.

B.4.3 Output of Fit Scaling

At each iteration, a new interaction is made for every number of varied linear combinations up to the total number of groups. The information for these are stored in ouput-mults.dat in the form of multiplicative scaling factors that need to be applied to the current Hamiltonian to recover the full interaction. This file is used mainly as a guide in determining which parameters are important at different varied linear combination numbers.

Each row represents a single interaction for a varied linear combination number starting at 0 VLC or the *ab initio* interaction. The second half of the row represent the statistical uncertainty introduced by the fit to each parameter group.

B.5   List of Functions

There are many small functions that are clear in their usage by their name and are short enough to understand by simply reading them. The larger and more complex functions are listed here and their usage is described (this list is still being expanded on).

B.5.1   General Functions

These functions are very straightforward, and serve to clean up the code by not having to repeat simple (but lengthy) commands. **swap_element_label(z, fixlength=False)**
This function will exchange a proton number Z for the corresponding chemical element symbol, and vice-versa. The option *fixlength* can require that all symbols are returned as two characters in length by appending an underscore to one-letter symbols.

cycle_lbl(x)

NuShellX uses a single character to express the number of protons or neutrons a nucleus has in the model space. This requires using letters for those numbers greater than 9, which is accomplished with this function.

os_path(path)

A simple command to ensure that text strings meant to be interpreted as paths in the file structure are interpreted that way by Finch and NuShellX.

make_folder(path)

Check is a folder exits at *path* and if not, create one.

rms_from_lists(x, y)

Take the rms deviation between any two generic lists.

write_csv_file(fn, list)

Store *list* as a csv formatted file with name/path *fn*.

B.5.2 The Hamiltonian Class and its Companions

The Hamiltonian class is an object that stores the necessary information to describe an isospin-nonconserving interaction. It contains a number of methods and has associated functions that allow one to compare, change, and write interaction files that can be read by either Finch of NuShellX as needed. To initiate an instance of this class a Finch answer file (*.fans) is needed. To see the form of this input, see Section 5 on Sample Inputs.

__init__(self, ans_file, group_folder='groups')

The initialization of the class, which reads in the data in the answer file (ans_file). In here the mass dependence can be set for the interaction, and the two-body terms are typed and grouped according to conditions set in **type_tbme** and **group_tbme**. The groups are then stored by calling **make_files**. Finally a group number is applied to the two-body terms using **group_number** to aid in manipulation of the parameters in other functions.

strength_list(self)

155

Returns a python list showing the representative strength of each fitting group in order, to allow for normalization of the error matrix and vector found in **perform_fit**. If there is more than one parameter in a group, the first parameter is taken as the representative strength, otherwise it is just the strength of the single parameter. This can be changed however you like.

comparison_to_bg(self, bg_ham, name)

To better aid in comparisons between the fitted interactions and the original interaction *bg_ham*, this function creates an *.int file showing the original SPE and TBME in comments. The file should still work in NuShellX with these added comments.

make_files(self, a_min, a_max, group_folder)

Takes the total Hamiltonian and creates the necessary *.int files for calculation. These include a hamil.int file that contains the full interaction at a specific mass A for masses between *a_min* and *a_max*, and group*.int files that define the parameter groups at each mass. Additionally, a file is created called parts.nux that lists the group*.int files so that NuShellX can calculate their overlaps with the full wavefunctions.

full_tbme(self)

If the Hamiltonian includes more than one source of two-body terms (such as Coulomb, isotensor, or isovector), than this method will combine them into a single interaction to be written into a file for use in NuShellX.

full_spe(self)

If the Hamiltonian includes more than one source of single-particle energies (such as Coulomb, isotensor, or isovector), than this method will combine them into a single interaction to be written into a file for use in NuShellX.

normalize_scale(self, a)

Universal interactions can contain a mass dependence in the two-body (and in principle the one-body) terms, and this method will normalize the interaction to a specific mass A.

int_at_mass(self, a, folder)

The interaction is collected and normalized to a mass A, and stored as an *.int file in **folder**.

store(self, folder)

A function to store the interaction in *.fans format and in the NuShellX *.int format.

make_isotensor(self, alpha)

A method to create the isotensor interaction in a given strong interaction for a given isotensor strength *alpha*. The isotensor strength is modeled as the scaled increase of the *pn* $T = 1$ two-body terms over the average of the *nn* and *pp* terms.

make_isovector(self, alpha)

A method to create the isovector interaction in a given strong interaction for a given isovector strength *alpha*. The isovector strength is modeled as a scaled increase/decrease of the *nn*/*pp* terms so that their average remains the same to avoid interference with **make_isotensor**.

int_file(self, spe, tbme, name, replace_k=True)

The generic interaction file creation method, with options to allow other functions to effectively utilize it in specific cases.

write_groups(self, folder)

This function performs the work described in **make_files** for a given interaction normalized to some mass. It also generates the 'fit_labels.dat' file which contains a description of what is contained in each two-body interaction group.

group_number(row)

Determines the numerical label for a given group name using 'fit_labels.dat' and returns it.

group_tbme(row)

Using the rules defined in this function, a two-body matrix element is sorted into a group and a label corresponding to that group is returned.

type_tbme(row)

Determines the type of two-body matrix element (*pp*, *pn*, *nn*).

read_tbme(name)

Reads in a set of two-body matrix elements in a file located at *name*.

read_spe(name)

Reads in a set of single-particle energies in a file located at *name*.

update_hamiltonian(old_ham, bg_ham, mults)

A new Hamiltonian class instance is initialized, and using the scaling factors (*mults*) generated in **perform_fit** are used to transform the *old_ham* into a new interaction. The background interaction is also sent here so that the rms deviation between the new interaction and the *ab initio* can be calculated.

order_tbme(df)

This function will reorder the two-body dataframe into the standardized ordering used by NuShellX. This aids in readability and comparisons between interactions.

B.5.3 Running NuShellX and Extracting Results

This section of code is the main gateway to manipulating NuShellX and collecting and formatting its results. The main time save is found here in the form of python multiprocessing, which allows for many nuclei to be calculated at once on a multi-core machine.

setup_dataframe(file, ham)

The nuclear levels included in the data set are read in here and stored in a pandas dataframe. This dataframe is then used to determine the needed calculations.

generate_ans(fit_loc, a, z, j, p, jnum, min_error)

The NuShellX answer file is generated here at *fit_loc* for a nucleus with the properties *a, z, j, p*. The minimum error parameter refers to the minimum experimental error for a level in the nucleus you are trying to calculate. To save time, nuclei with high errors don't need to be fully calculated. See comments in code for further detail.

This function also copies in the interaction to be used for calculation and the parts.nux file.

single_calc(x)

Called from **run_multiproc**, this runs in parallel to calculate all nuclei in the data set and retrieve the results. The parameter *x* is unwrapped into *df_nuc*, *group_count*, and *run_name* which are the

subset of the dataframe relevant to a single nucleus at a single spin, the number of groups/parameters in the fit, and the folder in which to store the results.

A path is made for the nucleus to be calculated in, performs those calculations, and extracts the list of overlaps (contributions) to the state energies corresponding to the groups/parameters you are fitting. These are saved for use in the fitting procedure.

run_multiproc(df, r_name, group_count)

Takes in the pandas dataframe containing the nuclear level data, splits it into chunks and initiates the calculations. Once all calculations are complete the code will continue.

read_lpt(location, lineskips=6, corner=False)

The main output file in NuShellX for energy levels has the extension *.lpt. This function reads in these lpt files (check line skips length if this fails, different interactions require different numbers of lines to be skipped), and stores them as a dataframe.

B.5.4   Performing the Fit

Here the data collected by run_multiproc is used to set up the data error matrix and vector, perform the SVD, and update the Hamiltonian to allow a new iteration to begin. Along with binding and excitation energy inputs as data, this function has the (off by default) ability to also include the mirror energy differences, c-coefficients of the IMME, and double energy differences of mirror pairs. This is useful to constrain the isospin non-conserving interactions.

avg_group_ratios(a, b)

Find the average ratio between parameters in the defined groups for two interactions a and b. This is being phased out in favor of normalizing the error_matrix and error_vectors in **perform_fit** accomplished using the class method **strength_list.**

setup_b_list(df)

Takes the levels dataframe and determines if any mirror pairs are included, and prepares the program to fit on those mirror energy differences.

setup_c_list(df)

Similar to the above, but checks for complete $T = 1$ triplets to allow for fitting on the c-coefficients.

setup_b_diff_list(df)

Similar to the above, but checks for specific differences between mirror pairs, meant for fitting the isovector strength in the *sd* shell data.

subset_groups(group_list, hold, no_energy=False)

As the code allows for groups to be held constant, we need a way to extract a subset of a list that corresponds to those groups that are actually fit.

superset_groups(group_list, hold, dimension, no_energy=False)

As the code allows for groups to be held constant, we need a way to build up a superset of a list that corresponds to those groups that are actually fit.

perform_fit(level_data, folder, cur_ham, bg_ham, vlc, dim, held_groups)

This is the meat of the program, where the fit is actually performed on the data given the NuShellX results. Check back for further documentation.

setup_fit(df, store_output, iterate_fit, multipliers, fit_type)

To allow for multiple data types to be included in a single fit, this sub function was created. It generalizes the generation of the error matrix and error vector.

read_xfit(loc, nuc, k)

Creates a python list from the extracted overlaps for the fitting groups collected by **single_calc**.

b_ovl_list(nuc_1, nuc_2, num)

Creates an overlap list for a mirror pair found in the data.

tbme_plot(r_name, bg_ham, curr_ham, vlc_num)

A very bare-bones plotting function to give quick glances at the changes in the two-body matrix elements during the fitting procedure.

BIBLIOGRAPHY

BIBLIOGRAPHY

[1] NNDC, *Nuclear chart*, 2021.

[2] M. Thoennessen, *Discovery of nuclides project*.

[3] C. R. Nave, *Hyperphysics*.

[4] J. J. Thomson, Philosophical Magazine **101**, 237 (1904).

[5] N. B. D. phil., The London, Edinburgh, and Dublin Philosophical Magazine and Journal of Science **26**, 1 (1913).

[6] G. Gamow, Proc. R. Soc. Lond. A **126**, 632 (1930).

[7] C. F. v. Weizsäcker, Proc. R. Soc. Lond. A **96**, 431 (1935).

[8] Wikipedia, *Semi-empirical mass formula — Wikipedia, the free encyclopedia*, `http://en.wikipedia.org/w/index.php?title=Semi-empirical\%20mass\%20formula&oldid=1028181413`, [Online; accessed 08-July-2021], 2021.

[9] B. A. Brown, *Lecture notes in nuclear structure*.

[10] NobelPrize.org, *The nobel prize in physics 1963*.

[11] W. D. M. Rae, *Nushell*.

[12] B. A. Brown and W. D. M. Rae, *Nushellx@msu*.

[13] S. R. Stroberg, H. Hergert, S. K. Bogner, and J. D. Holt, Annual Review of Nuclear and Particle Science **69**, 307 (2019).

[14] A. Magilligan and B. A. Brown, Phys. Rev. C **101**, 064312 (2020).

[15] B. A. Brown and W. A. Richter, Phys. Rev. C **74**, 034315 (2006).

[16] M. Honma, T. Otsuka, B. A. Brown, and T. Mizusaki, Phys. Rev. C **65**, 061301 (2002).

[17] M. Honma, T. Otsuka, B. A. Brown, and T. Mizusaki, Phys. Rev. C **69**, 034335 (2004).

[18] M. Honma, T. Otsuka, B. A. Brown, and T. Mizusaki, Eur. Phys. Jour. **A25**, 499 (2005).

[19] Y. Utsuno, T. Otsuka, B. A. Brown, M. Honma, T. Mizusaki, and N. Shimizu, Phys. Rev. C **86**, 051301 (2012).

[20] R. S. Lubna, K. Kravvaris, S. L. Tabor, V. Tripathi, A. Volya, E. Rubino, J. M. Allmond, B. Abromeit, L. T. Baby, and T. C. Hensley, Phys. Rev. C **100**, 034308 (2019).

[21] R. S. Lubna, K. Kravvaris, S. L. Tabor, V. Tripathi, E. Rubino, and A. Volya, Phys. Rev. Research **2**, 043342 (2020).

[22] S. Mukhopadhyay, B. P. Crider, B. A. Brown, S. F. Ashley, A. Chakraborty, A. Kumar, M. T. McEllistrem, E. E. Peters, F. M. Prados-Estévez, and S. W. Yates, Phys. Rev. C **95**, 014327 (2017).

[23] W. Heisenberg, Z. Phys. **77** (1932).

[24] E. P. Wigner, Proc. of the R.A. Welch Foundation Conf. on Chemical Research, Houston **Vol. 1**, edited by W. O. Millikan (1957).

[25] S. Weinberg and S. B. Treiman, Phys. Rev. **116**, 465 (1959).

[26] P.-G. Reinhard and W. Nazarewicz, Phys. Rev. C **81**, 051303 (2010).

[27] J. Dobaczewski, W. Nazarewicz, and P.-G. Reinhard, Journal of Physics G: Nuclear and Particle Physics **41**, 074001 (2014).

[28] B. H. Wildenthal, Progress in Particle and Nuclear Physics **11**, 5 (1984).

[29] B. A. Brown and B. H. Wildenthal, Annual Review of Nuclear and Particle Science **38**, 29 (1988).

[30] W. A. Richter, S. Mkhize, and B. A. Brown, Phys. Rev. C **78**, 064302 (2008).

[31] W. Ormand and B. Brown, Nuclear Physics A **491**, 1 (1989).

[32] Y. H. Lam, N. A. Smirnova, and E. Caurier, Phys. Rev. C **87**, 054304 (2013).

[33] M. Hjorth-Jensen, T. T. Kuo, and E. Osnes, Physics Reports **261**, 125 (1995).

[34] S. R. Stroberg, A. Calci, H. Hergert, J. D. Holt, S. K. Bogner, R. Roth, and A. Schwenk, Phys. Rev. Lett. **118**, 032502 (2017).

[35] S. R. Stroberg, S. K. Bogner, H. Hergert, and J. D. Holt, *Non-empirical interactions for the nuclear shell model: an update*, 2019.

[36] M. Wang, G. Audi, F. G. Kondev, W. Huang, S. Naimi, and X. Xu, Chinese Physics C **41**, 030003 (2017).

[37] G. Lotay, personal communication, 2019.

[38] E. K. Warburton, J. A. Becker, and B. A. Brown, Phys. Rev. C **41**, 1147 (1990).

[39] J. M. R. Fox and C. W. Johnson, *Uncertainty quantification of an empirical shell-model interaction using principal component analysis*, 2019.

[40] R. G. Thomas, Phys. Rev. **88**, 1109 (1952).

[41] J. B. Ehrman, Phys. Rev. **81**, 412 (1951).

[42] L. Huth, V. Durant, J. Simonis, and A. Schwenk, Phys. Rev. C **98**, 044301 (2018).

[43] G. A. Miller and J. E. Spencer, Annals of Physics **100**, 562 (1976).

[44] R. B. Wiringa, V. G. J. Stoks, and R. Schiavilla, Phys. Rev. C **51**, 38 (1995).

[45] B. Longfellow, A. Gade, B. A. Brown, D. Bazin, P. C. Bender, M. Bowry, P. D. Cottle, B. Elman, E. Lunderberg, A. Magilligan, M. Spieker, D. Weisshaar, and S. J. Williams, Phys. Rev. C **99**, 064330 (2019).

[46] B. A. Brown, W. A. Richter, and R. Lindsay, Phys. Lett. B **483**, 49 (2000).

[47] L. O. Lamm, C. P. Browne, J. Görres, S. M. Graff, M. Wiescher, A. A. Rollefson, and B. A. Brown, Nuclear Physics **A510**, 503 (1990).

[48] N. M. Clarke, S. Roman, C. N. Pinder, and P. R. Hayes, J. Phys. G: Nucl. Part. Phys. **19**, 1411 (1993).

[49] B. A. Brown, A. E. Champagne, H. T. Fortune, and R. Sherr, Phys. Rev. C **48**, 1456 (1993).

[50] D. Seweryniak, P. Woods, B. Blank, M. Carpenter, T. Davinson, S. Freeman, J. Görres, A. Heinz, R. Janssens, H. Mahmud, T. Khoo, Z. Liu, G. Mukherjee, E. Rehm, F. Sarazin, J. Shergur, M. Shawcross, S. Sinha, and A. Woehr, Physics Letters B **590**, 170 (2004).

[51] J. Wallace, P. Woods, G. Lotay, A. Alharbi, A. Banu, H. David, T. Davinson, M. McCleskey, B. Roeder, E. Simmons, A. Spiridon, L. Trache, and R. Tribble, Physics Letters B **712**, 59 (2012).

[52] B. Glassman, D. Pérez-Loureiro, C. Wrede, J. Allen, D. Bardayan, M. Bennett, B. Brown, K. Chipps, M. Febbraro, M. Friedman, C. Fry, M. Hall, O. Hall, S. Liddick, P. O'Malley, W. Ong, S. Pain, C. Prokop, S. Schwartz, P. Shidling, H. Sims, P. Thompson, and H. Zhang,

Physics Letters B **778**, 397 (2018).

[53] J.-C. Thomas, L. Achouri, J. Äystö, R. Béraud, B. Blank, G. Canchel, S. Czajkowski, P. Dendooven, A. Ensallem, J. Giovinazzo, N. Guillet, J. Honkanen, A. Jokinen, A. Laird, M. Lewitowicz, C. Longour, F. de Oliveira Santos, K. Peräjärvi, and M. Stanoiu, The European Physical Journal A - Hadrons and Nuclei **21**, 419 (2004).

[54] H. T. Fortune, Phys. Rev. C **96**, 054329 (2017).

[55] J. Tian, N. Wang, C. Li, and J. Li, Phys. Rev. C **87**, 014313 (2013).

[56] G. Audi, F. G. Kondev, M. Wang, W. Huang, and S. Naimi, Chinese Physics C **41**, 030001 (2017).

[57] I. Mukha, L. V. Grigorenko, D. Kostyleva, L. Acosta, E. Casarejos, A. A. Ciemny, W. Dominik, J. A. Dueñas, V. Dunin, J. M. Espino, A. Estradé, F. Farinon, A. Fomichev, H. Geissel, A. Gorshkov, Z. Janas, Kami ński, O. Kiselev, R. Knöbel, S. Krupko, M. Kuich, Y. A. Litvinov, G. Marquinez-Durán, I. Martel, C. Mazzocchi, C. Nociforo, A. K. Ordúz, M. Pfützner, S. Pietri, M. Pomorski, A. Prochazka, S. Rymzhanova, A. M. Sánchez-Benıtez, C. Scheidenberger, P. Sharov, H. Simon, B. Sitar, R. Slepnev, M. Stanoiu, P. Strmen, I. Szarka, M. Takechi, Y. K. Tanaka, H. Weick, M. Winkler, J. S. Winfield, X. Xu, and M. V. Zhukov, Phys. Rev. C **98**, 064308 (2018).

[58] I. Mukha, L. V. Grigorenko, X. Xu, L. Acosta, E. Casarejos, A. A. Ciemny, W. Dominik, J. Duénas-Dıaz, V. Dunin, J. M. Espino, A. Estradé, F. Farinon, A. Fomichev, H. Geissel, T. A. Golubkova, A. Gorshkov, Z. Janas, Kami ński, O. Kiselev, R. Knöbel, S. Krupko, M. Kuich, Y. A. Litvinov, G. Marquinez-Durán, I. Martel, C. Mazzocchi, C. Nociforo, A. K. Ordúz, M. Pfützner, S. Pietri, M. Pomorski, A. Prochazka, S. Rymzhanova, A. M. Sánchez-Benıtez, C. Scheidenberger, P. Sharov, H. Simon, B. Sitar, R. Slepnev, M. Stanoiu, P. Strmen, I. Szarka, M. Takechi, Y. K. Tanaka, H. Weick, M. Winkler, J. S. Winfield, and M. V. Zhukov, Phys. Rev. Lett. **115**, 202501 (2015).

[59] M. B. Bennett, C. Wrede, B. A. Brown, S. N. Liddick, D. Pérez-Loureiro, D. W. Bardayan, A. A. Chen, K. A. Chipps, C. Fry, B. E. Glassman, C. Langer, N. R. Larson, E. I. McNeice, Z. Meisel, W. Ong, P. D. O'Malley, S. D. Pain, C. J. Prokop, H. Schatz, S. B. Schwartz, S. Suchyta, P. Thompson, M. Walters, and X. Xu, Phys. Rev. Lett. **116**, 102502 (2016).

[60] D. Melconian, S. Triambak, C. Bordeanu, A. Garcıa, J. C. Hardy, V. E. Iacob, N. Nica, H. I. Park, G. Tabacaru, L. Trache, I. S. Towner, R. E. Tribble, and Y. Zhai, Phys. Rev. Lett. **107**, 182301 (2011).

[61] D. Melconian, S. Triambak, C. Bordeanu, A. Garcıa, J. C. Hardy, V. E. Iacob, N. Nica, H. I. Park, G. Tabacaru, L. Trache, I. S. Towner, R. E. Tribble, and Y. Zhai, Phys. Rev. C **85**, 025501 (2012).

[62] B. E. Glassman, D. Pérez-Loureiro, C. Wrede, J. M. Allen, D. W. Bardayan, M. B. Bennett, B. A. Brown, K. A. Chipps, M. Febbraro, C. Fry, M. R. Hall, O. Hall, S. N. Liddick, A. Magilligan, P. O'Malley, W.-J. Ong, S. D. Pain, P. Shidling, H. Sims, P. Thompson, and H. Zhang, *Superallowed* $0^+ \rightarrow 0^+$ *β decay of t* = 2 20*mg: q_{ec} value and βγ branching*, 2019.

[63] IDS Collaboration, Lund, M. V., Andreyev, A., Borge, M. J. G., Cederkäll, J., De Witte, H., Fraile, L. M., Fynbo, H. O. U., Greenlees, P. T., Harkness-Brennan, L. J., Howard, A. M., Huyse, M., Jonson, B., Judson, D. S., Kirsebom, O. S., Konki, J., Kurcewicz, J., Lazarus, I., Lica, R., Lindberg, S., Madurga, M., Marginean, N., Marginean, R., Marroquin, I., Mihai, C., Munch, M., Nacher, E., Negret, A., Nilsson, T., Page, R. D., Pascu, S., Perea, A., Pucknell, V., Rahkila, P., Rapisarda, E., Riisager, K., Rotaru, F., Sotty, C., Stanoiu, M., Tengblad, O., Turturica, A., Van Duppen, P., Vedia, V., Wadsworth, R., and Warr, N., Eur. Phys. J. A **52**, 304 (2016).

[64] A. Piechaczek, M. Mohar, R. Anne, V. Borrel, B. Brown, J. Corre, D. Guillemaud-Mueller, R. Hue, H. Keller, S. Kubono, V. Kunze, M. Lewitowicz, P. Magnus, A. Mueller, T. Nakamura, M. Pfützner, E. Roeckl, K. Rykaczewski, M. Saint-Laurent, W.-D. Schmidt-Ott, and O. Sorlin, Nuclear Physics A **584**, 509 (1995).

[65] A. A. Kwiatkowski, B. R. Barquest, G. Bollen, C. M. Campbell, D. L. Lincoln, D. J. Morrissey, G. K. Pang, A. M. Prinke, J. Savory, S. Schwarz, C. M. Folden, D. Melconian, S. K. L. Sjue, and M. Block, Phys. Rev. C **80**, 051302 (2009).

[66] Blank, B., Adimi, N., Alcorta, M., Bey, A., Borge, M. J. G, Brown, B. A., de Oliveira Santos, F., Dossat, C., Fynbo, H. O. U., Giovinazzo, J., Knudsen, H. H., Madurga, M., Magilligan, A., Matea, I., Perea, A., Sümmerer, K., Tengblad, O., and Thomas, J. C., Eur. Phys. J. A **57**, 28 (2021).

[67] D. H. Wilkinson, Phys. Rev. C **7**, 930 (1973).

[68] B. Brown and B. Wildenthal, Atomic Data and Nuclear Data Tables **33**, 347 (1985).

[69] W.-T. Chou, E. K. Warburton, and B. A. Brown, Phys. Rev. C **47**, 163 (1993).

[70] G. Martınez-Pinedo, A. Poves, E. Caurier, and A. P. Zuker, Phys. Rev. C **53**, R2602 (1996).

[71] P. Gysbers et al., Nat. Phys. **15**, 428 (2019).

[72] P. Bączyk, J. Dobaczewski, M. Konieczka, W. Satuła, T. Nakatsukasa, and K. Sato, Physics Letters B **778**, 178 (2018).

[73] M. S. Martin, S. R. Stroberg, J. D. Holt, and K. G. Leach, *Testing isospin symmetry breaking in ab initio nuclear theory*, 2021.

[74] S. Michimasa, M. Kobayashi, Y. Kiyokawa, S. Ota, D. S. Ahn, H. Baba, G. P. A. Berg, M. Dozono, N. Fukuda, T. Furuno, E. Ideguchi, N. Inabe, T. Kawabata, S. Kawase, K. Kisamori, K. Kobayashi, T. Kubo, Y. Kubota, C. S. Lee, M. Matsushita, H. Miya, A. Mizukami, H. Nagakura, D. Nishimura, H. Oikawa, H. Sakai, Y. Shimizu, A. Stolz, H. Suzuki, M. Takaki, H. Takeda, S. Takeuchi, H. Tokieda, T. Uesaka, K. Yako, Y. Yamaguchi, Y. Yanagisawa, R. Yokoyama, K. Yoshida, and S. Shimoura, Phys. Rev. Lett. **121**, 022506 (2018).

[75] S. R. Stroberg, J. D. Holt, A. Schwenk, and J. Simonis, Phys. Rev. Lett. **126**, 022501 (2021).

[76] K. Hebeler, S. K. Bogner, R. J. Furnstahl, A. Nogga, and A. Schwenk, Phys. Rev. C **83**, 031301 (2011).

[77] A. P. Zuker, Phys. Rev. Lett. **90**, 042502 (2003).

[78] J. Ash, H. Iwasaki, Mijatovi ć, T. Budner, R. Elder, B. Elman, M. Friedman, A. Gade, M. Grinder, J. Henderson, B. Longfellow, A. Revel, D. Rhodes, M. Spieker, Y. Utsuno, D. Weisshaar, and C. Y. Wu, Phys. Rev. C **103**, L051302 (2021).

[79] A. Gade, J. A. Tostevin, V. Bader, T. Baugher, D. Bazin, J. S. Berryman, B. A. Brown, D. J. Hartley, E. Lunderberg, F. Recchia, S. R. Stroberg, Y. Utsuno, D. Weisshaar, and K. Wimmer, Phys. Rev. C **93**, 031601 (2016).

[80] W. Catford, L. Fifield, T. Ophel, N. Orr, D. Weisser, and C. Woods, Nuclear Physics A **489**, 347 (1988).

[81] L. Coraggio, G. De Gregorio, A. Gargano, N. Itaco, T. Fukui, Y. Z. Ma, and F. R. Xu, Phys. Rev. C **102**, 054326 (2020).

[82] O. B. Tarasov, D. S. Ahn, D. Bazin, N. Fukuda, A. Gade, M. Hausmann, N. Inabe, S. Ishikawa, N. Iwasa, K. Kawata, T. Komatsubara, T. Kubo, K. Kusaka, D. J. Morrissey, M. Ohtake, H. Otsu, M. Portillo, T. Sakakibara, H. Sakurai, H. Sato, B. M. Sherrill, Y. Shimizu, A. Stolz, T. Sumikama, H. Suzuki, H. Takeda, M. Thoennessen, H. Ueno, Y. Yanagisawa, and K. Yoshida, Phys. Rev. Lett. **121**, 022501 (2018).

[83] B. A. Brown, Physics **3**, 104 (2010).

[84] B. A. Brown, Phys. Rev. C **58**, 220 (1998).

[85] *DFT mass tables*, 2021.

[86] J. Bartel, P. Quentin, M. Brack, C. Guet, and H.-B. Håkansson, Nuclear Physics A **386**, 79 (1982).

[87] M. Kortelainen, T. Lesinski, J. Moré, W. Nazarewicz, J. Sarich, N. Schunck, M. V. Stoitsov, and S. Wild, Phys. Rev. C **82**, 024313 (2010).

[88] L. Neufcourt, Y. Cao, W. Nazarewicz, E. Olsen, and F. Viens, Phys. Rev. Lett. **122**, 062502 (2019).

[89] S. M. Lenzi, F. Nowacki, A. Poves, and K. Sieja, Phys. Rev. C **82**, 054301 (2010).

[90] B. Bharti, P. C. Srivastava, and K. Kaneko, Journal of Physics G: Nuclear and Particle Physics **47**, 065105 (2020).

[91] G. Hagen, M. Hjorth-Jensen, G. R. Jansen, R. Machleidt, and T. Papenbrock, Phys. Rev. Lett. **109**, 032502 (2012).

[92] G. Hagen, P. Hagen, H.-W. Hammer, and L. Platter, Phys. Rev. Lett. **111**, 132501 (2013).

[93] H. Hergert, S. K. Bogner, T. D. Morris, S. Binder, A. Calci, J. Langhammer, and R. Roth, Phys. Rev. C **90**, 041302 (2014).

[94] G. Hagen, M. Hjorth-Jensen, G. R. Jansen, and T. Papenbrock, Physica Scripta **91**, 063006 (2016).

[95] J. D. Holt, J. Menéndez, J. Simonis, and A. Schwenk, Phys. Rev. C **90**, 024312 (2014).

[96] S. Michimasa, M. Kobayashi, Y. Kiyokawa, S. Ota, R. Yokoyama, D. Nishimura, D. S. Ahn, H. Baba, G. P. A. Berg, M. Dozono, N. Fukuda, T. Furuno, E. Ideguchi, N. Inabe, T. Kawabata, S. Kawase, K. Kisamori, K. Kobayashi, T. Kubo, Y. Kubota, C. S. Lee, M. Matsushita, H. Miya, A. Mizukami, H. Nagakura, H. Oikawa, H. Sakai, Y. Shimizu, A. Stolz, H. Suzuki, M. Takaki, H. Takeda, S. Takeuchi, H. Tokieda, T. Uesaka, K. Yako, Y. Yamaguchi, Y. Yanagisawa, K. Yoshida, and S. Shimoura, Phys. Rev. Lett. **125**, 122501 (2020).

[97] E. Leistenschneider, E. Dunling, G. Bollen, B. A. Brown, J. Dilling, A. Hamaker, J. D. Holt, A. Jacobs, A. A. Kwiatkowski, T. Miyagi, W. S. Porter, D. Puentes, M. Redshaw, M. P. Reiter, R. Ringle, R. Sandler, C. S. Sumithrarachchi, A. A. Valverde, and I. T. Yandow, Phys. Rev. Lett. **126**, 042501 (2021).

[98] Z. Meisel, S. George, S. Ahn, D. Bazin, B. A. Brown, J. Browne, J. F. Carpino, H. Chung, R. H. Cyburt, A. Estradé, M. Famiano, A. Gade, C. Langer, Mato š, W. Mittig, F. Montes, D. J. Morrissey, J. Pereira, H. Schatz, J. Schatz, M. Scott, D. Shapira, K. Smith, J. Stevens, W. Tan, O. Tarasov, S. Towers, K. Wimmer, J. R. Winkelbauer, J. Yurkon, and R. G. T. Zegers, Phys. Rev. C **101**, 052801 (2020).